Ludwig-Maximilians-Universität München

Fakultät für Physik

The $\pi^-\eta$ and $\pi^-\eta'$ Systems in Exclusive 190 GeV π^-p Reactions at COMPASS (CERN)

Autor:

Tobias Schlüter

Gutachter:

Prof. Dr. Wolfgang Dünnweber

Prof. Dr. Otmar Biebel

Abgabedatum: 2012-06-27

Datum der mündlichen Prüfung: 2012-08-02

Dissertation der Fakultät für Physik der Ludwig-Maximilians-Universität München

Zusammenfassung

Diese Dissertation widmet sich der Analyse der Eigenschaften der Systeme $\pi^-\eta$ und $\pi^-\eta'$. Wir untersuchen dazu Daten, welche das COMPASS-Experiment am CERN im Jahr 2008 bei den Reaktionen $\pi^- p \to \pi^-\pi^-\pi^+\pi^0 p$ bzw. $\pi^- p \to \pi^-\pi^-\pi^+\eta$ mit niedrigem Impulsübertrag auf das Targetproton ($0.1\,\mathrm{GeV}^2 < -t < 1\,\mathrm{GeV}^2$) aufgezeichnet hat. Die isoskalaren Mesonen η und η' erscheinen dann als Peaks in den invariante-Masse-Spektren der Dreikörpersysteme $\pi^-\pi^+\pi^0$ bzw. $\pi^-\pi^+\eta$, die jeweils im Endzustand $\pi^-\pi^+\gamma\gamma$ selektiert wurden. Wir zerlegen die so gewonnenen Zweikörpersysteme nach Partialwellen. Wir finden eine einfache Vorschrift, welche es erlaubt allein anhand von Phasenraumfaktoren mit guter Übereinstimmung die Amplituden der geraden Partialwellen D_+ ($J^P = 2^+$) und G_+ ($J^P = 4^+$) zwischen den beiden Endzuständen zu übersetzen. Desweiteren gehen wir die Frage nach, ob eine beobachtete Intensität der P_+-Welle mit einer Resonanz identifiziert werden kann. Ihr neutraler Isospinpartner hätte Quantenzahlen $J^{PC} = 1^{-+}$, welche nicht mit einem Fermion-Antifermion-Zustand identifiziert werden können, welche also nicht einem Quarkmodellzustand zugeordnet werden können. Zudem identifizieren wir die bekannten Mesonen $a_2(1320)$ und $a_4(2040)$, deren Verzweigungsverhältnisse wir bestimmen

Bevor wir zu diesen Ergebnissen kommen, beschreiben wir die bekannten Eigenschaften der starken Wechselwirkung im Hinblick auf die Systematisierung mesonischer Systeme. Wir diskutieren die im von uns betrachteten Bereich hoher Energien und niedriger Impulsüberträge übliche Behandlung von Streuprozessen als t-Kanalaustausch sogenannter Regge-Trajektorien und erörtern Symmetrieeigenschaften, welche die Datenanlyse erheblich vereinfachen.

Anschließend diskutieren wir das COMPASS-Experiment, wobei wir besonderes Gewicht auf die Teile legen, welche bei der Gewinnung der in dieser Arbeit analysierten Daten wesentlich waren. Insbesondere beschreiben wir den als Teil dieser Arbeit entwickelten Sandwich-Veto-Detektor, ein elektromagneitsches Kalorimeter, welches als wesentlicher Teil des Triggersystems die verwertbaren Daten um einen Faktor > 3 anreicherte, indem es Ereignisse ausschloss, in welchen Reaktionsprodukte das Spektrometer verfehlten.

Um die Datenselektion mit bestmöglicher Qualität durchführen zu können, wurde im Rahmen dieser Arbeit ein datenbasiertes Eichverfahren für die elektromagnetischen Kalorimeter des COMPASS-Experiments entwickelt. Eine Software zum kinematischen Fit wurde ebenso entwickelt und benutzt, um eine möglichst hohe Auflösung zu erzielen. Wir zeigen kinematische Größen, die die vorliegenden Produktionsmechanismen verdeutlichen.

Wir erläutern das Analyseverfahren der sogenannten Partialwellenanalyse in seiner Anwendung auf die betrachteten periphär produzierten Systeme aus zwei Pseudoska-

laren Teilchen und die benutzten Softwarelösungen, welche teilweise eigens für diese Arbeit entwickelt wurden. Diese Techniken wenden wir auf die Daten an und kommen so zu den bereits oben erwähnten Ergebnissen. Wir vergleichen auch die Ergebnisse, die wir mit zwei verschiedenen Ansätzen erhalten. Beim einen wird das $\pi^-\eta^{(\prime)}$-System als Zweikörpersystem behandelt, beim anderen werden die Dreikörperzerfälle $\eta \to \pi^-\pi^+\pi^0$ bzw. $\eta' \to \pi^-\pi^+\eta$ zur Untergrundseparation benutzt und somit ein Vierkörpersystem behandelt.

Wir heben an dieser Stelle besonders hervor, dass wir eine einfache Transformation finden, welche es erlaubt die beobachteten Partialwellen D_+ und G_+ mit Quantenzahlen $J^P = 2^+$ bzw. 4^+ zwischen den beiden Systemen $\eta\pi^-$ und $\eta'\pi^-$ als qualitativ gleichartig zu erkennen. Wir stellen aber auch fest, dass diese Gleichartigkeit für die spin-exotische P_+-Welle nicht gegeben ist.

Zuletzt führen wir in Analogie zu früheren Analysen Modellfits durch, in welchen wir Parametrisierungen der Daten anhand von Breit-Wigner-Resonanzamplituden finden, und nutzen diese, um Verzweigungsverhältnisse der bekannten $a_2(1320)$ und $a_4(2040)$ Mesonen zu gewinnen. Wir vergleichen diese mit den Vorhersagen aus der Theorie der η-η'-Mischung, und im Falle des $a_2(1320)$, mit früheren Messungen.

In Anhängen sammeln wir einige nützliche Formeln und außerdem Ergebnisse, welche nicht zum Hauptteil dieser Arbeit passen.

Contents

List of Figures

1. Introduction

The structure of particle physics has remained stable ever since the introduction of what is now called the Standard Model of particle physics some forty years ago. It is a gauge field theory which divides the elementary particles into two categories: the leptons, subject to the electroweak interaction, and the hadrons, subject to both the electroweak interaction and the strong interaction $SU(3)$. These interactions are themselves mediated by quantized fields which number four in the case of the electroweak interaction, the massless photon and the massive vector gauge bosons Z, W^+, W^-, and the massless gauge boson of the strong interaction, the gluon. The building particles of the standard model have been all identified in the laboratory with one exception: at the time of this writing the experimental discovery of the last remaining ingredient, the Higgs boson, part of the mechanism of electroweak symmetry breaking which lends the weak gauge bosons Z, $W^\pm$ their masses, is imminent. First indications of this boson were found in the vicinity of a mass of 125 GeV, but only in the summer of 2012 enough data will be available to confirm or refute these indications.

Quantum Chromodynamics (QCD), the theory of the strong interaction,[1] on the other hand has been vindicated in the laboratory time and again, but it poses its own challenges: its low-energy regime is that of strong coupling where perturbative expansions in terms of the coupling strength become impossible. Only at high-energies does the so-called running of the coupling constant allow for perturbative calculations, and the theory has enjoyed tremendous success in this region. At low energies however, calculations need to rely on models that capture the properties of the theory essential to the task at hand. This does especially apply to the manifestations of the strong interaction that lead the way to the discovery of quantum chromodynamics: namely the structure of mesons and baryons. The symmetries and structures of these particles could be understood in a framework of underlying fractionally-charged fermions, combining in groups of two (particle-antiparticle, the mesons) or three (particles or antiparticles, the baryons), the quarks [Gell-Mann, 1964; Zweig, 1964a,b]. Yet, while the observed regularities in the meson and baryon spectra lead to the discovery of the underlying theory, QCD, This underlying theory didn't allow for calculation of the properties of the hadrons. Various approaches to the problem have been developed.

Chiral Perturbation Theory One such approach to low-energy QCD comes from effective field theories, especially Chiral Perturbation Theory [Gasser and Leutwyler, 1984, 1985; Weinberg, 1979]. This is an effective theory of the light mesons which respects

[1] A complete set of references covering the history and current research of this field is given in Ref. [Kronfeld and Quigg, 2010].

the internal symmetries of QCD together with a so-called power counting scheme which allows a systematic expansion in terms of particle momenta and/or energies. As such it can be used to calculate the interactions of the light mesons. By use of dispersion relations which follow from unitarization and analyticity requirements, it has recently been used successfully to describe two-pion states up to the $K\bar{K}$ threshold [Ruiz de Elvira et al., 2011]. To lowest order chiral perturbation theory is equivalent to the pre-QCD current algebra, yet the systematic expansion possible with chiral perturbation theory has proven successful in the calculation of processes such as the $\eta \to 3\pi$ decays which is hugely underestimated in the lowest order approximation and thus current algebra, or the two-photon decays of the π^0 and η mesons, which are the main confirmation of the existence of $SU(3)_{\text{color}}$. The theory has been expanded by also including in the power-counting scheme systematically the effects of the $1/N_C$ expansion which allows inclusion of the η' meson [Leutwyler, 1998]. We will discuss the special role of the η and η' mesons in Sec. 1.1.2.

The Constituent Quark Model Here, quarks interact via a potential that is derived from the static approximation to QCD [Godfrey and Isgur, 1985]. This model can account for the known meson resonances but lacks predictive power in the low-mass range, where relativistic effects become important. Especially in the isoscalar sector, though, it fails to account for some of the lower-lying states.

The Bag Model This model describes hadrons by confining quarks, antiquarks and gluons into a finite-volume where they interact among themselves [Johnson, 1975]. Hadronic collisions then lead to overlap between these bags, and thus interactions between the virtual particle seas of the two hadrons.

Lattice QCD In this approach, spacetime is discretized as a four-dimensional lattice. QCD is then approximated as a theory on this discrete lattice. The path-integrals decribing the amplitudes of the theory then become regular integrals which can be evaluated with lots of computing power. This approach is limited in that the finite available computing time, and calculations have to be performed at unphysical values of the inputs (usually, for instance the pion mass which in current calculations is taken around 700 MeV). A recent summary giving up-to-date predictions for the meson spectrum can be found in [Dudek, 2011].

The flux-tube model This is a model derived from lattice calculation where the binding interaction between the quarks is described as a string of massive beads. Excitations of the string then lead to excited mesonic states [Isgur and Paton, 1985].

Lattice QCD, the bag model, and the flux-tube model have in common the prediction of integral-spin states which cannot be understood as bound states of quark-antiquark pairs. Their existence is also expected from QCD sum rule considerations. These are on the one hand glueballs, which are manifestations of the self-interaction of the non-commutative $SU(3)$ theory, and on the other hand so-called hybrid states where besides

constituent quarks and antiquarks also gluonic degrees of freedom are excited. Reviews of the topic are for instance Refs. [Amsler and Törnqvist, 2004; Crede and Meyer, 2009; Klempt and Zaitsev, 2007; Meyer and Van Haarlem, 2010]. References and predictions from various models are given in Table 1.1.

Model	Mass [GeV]	References
Bag Model	$1.3 - 1.8$	[Barnes et al., 1983; Chanowitz and Sharpe, 1983]
Flux-Tube Model	$1.8 - 2.0$	[Barnes et al., 1995, 1997; Close and Page, 1995; Isgur et al., 1985; Page, 1997; Page et al., 1999]
QCD Sum rules	$1.3 - 1.5$, $2.1 - 2.5$	[Balitsky et al., 1982; Govaerts et al., 1987; Latorre et al., 1987]
Lattice QCD	1.6-2.0	[Bernard et al., 2003]

Table 1.1.: Predictions of various models for the lightest hybrid meson with quantum numbers $J^{PC} - 1^{-+}$.

We comment on the experimental status of the hybrid resonances relevant to the analysis work discuss in this thesis in Sec. 1.2. But first we will turn to addressing in more detail the structure of QCD and the meson spectrum. After discussing the current experimental evidence for hybrid mesons in the $\pi^-\eta$ and $\pi^-\eta'$ systems, we will discuss some of the properties of the diffractive reactions that produce the $\pi^-\eta^{(\prime)}$ system we discuss. Next, we will give a quick review of the COMPASS experiment at CERN where the data for this analysis were obtained and we will dwell on the sandwich veto detector, whose design, assembly, installation and maintenance was undertaken as part of the work leading to this thesis. After that we shall turn to the analysis: we discuss the data event selection, the analysis procedure and its implementation and the results of these partial-wave fits. Finally we conclude. In appendices we collect various stuff that didn't fit the mainline of the text but which is nevertheless interesting or important.

1.1. Quantum Chromodynamics

1.1.1. Structure of the Theory

Quantum chromodynamics (QCD) is the accepted theory of the strong interaction. Particles subject to the strong interaction are called *hadrons*. The fundamental degrees of freedom of the strong interaction are the quarks and the gluons. The Lagrangian of

QCD can be written

$$\mathcal{L} = \sum_q \bar{\psi}_{q,a}(\mathrm{i}\gamma_\mu \partial^\mu \delta_{ab} - g_s \gamma^\mu t^C_{ab} A^C_\mu - m_q \delta_{ab})\psi_{q,b} - \frac{1}{4} F^A_{\mu\nu} F^{A\,\mu\nu}. \tag{1.1}$$

The sum runs over all quarks, six in total. The additive quantum numbers of the quarks are summarized in Tab. 1.2. Repeated indices are summed over and spinor indices are omitted. The various symbols have the following meaning: the $\psi_{q,a}$ are the quark fields. They are Dirac spinors and reside in the fundamental representation of the color group $SU(3)$, the color indices a, b run from 1 to $N_C = 3$. The strong coupling constant g_s together with the quark masses m_q are the experimental inputs to the theory. A^C_μ are the gluon fields. They reside in the adjoint representation of the color group, the color index C runs from 1 to $N_C^2 - 1 = 8$. The t^C_{ab} are the $SU(3)$ generators, usually given in the form of the Gell-Mann matrices. They obey the $SU(3)$ algebra

$$t^A t^B - t^B t^A = \mathrm{i} f_{ABC} t^C, \tag{1.2}$$

with f_{ABC} the $SU(3)$ structure constants. With these the Yang-Mills field strength takes the form

$$F^A_{\mu\nu} = \partial_\mu A^A_\nu - \partial_\nu A^A_\mu - g_s f_{ABC} A^A_\mu A^B_\nu. \tag{1.3}$$

The vertices of the theory are shown in Fig. 1.1. The gluon only couples to a pair of quarks of the same flavor. This is encoded by the conserved flavor quantum numbers isospin, strangeness, charm, bottomness and topness. The special role of isospin is due to the low mass of the u and d quark leading to an almost exact symmetry which will be discussed below. A manifestation of the conservation of these flavor quantum numbers is the observed behavior of the strange particles: these particles such as the kaons are produced copiously in the strong interaction, yet turn out to be long-lived, only decaying via the weak interaction. For instance, the lightest strange particle, the charged kaon, has a lifetime $c\tau = 3.712\,\mathrm{m}$. Strange particles are only produced in pairs, and there lies the explanation of the seeming discrepancy between the easy production and difficult decays: strange particles contain a strange quark. The strong interaction can produce these quarks only in conjunction with their corresponding antiquark. If this pair ends up in different particles, then the strange quark and antiquark can no longer disappear via the strong interaction, as there is no corresponding antiquark around. Strangeness is not conserved in the weak interaction and therefore the lightest strange particles decay weakly.

1.1.2. Quarks and Mesons

Meson Composition

Mesons are strongly interacting particles, i.e. hadrons, of integral spin. Like all hadrons they are colorless, i.e. their decomposition in terms of the fundamental degrees of freedom of QCD, quarks and gluons, has to be that of a scalar in color-space. The simplest such

Quark	d	u	s	c	b	t
Electric Charge	$-\frac{1}{3}$	$+\frac{2}{3}$	$-\frac{1}{3}$	$+\frac{2}{3}$	$-\frac{1}{3}$	$+\frac{2}{3}$
Baryon Number	$\frac{1}{3}$	$\frac{1}{3}$	$\frac{1}{3}$	$\frac{1}{3}$	$\frac{1}{3}$	$\frac{1}{3}$
Isospin	$\frac{1}{2}$	$\frac{1}{2}$	0	0	0	0
Isospin z-component	$-\frac{1}{2}$	$\frac{1}{2}$	0	0	0	0
Strangeness	0	0	-1	0	0	0
Charm	0	0	0	1	0	0
Bottomness	0	0	0	0	-1	0
Topness	0	0	0	0	0	1

Table 1.2.: Additive quantum numbers of the quarks.

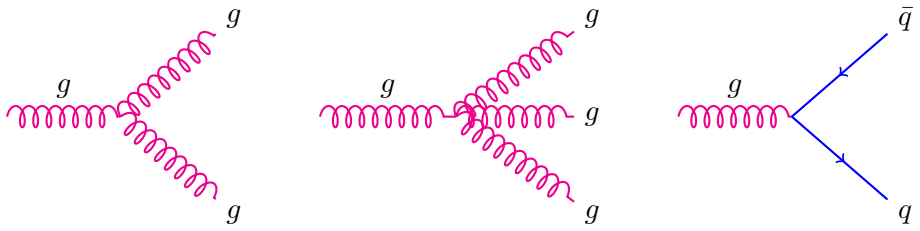

Figure 1.1.: Fundamental vertices of the strong interaction.

objects are bound states of a quark and an anti-quark.[2] A quark lives in the fundamental representation $SU(3)_{\text{color}}$, commonly denoted 3. An anti-quark likewise lives in the complex-conjugate of the fundamental representation, i.e. $\bar{3}$. The Clebsch-Gordan series for this is (see e.g. [Jones, 1990])

$$3 \otimes \bar{3} = 8 \oplus 1, \tag{1.4}$$

so that a quark-antiquark pair can reside either in the adjoint representation 8 of $SU(3)_{\text{color}}$ or indeed in the scalar, color-singlet representation. Such a state would be called a *quark-model meson*.

Similarly, a pair of gluons, which reside in the adjoint representation of $SU(3)_{\text{color}}$, the color octet 8, can form a colorless state via

$$8 \otimes 8 = 27 \oplus 10 \oplus \bar{10} \oplus 8 \oplus 8 \oplus 1, \tag{1.5}$$

where besides a number of higher representation also the scalar representation appears. Such a state would be called a *glueball*. Alternatively, as a pair of two quarks can also reside in the color octet 8, such a pair can also combine with a gluon to form a *hybrid meson*. Also, more complex objects can be imagined, say a *molecule* composed of two quark-antiquark pairs, both either in the color octet or color singlet representation.

Quantum Numbers

Restricting ourselves to mesons composed of a quark q and its own antiquark $\bar{q}$, the possible quantum numbers J^{PC} can be derived right away (e.g. [Landau and Lifchitz, 1989]). Fermion and anti-fermion have opposite intrinsic parity, the product of their parities is therefore $\eta_q \eta_{\bar{q}} = -1$. Accordingly, the parity of a state with orbital angular momentum L is

$$P = \eta_q \eta_{\bar{q}} (-1)^L = (-1)^{L+1}. \tag{1.6}$$

Fermi-symmetrization requires that the wave function of the $q\bar{q}$ system change sign under simultaneous exchange of the coordinates, the spins and the charge variables of system. The first again gives a factor $(-1)^L$, the second gives $(-1)^{S+1}$, where S is the spin of the combined system. The factor comes about because the singlet (triplet) combination $S = 0$ ($S = 1$) is anti-symmetric (symmetric). The exchange of the charge variables is mediated by charge conjugation C. So one has

$$(-1) = (-1)^L (-1)^{S+1} C,$$

and therefore

$$C = (-1)^{L+S}. \tag{1.7}$$

One now sees that CP conservation demands that spin and orbital momentum are conserved separately, so one can use them meaningfully to classify possible $q\bar{q}$ states.

[2] A readable introduction to the implications of the quark model is Ref. [Lipkin, 1973]

This follows from

$$CP = (-1)^{L+S}(-1)^{L+1} = (-1)^{S+1}, \tag{1.8}$$

where only S appears which can only take the values 0, corresponding to $CP = -1$, and 1, corresponding to $CP = +1$. Conservation of CP therefore implies separate conservation of S and L.

With this in mind one can write down the possible quantum numbers J^{PC} of the $q\bar{q}$ system. Quantum numbers that don't fit into this scheme are called *exotic quantum numbers*. Using spectroscopic notation, the possible quantum numbers up to $L = 2$ are given in the following table:

$^{2S+1}L_J$	$^1S_0$	$^3S_1$	$^1P_1$	$^3P_0$	$^3P_1$	$^3P_2$	$^1D_2$	$^3D_1$	$^3D_2$	$^3D_3$
J^{PC}	0^{-+}	1^{--}	1^{+-}	0^{++}	1^{++}	2^{++}	2^{-+}	1^{--}	2^{--}	3^{--}

Mesons not composed of a quark and its anti-quark have well-defined spin J and intrinsic parity P, but they are not eigenstates of the charge conjugation operation C. Besides all charged mesons this also applies to flavored quarks which are mesons whose quark composition contain at least one quark that is not u or d, say $d\bar{s}$ for the K^0. The identification of a charged state with an exotic quantum number state therefore has to rely on additional classification beyond J^P. This is afforded by the systematization of mesons into multiplets.

Isospin, $SU(3)_{\text{flavor}}$: Meson Multiplets

Isospin is an approximate symmetry of nature, it was originally introduced by Heisenberg in the context of a systematic description of nuclear levels [Heisenberg, 1932]. Here, he made the observation that protons and neutrons are the same object with respect to the strong interaction with one exception: the wave-function has to be antisymmetric under exchange of two protons or two neutrons, but no such symmetry requirement exists for the exchange of a proton and a neutron. Therefore, the nuclear level scheme can be decomposed according to the symmetries under exchanges of particles. Such a decomposition naturally leads to the representation theory of $SU(2)$ – the same group that is used to classify the spin-states of systems of electrons. The symmetry transformation of this symmetry in the case of the nucleus leads to exchanges of protons and neutrons and therefore links different isotopes. From this comes the name *isotopic spin*, later shortened to *isospin*.

The same reasoning applies to the fundamental building blocks of hadrons, quarks. Here to good approximation the u and d quarks can be considered massless and therefore identical as far as the strong interaction is concerned. Hence, states can be grouped into so-called *iso-multipletts* according to the representation theory of $SU(2)$ [Gell-Mann, 1964; Zweig, 1964a,b]. One collects the u and d quark into an isospin doublet

$$\begin{pmatrix} u \\ d \end{pmatrix}, \tag{1.9}$$

where the u has isospin $(I, I_z) = (\frac{1}{2}, \frac{1}{2})$ and the d quark the corresponding $(I, I_z) = (\frac{1}{2}, -\frac{1}{2})$. The antiquarks then form an isospin doublet as well,

$$\begin{pmatrix} -\bar{d} \\ \bar{u} \end{pmatrix} \tag{1.10}$$

(the minus sign comes from the translation of the complex conjugate representation of the anti-particles to the representation of the particles, which mimics the traditional usage). From this one can now build, taking for illustration the $L = S = 0$ mesons, the isotriplet

$$\begin{aligned} \pi^+ &= -u\bar{d}, \\ \pi^0 &= \frac{1}{\sqrt{2}}(u\bar{u} - d\bar{d}), \\ \pi^- &= d\bar{u}, \end{aligned} \tag{1.11}$$

and the isosinglet

$$\eta_q = \frac{1}{\sqrt{2}}(u\bar{u} + d\bar{d}). \tag{1.12}$$

The latter is not to be confused with the physical η which also has admixture from the s quark. The minus signs come about because the natural representation for antiquarks is the complex-conjugate representation, but in order to save the writing of upper and lower indices the equation is written in terms of the same representation for quarks and antiquarks.

Isospin invariance being to good approximation a conserved quantity of the strong interaction, the treatment of interactions can be much simplified by the introduction of a common quantum number linking particles in an isospin multiplet. This is G-parity. Its corresponding operator is defined as a charge-reversing rotation in isospin space followed by charge conjugation. The usual choice is

$$G = Ce^{\mathrm{i}\pi I_y}. \tag{1.13}$$

Keeping in mind that $C\pi^0 = +\pi^0$, $C\pi^\pm = -\pi^\mp$, and employing standard theory of the rotation group, one thus arrives at

$$G\pi^0 = -\pi^0, \qquad G\pi^\pm = -\pi^\pm, \tag{1.14}$$

and the pions indeed have the same G-parity. We also see that, inserting Eq. (1.7), we can write

$$G = C(-1)^I = (-1)^{L+S+I} \tag{1.15}$$

for each multiplet, where the second identity is derived from the quark model. G-parity conservation explains for instance that the isospin triplet vector meson $\rho(770)$ cannot decay to three pions even though phase space allows this, while on the other hand the isospin singlet vector meson $\omega(782)$ decays to three final state pions but not two. It also

explains why the three-pion decay of the η meson ($G = +1$) happens at such a glacial pace, comparable to the electromagnetic decay $\eta \to \gamma\gamma$: G-parity conservation forbids the decay, so it has to take place via the isospin-breaking electromagnetic interaction.

Using G-parity, the concept of *exotic quantum numbers* can be extended to charge states. By this, for instance an $I = 1$ state with $J^{PG} = 1^{--}$ would be considered exotic, as its neutral isospin partner has exotic quantum numbers $J^{PC} = 1^{-+}$.

In practice, the s quark is also much lighter than the other quarks, and one arranges the light mesons according to $SU(3)_{\text{flavor}}$, which takes care of the symmetrization requirements imposed by Fermi statistics. By this, the light mesons are classified into flavor nonets. This is illustrated in Fig. 1.2 for the pseudoscalar mesons ($J^{PC} = 0^{-+}$) and in Fig. 1.3 for the vector mesons ($J^{PC} = 1^{--}$). The quark content is given together with the name of the respective mesons in the corners. The quark content for the mesons in the center is given by linear combinations of the quark-antiquark pairs of the various flavors. Here, since flavor symmetry is not an exact symmetry, and a transition such as $s\bar{s} \to u\bar{u} + d\bar{d}$ therefore does not violate conservation laws, the various states with the same J^{PC} mix. On the other hand, to the approximation that isospin is conserved, the $I = 1$ states $\pi^0; \rho^0$ don't mix with the $I = 0$ states $\eta, \eta'; \omega, \phi$.

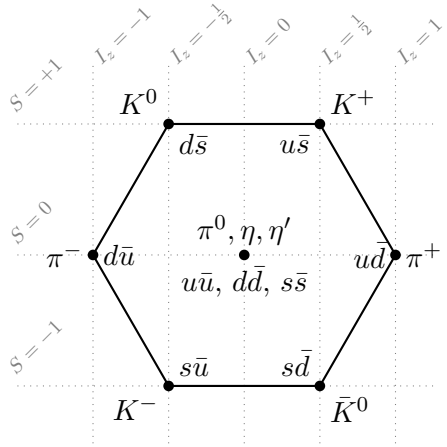

Figure 1.2.: Light scalar nonet. The quark contributions to the mesons are indicated. For the quark content of the neutral mesons π^0, η, η' see the text.

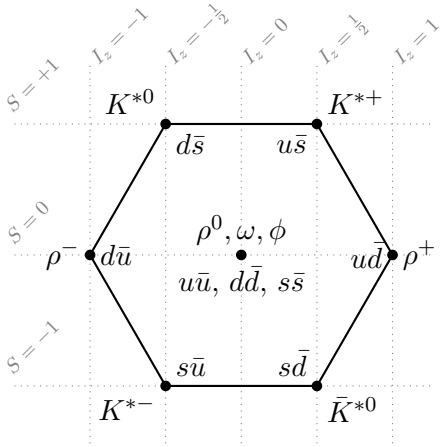

Figure 1.3.: Light vector nonet. The quark contributions to the mesons are indicated. For the quark content of the neutral mesons ρ^0, ω, ϕ see the text.

Mixing in the iso-scalar sector is commonly parametrized in terms of the $SU(3)$ singlet and octet states which can be written using the generic notation ψ_1 and ψ_8 for the singlet

and octet, respectively,

$$\begin{aligned}\psi_1 &= \frac{1}{\sqrt{6}}(u\bar{u} + d\bar{d} - 2s\bar{s}),\\ \psi_8 &= \frac{1}{\sqrt{3}}(u\bar{u} + d\bar{d} + s\bar{s}).\end{aligned} \tag{1.16}$$

The physical states are obtained from these by an orthogonal transformation, to wit

$$\begin{aligned}\psi' &= \psi_8 \cos\theta - \psi_1 \sin\theta,\\ \psi &= \psi_8 \sin\theta + \psi_1 \cos\theta.\end{aligned} \tag{1.17}$$

For the vector and tensor mesons, the physical states are found to be very close to the case of ideal mixing, where the physical states are mostly $d\bar{d} + u\bar{u}$ and $s\bar{s}$, respectively. In the pseudoscalar case on the other hand, determinations of the mixing angle yield a wide range of values [Feldmann, 2000]. This is attributed to a more complicated mixing scheme, where the decay constants, low-energy effective parameters of chiral perturbation theory which are relevant to most determinations of the mixing parameters, mix in a way independent of the particle wave functions. On the other hand, it is found that up to OZI violating terms, the mixing angle ϕ can be determined in a process-independent way [Feldmann et al., 1998], provided it is defined in the flavor basis where the basis states

$$\begin{aligned}\eta_q &= \frac{1}{\sqrt{2}}(u\bar{u} + d\bar{d}),\\ \eta_s &= s\bar{s},\end{aligned} \tag{1.18}$$

mix to form the physical states via

$$\begin{aligned}\eta &= \eta_q \cos\phi - \eta_s \sin\phi,\\ \eta' &= \eta_q \sin\phi + \eta_s \cos\phi.\end{aligned} \tag{1.19}$$

The mixing angle can be accessed from decay branchings of quarkonium mesons [Bramon et al., 1999]. Assuming no strange-quark content in the decaying mesons, which is found to good approximation for the tensor mesons ($J^{PC} = 2^{++}$), one can derive the relative branching for the a_2 and a_4 mesons

$$\frac{\Gamma(a_J \to \eta'\pi)}{\Gamma(a_J \to \eta\pi)} = \tan^2\phi \left(\frac{k_{\eta'\pi}}{k_{\eta\pi}}\right)^{2J+1}, \tag{1.20}$$

where $J = 2$ or $J = 4$ and $k_{\eta\pi}$, $k_{\eta'\pi}$ are the breakup momenta at the nominal mass of the decaying meson [Bramon et al., 1999]. From the known branchings of the $a_2(1320)$, $\phi = 43.1^\circ \pm 3.0^\circ$ is found, consistent with the overall average $\phi = 39.3^\circ \pm 1.0^\circ$ determined from a variety of experimental inputs [Feldmann et al., 1998]. A determination of the relative branching fraction $\Gamma(a_4 \to \eta'\pi)/\Gamma(a_4 \to \eta\pi)$ would be a new input, and will be

pursued in this thesis. Recent studies find a small gluonic contribution in the η', leading to a more complicated mixing scheme [Ke et al., 2010; Mathieu and Vento, 2010a,b].

The comparatively large mass of the η' is due to the chiral anomaly, according to which even in the chiral limit $m_u = m_d = m_s = 0$ chiral symmetry is not fully restored. Therefore chiral symmetry leads to only eight massless Goldstone bosons (π^0, $\pi^\pm$, $K^\pm$, K^0, $\bar{K}^0$, η_8), leaving the η_1 massive even in this limit ['t Hooft, 1986].

1.2. Previous Analyses of the $\pi^-\eta$ and $\pi^-\eta'$ Systems

The $\eta\pi$ and $\eta'\pi$ complexes have attracted quite some interest in the past. Even though hybrid meson decays are expected to be suppressed to two S-wave mesons [Barnes et al., 1997; Close and Page, 1995; Isgur et al., 1985; Page, 1997], these are attractive candidates for the experimental discovery of such mesons. This is because decays of the preferred P-wave meson such as $\pi^- f_1(1285)$ or $\pi^- b_1(1235)$ lead to much more complicated final states. For instance, the b_1 decays dominantly to $\pi\omega(782)$, which, if followed by the dominant $\omega \to \pi^-\pi^+\pi^0$, leads to a final state with five pions with no phase-space boundaries nearby that allow unique identification of the intermediate states. We illustrate this channel in App. I. We also point out that our selection of $\pi\eta'$ data also contains the $\pi^- f_1$ data in an intermediate step, see Fig. 4.9a. We show some results of a preliminary partial-wave analysis in App. H.

Instead of these more complicated states, first hints of an spin-exotic state with quantum numbers 1^{-+} were found in the $\pi^0\eta$ system by the GAMS collaboration in the reaction $\pi^-(100\,\text{GeV})p \to \pi^0\eta p$ [Alde et al., 1988]. They observed a state with mass $1406 \pm 20\,\text{MeV}$ and width $180 \pm 30\,\text{MeV}$ which they found resonating against the dominant $a_2(1320)$. These results were questioned in Ref. [Tuan et al., 1988] and a later reanalysis by members of the collaboration could not confirm the results, a resonant interpretation could not be confirmed or excluded (see [Sadovsky, 1999]).

In 1993 the VES collaboration studied the reaction $\pi^- N \to \pi^-\eta N$ at a beam momentum of 37 GeV, finding a broad P-wave enhancement around 1.4 GeV [Beladidze et al., 1993]. At the same time at KEK the reaction $\pi^- p \to \pi^-\eta p$ was studied at beam momentum 6.3 GeV. They found a P-wave resonance with parameters very close to the $a_2(1320)$ observed in D-wave. Leakage could not be excluded [Aoyagi et al., 1993].

The E852 collaboration claimed evidence for an exotic meson in 1997, studying the reaction $\pi^- p \to \pi^-\eta p$ at a beam momentum of 18 GeV. They successfully parametrized this as a Breit-Wigner function, distorted by a polynomial, with parameters $m = 1370 \pm 16^{+50}_{-30}\,\text{MeV}$ and $\Gamma = 385 \pm 40^{+65}_{-105}$ [Chung et al., 1999; Thompson et al., 1997]. Simultaneously, the Crystal Barrel collaboration analyzed the annihilation reaction $\bar{p}d \to \pi^-\pi^0\eta p_{\text{spectator}}$ at rest. Their data required a $\eta\pi$ P-wave resonance with parameters $m = 1400 \pm 20 \pm 20\,\text{MeV}$ and $\Gamma = 310 \pm 50^{+50}_{-30}\,\text{MeV}$ [Abele et al., 1998]. They also found that an $\eta\pi$-P-wave contribution was necessary to accurately describe the Dalitz plot in $\bar{p}p$-annihilation at rest into $\pi^0\pi^0\eta$ [Abele et al., 1999]. Unlike the other cited experiments, where the data are dominated by the $a_2(1320)$, the $\bar{p}d$ annihilation data show contributions comparable in size for both the P-wave and the $a_2(1320)$.

Returning to charge-exchange data, an analysis of E852 data published in 2003 on the reaction $\pi^- p \to \eta\pi^0 n$ found a P-wave that could not be accomodated with a Breit-Wigner resonance description [Dzierba et al., 2003]. A 2006 analysis of the same reaction by the E852 collaboration found a P-wave resonance, with parameters $m = 1257 \pm 20 \pm 25\,\text{MeV}$ and $\Gamma = 354 \pm 64 \pm 60\text{MeV}$. They did not take the unnatural exchange waves into account when interpreting the data, nor did they allow the parameters of the D_+-wave resonance $a_2(1320)$ to vary during the fit.

The discovery of an exotic meson decaying to $\eta\pi$ immediately lead to the question of whether it could also be observed in the $\eta'\pi$. Group theoretic considerations made after the initial observations by the GAMS collaboration predicted that a state with gluonic contributions should couple much stronger to the $\eta'\pi$ system than to the $\eta\pi$ system [Close and Lipkin, 1987].

In a 1993 analysis of the $\pi^- p \to \pi^-\eta' p$ channel, the VES collaboration found a P-wave comparable in size to the D-wave, but could not establish its resonant nature [Beladidze et al., 1992, 1993]. In 2001, on the other hand, the E852 collaboration claimed a resonance in the same reaction with parameters $m = 1597 \pm 10^{+45}_{-1-}\,\text{MeV}$ and $\Gamma = 340 \pm 40 \pm 50\,\text{MeV}$ [Ivanov et al., 2001]. Reanalysis of the VES data did not yield conclusive results on the resonant character [Amelin et al., 2005]. A 2004 analysis of the charge-exchange reaction $\pi^- p \to \eta'\pi^0 n$ found P-wave production predominantly through unnatural partial waves. They therefore concluded that the coupling of the P-wave to $\rho\pi$ is small [Amelin et al., 2004]: $BR(\pi_1 \to \rho\pi) < 0.03$) (where the label is not meant to imply a resonant character).

Likewise, the Crystal Barrel collaboration investigated whether an exotic $\pi\eta'$ resonance appears in $p\bar{p}$ annihilation at rest. In the final state $\pi^0\pi^0\eta'$ their analysis shows no sign of a P-wave resonance, its inclusion in the fit showed no improvements in fit quality finding only very little intensity in that wave [Abele et al., 1997]. Unlike the neutral case, a preliminary analysis of $\pi^-\pi^+\eta'$ data found a P-wave resonance with parameters $m = 1555 \pm 50\,\text{MeV}$ and $\Gamma = 468 \pm 80\,\text{MeV}$ which accomodates for up to 20% of their data [Reinnarth, 2001].

Most recently, the CLEO collaboration studied the decays $\chi_{c1}(3510) \to \eta\pi^+\pi^-$ and $\chi_{c1} \to \eta'\pi^+\pi^-$ and found an exotic P-wave in $\eta'\pi$ consistent with the $\pi(1600)$, but they also could not firmly establish its resonant nature [Adams et al., 2011].

A combined analysis of $\eta\pi^0$ and $\eta'\pi^0$ data interpreted the observed P-wave as remnants of final-state interaction [Szczepaniak et al., 2003]. Also the mass-difference between the resonance observed in $\pi\eta$ data (around 1400 MeV) and the $\pi\eta'$ data (closer to 1600 MeV) was interpreted as the result of final-state interaction [Donnachie and Page, 1998].

To summarize the state of exotic resonances in the $\pi\eta$ and $\pi\eta'$ systems, we collect some remarkable features of these data:

- neutral final states in the reaction $\pi^- p \to \eta\pi^0 n$, disfavors the production of the 1^{-+} resonance rendering a coupling to $\pi\rho$ unlikely [Tuan et al., 1988],
- an exception is the Crystal Barrel data on the $\pi^-\pi^0\eta$ final state,
- the masses found in the two decays $\pi\eta$ and $\pi\eta'$ are at tension, but this tension

can be resolved in re-scattering models, which are probably not applicable to the Crystal Barrel data,

- but models with re-scattering can do without a resonance at all;
- all scattering data relies in their analysis on the interpretation of phase-motions relative to a strong D-wave. the structure of this D-wave is not understood. Additionally, the interpretation of the phase-motions is not as straightforward as it may seem, we comment on this in Sec. 7.2.

Besides the $\eta\pi$ and $\eta'\pi$ final states, exotic waves were also found in the $\pi^- f_1$ [Kuhn et al., 2004] and $\pi^- b_1$ [Amelin, 1998; Dorofeev et al., 2002; Lu et al., 2005] systems. Their results find resonant states compatible with the $\pi(1600)$ but this interpretation requires the introduction of additional new states in other partial waves, in order to correctly describe the observed phase-motions. Also in the $\pi\rho$ channel claims of the exotic resonance $\pi_1(1600)$ have been made, by E852 [Adams et al., 1998; Chung et al., 2002], and also by the COMPASS collaboration [Alekseev et al., 2010]. Nevertheless, the VES collaboration found that the presence or absence of an exotic $\pi\rho$ wave depends on assumptions made in their analysis [Amelin et al., 2005]. A second analysis of a much-enlarged sample of E852 data on the $\pi^-\pi^+\pi^-$ and $\pi^-\pi^0\pi^0$ final states found no exotic resonance [Dzierba et al., 2006]. An observation of a 1^{-+} in the $\pi\rho$ channel would engender a large production cross-section in photoproduction experiments, due to vector meson dominance, nevertheless recent, preliminary analyses of CLAS data on the reaction $\gamma p \to \pi^+\pi^+\pi^- n$ show no significant contribution of this wave [Bookwalter, 2011].

2. Particle Production

High-energy scattering leads to the production of additional particles. We will concern ourselves with the domain of high-energy and small momentum transfers, where a number of characteristic features obtain [Rossi et al., 1975]. The most important feature for this analysis is the diffractive excitation of the beam particle [Feinberg and Pomerančuk, 1956; Good and Walker, 1960], where the beam particle is excited into a state with the same conserved charges, but (perhaps) different angular momentum and parity. The framework where the dynamics of this class of processes is best described is Regge theory, originally developed as an alternative approach to solving the Schrödinger equation [Regge, 1959], where angular momentum ℓ is allowed to take arbitrary complex values. The allowed eigenvalues of mass m then increase with ℓ due to the increasing centrifugal potential. These lines are the Regge trajectories $\alpha(m^2)$. It is then found that mesons (or baryons) can be classified into linear trajectories where one has $\ell = \alpha(m^2)$ at the physical angular momenta and masses [Chew and Frautschi, 1962]. Regge theory additionally allows deriving asymptotic properties of scattering cross-sections in the regime of high-energy scattering at low-momentum transfer relevant to us. We will thus briefly discuss the main features of the scattering amplitudes as given by Regge theory.

Since the Regge approach to relativistic scattering is based on the analyticity and crossing requirements for the amplitudes [Mandelstam, 1959; Omnès and Froissart, 1963], we shall briefly discuss them. The Lorentz-invariant amplitude of the (spin-averaged) scattering process $1 + 2 \to 3 + 4$ is a function of the four-momenta $p_1 \dots p_4$ of the external particle. Since it is Lorentz-invariant, it is actually a function of Lorentz-invariant combinations of these. Besides the masses $m_i^2 = p_i^2$ these are habitually chosen as the Mandelstam variables

$$s = (p_1 + p_2)^2, \quad t = (p_1 - p_3)^2, \text{ and } u = (p_1 - p_4)^2. \tag{2.1}$$

Since

$$s + t + u = \sum_i m_i^2, \tag{2.2}$$

actually only two of the Mandelstam variables are independent, and we write the amplitude as $A(s, t)$. s is square of the center of mass energy of the scattering process, t the momentum transfer variable. The Mandelstam hypothesis is that the amplitude for the crossed t-channel process

$$1 + \bar{3} \to \bar{2} + 4 \tag{2.3}$$

is the analytical continuation of the amplitude $A(s, t)$ of the s-channel process $1 + 2 \to 3 + 4$ where one identifies $p_3 = -p_{\bar{3}}$ and $p_2 = -p_{\bar{2}}$ in the calculation of the Mandelstam variables, and likewise for the crossed u-channel process $1 + \bar{4} \to 2 + \bar{3}$. In the Regge-

exchange approach, an asymptotic expression for $A(s,t)$ in the physical region of the s-channel process is then calculated by summing the important terms of the partial-wave series for the t-channel process by transforming the series into an integral over complex angular momenta.

2.1. Regge Description of High-Energy Scattering

In terms of Regge trajectories, the amplitude for the s-channel process $AB \to CD$ can be written as

$$A(s,t) = \gamma_{AC}(t)\gamma_{BD}(t)\frac{\exp(-\mathrm{i}\pi\alpha(t)) + \mathcal{S}}{\sin\pi\alpha(t)}\frac{1}{\Gamma(\alpha(t))}\left(\frac{s}{s_0}\right)^{\alpha(t)}, \tag{2.4}$$

where $\gamma_{AC}(t)$, $\gamma_{AB}(t)$ are the couplings of the Regge trajectory $\alpha(t)$ to the particles AC and BD, respectively, $s_0 \approx 1\,\mathrm{GeV}^2$ is the hadron mass scale and $\mathcal{S} = \pm 1$ the signature of the Regge trajectory [Collins and Martin, 1982, 1984]. The term $(\Gamma(\alpha(t)))^{-1}$ cancels the unphysical poles of the *Regge propagator* $(\sin\pi\alpha(t))^{-1}$ at negative $\alpha(t)$. The signature factor $\exp(-\mathrm{i}\pi\alpha(t)) + \mathcal{S}$ cancels odd/even poles. The amplitude then has even/odd poles for positive integral $\alpha(t)$ which correspond precisely to the t-channel exchanges of the particles on the Regge trajectory. The splitting into even and odd trajectories is necessary because they exhibit different symmetry under the crossing $s \leftrightarrow u$, it is therefore specific to a relativistic treatment [Frautschi et al., 1962; Gell-Mann, 1962].

Two important properties of the Regge amplitude Eq. (2.4) are the following: on the one hand the factorization property implies simple relations between the cross-section of processes where the same Regge trajectories are exchanged, which is experimentally verified, comparing e.g. the cross-section of $\pi p \to \pi p$ and $pp \to pp$ scattering. On the other hand, the total s-channel cross-section behaves as

$$\frac{\mathrm{d}\sigma}{\mathrm{d}t} \sim s^{-2}|A(s,t)|^2 \sim F(t)\left(\frac{s}{s_0}\right)^{2\alpha(t)-2}, \tag{2.5}$$

which allows predictions of the asymptotic behavior of the cross-sections. Especially, since all known meson and baryon trajectories are reasonably well approximated by the linear

$$\alpha(t) = \alpha_0 + \alpha' t, \tag{2.6}$$

with $\alpha_0 \approx 0.5\,\mathrm{GeV}^{-1}$ and $\alpha' > 0$, one finds that the cross-section

$$\frac{\mathrm{d}\sigma}{\mathrm{d}t} \sim F(t)\left(\frac{s}{s_0}\right)^{2\alpha_0-2}\exp(2\alpha'\log(s/s_0)t) \tag{2.7}$$

rapidly decreases as a function of s, and for small $|t|$ one has approximately $\mathrm{d}\sigma/\mathrm{d}t \sim s^{-1}$.

The total cross-section $\sigma_T(AB) = \sigma(AB \to \text{anything})$ is related to the forward elastic

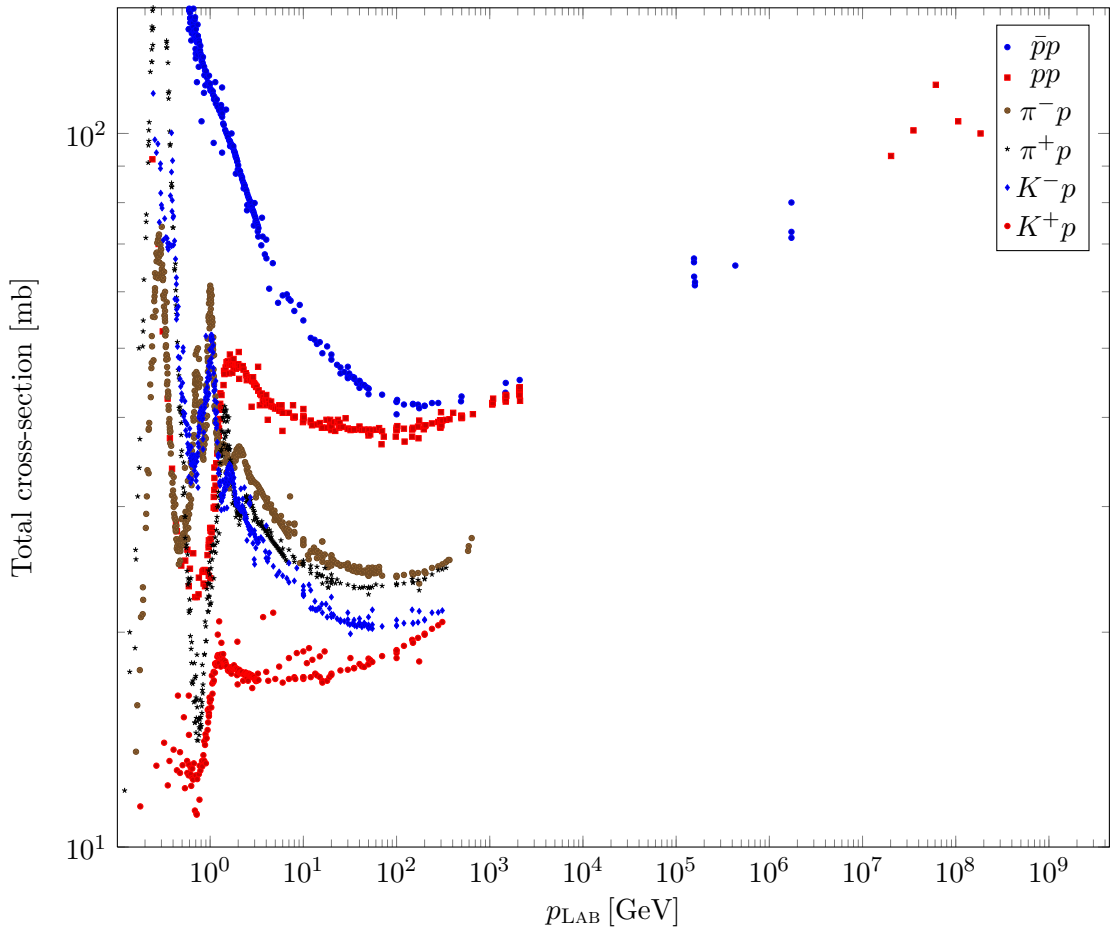

Figure 2.1.: Total cross section for various hadronic interactions. At low energies sharp peaks due to resonance scattering are observed, then at intermediate energies the cross-sections fall continuously until the high-energy regime takes over, leading to an increase in cross-sections up to the ultra-high energy collisions observed in cosmic rays. The COMPASS beam energy of 191 GeV lies well in the high-energy regime of rising cross-sections. Data from [Nakamura et al., 2010].

amplitude by the optical theorem

$$\sigma_T(AB) \sim \frac{1}{s}\mathrm{Im}\, A_{AB\to AB}(s, t=0) \sim s^{\alpha(0)-1} \tag{2.8}$$

(use has been made of the realness of $\gamma_{AB}(t)$ and $\alpha(t)$). Experimentally, one observes an increase of hadronic cross-sections for very large momenta, see Fig. 2.1. The increase is found to follow approximately $\sigma_T \sim s^{0.081}$ [Donnachie et al., 2002] . Hence, the main process in high-energy hadron scattering is not meson or baryon exchange. Instead, it is assumed to be a manifestation of gluon exchange. Its properties can be well described by a Regge pole, the *Pomeron*, with $\alpha_P(0) = 1.07$. Experiment appears to confirm the same factorization behavior as in Eq. (2.4), but the picture of elastic hadron-hadron scattering as mediated by exchanges of a single such Pomeron pole cannot be complete because the exponentially increasing cross-section predicted from Eq. (2.8) violates unitarity as expressed by the Froissart bound

$$\sigma_T(s) < \frac{1}{m_\pi^2}\log^2(s/s_0) \quad (s \to \infty). \tag{2.9}$$

The Pomeron is a flavorless Regge pole corresponding to exchanges with quantum numbers $J^P = 0^+, 1^-, 2^+, \ldots$. As such it is understood as exchange of gluonic ladders [Donnachie et al., 2002]. It is found to couple to protons as a non-conserved vector current [Close and Schuler, 1999a,b]. The gluonic character of the Pomeron makes the excitation of mesons by Pomerons, e.g. in the diffractive $\pi^- p$ processes studied in this thesis, a prime candidate for the production of hybrid mesons.

Regge theory has been extended to the description of multiparticle processes such as $AB \to CDE$ [Hong-Mo et al., 1967a,b; Kibble, 1963]. For a modern view see e.g. Ref. [Kaidalov et al., 2003]. The formalism was applied to the process $\pi p \to K\bar{K}p$ in Ref. [Shimada et al., 1978]. This work is of interest, because the P-wave contribution in this channel appears to be correctly described by these models with no additional resonance. The authors also find that resonance-like phase-shifts can be produced by this type of model, extending previous results for scattering experiments [Schmid, 1968]. This makes the task of disentangling resonances from non-resonant backgrounds more difficult both conceptually and experimentally. Whether the same formalism can also be applied to the analysis of the $\eta\pi$ and $\eta'\pi$ channels, and whether it can accomodate for the P-wave contributions remains an interesting question for theoretical study.

The different production mechanisms expected to participate in the production of the $\pi^-\eta$ system analyzed in this thesis are depicted in Fig. 2.2. These diagrams have in common that the recoiling proton participates via the exchange of the Pomeron, a natural-parity Regge trajectory. Therefore, the available quantum numbers of the $\pi^-\eta$ system will be the same for the three processes and theoretical insights will have to be used to distinguish the three. Additionally, crossing symmetry and the duality hypothesis from scattering theory (see e.g. Ref. [Collins and Martin, 1982, 1984])[1] suggest that the

[1] These requirements are what lead to the famous Veneziano model [Veneziano, 1968], one of the origins of string theory.

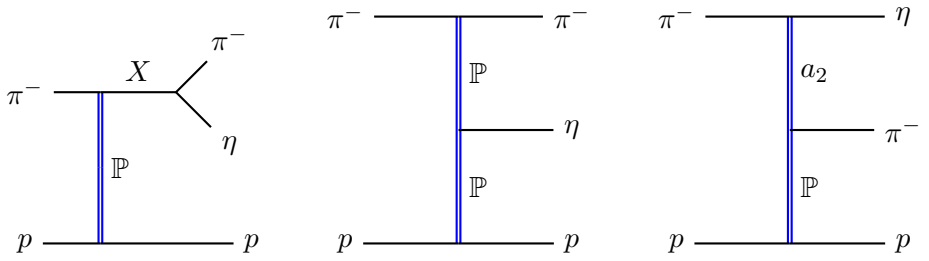

(a) Resonance production (b) Central production of the η (c) Pomeron-$a2$ exchange

Figure 2.2.: Expected production mechanisms. Reggeized exchanges are indicated in blue. Besides direct production of a resonance (denoted X) which then decays into the final state particles $\pi^-\eta$ (or η' throughout), an η can be produced at central rapidities by double-Pomeron exchange. Additionally, a leading η can be produced in a Deck-like process by the exchange of a Regge trajectory, here the leading candidate is the Reggeized a_2.

amplitudes for the processes in Figs. 2.2a and 2.2c are not only closely related but cannot be treated separately in a consistent manner. Therefore, a clearcut separation into the different classes may not be feasible.

2.2. The reflectivity basis

In the study of diffractive beam excitation one is interested in reactions of the type $A + B \to R + C$ where R is the state under investigation and the particles A, B, C are known (π^-, p, p in the case under consideration). On the other hand, the initial state is unpolarized and the polarization of the recoiling proton C is not measured. Therefore the state of R is not fully determined, but instead described by a density matrix. If all other kinematic variables are known, the density matrix can have at most rank two [Hansen et al., 1974; Thompson et al., 1975], but additional sources of incoherence, such as integration over t or $m(C)$ may require higher rank density matrices. Parity conservation implies further restrictions on the density matrix. Namely, the density matrix is block-diagonal in the eigenvalues of the *reflection operator*

$$\Pi_y \equiv P \exp(-\mathrm{i}\pi J_y), \tag{2.10}$$

where y is the direction orthogonal to the production plane defined by the momenta of A and B in the rest-frame of R, P is the parity operator and J_y is the generator of infinitesimal rotations about the y-axis. Compared to using parity without additional rotation, this operation has the advantage that the particle momenta remain unaffected by this reflection operator. Rotational invariance implies that invariance under reflection is equivalent to invariance under the parity operation.

Given a basis of angular momentum eigenstates $|E\eta Jm\rangle$ characterized by their intrinsic parity η, total angular momentum J, angular momentum projection m and other quantum numbers labelled collectively E, the corresponding properly normalized (bosonic) eigenstates of the reflectivity operator are given by

$$|E\,\epsilon\,\eta\,J\,m\rangle = \theta(m)\left(|E\,\eta\,J\,m\rangle - \epsilon\eta(-1)^{J-m}\,|E\,\eta\,J\,-m\rangle\right), \tag{2.11}$$

where m now takes only non-negative values and normalization requires $\theta(m) = 1/\sqrt{2}$ for $m > 0$ and $\theta(0) = 1/2$ [Chung and Trueman, 1975]. For sake of ulterior convenience, we have defined the *reflectivity* ϵ such that

$$\Pi_y\,|E\,\epsilon\,\eta\,J\,m\rangle = -\epsilon\,|E\,\epsilon\,\eta\,J\,m\rangle\,. \tag{2.12}$$

There is only one $m = 0$ state, as $|E\,\epsilon\,\eta\,J\,0\rangle = 0$ if $\epsilon = \eta(-1)^J$, and therefore both bases (J, m) and (ϵ, J, m) contain the same number of states. We will show why the seemingly unnatural choice for the sign of ϵ turns out very natural.

2.3. Correspondence Between Naturality and Reflectivity

We now specialize to the *Gottfried-Jackson frame* which is also known as *t-channel helicity frame*. In this frame, the y axis is orthonal to the production plane as before. It is a rest frame of the produced system and for the sake of definiteness, we choose the direction of y as given by the cross-product of the (boosted) target and recoil momenta. The z axis is chosen along the direction of the beam. The direction of x is given by the right-hand rule. This is the frame we shall use throughout the remainder of this work.

The Gottfried-Jackson frame is special in that the exchanged naturality $\eta(-1)^J$ corresponds to the reflectivity ϵ defined above, at least in the limit of high-energy scattering at small angles, i.e. s large and t small. In Ref. [Gottfried and Jackson, 1964] this is only shown on the level of intensities for the case of a single angular momentum being present, and the general statement is quoted throughout the literature, e.g. Ref. [Ader et al., 1968; Thompson et al., 1975], but the proof is to our knowledge never made explicit, though all the prerequisites appear e.g. in [Cohen-Tannoudji et al., 1968]. The proof is quite simple. First, the t-channel helicity states have the following symmetry

$$\mathscr{M}^J_{\lambda_3\lambda_1\lambda_4\lambda_2} = \eta\eta_4\eta_2(-1)^{J+s_4-s_2}\mathscr{M}^J_{\lambda_3\lambda_1-\lambda_4-\lambda_2}, \tag{2.13}$$

for the Jth partial wave in the scattering process $1 + 2 \to 3 + 4$ where intrinsic parity η is exchanged. λ_i, s_i and η_i refer to the helicity, spin and intrinsic parity of particle i. The t-channel helicity amplitude (leaving aside other partial waves to avoid clutter) is then

$$\mathscr{M}_{\lambda_3\lambda_1\lambda_4\lambda_2} = (2J+1)d^J_{\lambda\mu}(\cos\theta_t)\mathscr{M}^J_{\lambda_3\lambda_1\lambda_4\lambda_2} \tag{2.14}$$

with $\lambda = \lambda_1 - \lambda_3$, $\mu = \lambda_2 - \lambda_4$. Now in the forward-region of the s-channel process, $s \gg t$

and thus $\cos\theta_t$ large.[2] The asymptotic behavior of the Wigner functions is [Kibble, 1963]

$$d^J_{-\lambda\mu}(\cos\theta_t) \xrightarrow[\cos\theta_t\to\infty]{} (-1)^\lambda d^J_{\lambda\mu}(\cos\theta_t). \tag{2.15}$$

In this limit one then has

$$\mathscr{M}_{\lambda_3\lambda_1\lambda_4\lambda_2} \to \eta\eta_4\eta_2(-1)^J(-1)^{\lambda_4-\lambda_2}(-1)^{s_4-s_2}\mathscr{M}_{\lambda_3\lambda_1-\lambda_4-\lambda_2}. \tag{2.16}$$

With this at hand, we can prove the statement that we are after. Taking the reaction $p(\frac{1}{2}^+)+\pi(0^-)\to p(\frac{1}{2}^+)+X({s_4}^{\eta_4})$, where X is produced in a state of defined reflectivity ϵ (where the sign convention is as above) and spin substate m, we have

$$\mathscr{M}^\epsilon_{\lambda_3\lambda_1 m0} \equiv \theta(m)\left(\mathscr{M}_{\lambda_3\lambda_1 m0} - \epsilon\eta_4(-1)^{s_4-m}\mathscr{M}_{\lambda_3\lambda_1-m0}\right). \tag{2.17}$$

Inserting Eq. (2.16), this reduces to

$$\mathscr{M}^\epsilon_{\lambda_3\lambda_1 m0} \to \theta(m)(1+\eta(-1)^J\epsilon)\mathscr{M}_{\lambda_3\lambda_1 m0}, \tag{2.18}$$

which is zero for $\eta(-1)^J \neq \epsilon$, proving the statement. For $m=0$ the statement holds exactly because one then has $\lambda=0$ in Eq. (2.15) and both sides are equal independent of the value of $\cos\theta_t$.

In order to avoid the perhaps confusing convention for the sign of the reflectivity ϵ, we will distinguish the two classes by the terms natural-parity waves ($\epsilon=+1$) and unnatural-parity waves ($\epsilon=-1$). Since all the production mechanisms depicted in Fig. 2.2 are mediated via a natural exchange from the proton, all of them contribute to the natural-parity, positive reflectivity waves.

[2] Note that outside the physical region of the t-channel $\cos\theta_t$ is not restricted to the range $[-1,1]$.

3. The COMPASS Experiment

The COmmon Muon Proton Apparatus for Structure and Spectroscopy (COMPASS) experiment at CERN [Baum et al., 1996] is a fixed-target experiment attached to CERN's M2 beamline whose magnetic spectrometer which is also equipped with calorimeters is capable of high-resolution measurements of both neutral and charged final-state particles with wide momentum range. It formed out of a synthesis of the proposed HMC [Nappi et al., 1995] and CHEOPS [Alexandrov et al., 1995] experiments. Where the HMC collaboration wanted to pursue measurements of the spin-structure of the nucleon using deep-inelastic scattering with a muon beam, the CHEOPS collaboration aimed at studying the hadronic spectrum in reactions of a hadronic beam with nuclear targets. In 2010, the successor experiment COMPASS-II was proposed [Gautheron et al., 2010] and since 2012 it is pursuing its wide-ranging physics programmes.

Why do these different physics programmes converge at the same experiment? Because the beams offered by the M2 beamline are unique as it allows both high-intensity, high-energy polarized muon beam and flexible high-energy hadron beams, both positively and negatively charged. These beams are produced in the following way: the Super Proton Synchrotron (SPS), see Fig. 3.1, emits a 450 GeV proton beam. This proton beam is injected into the M2 beamline, where it hits a Beryllium target, called *production target*, leading to a large number of secondary hadrons. In order to produce a polarized muon beam this production target is chosen far away from the spectrometer, allowing the hadrons to decay. Remaining hadrons are then scraped away by hadron absorbers after which the remaining muon beam is focused and steered to the target. The beam muons are polarized because their dominant production modes are the decays $\pi \to \mu\nu_\mu$ and $K \to \mu\nu_\mu$ of the pseudoscalar mesons. The handedness of the neutrinos then implies polarization of the muons. In order to obtain a hadron beam, a production target closer to the spectrometer target is chosen, thus leading to an almost pure hadron beam. The hadron beam at 191 GeV, chosen in the 2008 and 2009 hadron spectroscopy campaigns has the following composition at the COMPASS target: for the positive beam $\pi^+ : K^+ : p = 0.240 : 0.014 : 0.746$, for the negative beam $\pi^- : K^- : \bar{p} = 0.968 : 0.024 : 0.008$ [Alekseev et al., 2012]. In this thesis we analyze data taken with this negatively charged beam impinging on a liquid hydrogen target. Therefore the exposition will focus on the corresponding spectrometer setup. The spectrometer setup used in the muon beam campaigns until 2006 is described to great detail in [Abbon et al., 2007]. A publication on the modifications made since is forthcoming [Alekseev et al., 2012].

We shall now discuss the COMPASS spectrometer. Overall, it consists of a beam definition stage, the target and two spectrometer stages, each equipped with tracking and particle identification. An overview is presented in Fig. 3.3.

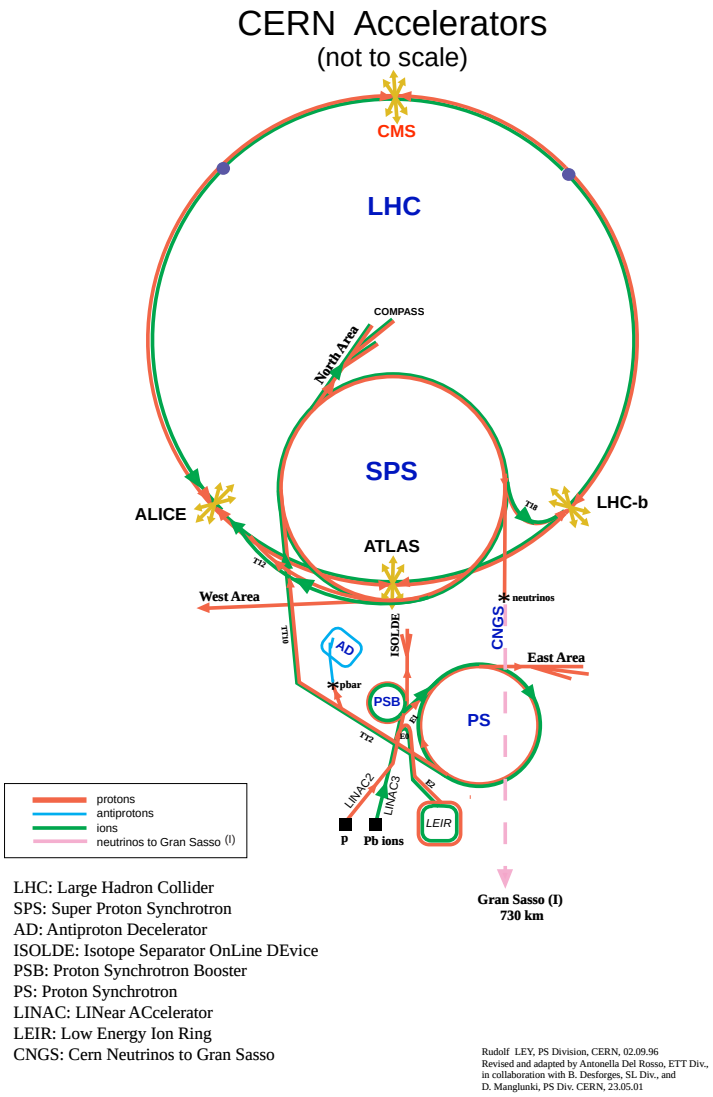

Figure 3.1.: The CERN accelerator complex (not to scale). The COMPASS experiment sits at the center of the large ring. Picture from `http://ps-div.web.cern.ch/ps-div/PSComplex/accelerators.pdf` (visited 2012-05-23).

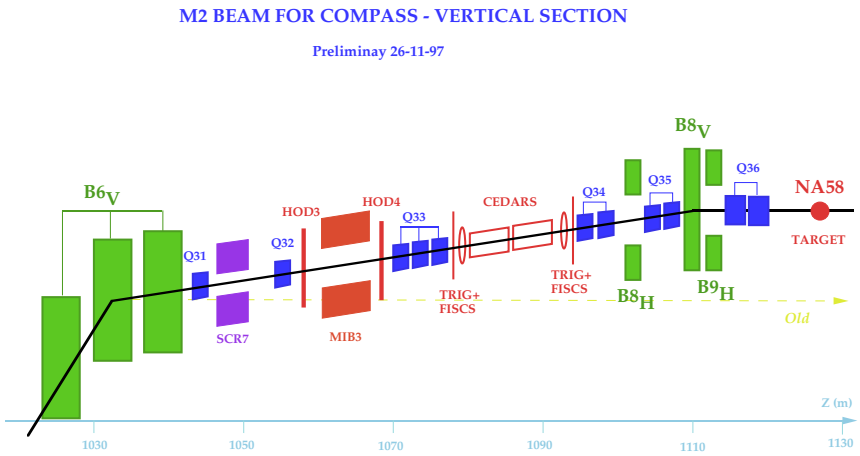

Figure 3.2.: Schematic view of the final stages of the M2 beamline. The beam enters from the lower left, passes through the beam optics and the CEDAR detectors, finally hitting the COMPASS target (labelled NA58 target). Various items in the pictures are bending magnets in green, scrapers in violet, quadrupoles in blue and particle detectors in red. Figure from `http://sl.web.cern.ch/SL/eagroup/NewM2/main.html` (visited 2012-05-22).

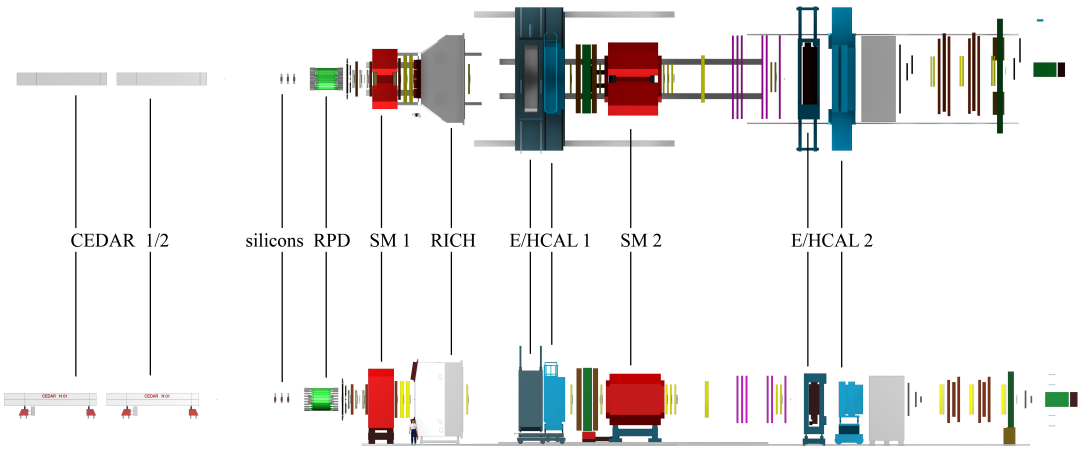

Figure 3.3.: Top and side views of the COMPASS 2008/09 spectrometer [Jasinski, 2012]. Along the beam direction, from left to right, we see the CEDAR detectors used for beam particle identification. Next, the upstream Silicon stations used for vertexing of the beam particle. The recoil proton detector (RPD) follows next, it contains the target. An enlarged view of the target region around the RPD is found in Fig. 3.4. The target region is followed by a number of tracking stations and the first spectrometer magnet, SM1. Subsequent tracking stations are followed by the Ring Imaging Cherenkov (RICH) detector, used for charged particle identification and the electromagnetic and hadronic calorimetry (ECAL1 and HCAL1) of the large angle spectrometer. After muon identification and small angle detectors (not labelled) we see the second spectrometer magnet (SM2), which again is followed by a number of tracking stations and electromagnetic and hadronic calorimetry (ECAL2 and HCAL2). The remainder of the spectrometer is devoted to muon identification. The picture is not to scale. The distance from the target to the first spectrometer magnet is approximately 7 m, and from the target to ECAL2 approx. 33 m.

3.1. Beam Definition

In the 2008/09 setup the following properties of the beam particles are determined on their way to the target:

- two CEDAR detectors [Bovet et al., 1978; Jasinski, 2012] are used to identify the beam particle. For the purposes of the analysis discussed in this work, they can be used to suppress backgrounds from the kaonic part of the beam. Use of this information didn't alter the results of the analysis, so no use was made of the CEDAR information, and we won't discuss it further,
- Silicon detectors and scintillating fiber detector precisely measure the trajectory of the beam particle in order to reconstruct as precisely as possible the vertex of the target interaction,
- a Beam telescope is used as part of the trigger (discussed below),
- additionally, a Beam Momentum Station (BMS) can be moved into the beamline, forming a telescope around the bending magnet near $B6_V$ in Fig. 3.2. The BMS allows to determine the momentum of the beam particles at the per-cent level. Since it introduces a significant amount of material, and since the momentum spread of the hadron beam is already smaller than the resolution of the BMS, it is not used with the hadron beams.

3.2. The Target Region

During the 2008 and parts of the 2009 hadron spectroscopy campaigns, the target of the COMPASS spectrometer was a cylindrical liquid hydrogen cell of 40 cm length and 35 mm diameter, positioned along the nominal beam axis. This cell was installed inside a recoil proton detector (RPD), a time-of-flight detector intended to trigger on recoiling slow protons while also determining their momentum and direction of emission [Bernhard, 2007]. A cross-section of the target region is shown in Fig. 3.4. This detector consists of two rings of scintillator slabs arranged on cylinders concentric with the target. The inner ring consists of 12 identical 5 mm thick scintillators which are read out individually with photomultiplier tubes at both the upstream and downstream ends. The outer ring is composed similarly from 24 scintillators which are arranged such that the azimuthal resolution of the coincidence between the inner and the outer ring is maximized, i.e. half the scintillators of the outer rings are centered relative to the elements of the inner ring, half are aligned with the boundaries between the scintillators of the inner ring. The detector covers the angular range from 55° to 125° as seen from the target center. A proton can be detected when it passes through the inner ring of scintillators, depositing its remaining energy in the outer ring. This requires a minimal momentum transfer $|t| \approx 0.07\,\mathrm{GeV}^2$. As a trigger component, the RPD triggered on positively identified protons with a timing resolution better than 350 ps (rms). The proton momentum is measured by correlating the times of signals in the inner and outer scintillator rings. Its

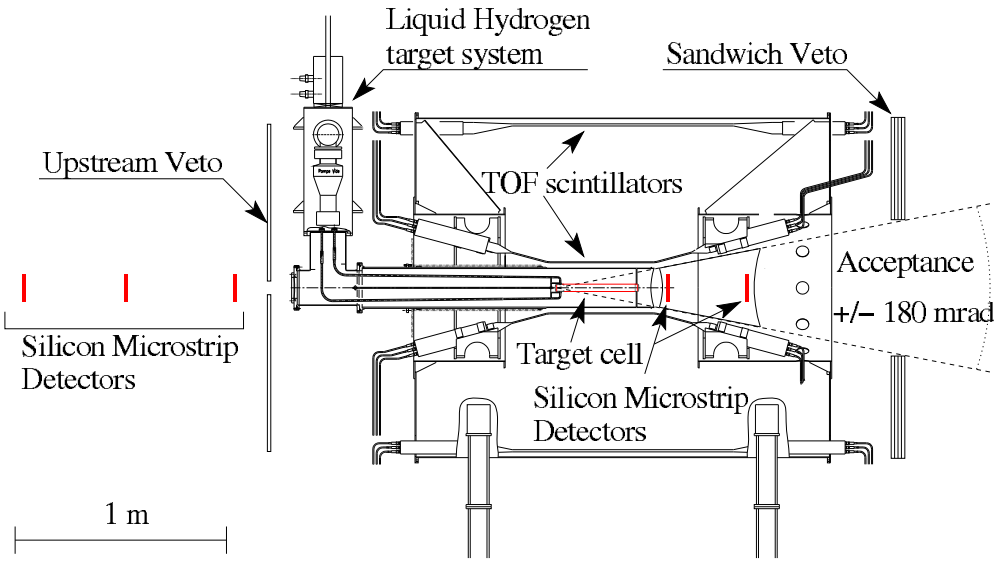

Figure 3.4.: The target region showing the liquid hydrogen target inside the RPD detector. The beam enters from the left, passing through three silicon detector stations on its way. Off-axis beam particles are rejected via the upstream veto. Two silicon downstream of the target allow for precise vertexing even at small emission angles. The time of flight scintillators of the RPD detector are indicated. Finally particles outside the spectrometer acceptance are rejected by the sandwich veto.

emission point along the beam axis and the angle of the proton is determined from the correlation between the upstream and downstream photomultipliers. The proton is then identified by its specific energy loss in the inner and outer rings.

In the target area there is also the upstream veto which is used to suppress particles entering the target region close to the nominal beam axis but outside of the target radius. Tracking around the target is discussed in the following section, and the sandwich veto detector which is situated at the downstream end of the target region is discussed in detail in Sec. 3.6. Its purpose is to suppress events where particles are emitted outside the spectrometer acceptance of approximately $\pm 10.3^\circ$ as seen from the upstream edge of the target.

3.3. Tracking

The purpose of a particle physics experiment is to provide information on event kinematics in such a way that the underlying dynamics can be studied. In particle collisions, particle paths may change and new particles may be created. The task is then to learn as much about the particles as possible. Such information concerns their points of emissions, their momenta and energies, their charges and masses, and any other properties that may be of interest. Short-lived particles that decay immediately after their production have to be reconstructed from their decay objects. On the other hand, long-lived particles can be detected individually in their course of interaction with the spectrometer. In the context of a typical particle physics experiment, the following particles are considered long-lived, and we will discuss their detection in what follows: the photon, the electron, the muon, the pions, the kaons, the neutron, the proton, the $\Lambda(1115)$, the $\Sigma^+(1190)$ and $\Sigma^-(1197)$ and the $\Xi(1320)$ together with their antiparticles. Additionally, atomic nuclei can have lifetimes exceeding the age of the universe, but we shall not consider them specially. Lastly, neutrinos are long-lived but escape detection outside of specifically designed experiments.

Out of these long-lived particles, we shall first turn towards the detection of the charged ones, $e^\pm, \mu^\pm, \pi^\pm, K^\pm, \bar{p}, p$. The three main processes allowing for the detection of charged particle trajectories are ionization energy losses, transition radiation and Cherenkov radiation. Uses of the latter is discussed in Sec. 3.4, we won't discuss transition radiation further, and we will now turn to ionization.

3.3.1. Physical Foundations

High-energy particles traversing material undergo a series of collisions with the electrons in the material. This energy loss per amount of material traversed is approximately given by the Bethe-Bloch formula, found in any textbook, e.g. Ref. [Leo, 1994],

$$-\frac{1}{\rho}\frac{\mathrm{d}E}{\mathrm{d}x} = 2\pi r_e^2 m_e N_0 \frac{Z}{A}\frac{z^2}{\beta^2}\left\{\ln\left[\frac{2m_e\beta^2}{(1-\beta^2)I}\right] - 2\beta^2 + C\right\}, \tag{3.1}$$

where x is the length of material traversed, r_e the classical electron radius, m_e the mass of the electron, N_0 the Avogadro constant, Z the atomic number of the material traversed, A its molar mass, ze the charge of the traversing particle, and β its velocity. Finally, I is the effective ionization potential and a property of the material and C summarizes corrections necessary for small energies (where the atomic shell structure becomes important) and very high energies (where faster traversal of the material leads to less polarization and therefore weaker shielding of the electromagnetic field). Electrons additionally suffer energy losses due to bremsstrahlung, which we shall discuss in Sec. 3.4.3.

How is the energy loss detected? There are essentially two ways: either the electrons which have become separated from the atomic cores are collected and their charge is amplified to a measurable signal, or light emitted by recombination of ions and electrons as well as from molecular deexcitation is detected. The former processes are relevant in semiconductor detectors and gaseous detectors, the latter in scintillation detectors.

3.3.2. Tracking Detectors in the COMPASS Experiment

Before turning to the individual detectors in the COMPASS setup, we shall discuss the information obtained from the detectors. Each particle detector measures coordinates and time of particle traversal. The detectors are planar and oriented orthogonally to the beam axis along which they are installed. Most detector planes measure a single coordinate, except for the pixelized GEM and Micromegas detectors which measure two coordinates. The one-dimensional detectors are arranged in stations combined from several planes oriented along the x and y axis, and – in order to resolve left-right ambiguities and ambiguities resulting from different tracks hitting the same detectors strip – at 20 or 45 degree angles with respect to these axes. Neglecting the extension along the beam axis, each station can then measure a point in space.

Very Small Area Trackers These are the detectors placed in the vicinity trajectory of the (undeflected) beam. Requirements on these are high-rate capability and very good spatial resolution for efficient vertexing.

Scintillating Fiber (SciFi) stations are detectors built from several layers of wavelength shifting fibers which are used as scintillator medium. These are arranged along the various spatial directions. These detector can stand high rates on the order of $3 \cdot 10^6\,\mathrm{Hz}$ per fiber, are highly efficient ($> 96\%$) and deliver good time resolution (on the order of 400 ps). Besides tracking, they are also used as parts of the beam trigger. A total of eight stations of varying size were installed in the spectrometer.

Silicon detectors are used as vertex detector in the immediate vicinity of the target. Their role as vertex detectors is due to their spatial resolution: up to $8\,\mu\mathrm{m}$ (rms) can be achieved and a time resolution of the order of 1.3 ns (rms). The silicon detectors are semiconductor detectors where traversing particles excite electrons and holes into the valence band. A current due to these electrons is then detected. The silicon detectors were cooled to cryogenic temperatures (liquid nitrogen) to minimize radiation induced efficiency losses.

Additionally, the newly developed pixel readout for the central area of the GEM detectors, allowed their use in very small angle tracking. This is discussed below.

Small Area Trackers These cover the area close to the beam at distances from around 2.5 cm to 40 cm. Here, again high spatial resolution is required as well as radiation hardness, combined with a small material budget along the beam direction. Two types of the detectors were used for this purpose: gas-electron mulatiplier (GEM) detectors and micromesh gaseous (Micromegas) detectors. COMPASS was the first large-scale experiment to use either type of detector. Both detectors are gaseous detectors separating the drift from the amplification stage. In the Micromegas detectors, ionization electrons drift towards a fine metallic mesh, the eponymous micro mesh. Beyond the mesh, the electrons are accelerated leading to the typical ionization cascade of gaseous detectors. The readout allows for a spatial resolution of 90 μm (rms) while a temporal resolution of 9 ns (rms) could be obtained over the active area of $40 \times 40\,\mathrm{cm}^2$ with a circular dead zone of radius 5 cm in the central region.

The GEM detectors employed by COMPASS [Ketzer et al., 2004] use three layers of GEM foils to ensure safe operation at high rates by a reduced conversion time. The GEM detectors provide a spatial resolution of 70 μm (rms) and a temporal resolution of 12 ns over the active area of $31 \times 31\mathrm{cm}^2$. Again, the detector center was not powered. In 2008 a new pixelized GEM detector was installed in the COMPASS experiment, allowing use of the detector even in the central region. These were installed in five stations, one upstream of the first spectrometer magnet SM1, adding redundancy in the very central region of the spectrometer, and two upstream and downstream of SM2, each. In 2009 a pixelized Micromegas station was also installed for testing purposes upstream of SM1.

Large Area Trackers Finally, the area away from the beam was covered with several types of wire drift detectors. Next to SM1 three drift chambers with an active area of $180 \times 127\mathrm{cm}^2$ and 176 pairs of wires running at opposite-sign high voltages were installed, providing a spatial resolution of 190 μm. Wire detectors rely on an external time source to determine the distance of particle impacts from the wires. Therefore they do not provide time measurements on their own.

A number of multiwire proportional chambers is installed over the whole spectrometer. The active area is depending on the station either $178 \times 120\,\mathrm{cm}^2$ or $178 \times 80\,\mathrm{cm}^2$. Wires are spaced apart by 2 mm, and the total resolution is 1.6 mm.

Another type of tracking detectors in COMPASS are the straw tube drift chambers [Bychkov et al., 2006], straw detectors for short. In these, each individual wire is placed in a surrounding tube, ensuring the mechanical stability over the large area. The active area of $323 \times 280\,cm^2$ is covered with tubes of diameter 6.14 mm in the central region and 9.65 mm in the region away from the beam. The inner part achieves a spatial resolution of 190 μm. The straw detectors are installed as the last part of tracking before particle identification in each spectrometer stage, i.e. right upstream of the RICH in the large-angle spectrometer and upstream of ECAL2 in the small-angle spectrometer.

Finally, a large area drift chamber (W45) is installed in the vicinity of ECAL2. Its

active area is $500 \times 250\,\mathrm{cm}^2$, giving a resolution of 0.5 mm. Its large wire spacing of 4 cm leads to huge dead time, requiring a dead zone in the central 50 – 100 cm.

Hodoscopes Mostly for the purpose of muon identification and triggering, COMPASS is also equipped with several large trigger hodoscopes consisting of scintillators. The resulting light is read out by photomultipliers.

These trackers combined lead to a reconstruction performance on the order of 90 % measured as the ratio of reconstructed tracks over generated tracks in Monte Carlo calculations for tracks with momentum above a lower limit of approx. 1 GeV. A weak point of the setup is the lack of redundancy in the very small area tracking. In the 2008 setup, only three tracking planes are available in central region of the spectrometer upstream of SM1: two Silicon stations and one PixelGEM detector. Especially for displaced decays such as those of the long-lived neutral K^0_S, efficiency drops dramatically for decays downstream of the silicon detectors. We shall now discuss the reconstruction of individual tracks, from which we shall turn to vertexing and the associated questions concerning the reconstructions of K^0_S and other intermediate particles.

3.3.3. Track Reconstruction

Analysis in particle physics is a process of subsequent abstractions: electrical signals in detectors are associated with detector hits. Hits in several planes of the same detector station or in neighboring read-out strips of detectors are combined into clusters which contain temporospatial information on particle passages. These clusters are combined into particle tracks which combine several clusters to obtains tracks characterized by trajectories, particle charge and momentum. Tracks are combined into events, together with further properties of the events such as vertex location, calorimeter information etc. Events are then grouped into physical classes based on cuts, topological characteristics and so on. Different levels of analysis require different levels of abstraction, but most physics analysis begins on the level of tracks and vertices as for what concerns charged particles.

The track reconstruction program uses information on the magnetic fields in the spectrometer setup, the positions and readout geometries of the detectors and the material distribution in the spectrometer in order to obtain information on the trajectories and momenta of charged particles traversing the spectrometer.[1] Magnetic fields in the spectrometer are confined to the areas of the spectrometer magnets SM1 and SM2 (and, in setups with polarized target, the target area). Since outside of magnetic (and electric) fields, particles propagate on straight lines, the first step in track reconstruction is

[1] During the course of this thesis a new way of storing and handling information on materials in the spectrometer was devised and implemented, making available all of the information in the Monte Carlo software also to the reconstruction software. This contrasts with a previous, averaged description using so-called material maps which turned out to be very unwieldy and incapable of describing small but important objects such as the RICH beam pipe. The code making this possible are `TGeoManager` and related classes in the ROOT framework [Antcheva et al., 2009]. Recent data productions of the COMPASS experiment make exclusive use of this new approach.

the identification of reasonably straight lines of clusters in the field-free regions of the spectrometer. The second step makes use of the fact that trajectories are only deflected very little in projections parallel to magnetic fields. The tracking algorithm thus tries to *bridge* candidate tracks across the magnets in such a projection. Once such a candidate track has been found, the Kalman filter algorithm (e.g. [Frühwirth et al., 2000]) is used to combine the individual clusters to a single trajectory, obtaining the particle momentum and its traversed radiation length (as a measure of multiple scattering) as well as the covariance matrix of the track parameters in the process. In App. B we give some useful formulae concerning track parametrization and the momentum determination. It is worth keeping in mind that the radius of curvature of a track is measured, and thus the charge-momentum ratio q/P, and thus errors are given in terms of the inverse momentum. The iterative Kalman filter algorithm allows successive incorporation of the information from the individual detector planes, and is mathematically equivalent to the much more expensive solution of a least-squares problem incorporating the information of all detector planes [Kalman, 1960]. Unlike the least-squares approach, the sequential move from detector plane to detector plane allows for the straightforward incorporation of the effects of material.

3.3.4. Vertex Reconstruction

Tracking as described above does not teach anything about the physical interactions leading to the appearance of these tracks. In order to gain insight on these, tracks have to be combined in order to find common points of origin or disappearance (in the case of the beam track). The points are what is referred to as vertices. Besides being closer to the physical quantities of interest, the condition that the two tracks meet, allows enhanced determination of the track parameters. The COMPASS reconstruction allows for two classes of vertices which are called

- *primary vertices* where a beam particle measured in the beam telescope could be matched with any number of particles in the spectrometer, and
- *secondary vertices* which are restricted to pairs of oppositely charged spectrometer tracks. Possible origins of such pairs of tracks are the conversion of photons into e^+e^- pairs on traversal of material, and the decays of the long-lived K^0_S meson and Λ baryon.

The reconstruction software does not allow for multiparticle secondary interactions of so-called kinks, where a charged particle decays into another charged particle and a neutral particle, leaving a characteristic corner (the kink) in bubble-chamber imagery. This appears for instance in the decay of the Σ^+ baryon which decays predominantely either to $p\pi^0$ (where the track after the kink corresponds to the proton, and the π^0 is not seen) or to $n\pi^+$ (where the track after the kink corresponds to the pion, and the neutron is not seen). Additionally note that the recoiling proton is not included in the reconstruction of the primary vertex. As it is reconstructed in the recoil proton detector it is not available to the common tracking software.

Let's discuss the reconstruction of secondary vertices (so-called V_0 vertices) first. The reconstruction software calculates the closest distance of approach (CDA) between all pairs of oppositely charged pairs of reconstructed tracks.[2] All such pairs which closely approach each other are then fit into a vertex, meaning that a common point of origin together with a set of track parameters is found, where the tracks extrapolated to where they were measured coincides with the measured values. This proceeds as follows: the reconstructed tracks are extrapolated to some plane, e.g. the most upstream detector plane with hits associated with one of the tracks. Let $\boldsymbol{p}_{1,2}$ be the track parameters of the tracks in this plane and $\boldsymbol{C}_k$ their covariance matrices. The goal is to find a vertex location $\boldsymbol{x}$ and track parameters in the vertex $\boldsymbol{q}_{1,2}$ such that the extrapolations $\boldsymbol{h}_k(\boldsymbol{x}, \boldsymbol{q}_k)$ from $\boldsymbol{x}$ to the plane of the $\boldsymbol{p}_k$ are closest to the $\boldsymbol{p}_k$ in the sense that

$$\begin{aligned}\chi^2 =&(\boldsymbol{h}_1(\boldsymbol{x}, \boldsymbol{q}_1) - \boldsymbol{p}_1)^T \boldsymbol{C}_1^{-1} (\boldsymbol{h}_1(\boldsymbol{x}, \boldsymbol{q}_1) - \boldsymbol{p}_1) \\ &+ (\boldsymbol{h}_2(\boldsymbol{x}, \boldsymbol{q}_2) - \boldsymbol{p}_2)^T \boldsymbol{C}_2^{-1} (\boldsymbol{h}_2(\boldsymbol{x}, \boldsymbol{q}_2) - \boldsymbol{p}_2)\end{aligned} \tag{3.2}$$

is minimized in $\boldsymbol{x}$, $\boldsymbol{q}_1$, $\boldsymbol{q}_2$. After linearizing the $\boldsymbol{h}_k$, this problem can be attacked with the techniques described in App. D.[3] Yet, the problem is actually in such a form that the Kalman filter technique can be applied, which becomes more computationally efficient as more tracks are considered. See e.g. [Frühwirth et al., 2000].

Primary vertices are reconstructed in the same way, only terms corresponding to the additional tracks (beam track, additional spectrometer tracks) have to be added in Eq. (3.2). In order to limit computation time, the Kalman filter algorithm is used, and the tracks are added subsequently instead of solving the complete least-squares problem at a single time. What the Kalman filter essentially does is that for each additional track k the following χ^2 is minimized

$$\begin{aligned}\chi^2 =&(\boldsymbol{h}_k(\boldsymbol{x}, \boldsymbol{q}_k) - \boldsymbol{p}_k)^T \boldsymbol{C}_k^{-1} (\boldsymbol{h}_k(\boldsymbol{x}, \boldsymbol{q}_k) - \boldsymbol{p}_k) \\ &+ (\boldsymbol{x} - \boldsymbol{x}_{k-1})^T \boldsymbol{C}_{\boldsymbol{x}_{k-1}}^{-1} (\boldsymbol{x} - \boldsymbol{x}_{k-1}),\end{aligned} \tag{3.3}$$

where $\boldsymbol{x}_{k-1}$ is the vertex position obtained after including track $k-1$, and $C_{\boldsymbol{x}_{k-1}}$ is its covariance matrix. Then, after all tracks have been added to the vertex, in a so-called smoothing step the information gained due to the subsequent tracks is propagated back to the track parameters of the tracks included earlier. The beam track is special as it enters the vertex instead of leaving it, but it can be handled mathematically in the same way. The COMPASS reconstruction software attempts to fit all tracks which are pointing to the target into a primary vertex. Only tracks which lead to huge increases in χ^2 are rejected. Additionally, for small targets or when other prior information on the

[2] To be precise: the CDA is calculated only in terms of the orthogonal distance of the tracks, i.e. the separation between the tracks is only considered in the same plane orthogonal to the beam axis. Owing to the small inclination of the tracks, this is a minor difference to the strict usage of the term.

[3] Note that in the notation $\boldsymbol{h}_k(\boldsymbol{x}, \boldsymbol{q}_k)$ it is tacitly assumed that the $\boldsymbol{q}_k$ are given at the point $\boldsymbol{x}$. Therefore each $\boldsymbol{q}_k$ contains only three additional unknowns (the momentum). Therefore, the first two terms in Eq. (3.2) (giving 10 terms in the case of a diagonal covariance matrix) suffice to obtain $\boldsymbol{x}, \boldsymbol{q}_1, \boldsymbol{q}_2$ (9 unknowns).

vertex location is available, this can be encoded in an inititial guess $\boldsymbol{x}_0$ with covariance $\boldsymbol{C}_0$.

During the course of this thesis a vertexing software was developed in order to facilitate the usage of kinematic constraints along the lines given in Ref. [Forden and Saxon, 1986] and also to improve vertex determination in events with few tracks but additional neutral particles, such as in events of the type $\pi^- p \to K_S^0 K_S^0 \pi^- p$, where the spectrometer only sees one outgoing track attached to the primary vertex together with the two displaced vertices corresponding to the $K_S^0 \to \pi^-\pi^+$ decays. If in such an event the pion from the initial interaction is emitted at small angles the primary vertex is only weakly constrained, and it can therefore be improved by using the information from the neutral particles, something not foreseen in COMPASS's standard software stack. This was not used in the analysis discussed in this thesis, as the error estimates from tracking and calorimetry turned out incompatible, making the effects of kinematic fits involving both tracking and calorimetery information intransparent. Nevertheless, this vertexing software was also used to reconstruct cascade decays in an inclusive selection. In these, the doubly-strange, charged Ξ baryon (or antibaryon throughout what follows) is produced in the primary vertex. After propagating a few centimeters it decays into a $\Lambda\pi^\pm$ pair. The neutral Λ again propagates some distance before decaying in a secondary vertex, either into $p\pi^-$ or $\bar{p}\pi^+$ (the anti-Lambda). This sequence of subsequent decays is a manifestation of the selection rule that strangeness, to leading order in the weak theory, changes by at most a unit at a time [Glashow et al., 1970]. The Ξ being a doubly-strange object thus has to decay in two steps. The data selection then proceeds by finding secondary vertices which match a Λ hypothesis. The Λ candidates are then kinematically fitted with the Lambda mass as constraint. Subsequently, the resulting Λ tracks are combined into new vertices with all tracks that could not be associated with either the primary vertex or the Λ decay vertex. In the resulting mass spectrum, Fig. 3.5, both the Λ ($\bar{\Lambda}$) and the $\Xi^\pm$ peaks stand out nicely. Their resolutions are found to be 2.0 MeV and 2.8 MeV respectively.

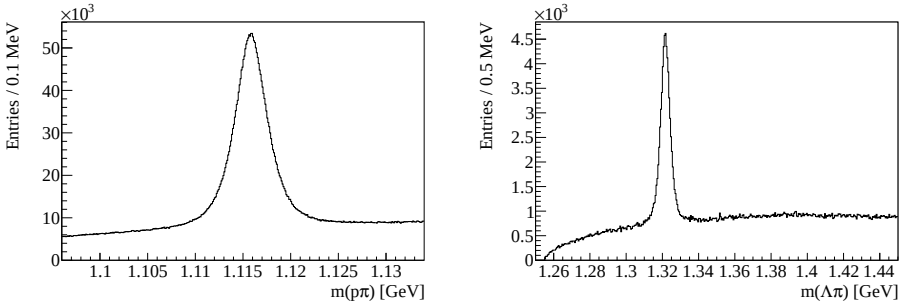

Figure 3.5.: Illustration of secondary and tertiary vertex reconstruction. The spectra show the invariant $p\pi$ mass distributions of an inclusive selection of $\Lambda \to p\pi^-$ and $\bar{\Lambda} \to \bar{p}\pi^+$ decays (left) and that of $\pi^\pm\Lambda$ pairs where pairs were selected as described in the text. For reference, the tabulated masses [Nakamura et al., 2010] are $m_\Lambda = 1115.683 \pm 0.006\,\text{MeV}$ and $m_{\Xi^\pm} = 1321.71 \pm 0.07\,\text{MeV}$.

3.4. Particle Identification

3.4.1. Velocity Measurement by Cherenkov Radiation

Particles travelling through a medium at speeds exceeding the speed of light in that medium emit Cherenkov light as a result of the electro-magnetic field in the medium not being able to adapt quickly enough to the passage of the particle. Given the refractive index n of the medium and the particle's velocity $\beta > 1/n$, Cherenkov light will be emitted at an angle θ relative to the direction of flight of the particle. This angle is given by

$$\cos\theta = \frac{1}{\beta n}. \tag{3.4}$$

The ring imaging Cherenkov detector (RICH) design which is employed at COMPASS [Abbon et al., 2011], see Fig. 3.6, uses this light to measure velocities of particles in the following way: light emitted upon the particle's traversal is reflected by a wall built of spherical mirrors. In their focal plane a large number of photodetectors is installed. This geometry projects onto circles in the focal plane all light emitted at fixed angles relative to the straight-line trajectories. The radii of the circles are then a measure of the particle velocities and the positions of the rings allows the association to the individual tracks reconstructed by the tracking system. Given the kinematic relation

$$\beta = \frac{p}{E}, \tag{3.5}$$

and assuming the momentum measured by the tracking system, the particle's energy can then be determined and therefore its mass via the mass-shell relation $m^2 = E^2 - p^2$. This procedure is limited towards low velocities, as particles can only be identified if they emit any Cherenkov light (the requirement $\beta > 1/n$ from above), and it is limited for high velocities, as the emission angles of the different particle species become arbitrarily close as $p \to \infty$ because then $\beta \to 1$ and $\cos\theta \to 1/n$ independent of the particle mass. The relation between momentum and Cherenkov angle is shown in Fig. 3.7, where pions, Kaons and (anti-)protons appear as distinctive bands. The RICH gas C_4F_{10} has a refractive index of 1.0014 at a wavelength $\lambda = 400\,\text{nm}$ [Ullaland, 2005], giving a limiting angle of approx. 5.3 rad. The implementation in COMPASS makes use of both the momentum information and the discrete particle masses to calculate a likelihood function giving the relative likelihoods that a particle is identified as any of electron, pion, kaon or proton.

For the work covered in this study the RICH contributes only via the RICH beam pipe which is a four meter long helium-filled steel pipe oriented along the beam axis installed in the center of the RICH detector. Its diameter is 10 cm with a wall thickness of 0.3 mm. Its purpose is to prevent the interaction of undeflected beam particles with the RICH gas, both in order to reduce ionization of the gas and in order to reduce Cherenkov light by fast particles which cannot be identified anyway. Unfortunately, the material budget of the RICH pipe turned out to be significant. Due to the low angle of emission, photons emitted from the target routinely pick up more than a radiation

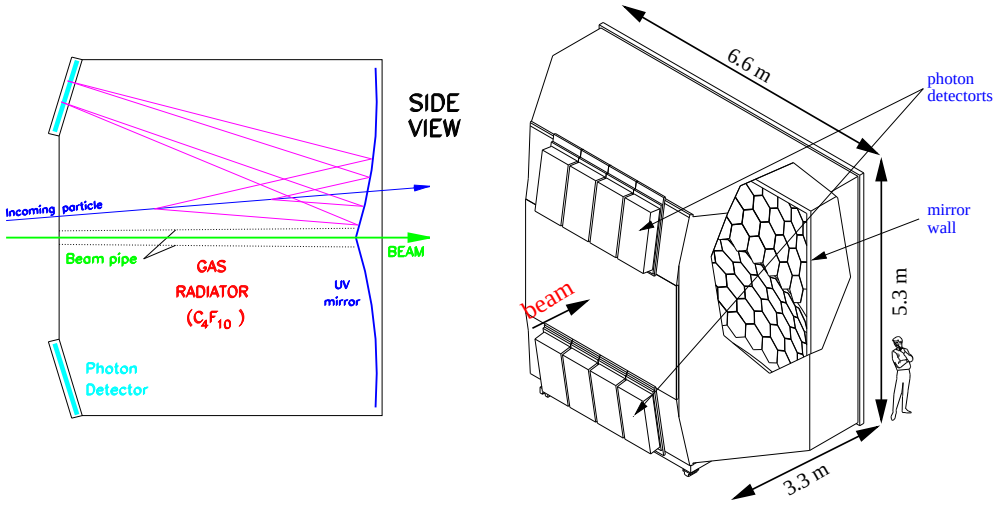

Figure 3.6.: Illustration of the RICH functioning principle (left) and a sketch of its design (right). Source: `http://wwwcompass.cern.ch/compass/detector/rich/rich_figures.html` (2012-05-24).

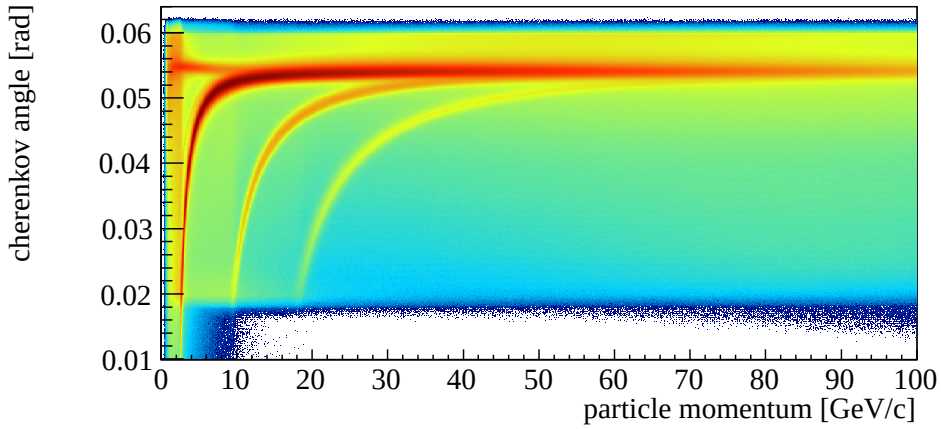

Figure 3.7.: The Cherenkov emission angle as function of momentum, reconstructed from 2008 COMPASS data [Jasinski, 2012]. From right to left one observes three bands, corresponding to (anti-)protons, kaons and pions respectively. In the upper left corner one observes the contribution from electrons.

length when propagating through the RICH pipe. Monte Carlo studies undertaken in the LMU group suggest that 21% of the photons interesting for the final states studied in this thesis are lost there [Diefenbach, 2011]. It has also been found that a significant fraction of pions interacts in the material of the RICH pipe. For the 2012 run a new, Kapton-based design was implemented.

3.4.2. Muon Identification

We shall briefly mention muon identification which is an important part of the COMPASS muon programme, but which is not used in the COMPASS hadron programme. Muons can traverse large amounts of material without any interaction. Unlike Pions, which are of comparable mass, muons do not interact strongly. Bremsstrahlung is also suppressed compared to electrons. Therefore the main process of energy loss for a muon is multiple scattering, a process which absorbs only a small fraction of the muon energy per given length. This property is used in muon identification: muons traverse both the electromagnetic and hadronic calorimeters behind which concrete absorbers are placed. Behind these concrete aborbers large tracking detectors are placed. If a track after extrapolation through all of this material can be identified with a hit in these planes, then it is considered a muon track.

3.4.3. Calorimetry

Calorimetry is the process of particle energy measurement by total absorption. It is also a means of particle identification, as different particles behave differently in calorimeters. In the preceding section we mentioned muons which are typically not all absorbed in calorimeters. In COMPASS calorimetry in both stages is divided into two parts: electromagnetic and hadronic calorimetry. The reason for this distinction is that it takes a significantly larger amount of material to absorb high energy hadrons than it takes to absorb electrons or photons. We do not discuss hadronic calorimetry further, only noting in passing that these are the tool to detect neutrons and the long-lived neutral kaon K_L^0 at high energies. Charged pions are identified by their low probability of interacting in the electromagnetic calorimeter and their absorption in the hadronic calorimeter. Additionally, the increased width of hadronic showers compared to electromagnetic showers can be made use of in a COMPASS-like setup [Binon et al., 1988; Davydov et al., 1977]. Calorimeters which unify electromagnetic and hadronic calorimetry are discussed e.g. in Ref. [Wigmans, 2000].

Physical Foundations

The basic processes of interaction between high-energy photons and matter is pair conversion, where in the field of a nucleus a photon can turn into an electron-positron pair by transferring a small amount of energy to the nucleus. High-energy electrons in passing close to nuclei radiate photons, the so-called *bremsstrahlung* process. Now the photon produced in a bremsstrahlung process can convert into a electron-positron pair, and these in turn can also undergo bremsstrahlung processes. Thus, a whole cascade of

particles can be produced from an initial photon or electron. This cascade is called an electromagnetic shower, and it is by means of such a shower that the electromagnetic calorimeter measures the energy and impact point of the inital particle. The following conditions have to be met in order to allow the forming of a shower:

- the material has to be dense in order to maximize the efficiency as a conversion target,
- it has to contain lots of nuclei with large electrical charge and which are heavy, and
- there must be a way of obtaining a signal from the calorimeter, preferably not by having to measure the temperature increase due to the impact, even though that is suggested by the term "calorimetry."

COMPASS employs two principles of electromagnetic calorimeters: lead-glass calorimeters and sampling calorimeters. Useful formulae for describing the material properties are collected in App. A. The two fundamental properties in describing the development of electromagnetic showers are the radiation length X_0 and the critical energy E_{crit}. The radiation length of a material is the thickness of material after which the energy of a high-energy electron has on average been reduced by a factor of 1/e. The bremsstrahlung energy loss is proportional to the electron energy and is, as a function of the traversed length of material X and the radiation length, given by

$$\left(\frac{\mathrm{d}E}{\mathrm{d}X}\right)_{\text{brems}} = -\frac{E}{X_0}. \tag{3.6}$$

The critical energy E_{crit} is the energy at which the ionization loss per radiation length X_0 equals the electron energy. Hence, it is the energy above which the energy loss can sensibly be decribed in terms of electromagnetic cascades. The conversion probability for a high-energy photon is also given in terms of the radiation length. Namely, a radiation length is the length after which a photon has underwent a pair production process with a probability of

$$P_{\gamma\to e^+e^-}(X_0) = 1 - \exp(-7/9) \approx 54\%. \tag{3.7}$$

The appearance of the radiation length in both Eqs. (3.6) and (3.7) is due to the fact that in both processes the underlying physics process is the same, but with an electron (positron) and the photon exchanged between initial and final state.

A simplified description of the main properties of electromagnetic showers is the following: after passing through a path of length X_0, a photon of energy E_0 will be replaced by an electron-positron pair with average particle energy $E_0/2$ with a probability of 54%. After another layer of thickness X_0 these will have emitted bremsstrahlung with an average energy of $E_0(1 - e^{-1})/2$. Thus after a total thickness of nX_0, one expects approximately 2^n particles with average energy $E_0/2^n$ in the shower. Hence the shower discontinues, once $E_0/2^n < E_{\text{crit}}$, leading to a total of

$$n_{\max} = \frac{\ln(E_0/E_{\text{crit}})}{\ln 2} \tag{3.8}$$

traversed radiation lengths. The transverse dimension of a shower is measured in terms of the Molière radius R_M which is given by

$$R_M = 21\,\mathrm{MeV} \cdot \frac{X_0[\mathrm{cm}]}{E_{\mathrm{crit}}}. \tag{3.9}$$

On average, 90% of the shower energy is deposited within a cylinder of radius R_M around the shower axis. The transverse dimensions of the calorimeter cells in the GAMS part of the calorimeter (see below) are similar to the Molière radii of the showers. Comparing the energy deposits in neighboring cells then allows for a precise determination of the impact points of the photon [Lednev, 2011]. Comparing reconstructed impact points with the reconstructed particle trajectories finally serves to indentify electrons, as they will deposit their energy in a photon-like shower, and it holds $E_{\mathrm{cluster}} = p_{\mathrm{track}}$.

The lead-glass calorimeters of the COMPASS experiment use the Cherenkov light emitted by the shower electrons to measure energy. The amount of Cherenkov light is roughly proportional to the total length T of the electron tracks in the shower which is given by [Kleinknecht, 2005]

$$T = \left(\frac{4}{3}X_0 + \frac{2}{3}t_0\right)\frac{E_0}{E_{\mathrm{crit}}}, \tag{3.10}$$

where t_0 is the range of the electrons at the critical energy (which given the low mass of the electrons is well above the Cherenkov threshold).

In order to allow for a higher radiation dose, the inner parts of ECAL2 employs sampling calorimeter blocks which use scintillators to measure the shower energy, and which are therefore sensitive to the energy deposited by the shower. A sampling calorimeter is longitudinally divided in alternating layers of absorbing material (lead) and readout material (scintillators). Only energy deposited in the scintillators is seen. It is therefore reasonable to study the energy deposit per unit of length, which is approximately given by [Kleinknecht, 2005]

$$\frac{\mathrm{d}E}{\mathrm{d}t} = E_0\frac{\beta^{\alpha+1}}{\Gamma(\alpha+1)}t^{\alpha}e^{-\beta t}, \tag{3.11}$$

with α, β properties of the material, and $t = X/X_0$ the traversed thickness of material in units of the radiation length. Detailed studies of the properties of electromagnetic showers were pursued in Ref. [Grindhammer and Peters, 1993; Grindhammer et al., 1990].

Electromagnetic Calorimeters in COMPASS

Both spectrometer stages are equipped with electromagnetic calorimeters, named ECAL1 in the large-angle spectrometer, ECAL2 in the small-angle spectrometer. Large angular coverage is necessary as photons can be emitted in any direction. ECAL1, installed in front of HCAL1 at a distance of approximately 12 m from the target, has a surface of $3.97 \times 3.86\,\mathrm{m}^2$ with a central hole of $1.07 \times 0.61\mathrm{m}^2$. It consists of a total of 1500 lead-glass blocks, each read out by a photo-multiplier tube. It consists of three types of lead

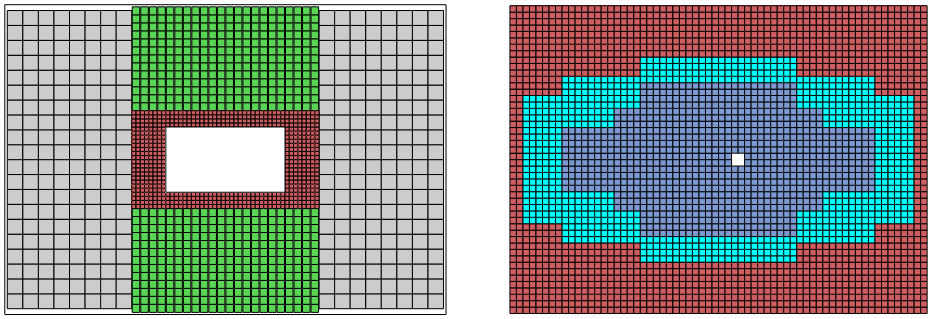

(a) ECAL1 (b) ECAL2

Figure 3.8.: Geometrical layout of the electromagnetic calorimeters. The different types of calorimeter blocks are indicated by different colors. Gray: OLGA, Green: Mainz, Red: GAMS, Cyan: Radiation Hard GAMS, Blue: SHASHLYK.

glass blocks, whose distribution is shown in fig. 3.8a. The central part consists of 508 lead-glass blocks of the type previously used in the GAMS-4000 experiment[Binon et al., 1986], arranged on a 44×24 matrix whose central part, corresponding to 28×16 blocks has been left empty to allow particles to reach the small-angle spectrometer. Matrices of lead-glass blocks made out of SF57 lead-glass [Adamovich et al., 1996] (called Mainz blocks) are installed above and below. Each of these blocks measures $7.5 \times 7.5 \times 36\,\mathrm{cm}^3$. In order to align these blocks with the GAMS blocks in the central part, 1.6 mm horizontal gaps have been left between the modules. These gaps are filled with iron where particles under low angle are expected. Finally, the outermost parts of ECAL1 are formed by the OLGA modules that measure $14.3 \times 14.3 \times 45.5\,\mathrm{cm}^3$ each, are made out of SF5 lead-glass [Astbury et al., 1985], and are arranged in 8×20 matrices on both sides.

	OLGA	Mainz	GAMS	rad.hard GAMS
lead glass type	SF5	SF57	TF1	TF101
fraction of PbO	55%	57%	50%	50%
density g/cm^3	4.08	5.51	3.86	3.86
X_0 [cm]	2.74	1.55	2.54	2.74
R_M [cm]	4.3	2.61	4.7	3.7
refractive index	1.67	1.89	1.65	1.67
length [X_0]	18.5	23.3	16.42	15.2

Table 3.1.: Properties of the different types of lead-glass. References given in the text.

ECAL2 consists of 3068 lead-glass blocks arranged on a 64×48 matrix, where a hole

of 2×2 blocks has been left around the nominal position of the beam, extrapolated to ECAL2. Each block has a cross-section of $3.83 \times 3.83\,\text{cm}$. In the 2008 and 2009 setups several rows of ECAL2 are not visible from the target due to the positioning of HCAL1.

Three different types of blocks are used: the outermost parts consists of TF1 lead-glass [Binon et al., 1986], surrounding radiation hardened lead-glass blocks made out of TF101 [Abbon et al., 2007; Kobayashi et al., 1994]. The central part is built out of the SHASHLYK type blocks depicted in fig. 3.9, which support radiation doses of several hundred kGy. They are sampling calorimeter blocks, composed of 155 layers of lead and scintillator where the scintillation light is collected by 16 wavelength shifting light fibers running through the length of each module converging onto a photomultiplier. The assembly can be seen in Fig. 3.9. The amount of scintillation light is proportional to the energy of the incident particles and the resolution has been measured to be $\sigma(E[\text{GeV}])/E = 6.6\%/\sqrt{E} \oplus 1\%$ in test beam measurements.[4]

Both ECALs are installed on a motorized support, allowing movement orthogonal to the beam direction. This is used to expose all parts of ECAL1 equally to an electron beam used to calibrate the energy response. Temporary drifts are monitored by LED and laser calibration systems, which deposes a defined amount of light in each cell and measure the response.

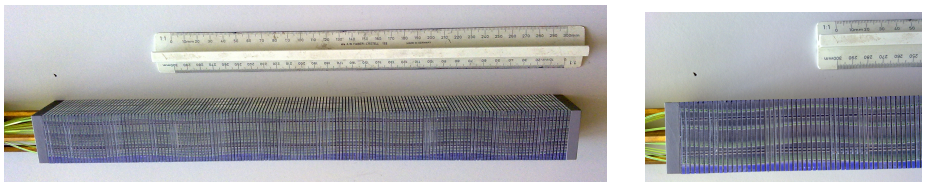

Figure 3.9.: A calorimeter block of the SHASHLYK type. The left picture shows the complete module except for the photomultiplier attachment which is off the picture to the left. The right picture shows a closeup where the scintillating fiber used for light collection can be clearly made out inside the transparent scintillators. The opaque gray parts in between the scintillators are the lead absorbers. Between the upper pair of fibers and the lower pair, two of the four steel wires holding the assembly together can be made out. They are attached to the Aluminum plates on both ends. Particles enter the assembly from the right. References given in the text.

Simulation of the ECAL response

The analysis described in this thesis makes heavy use of Monte Carlo simulations, several million events were simulated, each containing initially two photons. These simulations use COMPASS's modified version of GEANT3. GEANT3 simulates particle physics processes by following individual particles through a given material distribution while keeping track of energy losses and particles produced along the way [GEANT]. The

[4] G. Khaustov as quoted by Platchkov '08.

simulation time for each event is for the biggest part determined by the total path length traveled by simulated particles. As we saw above, this total path lengths grows approximately linearly with the energy contained in a shower. One thus expects several tens of meters of paths in a shower of, say, 20 GeV in the GAMS part of the calorimeters. This, together with the large number of particles that need to be created and destroyed in the course of the simulation makes the simulation of electromagnetic showers an expensive task. During the course of the thesis, two approaches to this problem were tried. On the one hand a geometrical simulation taking only the main effects into account. As this is discussed at length in Ref. [Diefenbach, 2011], we shall only summarize its main features below. Additionally, the Monte Carlo software was modified to replace the shower simulation in ECAL2 by an efficient, parameterized approach developed at DESY [Grindhammer and Peters, 1993; Grindhammer et al., 1990]. This latter approach yielded results identical to the complete simulation, while reducing the average time per event of the simulations by a factor of three without any tuning.

First, the geometrical simulation: in it only the most important aspects of the photon acceptance were simulated. Namely, the geometrical shapes of the electromagnetic calorimeters and the material contained in the RICH pipe described above were taken into account. Events from the Monte Carlo generator were then processed by tracing the photon trajectories, accepting them based on their hitting the calorimeters while taking into account the radiation length picked up in traversing the RICH beam pipe. Partial-wave analyses were performed using either only this purely geometrical simulation or combining it with a simulation where the charged tracks were simulated in the usual COMPASS Monte Carlo software. No significant differences in results were obtained, illustrating that the effects of acceptance are dominantly due to the geometry of the calorimeters.

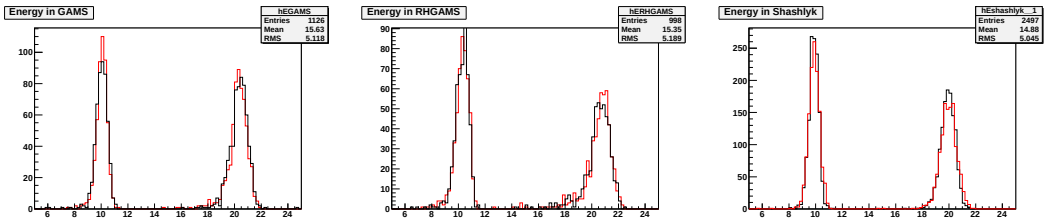

Figure 3.10.: Response of ECAL2 with the full simulation (red) and the parameterized GFLASH simulation for a sample of 10 GeV and 20 GeV photons hitting the individual calorimeter parts far from boundaries. From left to right the responses of the GAMS part, the radiation-hard GAMS part, and the SHASHLYK part are shown. Adjustment of the energy scale has not yet taken place, which explains the slight offset with respect to to the expected central values.

Second, a parameterized shower simulation was implemented. This meant replacing the tracking of individual photons and electrons through the calorimeter blocks with a parameterized approach, where the individual shower particles were replaced by a shower

object that, propagating on a straight line, deposits energy according to longitudinal and transverse parameterizations of electromagnetic showers. Additionally, the sampling SHASHLYK part of the calorimeter is replaced with an effective material, and effects of the sampling readout are simulated in the software, again in a parameterized fashion. Details can be found in Refs. [Grindhammer and Peters, 1993; Grindhammer et al., 1990]. Since most of the shower particles are of low energy, both the calorimeter signal and the processing time is dominated by the low-energy tails of the showers. Therefore, only the tails of the showers, produced by particles with energies below 5 GeV were simulated in this parameterized fashion. In order to not distort the shower shapes, and to correctly simulate particles leaving the calorimeter, the default setting was used according to which the shower parametrizations were only used when more than 90% of the shower tail was expected to be deposited in a single calorimeter cell. With these parameters and no additional tuning, results indistinguishable from the full Monte Carlo simulation were obtained, while using significantly less computing time. Fig. 3.10 shows a comparison of the simulated response of ECAL2 to fixed-energy photons with the standard simulation and with the parameterized simulation.

3.5. Trigger

The purpose of the trigger is two-fold: on the one hand it is intended to tag with high efficiency interesting events which then are recorded for further analysis, on the other hand it should ensure high purity by rejecting events that are not of the requested type or are contaminated by additional particles and the like in order to cope with the limited recording capacity of the experiment. The type of event of interest in this study is defined by a beam particle interacting in the target such that a recoil proton is ejected at large angles while no additional particles are produced in the target fragmentation area. In order to suppress events triggered by particles entering the spectrometer off the beam axis, veto hodoscopes upstream of the target cover the area from just outside the target cross-section up to several meters away. If a particle is found in these detectors, an event is not recorded. The other components in the main physics triggers are shown schematically in Fig. 3.11.

The main physics trigger is called DT0. It is defined as

$$\mathrm{DT0} = \mathrm{BT} \wedge \mathrm{RPD} \wedge \overline{\mathrm{VETO}},$$

here BT denotes the beam-trigger condition explained in Fig. 3.11, RPD denotes the recoil proton condition discussed in Sec. 3.2, and $\overline{\mathrm{VETO}}$ denotes the absence of a signal from the upstream hodoscopes explained above, the beam-killer hodoscope (see figure) or the sandwich veto detector, which will be discussed in detail below. Under typical conditions, approximately 0.2% of the $2{\cdot}10^8$ beam particles per 16.8 s lasting spill fullfilled this trigger condition.

Besides this physical trigger, events with a kaon trigger (requiring $\mathrm{BT} \wedge \mathrm{CEDARs} \wedge \overline{\mathrm{VETO}}$) were recorded. Additionally, events with only beam triggers and other diagnostic triggers were recorded with large prescaling factors. We shall now turn to the discussion

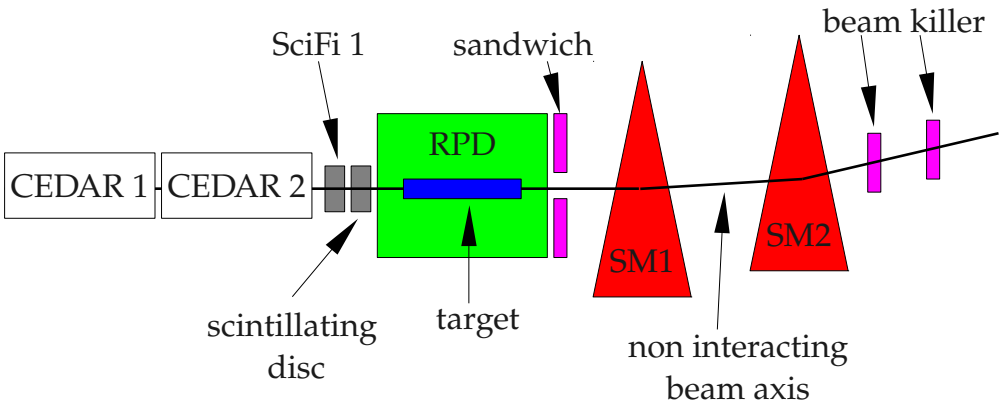

Figure 3.11.: Schematic view of the main trigger components. The beam enters the figure from the left, first passing through the CEDAR detectors which are the main part of the kaon trigger. The beam particle is identified by a coincide of a scintillating fiber detector (SciFi1) and a scintillating disk. The target is contained in the recoil proton detector (RPD) which identifies the proton leaving the target. Particles emitted outside the acceptance of the spectrometer are rejected by the sandwich veto detector. Finally, purity is enhanced by a suppression of non-interacting beam particles by the beam killer hodoscope which is installed right in front of ECAL2 along the nominal trajectory of the undeflected beam. Figure from Ref. [Jasinski, 2012].

of the sandwich veto detector which was developed and assembled during the course of this thesis.

3.6. The Sandwich Veto Detector

The requested event types have in common that the target proton remains intact.[5] It is emitted at large angles compared to the beam direction with momenta on the order of a few hundred MeV/c. This proton is detected by the recoil proton detector (RPD) which encloses the target with an angular range from 55° to 125° as seen from the centre. Apart from the recoiling proton no other particle is expected in the target fragmentation region. Inelastic, non-diffractive processes and diffractive excitations of the target produce the dominant background, yielding additional particles in this region. In order to enrich the recorded data with kinematically complete events of the required type, a veto trigger counter was needed that spans a large part of the angular range between the acceptances of the spectrometer and that of the RPD.

The sandwich veto detector designed, assembled, installed and operated durign this thesis is a $2\,\mathrm{m} \times 2\,\mathrm{m}$ detector with optically active wavelength shifting (WLS) fibre read-out that detects photons and charged particles falling in a solid angle of 1.15 sr outside of the spectrometer's geometric acceptance (Fig. 3.4). In principle the detector is a thin electromagnetic-calorimeter-type detector complying with the following demands: high rate capability, good time resolution, compact geometry, high efficiency for minimum ionizing particles and photons with energy above 100 MeV, and low false-veto probability.

At full use of the data recording capacity of 30 kHz, it is found that inclusion of the SW veto enriches the recorded sample with good candidate events by a factor of about 3.5. Apart from the event type described above, the SW veto is also useful in studies of exclusive events with excited recoil protons detected by the RPD or with nuclear recoils unnoticed by the RPD.

3.6.1. Detector Setup

Scintillators with WLS fibre readout

Light signals from scintillating material can be collected, converted and transported to photomultipliers by wavelength shifting fibres. This technique has been optimized by the Moscow-Protvino groups [Ivashkin et al., 1997; Karyukhin et al., 1996; Mineev et al., 2002; Yershov et al., 2005] with regard to good efficiency, fast timing and radiation hardness. It allows for compact large-area calorimeter designs.

The scintillator material used here is a polystyrene (DOW Styron 637) with additives of pTP (2% weight fraction) as primary fluor and POPOP (0.02% weight fraction) as secondary fluor. The intensity of the scintillation light assumes its maximum at 420 nm, the refractive index is $n = 1.59$.

[5] This chapter follows closely Ref. [Schlüter et al., 2011a].

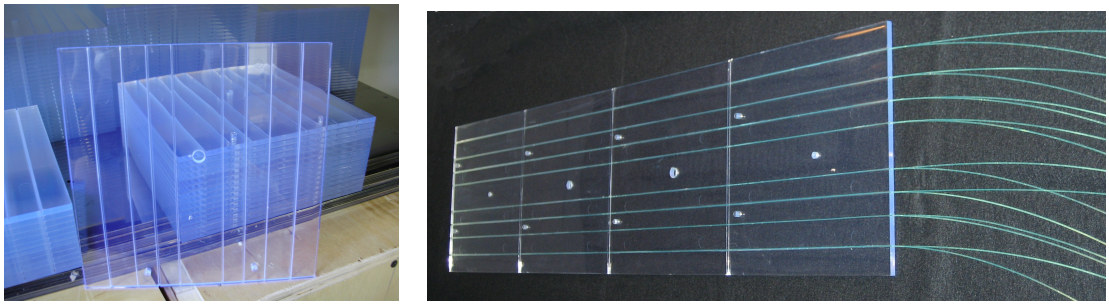

Figure 3.12.: Photographs of the scintillators used. Left: a single tile in front of stacks of several tiles. The eight grooves for fiber insertion run vertically. In the center, a hole for insertion of a sleeve through which a bolt passes. Near the bottom two knobs ensure correct alignment. Right: Single layer of 4 scintillator tiles with an area of 80 cm × 20 cm. Eight pairs of fibres are glued into grooves of 2.2 mm depth.

Tiles of an area 20 cm × 20 cm and thickness of 5 mm of the same type used by a previous cosmic muon experiment were manufactured at the Institute of High-Energy Physics (Protvino) by means of molding techniques [6]. Eight grooves of 1.4 mm width and 2.2 mm depth run in parallel over each tile for fibre accomodation. Four of these were included in the mold, the other four milled subsequently. Two small knobs were molded and a central hole was drilled to allow for stable stacking in sandwich layers.

Optically active fibres of 120 cm length are used for readout. The chosen type of multiclad fast green wavelength shifters (Bicron BCF-92, ⌀1 mm [St. Gobain 2005]) are characterised by absorption and emission maxima at 410 and 490 nm, respectively. Core and cladding refractive indices are $n = 1.60$ and 1.42, respectively, and the $1/e$ attenuation length is > 3.5 m.

For installation in the sandwich detector, 4 scintillator tiles or 4 stacked pairs of tiles are grouped in bars of an area of 80 cm×20 cm and thickness 5 mm or 10 mm, respectively. A four-tile bar has eight pairs of fibres for common readout (Fig. 3.12). Double layers consist of a layer as above, the fibres running on the upper side, on which another layer is stacked carrying only one fibre per groove, altogether 8 × 3 fibres.

The fibres are glued into the grooves with optical cement BC-600 [St. Gobain 2002] which has a refractive index $n = 1.56$. After mixing, this two-component glue is extruded into the groove with a syringe. The fibres are inserted such that they are fully covered with glue. For fibre-pair readout, a second string of glue is overlayed on the first fibre before inserting the second fibre. The far-side ends as seen from the photomultiplier are cut at an angle to suppress light reflection. This is validated by the absence of reflected photon signals. After hardening of the optical cement, scintillator bars have sufficient mechanical stability for subsequent handling.

In the final assembly the scintillator bars are wrapped with a single layer of white Tyvek paper R1025D (thickness 140 μm). This diffusive reflector is found to increase

[6] Details at `http://www.ihep.ru/scint/index-e.htm`

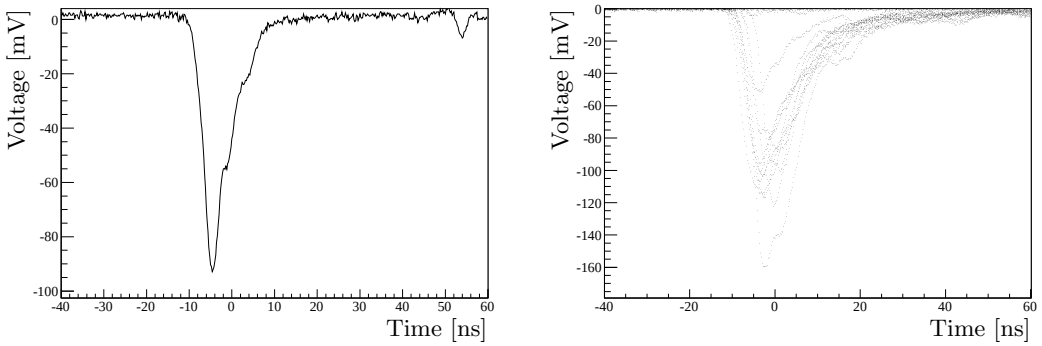

Figure 3.13.: Pulses from cosmic muons recorded with an oscilloscope connected to the photomultiplier anode from one bare double layer of 10 mm scintillator thickness (left), and from the final sandwich detector (right). An accidental single photoelectron show up on the tail of the left signal.

the light output by 25%. This was studied in Ref. [Dhibar, 2008].

Bundles of fibres from a single detector block (see below) are fed through a plexiglas cylinder. After fixation with epoxy glue, ends are cut and the front side is polished. It is attached to a XP2262B phototube. Initially XP2020 phototubes were employed, which have less gain but elsewise are suited as well. Both tubes are fast and provide quantum efficiencies of about 20%. The efficiency curves are rather flat, peaking at 420 nm [Photonis].

Cosmic ray tests were performed with trigger counters above and below scintillator tiles. Pulses from muons in a double layer, with most probable energy deposit of 1.9 MeV, produce signals of about 10 photoelectrons (Fig. 3.13). Rise times and decay times (20%-80%) of 3 and 6 ns are found. Comparing signals from the far and near end, we find a light attenuation of 25% over the length of 80 cm.

3.6.2. Sandwich Assembly

The SW has a total thickness of 5.1 radiation lengths. It consists of 12 blocks, each of an area of 80 cm × 40 cm minus cutouts for the central hole arranged on the 2 m × 2 m surface (Fig. 3.14). Each block is assembled from 5 steel-covered lead-plates and 5 scintillator layers, 3 of 10 mm and 2 of 5 mm thickness. As seen from the target entry, the hole is approximately conical with an opening angle of $\pm 10.3^\circ$. Each block is mounted on a steel plate of 8 mm thickness which is attached to an outer support frame. The complete detector has a mass of 2 t. It is held in the vertical position by a welded H-iron support frame which is stabilized by struts across the corners. These allow mounting the detector blocks in the horizontal position. The frame also carries a small multiplicity counter covering the inner hole on the spectrometer side. this counter was used as a trigger on events with low momentum transfer during the 2009 run [Alekseev et al., 2012].

The optically inactive layers of the calorimeter consist of 5 mm lead plates which have 1 mm steel glued to each side to accomplish sufficient stiffness for the assembly

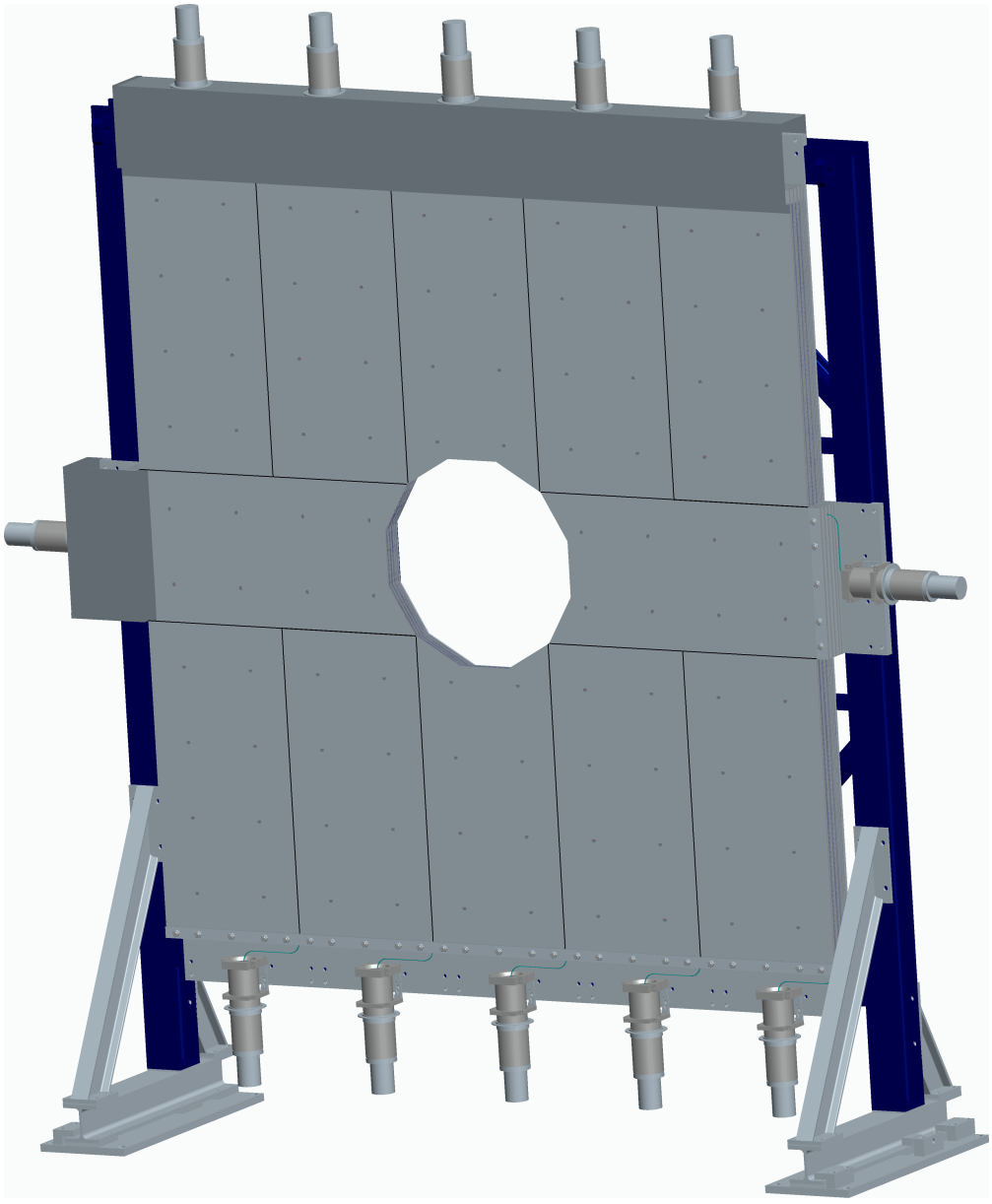

Figure 3.14.: Design of the veto detector. The light-shielding boxes are omitted for the lower 5 detector blocks and for one of the two horizontal detector blocks to uncover the photomultiplier assembly. The support frame has horizontal and vertical lengths of 228 and 256 cm, respectively.

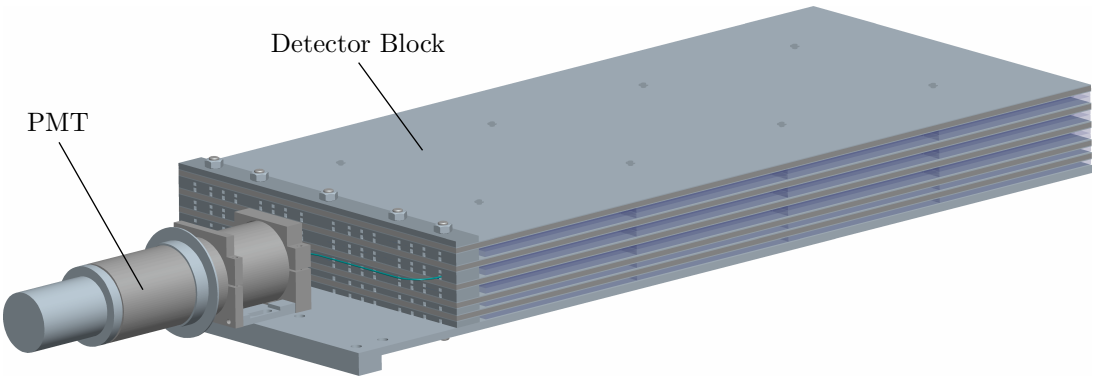

Figure 3.15.: View of a detector block with photomultiplier tube (PMT) enclosed in a cylinder of soft iron which is attached to the lower steel plate.

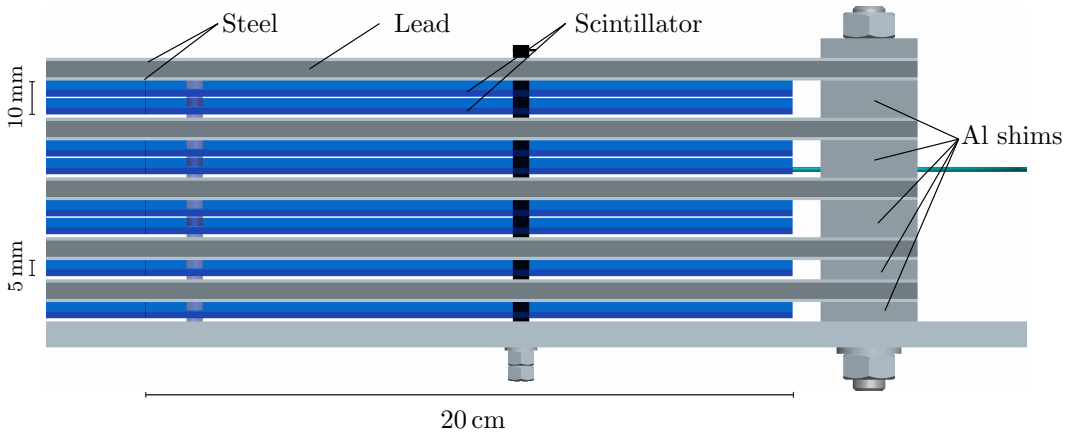

Figure 3.16.: Lateral cut of the near photomultiplier side of a detector block (PMT to the right). The cut is along one of the grooves in the scintillator tiles. One light fibre, out of a total 208, is shown emerging from a groove. Steel screws cramp the 5 steel-covered lead layers and the Al shims to the lower steel plate which is downstream in the vertical detector position. One of the bolts traversing the detector block is recognized.

(Figs. 3.15, 3.16). Each scintillator layer is formed by a pair of 80 cm × 20 cm scintillator bars lying side-by-side. Their positions are fixed by two knobs per tile, mentioned above, and by 8 bolts per detector block, traversing the central holes of the scintillator tiles (Fig. 3.15, 3.16), four of which have sleeves between the lead/steel plates ensuring their proper distance. To accomplish mechanical stability without exerting pressure on the scintillators, the lead/steel plates are cramped onto the rear steel plate where the correct distance is enforced by aluminum shims. In total a block has 64 scintillator plates which are grouped in 3 double layers on the upstream side (top in Figs. 3.15, 3.16) and 2 single layers on the downstream side. For the given amount of scintillators this order gives the best efficiency for low-energy photons according to Monte Carlo simulations (see below).

The light fibres are fed through channels in the shims. For common readout, the total of 208 fibres per block are bundled in a plastic cylinder which is attached to the entrance window of a XP2262B phototube. The stray magnetic field of the spectrometer's first stage dipole magnet necessitates magnetic shielding of the photomultipliers. This is accomplished by double cylinders made of μ-metal and soft iron, respectively (Fig. 3.15).

3.6.3. Monte Carlo Studies

The response of the detector to photons and charged particles was simulated with the Monte Carlo code GEANT4 [Agostinelli et al., 2003; Allison et al., 2006].[7] The energy deposit in the scintillator layers for perpendicularly impinging photons of various energies (Fig. 3.17) is characterized by a broad peak from showers and narrow peaks superimposed at lower energies. The first (second) narrow peaks are due to single electrons or, less frequently, positrons traversing only one of the scintillator layers of 5 mm (10 mm) thickness, respectively. Shown for comparison is the energy deposit of muons with $E_{kin} = 285\,\mathrm{MeV}$ and $E_{kin} = 160\,\mathrm{GeV}$ (used at COMPASS for spectrometer alignment). The most probable energy deposit of muons is almost independent of their energy in this range. This comes in spite of the energy loss at 160 GeV being considerably larger than in the minimum ionizing case (285 MeV): the additional energy loss is due to radiative processes: the ensuing photons pass through the assembly undetected, and e^+e^- pairs are mostly produced and stopped in a lead layer depositing no energy in the scintillators.

The fraction of photons with energy deposit above ΔE gives the efficiency for discriminator threshold corresponding to ΔE (Fig. 3.17). For threshold corresponding to one third of $\Delta E_{\mathrm{MIP}} = 7.5\,\mathrm{MeV}$, the most probable energy deposit of minimum ionizing particles, the efficiency is above 90% for energies above 100 MeV and drops to 80% for 50 MeV photons. This threshold was chosen in COMPASS runs after a pulse height calibration with muons of high energy (next section), however, halving the threshold is feasible at the noise level observed in the experiment.

In order to suppress delayed energy deposits from secondary processes induced by very soft hadrons, the simulated energy deposits were integrated over a timespan of 10 ns. This timespan is adapted to the observed signal broadening coming from light

[7] All plots were created using the `QGSP_BIC` physics list. No significant dependency on the choice of physics list was observed.

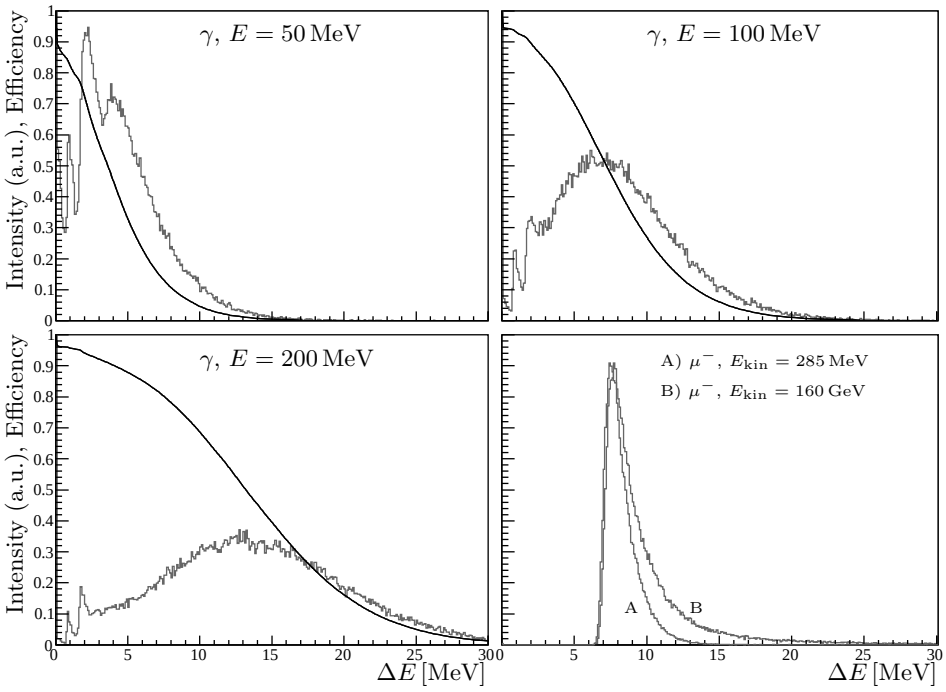

Figure 3.17.: Monte Carlo prediction of the energy deposit, summed over all scintillator layers, for photons and muons impinging perpendicularly on the veto detector (grey histograms). For photons, the black lines indicate the fraction of events above the value of ΔE, thus giving the efficiency as function of thresholds on the energy deposit.

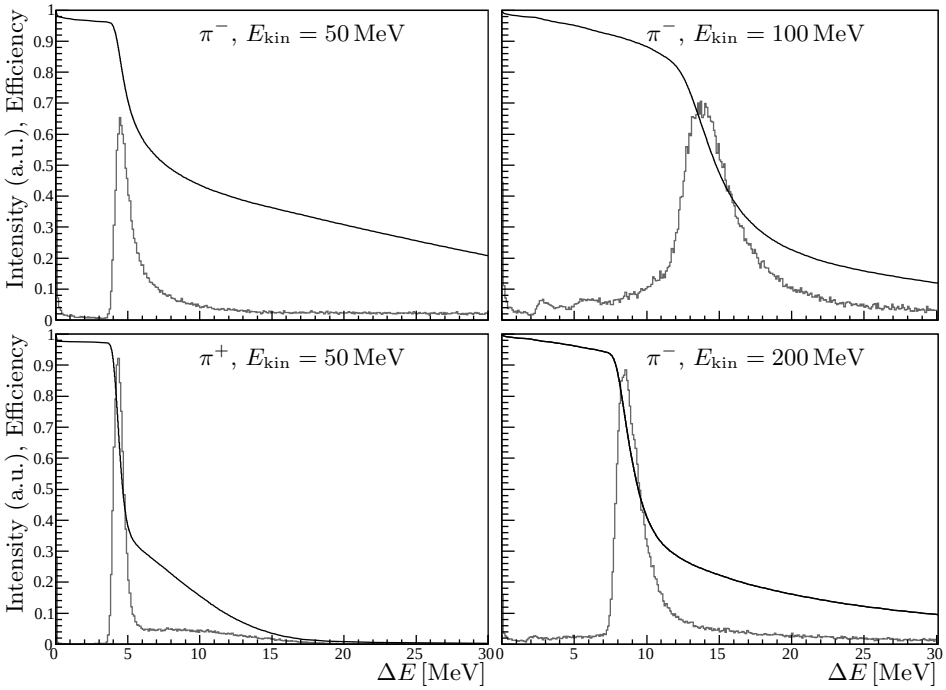

Figure 3.18.: Monte Carlo prediction of the energy deposit, summed over all scintillator layers, for π^+ and π^- impinging perpendicularly on the veto detector (grey histograms). Integration of ΔE was stopped after 10 ns which is relevant only in the case of 50 MeV (see text). For the black lines see Fig. 3.17.

collection and conversion in the scintillators and the WLS fibres (see below). Significant differences from the complete energy deposits occur only for hadrons of low energy.

For pions with kinetic energy above 50 MeV, efficiencies above 95% are obtained (Fig. 3.18). The edge at 4 MeV of the distribution of energy deposits for 50 MeV pions is due to their low range leading to stopping in the second lead/steel layer. The integration time of 10 ns is relevant for 50 MeV pions. For larger time spans the ΔE distribution develops a broad shoulder towards larger values (not shown). In the case of stopped negative pions, this is mostly due to secondary neutrons scattering in the scintillator material after being produced in the Pb layers. In the case of stopped positive pions, the broadening can be traced back to $\mu^+(e^+\bar{\nu}_\mu\nu_e)$ decay. These effects are not important for the present vetoing at sufficiently low threshold but should be kept in mind when pile-up is a concern. Pions with energy at or above 100 MeV yield a peak above or at $\Delta E_{\rm MIP}$ (Fig. 3.18, right) with insignificant dependence on the integration time and insignificant π^+/π^- difference, since the pions traverse the detector.

The first lead/steel layer corresponds to the range of 30 MeV pions. Up to this energy pions are not vetoed. This layer was chosen for the entry to suppress false vetoes from delta electrons accompanying valid events in the target. Monte Carlo simulations of delta electron production by 190 GeV pions traversing the 40 cm liquid hydrogen target

give a 1% probability for a veto signal induced by delta electrons.

3.6.4. Performance of the Veto Detector

Photomultiplier signals from cosmic muons traversing the final detector assembly have average rise times (20%-80%) of 3.3 ns, logarithmic decay times of 9 ns, and widths at half maximum of 12 ns (Fig. 3.13). These values are larger by a factor of almost 3 than those obtained for single photons and they are also larger than the corresponding values for a single double layer. These differences are attributed to the statistical spread of light collection times.

The total number of photoelectrons for minimum ionizing particles (MIP) impinging perpendicularly on the detector amounts to 45. Taking the quantum efficiency into account, this corresponds to 220 photons entering the photomultiplier window. It was observed that significant light collection only occurs in the fibers closest to the impact point (also [Ruschke, Private communication, May 2012]). More relevant for fast discrimination is the signal height. Because of the photoelectrons' time spread the resulting signal height corresponds to a lower number of single photoelectrons. It is found that the average signal height for MIPs corresponds to 18.7 single photoelectrons. For the COMPASS veto trigger a discriminator threshold corresponding to six times the single photoelectron level was chosen. The 10 ns coincidence time requirement of the COMPASS veto system was easily fulfilled.

The veto efficiency for MIPs was determined with 160 GeV/c muon beams using a halo trigger. A veto flag probability of 98% was obtained for muons with a reconstructed track traversing the SW detector. This value refers to homogeneous irradiation of the complete detector plane excluding the central hole. Tracks at the block edges contribute more than half of the missing 2%. Details in Ref. [Wöhrmann, 2010].

Hadron beam test runs with the SW excluded from the hardware trigger but recorded as flag demonstrate its proper operation. For events carrying the flag, the total momentum distribution of particles detected in the spectrometer is shifted towards lower momenta with respect to the incoming π^- momentum of 191 GeV/c due to the momentum carried away into the sandwich veto detector. This is attributed to target fragmentation. Such kind of events are strongly suppressed in the distribution without veto flag where a peak characteristic of exclusive kinematics stands out. This group of events is attributed to the processes of interest here, namely peripheral production of mesons. For this example, events with one (Fig. 3.19) or three reconstructed tracks in the spectrometer (Fig. 3.21) were selected, defining a total momentum vector. This vector and the momentum vector $\boldsymbol{p}_i$ of the incoming pion define an (oriented) plane which can be compared with the (oriented) plane defined by $\boldsymbol{p}_i$ and the momentum vector of the target-like recoil detected with the recoil detector. The "coplanarity angle" $\Delta\phi$ between these planes shows a peak at zero, characteristic of exclusive kinematics, for events with no SW veto signal, whereas events with a SW veto signal have a broad $\Delta\phi$ distribution. These distributions are shown in Figs. 3.20 and 3.22 for the two event classes. A peak in these latter distributions would indicate false vetoes. For these plots a total reconstructed momentum > 180 GeV/c was required, which largely suppresses events where

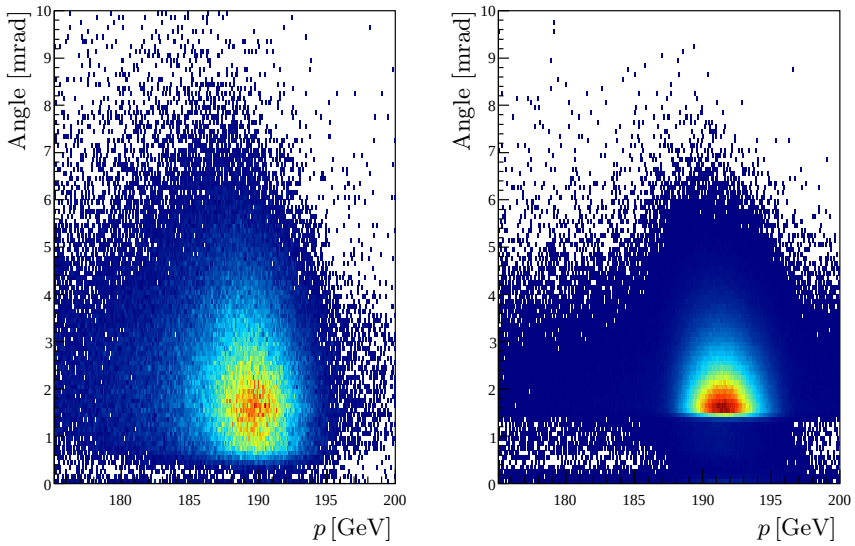

Figure 3.19.: Scattering angle vs. momentum for events with a single reconstructed track in the spectrometer. Right: events where no veto signal was produced by the sandwich detector, left: events where there was such a veto signal. In the right picture the elastic scattering peak is clearly visible at the nominal beam momentum of 191 GeV, a minimum scattering angle is enforced by the trigger condition that there be a recoiling proton. With the veto signal, the distribution is widenend and shifted to lower momenta. Additionally, the cutoff at low transverse momenta required by the trigger is not fulfilled.

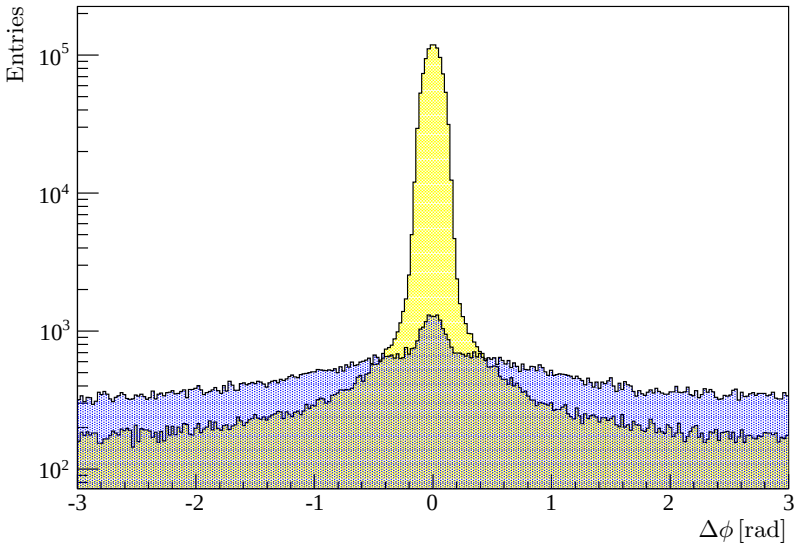

Figure 3.20.: Coplanarity angle (see text) for events with one reconstructed track and total momentum above 180 GeV recorded with (patterned filling) / without veto signal from the sandwich detector.

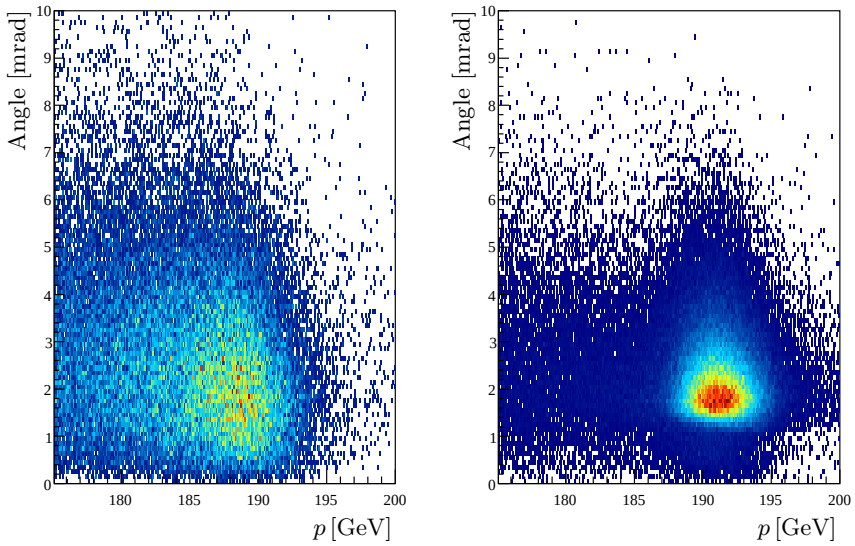

Figure 3.21.: Scattering angle vs. momentum for events from 191 GeV $\pi^- + LH_2$ with three reconstructed charged tracks in the spectrometer. The scattering angle and momentum p refer to the total momentum vector in the laboratory sytem evaluated from the three tracks. The left image shows events where a veto signal was produced by the sandwich detector, whereas in the right picture there was no such veto signal. Small scattering angles are suppressed by the requirement of a signal from the recoil proton detector.

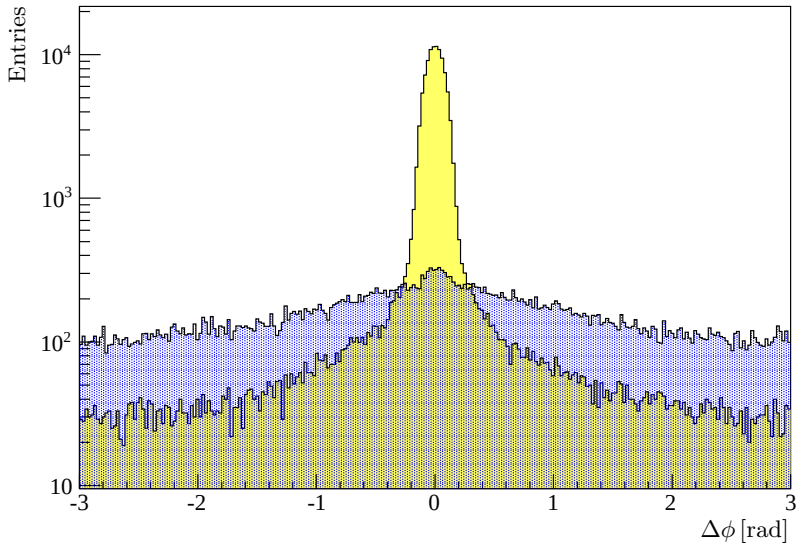

Figure 3.22.: Coplanarity angle (see text) for events with three reconstructed charged tracks with total momentum above 180 GeV recorded with (patterned filling) / without veto signal from the sandwich detector.

momentum was carried away by neutrals not taken into account here.

Important figures of merit are the enrichment factor of useful data in the recorded events and the probability of false vetos. The former is defined as the factor by which the physics trigger rate increases if the sandwich is not included in the veto. At given data recording capability of about 30 kHz in the present case, the rate of physics data recording is increased by this factor due to the SW veto. Enrichment factors of 3.3 to 3.8 were obtained in the hadron runs. Typical beam rates were $2 \cdot 10^8$ particles per spill with spill length and repetitions rate of 16.8 and 21 s, respectively, and SW rate of about 1 MHz. The probability for wrong vetoes was extracted from SW coincidences with noninteracting beam particles and also from the $\Delta\phi$ distributions as in Fig. 3.22. A probability of 1% was found for faulty SW vetoes, which agrees with estimates from the simulation of delta electron production.

3.6.5. Summary

A compact 2 m × 2 m sandwich detector of 5.1 radiation lengths total thickness was installed around the COMPASS spectrometer's entry for vetoing on incomplete detector events. Read-out by WLS fibres running in grooves over the scintillators allowed for MHz rates and fast triggering. A total energy deposit in the scintillators of 7.5 MeV, obtained for minimum ionizing particles (MIP), results in 220 photons entering the photomultipliers (PM). Statistical spread of light collection times leads to a signal rise time of 3.3 ns and logarithmic decay time of 9 ns, corresponding to 3 times the single photo electron values. The resulting MIP signal height corresponds to 18.7 photo electrons. The PM output was fed directly into the veto discriminator.

The veto efficiency for MIP's was found to amount to 98 % for a discriminator threshold corresponding to one third of the MIP signal height [Roushan, 2009; Wöhrmann, 2010]. Monte Carlo simulations yield efficiencies for this threshold which are above 95 % for pions with kinetic energy above 50 MeV and above 90 % (80 %) for 100 MeV (50 MeV) photons. The detector performed well for about 12 months of running time in 2 years, mostly with pion beams of 190 GeV/c impinging on a liquid hydrogen target. Rejecting events not completely covered by the spectrometer, it increased the fraction of useful data with complete kinematics by a factor of 3.5 as compared to data recording with inactive sandwich veto. Since this factor was obtained at full use of the data recording capacity of 30 kHz, it translates directly into a gain in statistics for the diffractive and central production processes under study.

4. Data Set and Event Selection

The analysis presented in this work uses data taken by the COMPASS experiment in its 2008 run, where a beam of negatively charged hadrons, consisting mostly of pions, passed through a liquid hydrogen target. Only data fulfilling the DT0 trigger requirement described in Sec. 3.5 were taken into account. In order to allow refinement of the selection criteria without having to repeatedly process the complete 2008 data sets, a two-step selection was employed where in the first step the data set was reduced by very general criteria before selecting in a second step the data used in the physics. These data sets were then refined to the final data sets of $\approx$ 120 000 events of the type $\pi^- p \to \pi^- \eta(\pi^-\pi^+\pi^0(\gamma\gamma))p$ and $\approx$ 50 000 events of the type $\pi^- p \to \pi^- \eta'(\pi^-\pi^+\eta(\gamma\gamma))p$.[1] Since this work involved the development of a calibration algorithm for the electromagnetic calorimeters, we will describe this algorithm after a short disgression on the procedure of reconstructing neutral particles from calorimeter data. After this we will turn to the data selection employed in the analysis.

4.1. Reconstructing Photon Four-Vectors

Photons are measured by detecting their energy deposits inside the electromagnetic calorimeters. Possible candidates are energy deposits that are not in the vicinity of reconstructed impact points of charged tracks. Any physics interpretation needs the full four-vector in order to be able to proceed. A four-vector for the massless photon is given by three quantities which can be chosen to be the energy E of the photon (as measured in the calorimeter) and its direction (which is given by two angles). The direction of the photon is determined by making a hypothesis about the point $\boldsymbol{x}$ of emission of the photon and linking this point to the point of impact $\boldsymbol{y}$ in the calorimeter. The three-vector $\boldsymbol{p}$ of the photon can then be determined as

$$\boldsymbol{p} = E \times \frac{\boldsymbol{y} - \boldsymbol{x}}{|\boldsymbol{y} - \boldsymbol{x}|}, \tag{4.1}$$

from which one has immediately $m_\gamma^2 = E^2 - \boldsymbol{p}^2 = 0$ as required.

All intermediate particles under consideration have very short lifetimes so that the point of their decay can be taken to be the reconstructed primary vertex. Take for illustration the relatively long-lived π^0 and have it pick up the complete available energy of 190 GeV. Its lifetime is $\tau = (8.4 \pm 0.5) \times 10^{-17}$ s [Nakamura et al., 2010] which translates to a decay length of $\ell = \gamma c\tau = (E/m_{\pi^0})c\tau \approx 35\,\mu$m, well below the tracking resolution

[1] Most of this work was done in collaboration with C. Raab and H. Wöhrmann and is also documented in their bachelor's and diploma theses [Raab, 2011; Wöhrmann, 2010], respectively.

in the beam direction. The lifetime of the π^0 being orders of magnitude above that of all other intermediate particles, it is clear that all photons can be assumed to originate in the location of the reconstructed primary vertex. On the other hand, secondary reactions may lead to γ emission away from the target, examples are processes as diverse as π^0 production in hadronic interactions away from the target,[2] the decay of the CP-even neutral Kaon $K_S^0 \to \pi^0\pi^0$ or the emission of Bremsstrahlung by δ-electrons. Moreover, charged particles whose tracks are not reconstructed or hadronic showers in the ECALs may lead to calorimeter clusters not associated with reconstructed charged tracks and will therefore have to be suppressed in the data selection.

In the case of $\pi^0 \to \gamma\gamma$ or $\eta \to \gamma\gamma$, another requirement that can be made in the selection is that the reconstructed mass of the photon pair be in the vicinity of the nominal π^0 or η mass. The invariant mass squared of the pair of photons with four-vectors $p_{1,2} = (E_{1,2}, \boldsymbol{p}_{1,2})$ determined as above is then

$$m_{\gamma\gamma}^2 = (p_1 + p_2)^2 = 2E_1E_2(1 - \cos\vartheta) = 4E_1E_2 \sin^2\frac{\vartheta}{2} \approx E_1E_2 \cdot \vartheta^2, \tag{4.2}$$

where ϑ is the angle between the directions of the two photons and use has been made of $p_1^2 = p_2^2 = 0$, i.e. $|\boldsymbol{p}_i| = E_i$. The approximation is valid for small values of ϑ. An important consequence of this is the following: for a given energy $E = E_1 + E_2$ of the decaying particle, there is a minimal angle $\vartheta_{\min}$ between the photons which is obtained in the case $E_1 = E_2 = E/2$ and it is given in the approximation of small angles

$$\vartheta_{\min} = \frac{2m_{\gamma\gamma}}{E}. \tag{4.3}$$

The photons will then be on a cone about the direction of flight of the decaying pseudoscalar, with apex at the point of decay, making an angle $\vartheta_{\min}/2 = m_{\gamma\gamma}/E$ with its direction. In the case of different energies, say $E_1 > E_2$ of the two photons, the photon with energy E_1 will move towards the initial direction of the decaying particle, i.e. to the inside of the cone, whereas the other photon will move away from the cone. Hence, for a given direction of the π^0, say, most photons will be concentrated in a small part of the calorimeter. In the case of COMPASS, for a π^0 with energy 40 GeV pointing at ECAL2, the base of the cone will be a circle of radius ~ 10 cm. I.e., one photon from the decay of the π^0 will be within this cone, the other outside at an arbitrarily large angle. On the other hand, the photons will always be separated by at least twice this radius.

4.2. ECAL Calibraton With π^0 Decays

The energy measurement in a calorimeter is much more sensitive to calibration issues and temporal fluctuations than the momentum measurement in tracking: whereas momentum measurement is determined by the quality of knowledge of the placement of the inert detectors and of the stable magnetic fields, the calorimeter measurement is

[2] We discuss structures of this kind in Ref. [Bernhard et al., 2012].

determined by the response of the individual calorimeter cells. These are read out with photomultiplier tubes which are individually subject to the influence of temperature, voltage fluctuations, their coupling to the calorimeter blocks are subject to condensation in optical contacts, etc. By the design of the GAMS-type calorimeter, where the block size is matched to the Molière radius of the block material, the bulk of the energy deposited in a shower is deposited in very few cells, so good calibration and monitoring of each indidual cell is mandatory. An initial calibration is obtained by illuminating the calorimeters with an electron beam. The defined energy of the electron beam can then be used to determine calibration coefficients describing the repsonse of each individual cell. Temporal fluctuations are then accounted for by a laser system in ECAL1 and a system of monitioring LEDs in ECAL2, where defined amounts of light are injected into the individual calorimeter cells. Comparing the calorimeter response to these light pulses at some later time to the responses recorded during the electron calibration runs then allows compensating for temporal fluctuations of the calorimeter. Temporal fluctuations of the LED or laser systems can be detected in part by observing systematic shifts over a large number of calorimeter cells.

In order to further refine the calibration, and to incorporate information obtained during the experiment, as a next step one performs a calibration based on physics data, a so-called π^0 calibration. Here photons from π^0 decays are used to enhance the calibration. Both these types of calibrations were not available during the 2008slot3 data production used in this work. We therefore developed our own π^0 calibration strategy, applied on top of the reconstructed data, in order to increase the quality of the data, as we observed clear deviations of the positions of observed π^0 and η peaks from their nominal values.

The π^0 calibration procedure determines calibration factors, which are applied to the energy values stored in the reconstructed DSTs. In order to do this, a superset of the events used in the analysis was pre-selected into a minimal data structure to allow fast processing. Then the following procedure was iterated:

1. Candidate events with a $\gamma\gamma$ mass near the π^0 or η mass are identified.

2. For each such event, scaling factors are calculated by means of a fit to the π^0 or η mass. These scaling factor, if applied to the energy values, yield the correct π^0 or η mass. These values are recorded, attributing them to the central calorimeter cell of each shower.

3. After processing all events, for each cell the average of the obtained scaling factors is calculated and stored.

4. From now on, each energy measurement is multiplied by the scaling factors, and the procedure is iterated.

The iteration continues until the scaling factors stabilize. With this procedure, scaling factors for most of the calorimeter cells can be obtained on a run-by-run basis. For cells farther away from the beam axis where smaller numbers of photons hit the calorimeter, averages are built over several runs.

The impact on the resolution of the calorimeters is illustrated in fig. 4.1, where $\gamma\gamma$ mass spectra are shown and the benefit to physics analysis is illustrated in fig. 4.2 where the $\gamma\gamma$ system falling in the η mass range is combined with a pair of pions $\pi^+\pi^-$, showing a decided improvement in resolution.

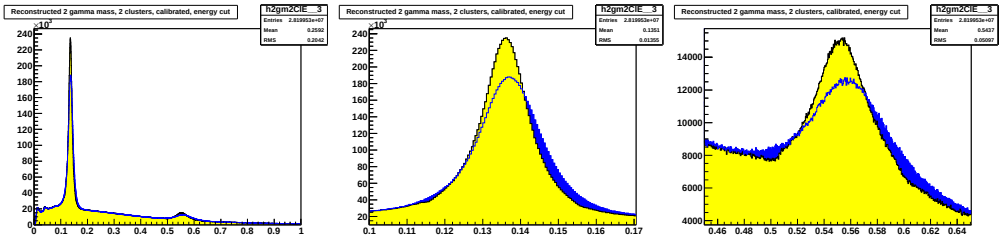

Figure 4.1.: Effect of π^0 calibration on $\gamma\gamma$ mass distribution. All plots show the same sample of exclusive events with two good ECAL clusters and three or five charged tracks. The blue histograms show the distribution before application of the π^0 calibration coefficients, yellow afterwards. The leftmost figure shows the complete mass range, the other two pictures zoom on the ranges of the π^0 (center) and η mass ranges. The peaks become noticeably sharper and move towards the nominal masses.

4.3. Preselection

Data selection was performed in two steps. First, the complete 2008 data sample was subjected to fairly loose cuts intended to on the one hand reduce the data set to a manageable size while on the other hand still allowing refinement of the selection cuts at a later stage. At the same time this preselection was intended to allow for a subsequent selection of a class of final states wider than the $\eta\pi^-$ and $\eta'\pi^-$ final states considered in this thesis. The effect of the cuts is summarized in table 4.1. In the following we will discuss the cuts individually.

In the following we shall discuss the individual cuts in the order in which they are applied.

DT0 Trigger The main physics trigger during the 2008 data taking was the DT0 trigger. Its purpose is to select events of the intended diffractive signature, defined by the recoiling proton. The trigger criteria are the following:

1. *Beam trigger:* coincidence between two beam definition counters is required.

2. *Recoil Proton Trigger:* angular coincidence between photomultiplier signals in the inner and outer ring of the RPD is required to ensure the required recoiling proton. An FPGA-based signal shape analysis to suppress electrron and pion backgrounds was foreseen but turned out to be unnecessary [Alekseev et al., 2012].

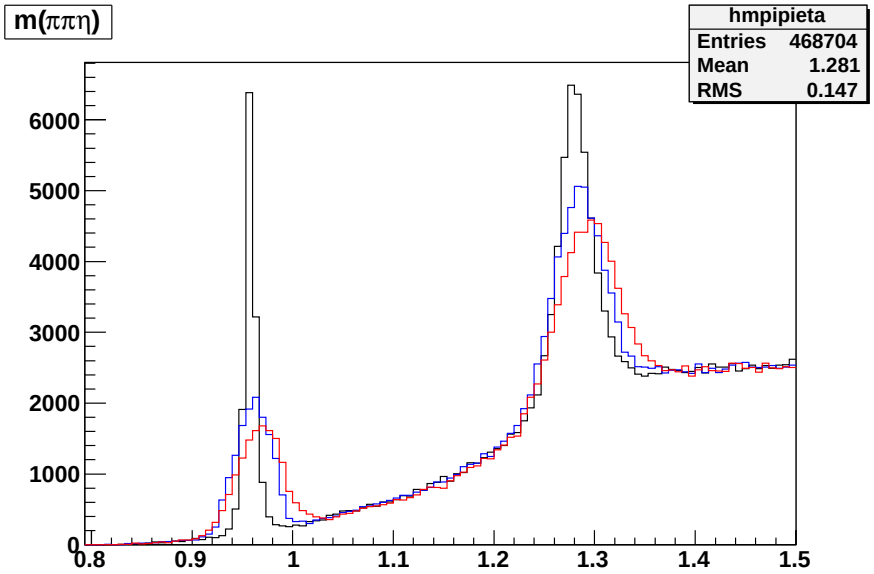

Figure 4.2.: Effect of calorimeter calibration. The figure shows reconstructed masses of the $\pi^-\pi^+\eta$ system where $\eta \to \gamma\gamma$ is selected by a mass window around the nominal η mass. The events are exclusive. The red histogram shows the data before any calibrations are applied, the blue historgram shows the data after π^0 calibrations are applied to the measured γ energies. The black histogram shows the effect of applying a one-constraint kinematic fit to the $\gamma\gamma$ system of the blue histogram. The peaks correspond to the $\eta'(958)$ and $f_1(1285)$ mesons. The improvement in both resolution and the actual determined mass value is clear.

	All Data	W33	W35	W37
Total Events	6 013 121 609	1 264 032 348	1 907 620 614	2 841 468 647
DT0 trigger	4 514 085 911	1 000 839 072	1 434 392 992	2 078 853 847
Best PV exists	3 827 890 956	810 913 642	1 225 881 401	1 791 095 913
PV in target	3 377 377 786	713 660 970	1 078 640 544	1 585 076 272
3,(4),5 tracks	953 331 520	202 024 797	305 753 075	445 553 648
Charge sum	598 861 361	127 622 315	192 356 151	278882895
2 or 4 gammas	136 350 868	9 899 311	51 616 068	74 835 489
energy cut	44 896 141	1 062 549	17 895 249	25 938 343

Table 4.1.: Cut-flows for the pre-selection. The number of events remaining after each cut is indicated. The numbers are also given for the individual data taking periods W33, W35, W37.

3. *No Veto:* Several veto detectors suppress a fraction of unwanted events. There are two classes of veto detectors: on the one hand vetos upstream of the spectrometer which are used to suppress events where particles entered the spectrometer without traversing the target. Such particles can be for instance muons from the beam halo or pions whose momenta are outside of the range accepted by the beam optics. The other class of veto detectors are downstream of the target. These are the sandwich veto detector discussed in Sec. 3.6, used to suppress events with particles produced outside the spectrometer acceptance, and the beam killer hodoscope which is used to suppress non-interacting beam particles. It is situated in front of ECAL2, and its main purpose is the suppression of pileup events, where two beam particles enter the spectrometer in close succession with only one interacting inside the target.

The bulk of the recorded data are taken with this trigger (which is not pre-scaled), amounting to 85 % of the total recorded data set.

Primary Vertex Reconstructed Near Target This cut requires that there actually be a primary vertex (shorthand for a vertex which was associated with a beam track) reconstructed in the vicinity of the target which at this stage is defined by the range $-75\,\mathrm{cm} < z < -25\,\mathrm{cm}$ and $r \leq 2\,\mathrm{cm}$ with z the coordinate along the nominal beam axis and r the distance from the nominal beam axis. The RPD requirement in the trigger by itself ensures that a large fraction of the primary vertices is indeed inside the target. Some space is left to be able to study the reconstruction quality at a later stage, e.g. in order to be able to study the safety margin needed to prevent including interactions in the target windows. The primary vertex distribution before this cut is shown in Fig. 4.3.

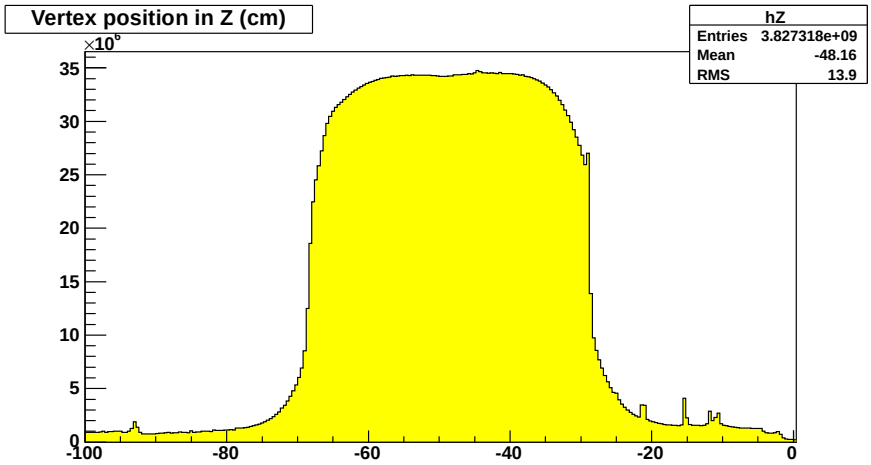

Figure 4.3.: Distribution of reconstructed primary vertices along z. This distribution is taken without any cuts besides requiring the DT0 trigger, therefore the bulk of the data is represented by elastic scattering events where the small scattering angle leads to decreased resolution. This explains the washed out edges of the target region.

Three to Five Outgoing Tracks in Primary Vertex The fundamental topological quality of a vertex is the number of tracks attached. The event categories of interest contain three or five charged pions, and thus these numbers were required. Note that the recoil proton is not included in COMPASS's tracking and therefore it is also not taken into account in vertexing nor in the numbers given.

Charge Conservation The diffractive scattering events are characterized by an $I = 0$ exchange, i.e. the fast system must have the same charge as the beam. Events where total charge is different from -1 must be badly reconstructed, and are therefore rejected.[3]

Two or Four Good ECAL Clusters In this initial step, the selection was prepared for a larger class of final states than were analysed in this thesis. Therefore, not only events with the two calorimeter clusters required for $\pi^0 \to \gamma\gamma$ or $\eta \to \gamma\gamma$ were selected, but also events with four clusters (as in the channel $\omega\pi^-\pi^0$, where an exotic state was claimed [Lu et al., 2005]). Only clusters which fulfilled the following criteria were considered in the selection:

1. no reconstructed track was associated with the cluster by the reconstruction.
2. a minimum energy was required for the cluster: 1 GeV in ECAL1, 4 GeV in ECAL2.
3. the cluster time t relative to the beam lies in the window $-8\,\text{ns} \leq t \leq 10\,\text{ns}$. The distribution of cluster times is illustrated in Fig. 4.4. The very sharp peaks near the expected time zero is evident.
4. if the cluster is reconstructed in ECAL2, it is required that it lies within the vertical range of ECAL2 that is visible from the target, i.e. $-17 \cdot 3.83\,\text{cm} \leq y \leq 16 \cdot 3.83\,\text{cm}$ ($3.83\,\text{cm} \times 3.83\,\text{cm}$ being the cross-section of the calorimeter cells).

The last cut comes about because part of HCAL1 overlaps the acceptance of ECAL2. Clearly an unwelcome feature of the spectrometer setup, this leads to a large loss of photons which can't be compensated in the simulation, both because the large fraction lost introduces large statistical fluctuation in the number of remaining photons but also because the simulation only takes the actual calorimeter blocks of HCAL1 into account but not the photomultipliers, support structure etc., leading to underestimation of the loss in MC simulations.

Total Energy Finally, in order to suppress data from incompletely reconstructed, non-exclusive events, the total energy E_{tot} defined sum of the energies of the reconstructed tracks (pion mass hypothesis) and of the calorimeter clusters (taking π^0 calibrations into account) is required to lie in a fairly large window about the nominal beam energy, namely $175\,\text{GeV} \leq E_{\text{tot}} \leq 205\,\text{GeV}$. The total energy distribution at this point is shown

[3] When studying this, we found a small fraction of particles where the charge assignment from tracking was overridden during vertexing (i.e. `PaTPar` and `PaTrack` had different charge assignments). We rejected such events.

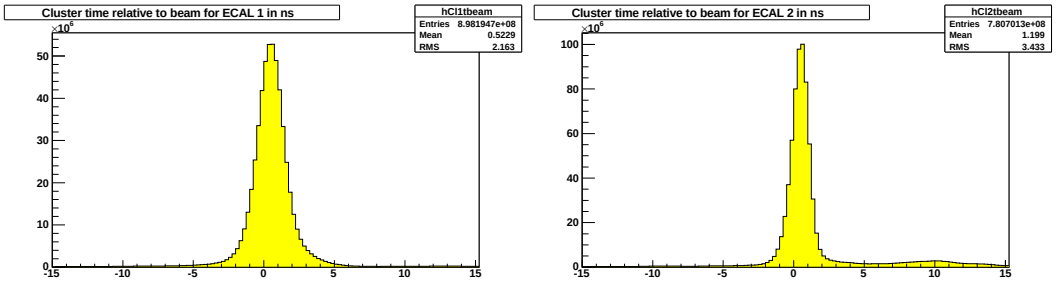

Figure 4.4.: Cluster time distribution for all clusters in ECAL1 (left) and ECAL2. The time is measured relative to the beam time and takes the distance of the calorimeters to the target into account. Therefore the weight of the distribution is expected to lie near 0 ns.

in Fig. 4.5. It is clear from the picture that a large fraction of non-exclusive events remains at this point in the selection, even though the exclusive peak at 191 GeV is becoming visible.

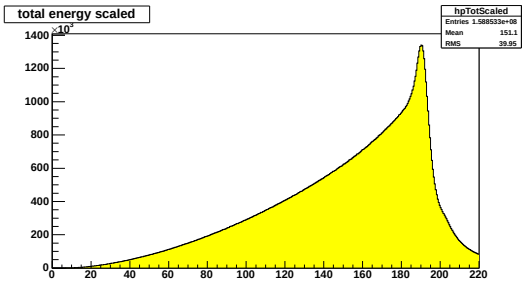

Figure 4.5.: Total energy distribution in the pre-selection sample.

4.4. Selection of PWA Input Trees

The preliminary selection decreased the data volume more than hundred-fold. The remaining data could be processed within half a day on a system with fast input-output or significantly faster on batch systems. This allowed iterative refining of the data selection cuts. The final states under consideration in this thesis have the following topologies: either three spectrometer tracks ($\pi^-\eta$, $\pi^-\eta'$) or five spectrometer tracks ($\pi^-\eta'$) and two photons ($m_{\gamma\gamma} = m_{\pi^0}$ mass for $\pi^-\eta$ and $\pi^-\eta'$ in the case of five tracks, $m_{\gamma\gamma} = m_\eta$ for $\pi^-\eta'$ in the case of three tracks). Other cuts describe features of the experiment. These latter cuts are common between the final states, and are defined as follows:

Primary Vertex Inside Target Cell Here the cut on the reconstructed primary vertex is tightened to include only events inside the target cell with sufficient safety margins to

suppress interactions in the target walls. With r and z as above, the cuts are $-67.5\,\mathrm{cm} \leq z \leq -29.5\,\mathrm{cm}$ and $r \leq 1.57\,\mathrm{cm}$.

Exactly Two Good ECAL Clusters The analysis is restricted to events with exactly two photons in the final state, and so are the data.

Momentum Conservation The cut on the total energy, defined as the sum of the photon energies (with π^0 calibration) and the energies of the charged tracks (pion hypothesis) is tightened to the range $186\,\mathrm{GeV} \leq E_{\mathrm{tot}} \leq 196\,\mathrm{GeV}$.[4]

Mass cuts The mass cuts used to select the various pseudoscalars were the following:

- $\pi^0 \to \gamma\gamma$ selection: $|m(\gamma\gamma) - m_{\pi^0}| < 20\,\mathrm{MeV}/c^2$.
- $\eta \to \gamma\gamma$ selection: $500\,\mathrm{MeV}/c^2 \leq m(\gamma\gamma) \leq 620\,\mathrm{MeV}/c^2$. The range is asymmetric about the nominal mass of approx. $547.9\,\mathrm{MeV}/c^2$ to account for an energy dependence in the ECAL response which shifts the mass of low-energy ηs to higher values.
- $\eta \to \pi^-\pi^+\pi^0$ selection: $|m(\pi^-\pi^+\pi^0) - m_\eta| < 20\,\mathrm{MeV}/c^2$, where the input Lorentz vector for the π^0 is obtained after a kinematic fit[5] of the two-gamma system to the π^0 mass.

An important nuance of all this is the following: we employ two different PWA programs which treat the decay of the isoscalar differently. In the LMU program it is assumed that all data input comes from $\pi\eta$ or $\pi\eta'$ events, and the isoscalar is considered a stable particle with a fixed mass. The Protvino program, only applicable to the three-track channels, on the other hand takes the experimental resolution of the isoscalar decay into account in order to separate the data from the background beneath the experimental peak. In order to cleanly separate this background, data in a broad window about the η or η' peak therefore has to be considered. Doing so would be detrimental for the LMU program or for the purpose of plotting $\pi^-\eta$ or $\pi^-\eta'$ distributions. Therefore, there are two windows employed when selecting the η or η': on the one hand a broad window for input into the Protvino program, on the other hand a tight window together with a kinematic fit for the LMU program input and for plots showing the data.

4.4.1. The $\pi^-\eta(\to \pi^-\pi^+\pi^0)$ Final State

Besides the common cuts, the following three cuts select this final state:

[4] It was found after the release of the data that doing this cut using the kinematically fit momenta of the $\gamma\gamma$ system has detrimental effects on the data quality, so this cut diverges from the description given in [Schlüter et al., 2011b].

[5] This is a least-squares fit where constraints from kinematics are introduced, in this case the requirement that the invariant mass of the photon pair equals the pi^-0 mass. A software for this was developed during the course of this thesis. It uses a simplified version of the approach given in App. D.

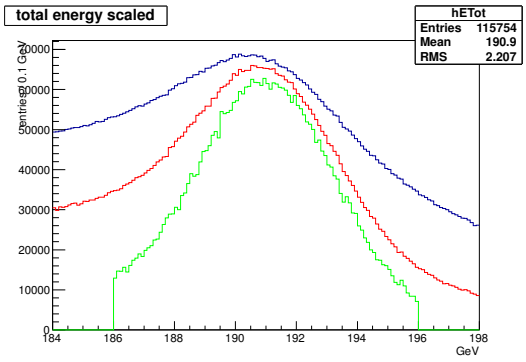

(a) Evolution of the exclusivity peak during the course of the selection (vertical scale arbitrary). Blue: sample after cut on three tracks. Red: sample after cut on π^0 candidate. Green: sample after cut on η candidate. The increase in definedness of the exclusive peak at 191 GeV is clear.

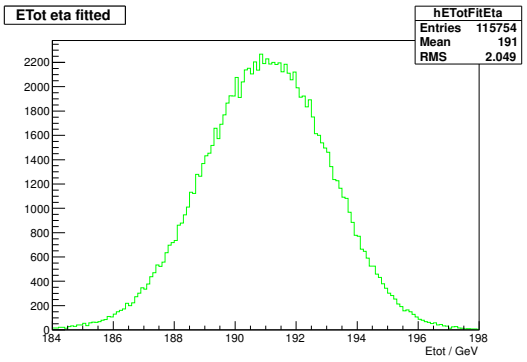

(b) Total energy distribution of the final sample after kinematic fit of the $\gamma\gamma$ system to the π^0 mass. No requirement on the complete event kinematics was made

Figure 4.6.: Exclusivity for $\pi^-\eta$ selection.

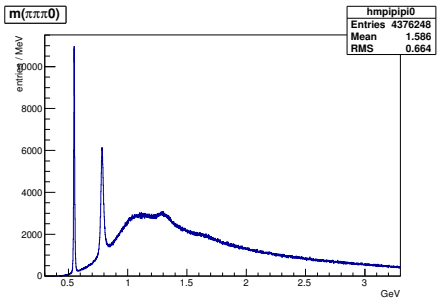

(a) Intermediate $\pi^-\pi^+\pi^0$ spectrum showing $\eta(548)$ and $\omega(782)$ peaks as well as a bump corresponding to $a_2(1320)$. Two entries per event.

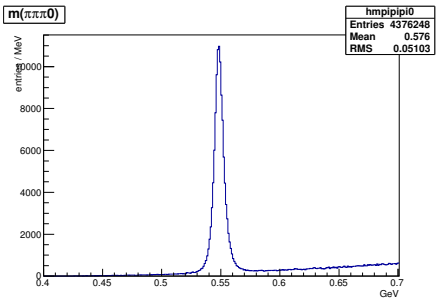

(b) Zoom on the η region in Fig. 4.7a.

Figure 4.7.: Intermediate mass spectra used for the η selection.

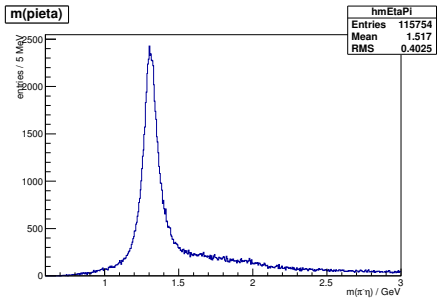

(a) Final $\pi^-\eta$ mass spectrum, clearly dominated by the $a_2(1320)$

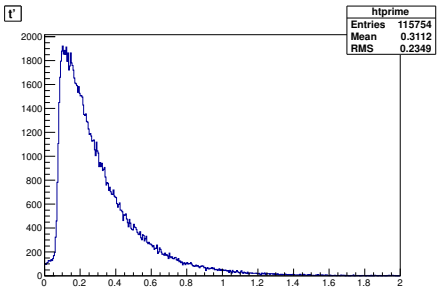

(b) t'-distribution of the final sample

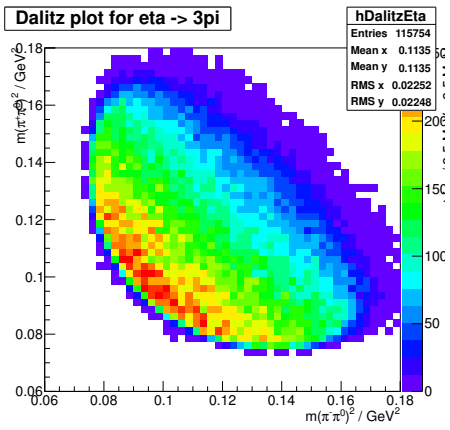

(c) Dalitz plot for the η decay. The strong slope across the plot stands out clearly.

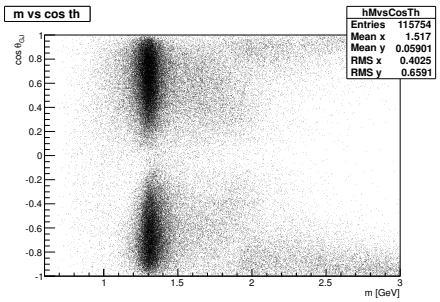

(d) Distribution in $\cos\vartheta_{\mathrm{GJ}}$ as function of mass

Figure 4.8.: Final spectra from the $\pi^-\eta$ selection.

- three reconstructed tracks are leaving the primary vertex,
- a $\pi^0 \to \gamma\gamma$ is found in the window given above, and
- one of the two combinations $\pi^-\pi^+\pi^0$ falls in the η window given above (for plots) or within $50\,\mathrm{MeV}/c^2$ about the tabulated η mass (for input to the Protvino program).

How the sequence of cuts improves the exclusivity of the data sample is illustrated in Fig. 4.6. The peak around the nominal total final state energy 191 GeV becomes more well-defined. The increase in quality introduced by the η-requirement is interesting in that it illustrates how the little available phase-space for the decay of the η acts as an efficient means of background suppression, rendering further requirements such as kinematic fits to the complete event dynamics unnecessary. Similar considerations apply to the $\pi^-\eta'$ final states discussed below.

The intermediate $\pi^-\pi^+\pi^0$ spectrum (two combinations per event) is shown in Fig. 4.7a. The well-known $\eta(548)$ and $\omega(782)$ resonances dominate the spectrum. A bump near the $a_2(1320)$ can also be made out clearly. Near $1700\,\mathrm{MeV}/c^2$ an enhancement appears to be present, consistent with the $\pi_2(1670)$ which is known to decay predominantly into three pions. From the zoom to the η region, it is clear that one can obtain a data set with very little contamination by means of a mass cut. The experiment's resolution was determined by a fit to the η peak (the natural width is entirely negligible). A fit with the double Gaussian form $A(ce^{-(m-m_\eta)^2/2\sigma_1^2} + e^{-(m-m_\eta)^2/2\sigma_2^2}) +$ linear background yielded the widths and relative weights $\sigma_1 = 3.17\,\mathrm{MeV}/c^2$, $\sigma_2 = 6.87\,\mathrm{MeV}/c^2$ and $c = 3.11$, respectively. The resolution is only weakly sensitive to the $\pi^-\eta$ mass.

The resulting $\pi^-\eta$ mass spectrum shown in Fig. 4.8a. It is dominated by the $a_2(1320)$ resonance, consistent with previous studies of the same channel in production experiments (e.g. [Beladidze et al., 1992; Thompson et al., 1997]). This is also illustrated by Fig. 4.8d, which shows the distribution in the variables $m(\eta\pi^-)$ and $\cos\vartheta_{\mathrm{GJ}}$, explained in Sec. 7.1 when the procedure of partial-wave analysis will be discussed. Here the spin-2 a_2 is identified as such by the presence of two maxima of the $\cos\vartheta_{\mathrm{GJ}}$ distribution around the a_2 mass. Another striking feature is the clustering of data near $\cos\vartheta_{\mathrm{GJ}} = \pm 1$ for $m(\eta\pi^-) > 2\,\mathrm{GeV}/c^2$, which has to be contrasted with assumptions of final states produced by decays of intermediate $\pi^-\eta$ resonances. We will discuss the content of this figure in more detail later when we turn to the analysis of the data.

4.4.2. The $\pi^-\eta'(\to \pi^-\pi^+\eta(\to \gamma\gamma))$ Final State

Besides the common cuts, the following three cuts select this final state:

- three reconstructed tracks are leaving the primary vertex,
- a $\eta \to \gamma\gamma$ is found in the window given above, and
- one of the two combinations $\pi^-\pi^+\eta$ falls within $20\,\mathrm{MeV}/c^2$ of the known η'-mass (for plots) or within $50\,\mathrm{MeV}/c^2$ (for input to the Protvino program).

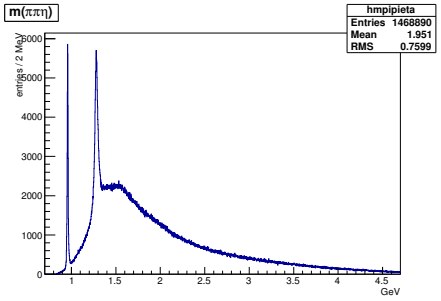

(a) Intermediate $\pi^-\pi^+\eta$ spectrum showing $\eta'(958)$ and $f_1(1285)$ peaks. Two entries per event.

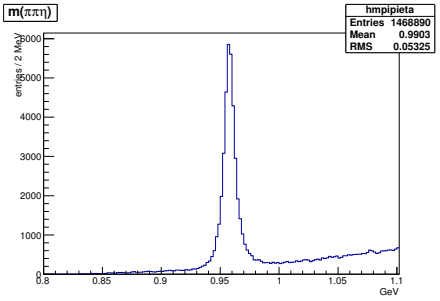

(b) Zoom on the η' region in Fig. 4.9a.

Figure 4.9.: Intermediate mass spectra used for the η' selection.

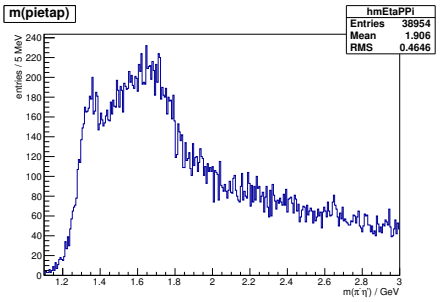

(a) Final $\pi^-\eta'$ mass spectrum, showing the $a_2(1320)$ peak near threshold overlaid on a broad structure which peaks around 1.6 GeV followed by a tail extending to higher masses.

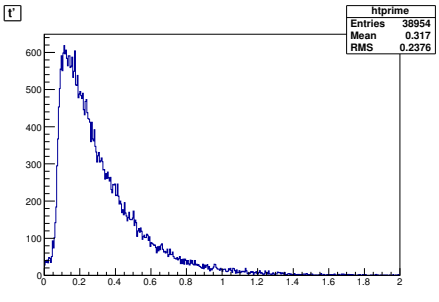

(b) t'-distribution of the final sample

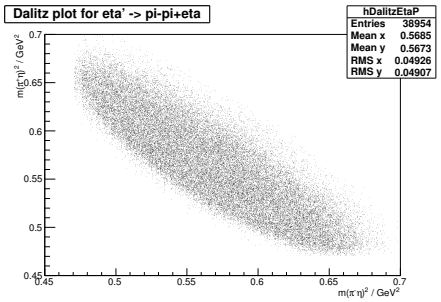

(c) Dalitz plot for the η' decay. The plot is much more homogeneous than the corresponding Fig. 4.8c for the $\eta \to \pi^-\pi^+\pi^0$ decay.

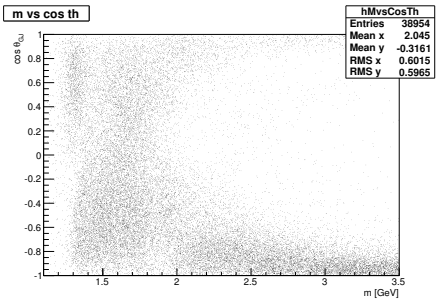

(d) Distribution in $\cos\vartheta_{\mathrm{GJ}}$ as function of mass

Figure 4.10.: Final spectra from the $\pi^-\eta'$ selection in the three-track final state.

Again, we illustrate the intermediate steps of the selection. The $\pi^-\pi^+\eta$ mass spectrum is shown in Fig. 4.9a. The strong peaks correspond to the $\eta'(958)$ and $f_1(1285)$ resonances. The η' region is shown in more detail in Fig. 4.9b, again very little background remains under the peak. A fit to the η' peak with the double Gaussian form $A(ce^{-(m-m_\eta)^2/2\sigma_1^2} + e^{-(m-m_\eta)^2/2\sigma_2^2}) +$ linear background yielded the widths and relative weights $\sigma_1 = 3.64\,\mathrm{MeV}/c^2$, $\sigma_2 = 9.01\,\mathrm{MeV}/c^2$ and $c = 2.86$, respectively. These numbers are remarkably similar to the ones found for the resolution of the $\eta \to \pi^-\pi^+\pi^0$ given above, underlining the weak dependence of these resolutions on the kinematic regime.

The $\pi^-\eta'$ mass spectrum obtained in the selection is depicted in Fig. 4.10a. The contrast with the $\pi^-\eta$ mass spectrum is striking: the a_2 only appears as a small peak on a broad structure which reaches its maximum near $1.6\,\mathrm{GeV}/c^2$. This broad structure falls rather steeply towards higher masses and is succeeded by a tail reaching towards high mass ranges. Again, the overall picture is consistent with previous analyses such as [Beladidze et al., 1992, 1993; Ivanov et al., 2001]. An important difference is COMPASS's reach towards higher $\pi^-\eta'$ masses. The region above $\approx 2\,\mathrm{GeV}$ has previously remained unexplored.

A more detailed view of the content of the data is found in Fig. 4.10d where again the distribution in the cosine of the angle ϑ_{GJ} is shown as a function of mass. Near the a_2 mass one again sees an inhomogeneous distribution, but now the intensity distribution for low masses is concentrated at positive values of $\cos\vartheta_{\mathrm{GJ}}$ but then shifts rapidly to negative values as mass increases. This is consistent with rapid phase motion of a spin-2 D-wave against a spin-1 P-wave as will be explained below. For higher masses up to approx. $2\,\mathrm{GeV}/c^2$ a complex picture emerges before the data again concentrate near the edges. The low fraction of data with $\cos\vartheta_{\mathrm{GJ}} \approx +1$ at high masses is partly due to acceptance effects. This will be explained in further detail in Sec. 5.

4.4.3. The $\pi^-\eta'(\to \pi^-\pi^+\eta(\to \pi^-\pi^+\pi^0(\to \gamma\gamma)))$ Final State

Besides the common cuts, the following three cuts select this final state:

- five reconstructed tracks are leaving the primary vertex,
- a $\pi^0 \to \gamma\gamma$ is found in the window given above,
- one of the six combinations $\pi^-\pi^+\pi^0$ (π^0 fitted kinematically) falls within the η window given above, and
- one of the two remaining combination of $\pi^-\pi^+\eta$ falls within $20\,\mathrm{MeV}/c^2$ of the known η' mass.

Due to the small available phasespace in the $\eta' \to \pi^-\pi^+\eta(\to \pi^-\pi^+\pi^0)$ decay, it often arises the case where several combinations of pions are compatible with the η mass hypothesis. Therefore this mass cannot be used in a constrained fit where one would ideally fit the η' system with three constraints, representing the three intermediate sharp states π^0, η and η'. Instead, we don't use the constraint on the intermediate η but instead use its mass spectrum to assure that the two-constraint fit to the π^0 and η' masses works

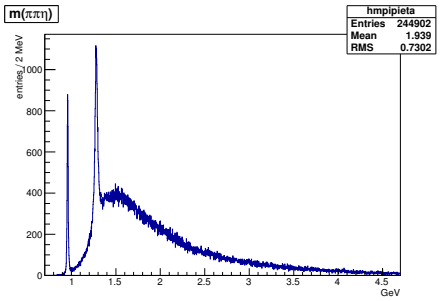

(a) Intermediate $\pi^-\pi^+\eta$ spectrum showing $\eta'(958)$ and $f_1(1285)$ peaks. Two entries per event.

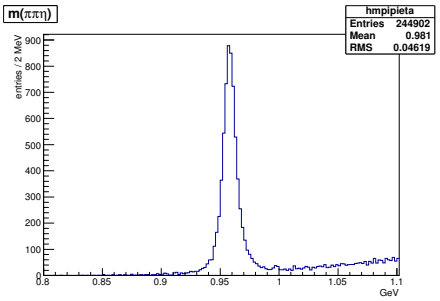

(b) Zoom on the η' region in Fig. 4.11a.

Figure 4.11.: Intermediate mass spectra used for the η' selection.

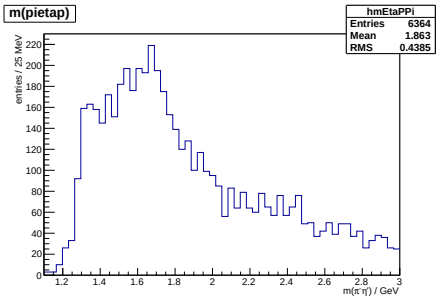

(a) Final $\pi^-\eta'$ mass spectrum, showing the $a_2(1320)$ peak near threshold overlaid on a broad structure which peaks around 1.6 GeV followed by a tail extending to higher masses.

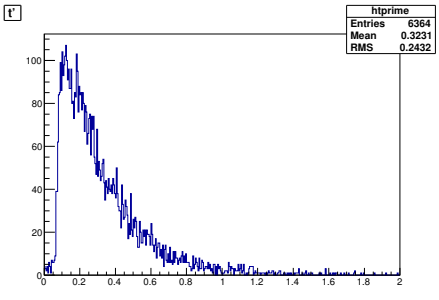

(b) t'-distribution of the final sample

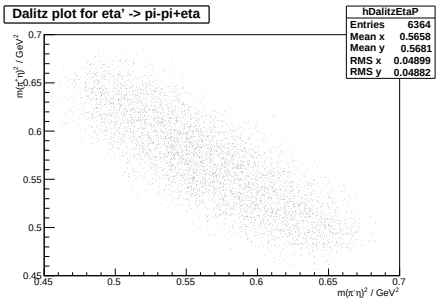

(c) Dalitz plot for the η' decay. The plot is much more homogeneous than the corresponding Fig. 4.8c for the $\eta \to \pi^-\pi^+\pi^0$ decay.

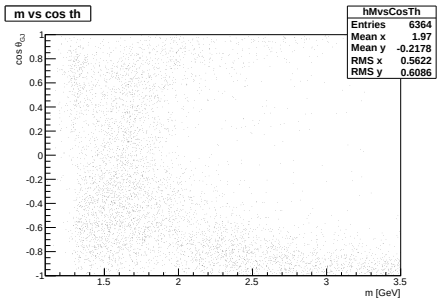

(d) Distribution in $\cos\vartheta_{\mathrm{GJ}}$ as function of mass

Figure 4.12.: Final spectra from the $\pi^-\eta'$ selection in the five-track final state.

as expected. This is illustrated in Fig. 4.13, where the green ditribution shows the mass spectrum of all η candidates where only the $\gamma\gamma$ system has been fitted to the π^0 mass and the blue spectrum shows the mass spectrum after the $\gamma\gamma$ system has been fitted with the π^0 and η' mass contraints. The η peak becomes slimmer and the background under the center of the peak is reduced.[6]

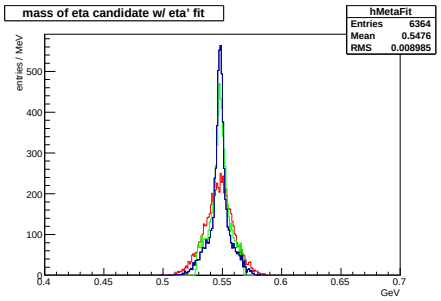

Figure 4.13.: Effect of kinematic fit. The picture shows how the kinematic fit of the $\eta' \to 4\pi\gamma\gamma$ improves the quality of the selection. Details, see text.

The data look very similar to the previous larger set, we shall only briefly highlight the differences. First, the size of the sample is significantly reduced. This is in part due to the ratio of the branching fractions $BR(\eta \to \gamma\gamma)/BR(\eta \to \pi^-\pi^+\pi^0) = 1.73$, but to a large part due to the reduced acceptance, which on the one hand comes about because of the larger number of tracks, which are only reconstructed with finite acceptance, and on the other hand the higher degree of pollution in the calorimeters where the charged pions shower in the spectrometer, and their secondaries end up in the calorimeters without being associated to any track by the reconstruction. This reduced acceptance also manifests itself in the faster decrease of the high-mass tail of the $\pi^-\eta'$ spectrum. Nevertheless, the features in the low-mass range $m(\eta'\pi^-) < 2\,\mathrm{GeV}/c^2$ are compatible to the three-track selection even without acceptance corrections.

4.4.4. The $\pi^-\eta'(\to \pi\pi\eta(\to \pi\pi\pi^0))$ Final State With Six Photons

As an illustration of the variety of final states in which the same physics appears, we study final states with three charged tracks and six photons in the calorimeter, either coming from the decay chain $\eta' \to \pi^0\pi^0\eta$ followed by $\eta \to \pi^-\pi^+\pi^0$ or from the decay chain $\eta' \to \pi^-\pi^+\eta$ followed by $\eta \to 3\pi^0$, whose relative branching fractions are [Nakamura et al., 2010]

$$\begin{aligned} \mathrm{BR}(\eta' \to \pi^+\pi^-\eta) \times \mathrm{BR}(\eta \to \pi^0\pi^0\pi^0) &= 43.2\% \times 32.57\% = 14\%, \\ \mathrm{BR}(\eta' \to \pi^0\pi^0\eta) \times \mathrm{BR}(\eta \to \pi^-\pi^+\pi^0) &= 21.7\% \times 22.74\% = 4.9\%. \end{aligned} \tag{4.4}$$

[6] Note that we didn't allow the charged tracks and the vertex to be altered by the fit. This was done regrettingly after writing software to obtain a complete covariance matrix for the vertex and extensive studies, because it was found that the scale of the error measurements returned from the reconstruction software is incompatible between the calorimeter clusters and the spectrometer tracks.

As in the case discussed in the previous section, the determination of the particles belonging to the intermediate η is not always uniquely possible, which in this case leads to some ambiguity in the selection. As we are not interested in the dynamics of the η' decay, we make no attempt to distinguish the two possibilities in the data selection, even though we make a cut on $\eta \to 3\pi^0$ which suppresses the decay chain where $\eta \to \pi^-\pi^+\pi^0$.

We perform the same common cuts as explained above, but requiring six good gamma clusters. After this, we require exactly three tracks in the reconstructed primary vertex, which is subjected to the target cut and the charge conservation cuts given above. We then sum the calorimeter cluster energies and the track energies, requiring the same exclusivity criterium as before. The mass spectrum of the resulting six gamma system is shown in Fig. 4.14. To extract the interesting data which always has three π^0s, we require that there is at least one combination of pairs of clusters that allows for three π^0s ($20\,\mathrm{MeV}/c^2$ window). The resulting 6γ mass spectrum can be seen in the same figure. The η peak can be seen quite prominently. Cutting on this peak ($50\,\mathrm{MeV}/c^2$ window) yields the mass spectrum shown in the left plot in Fig. 4.15 which is quite similar to Figs. 4.9a and 4.11a, except for the reduced statistics and the reduced resolution which is due to the absence of a kinematic fit. We now cut on the mass of the $\pi^-\pi^+\pi^0\pi^0\pi^0$ system and perform a one-constraint kinematic fit requiring the η' mass for the system $\pi^-\pi^+ + 6\gamma$ where only the measured directions and energies of the photons are allowed to vary. This gives us the $\pi^-\eta'$ mass spectrum shown on the right of Fig. 4.15, which again shows the same features as seen previously, even though with largely reduced statistics. These data were not further analyzed.

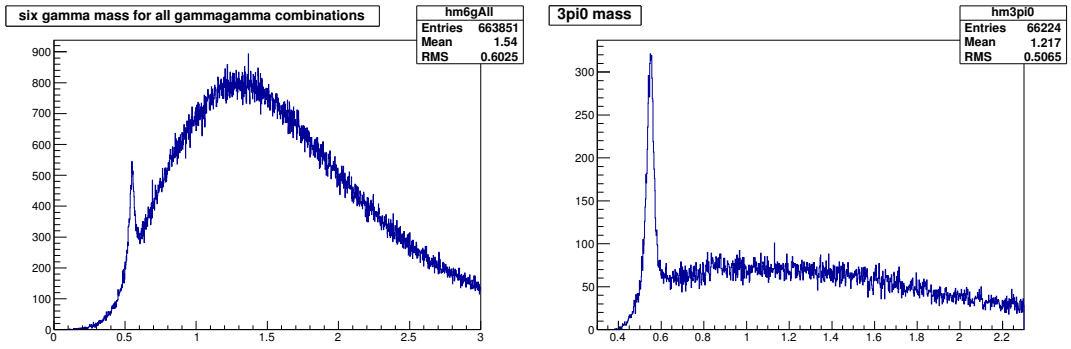

Figure 4.14.: Invariant mass of the six photon system without (left) and with the requirement of a combination which allows for three π^0s. This cut cleans the distribution considerably while the number of $\eta(548)$ remains approximately the same.

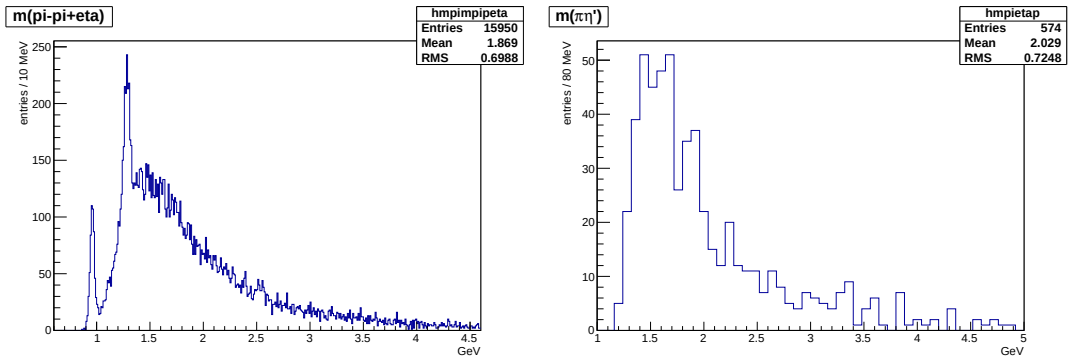

Figure 4.15.: Mass spectrum of the $\pi\pi\eta$ (left, two entries per event) and $\pi^{-}\eta'$ (right) systems with six photons in the final state.

5. Properties of Produced Particles

Kinematical Limits In Fig. 5.1 we show the kinematic limits on the particles we want to study. Due to the large discrepancy in mass, the η (η') will on average pick up a larger fraction of the initial beam momentum than the pion (the momentum transfer to the target proton is on the order of a few hundred MeV). At the same time, already at invariant $\pi^-\eta$ ($\pi^-\eta'$) masses close to threshold can the pion attain very low momenta, outside of the spectrometer acceptance, and we therefore expect a loss of efficiency in those ranges. As we have seen in Figs. 4.8d and 4.10d, the data actually populate the kinematic extremes at high masses.[1] Therefore the relative fractions in these regions of the distributions are distorted. We will see in the partial-wave results that indeed the different degrees of occupancy between the forward and backward regions seen in Fig. 4.8d, do not lead to the appearance of strong odd/even partial wave interference (which would provide for such an effect) but instead, taking acceptance into account, the odd partial waves remain very small.

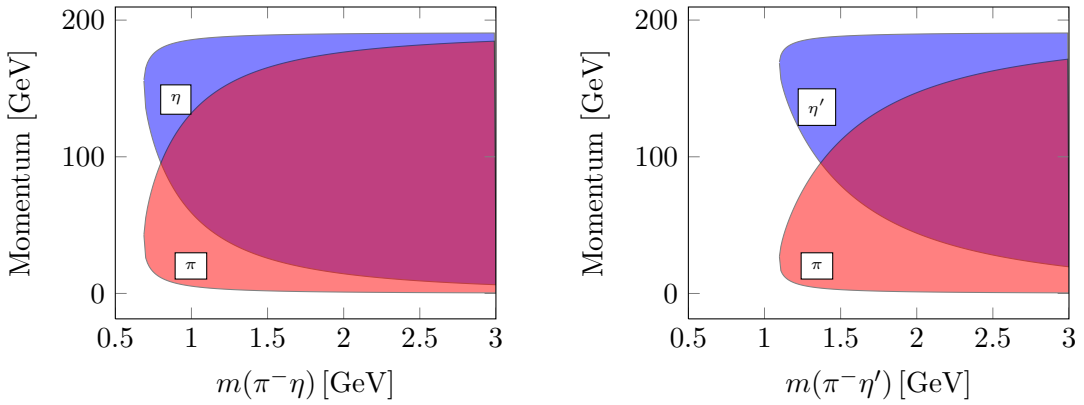

Figure 5.1.: Kinematics ranges for the decay of a $\pi^-\eta$ (left) or $\pi^-\eta'$ (right) system with total momentum $p = 191\,\text{GeV}$ as function of its invariant mass. The shaded areas indicate the possible momenta of the respective particles for a given invariant mass of the pair.

Rapidity Distributions Rapidity is the boost parameter y corresponding to the longitudinal velocity of a particle, where longitudinal refers to the beam direction. One has

[1] Note that due to the initial scattering, $\cos\vartheta_{\text{GJ}} = \pm 1$ does not coincide with the extremities shown in Fig. 5.1, but the difference is small due to the small scattering angle.

for a particle with longitudinal velocity component β_L

$$y = \operatorname{Arctanh} \beta_L = \operatorname{Arctanh} \frac{p_L}{E} = \frac{1}{2} \ln \frac{E + p_L}{E - p_L}. \tag{5.1}$$

Differences between rapidities are independent of the longitudinal velocity of the frame in which they are calculated. It is therefore meaningful to classify reactions according to differences in rapidity. Hadronic interactions at low momentum transfer show a phenomenology of so-called rapidity gaps, in which secondary particles cluster around certain distinct rapidity values with gaps of a few units of rapidity between the clusters. Generally, each rapidity gap can be identified with the exchange of a Reggeon [Gribov et al., 2009]. In the diffractive excitation process, which is the main focus of this thesis, there are two such clusters: one is formed by the recoil proton, the other by the decay products of the excited beam pion. In another process, and potential background to the beam pion excitation process, particles are produced at central rapidities. Here central means that the produced particles have a rapidity gap both with respect to the target and with respect to the forward going scattered beam. This process is referred to as central production. At the COMPASS beam energy we have for the beam particle, depending on its type, the following rapity difference between beam and target:

particle	$\pi^\pm$	$K^\pm$	$p/\bar{p}$
rapidity at 191 GeV/c	7.92	6.65	6.01

As an illustration of the differences in regime that can be observed, we show rapidity distribution for two data samples obtained with the same selection applied to different COMPASS data sets in Fig. 5.2: on the left, we show data from the reaction $\pi^- p \to \pi^- K^0_S K^0_S p$ [Schlüter, 2009; Schlüter, 2010], on the right data from the reaction $pp \to pK^0_S K^0_S p$.[2] One immediately sees one striking difference between the distributions: the rapidity distribution of the kaons in the case of a pion beam is composed of two parts: one which is very similar to the distribution seen in the proton data, and another part where the kaon and pion rapidities overlap. This latter case corresponds to diffractive excitations of the beam particle, and we conclude that it is relatively suppressed for the proton beam. On the contrary, the central production process behaves very similar between the two, as is expected from Regge factorization. The gap between the recoil proton and the kaons is due to the acceptance of the COMPASS spectrometer: slow particles will not enter the spectrometer, leading to the kind of incomplete events the sandwich veto detector of Sec. 3.6 is supposed to veto. The distribution is expected to be symmetrical because Lorentz-invariance dictates that the process is independent of inertial frame and the assignment of target and beam proton is equivalent to a particular choice of inertial frame.

The $\pi^-\eta$ and $\pi^-\eta'$ data shows both regimes, which we illustrate by showing rapidity distributions in the same way as before, but split into subsets of low and high invariant mass as indicated on the figure, Fig. 5.3. We see that at high invariant masses a rapidity

[2] All data in this chapter are shown without acceptance corrections.

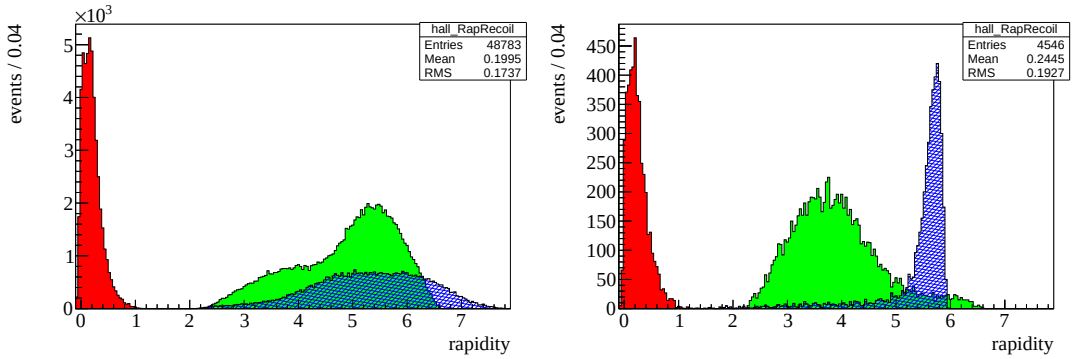

Figure 5.2.: Rapidity difference relative to the target. Both plots show the recoil proton in red, the Kaons in green, and the scattered beam particle in blue. Data are from the reactions $\pi^- p \to \pi^- K^0_S K^0_S p$ (left) and $pp \to p K^0_S K^0_S p$ (right) at a beam momentum of 191 GeV. The right edge of the beam particle distribution is shifted between the plots due to the different masses of the beam particles.

gap is found between the pion and the isoscalars, whereas at low invariant masses the particles remain in the same rapidity range. The $\pi^-\eta$ data is dominated by the $a_2(1320)$ decay whose dipole-like structure (cf. Fig. 4.8d) leads to the doubly-peaked distributions in the low-mass range. At high masses the distribution are very much in favor of an interpretation as central production of the $\eta^{(\prime)}$ meson. The also observed case where the $\eta^{(\prime)}$ meson is observed at leading rapidities can be understood as double-peripheral processes of the kind depicted in Fig. 2.2c. We are not aware of a previous experiment that could study the $\pi^-\eta^{(\prime)}$ systems over such a large range of invariant masses in exclusive reactions, thus allowing a study of physics from threshold well into the range of double-Regge exchanges.

Double-Pomeron Exchange We can investigate whether the centrally produced η and η' mesons of Fig. 5.3, i.e. those which are produced at low rapidities, are produced by double-Pomeron exchange. Models for the Pomeron predict specific angular distributions for this process [Close and Schuler, 1999b]. These models were found to be in agreement with the data of the WA102 experiment [Barberis et al., 1998, 1999]. The extraction of unambiguous results from the data on η or η' production would require a study of the energy dependence of their production, in order to understand the contribution from Reggeon-Pomeron interactions. Hence we shall only briefly show that the data are in accordance with the double-Pomeron prediction of the model cited above.

We take data where $2.5\,\text{GeV} < m(\eta^{(\prime)}\pi) < 3.5\,\text{GeV}$ to suppress both resonant contributions and regions with extreme momenta that may lead to a large acceptance effect. Then we select the subset of slow $\eta^{(\prime)}$, defined by $y - y_{\text{Target}} < 5$. For these data we plot the angle ϕ given by the center-of-mass angle between the planes defined on the one hand by the beam and the scattered pion, and on the other hand by the target and

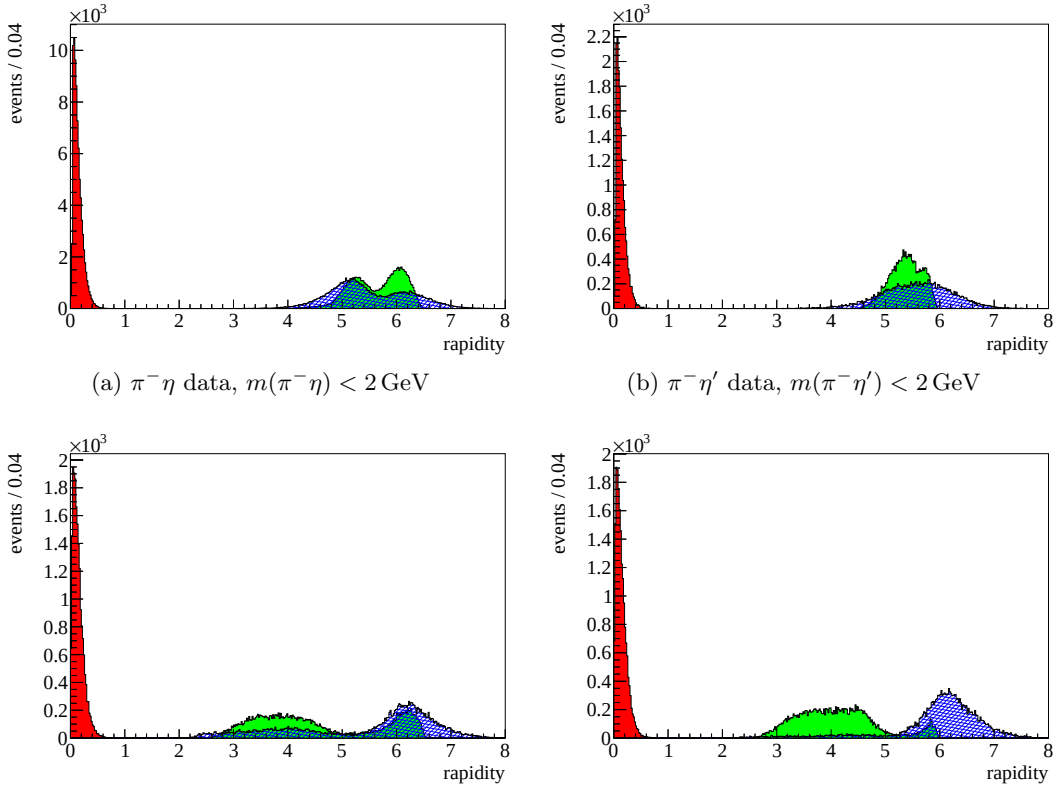

(a) $\pi^-\eta$ data, $m(\pi^-\eta) < 2\,\mathrm{GeV}$

(b) $\pi^-\eta'$ data, $m(\pi^-\eta') < 2\,\mathrm{GeV}$

(c) $\pi^-\eta$ data, $m(\pi^-\eta) > 2\,\mathrm{GeV}$

(d) $\pi^-\eta'$ data, $m(\pi^-\eta') > 2\,\mathrm{GeV}$

Figure 5.3.: Rapidity distribution for the $\pi^- p \to \pi^-\eta^{(\prime)}p$ data. The recoil proton is shown in red, the $\eta^{(\prime)}$ in green, and the pion in blue. At high masses rapidity gaps arise. A feature that cannot be seen from this kind of pictures is that events in the right-side bump of the π distributions correspond to events in the left-side bumps of the $\eta^{(\prime)}$ distributions and vice versa.

the recoil proton [Close and Schuler, 1999b]. For a vector-like Pomeron, this angle is expected to follow a $\sin^2\phi$ distribution. The distributions are shown in Fig. 5.4. We see that except for a slight shift of the distributions which we do not understand, the data agree with this prediction.

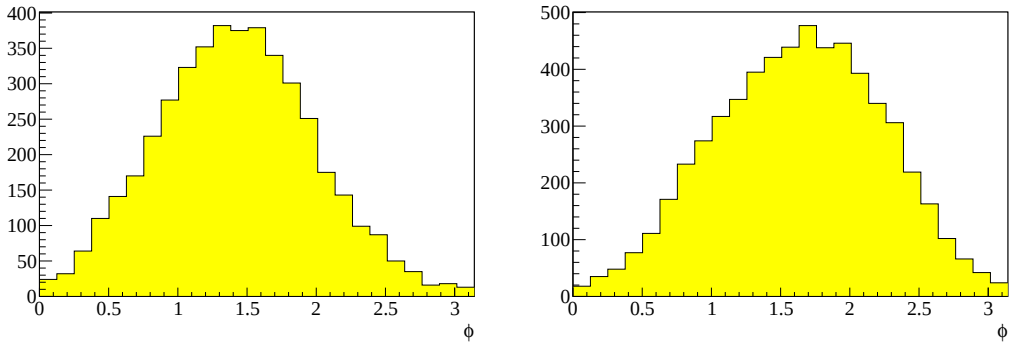

(a) $\pi^-\eta$ data (b) $\pi^-\eta'$ data

Figure 5.4.: Distribution of angular difference between the production planes in the center-of-mass frame. See text for details.

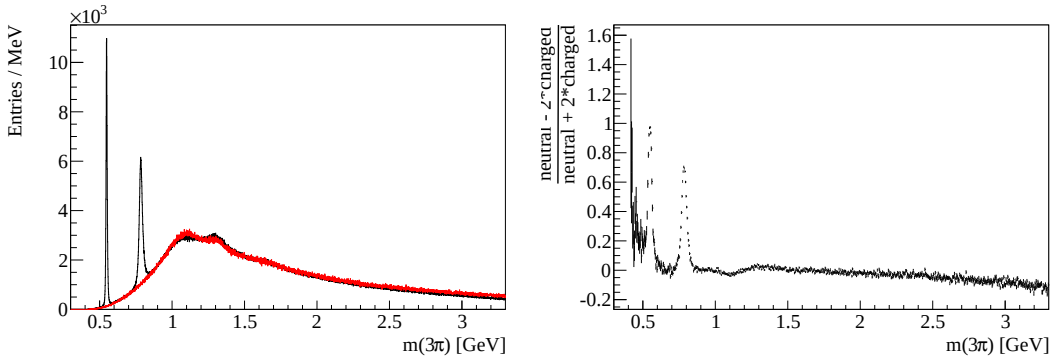

Figure 5.5.: Comparison of the neutral and charged 3π mass distributions in the reaction $\pi^-p \to \pi^-\pi^-\pi^+\pi^0$. Left: $m(\pi^-\pi^+\pi^0)$ (two entries per event, black) and $m(\pi^-\pi^-\pi^+)$ (height doubled, red). Right: ratio (neutral $-\ 2\times$ charged)/(neutral $+\ 2\times$ charged) with statistical error bars.

Isospin structure of the $\pi^-\pi^-\pi^+\pi^0$ system In Fig. 5.5 we illuminate the isospin structure of the final state $\pi^-\pi^-\pi^+\pi^0$ by comparing the distributions obtained in the neutral case $\pi^-\pi^+\pi^0$ (where there are two combinations per event) and the charged case $\pi^-\pi^-\pi^+$ (which we scale by a factor of two to compensate for the possibility of only a single combination). We see that except for the isospin zero resonances $\eta(548)$ and $\omega(782)$ these two systems are practically identical in content, even in spite the

absence of any acceptance corrections. Since the system $\pi^-\pi^-\pi^+$ has to have isospin ≥ 1, we see that the neutral system $\pi^-\pi^+\pi^0$ is also in a state of isospin ≥ 1 outside the known $I = 0$ resonances. There is no indication of the $\phi(1020)$ which would only appear in the neutral combination. The charged combination slightly overshoots the neutral near 1.1 GeV. This is probably due to the dominance of the $a_2(1320)$ in the $\pi^-\eta$ final state. The charged combinations of pions would then have to have an invariant mass which is below the mass of the $a_2(1320)$ by an amount comparable to the sum of a pion mass (140 MeV) and the breakup momentum of the $\eta(548)$ in the three pion decay (174 MeV). This was verified by not including in the charged combination data which is compatible with the η hypothesis. The stronger bump in the neutral case near 1.3 GeV does not offer an equally simple explanation. There is no fitting resonance listed in the particle tables [Nakamura et al., 2010]. On the other hand, cutting away all data with $m(\pi^-\pi^+\pi^0) < 850\,\text{MeV}$, i.e. also suppressing the ω contribution, makes it seem that this is strictly an acceptance effect: in this case the neutral and charged histograms, which necessarily have the same content after allowing for the two possible combinations in the neutral case, cross at approximately 2.4 GeV, with the neutral histogram being above the charged data throughout at lower masses and below at higher masses. With the same cut, the $a_2(1320)$ also stands out quite prominently out of both the charged and the neutral distributions. In the ratio plotted on the right, we see the effect of the lower mass of the π^0 compared to the charged pions near threshold. This shows that the background under the η cannot be estimated from the charged data, unlike in the case of the ω. We will not further consider the data outside the vicinity of the η peak. We also mention that a similar comparison is not possible in the case of the $\pi^-\pi^-\pi^+\eta$ final state as the mass of the η is quite different from that of the pions and there is no symmetry linking the different three-body systems.

t' Dependence of Cross-Section In general, peripheral particle production shows exponentially decreasing behavior as function of momentum transfer [Donnachie et al., 2002]. Additionally, changes in helicity introduce powers of momentum transfer (e.g. [Perl, 1974]). We are thus led to study the momentum transfer distributions approximating them with the functions $e^{-Bt'}$ or $t'e^{-Bt'}$. Our fits to the $\pi^-\eta'$ data are summarized in table 5.1. We note that these values fall in the expected range from e.g. other COMPASS analyses, but they are in stark contrast to the much wider slope, $B = 2.93\,\text{GeV}^{-2}$, that the E852 collaboration found when fitting with the simple exponential to data from the same reaction at lower beam energy [Ivanov et al., 2001]. These slopes were studied for our data in detail in Ref. [Wöhrmann, 2010].

mass bin [GeV]	fit with $A\exp(-B\|t\|)$	fit with $A\|t\|\exp(-B\|t\|)$
$m < 1.5$	5.5	8.2
$1.5 < m < 1.9$	5.1	7.5
$1.9 < m < 2.2$	4.8	7.1
$2.2 < m < 3$	4.6	6.9

Table 5.1.: Fit to the slope parameter B in units of GeV^{-2} for momentum transfer as function of mass for the $\pi^-\eta'$ data.

6. The Partial-Wave Analysis Procedure

Our analysis follows a procedure that separates the analysis and interpretation of the data. The first step decomposes the data into partial waves, where no resonant structures or behaviors are assumed. This is achieved by dividing the data into bins according to the invariant mass of the system, and analysing these bins independently. The procedure of analysis of the contents of the individual bins is explained in this chapter and the following chapter and pursued in Sec. 8. The interpretation of the data in terms of resonances or other structures is then pursued by fitting the results of this binned approach with mass-dependent functions, such as Breit-Wigner distributions or background terms. We do this in Sec. 9. As dependence on the invariant mass of the total system only enters in this second step, we call the fit in mass bins also "mass-independent partial-wave analysis" and the second step "mass-dependent partial-wave analysis." Where the mass-independent analysis tries to steer clear off any physical prejudice, the mass-dependent analysis has to make assumptions about the physics being present.

6.1. The Likelihood Function

As any fit, the partial-wave fit fits a theoretical model to data by adjusting free parameters in the model in order to maximize the agreement between the data and the model. In this particular case, the agreement is measured by the *extended likelihood function* and the model is that of an amplitude composed of different partial waves whose relative strengths and phases are given by the free parameters of the model, the so-called *production amplitudes* of the partial waves. The data are processed in independent bins of the invariant mass of the overall mesonic systems. In each such bin, the model then reproduces the data by calculating angular distributions based on a physical model of partial waves together with an acceptance description of the detector. Formally, this procedure can be written down in the following way: the physics model is contained in the partial-wave amplitudes $\psi_{ij}(\tau)$, where i, j identify the partial waves and τ are the variables characterizing the events. We use two indices i, j to divide the amplitudes into classes such that partial-waves with different i do not interfere. The intensity function is then

$$I(\tau) = \sum_i \left| \sum_j A_{ij} \psi_{ij}(\tau) \right|^2 , \tag{6.1}$$

with A_{ij} the production amplitudes which we aim to obtain. The overall normalization of $I(\tau)$ and thus A_{ij} will be determined by the fit as explained below. The equation can

immediately be rewritten

$$\begin{aligned} I(\tau) &= \sum_i \sum_{jk} \psi^*_{ij}(\tau) A^*_{ij} A_{ik} \psi_{ik}(\tau) \\ &\equiv \sum_i \sum_{jk} \psi^*_{ij}(\tau) \rho_{ijk} \psi_{ik}(\tau), \end{aligned} \tag{6.2}$$

where we have introduced the density matrix components ρ_{ijk}. The block-diagonal decomposition is based on physical and mathematical arguments [Chung and Trueman, 1975; Hansen et al., 1974], in the particular case of the two-body final state it can only be decomposed into two parts, corresponding to natural and unnatural parity exchanges in the t-channel, so we shall not dwell on this further. The reason for this is discussed in Sec. 7.2.

The intensity function is taken proportional to the differential cross-section $\frac{\mathrm{d}\sigma}{\mathrm{d}\tau}$ of a particular event. The probability of observing a particular event which has kinematic variables τ is called acceptance and we shall describe this acceptance by a function $\eta(\tau)$. The probability that a particular event characterized by its variables τ_i, given particular values of the production amplitudes, would be observed is then

$$P_i = \frac{I(\tau_i)}{\int \mathrm{d}\tau I(\tau)\eta(\tau)}, \tag{6.3}$$

where the integral covers all of phase-space. We abbreviate the integral in the denominator $\bar{N} = \int \mathrm{d}\tau I(\tau)\eta(\tau)$. In a particle physics experiment that runs for a finite interval of time, the number N of observed events is itself a random variable following the Poisson distribution. The extended likelihood formalism takes this into account by including this Poisson probability in the construction of the likelihood function

$$\mathcal{L} \equiv \frac{\mathrm{e}^{-\bar{N}} \bar{N}^N}{N!} \prod_{i=1}^{N} P_i, \tag{6.4}$$

where the $\bar{N}$ defined above now becomes the expected number of observed events, as the Poissonian term has its maximum for $N = \bar{N}$. Hence, it fixes the normalization of the intensity function and therefore the production amplitudes. Details on the properties of extended likelihood functions can be found in Refs. [Barlow, 1990; Orear, 1958]. Inserting the P_i from above, the expression immediately simplifies to

$$\mathcal{L} = \frac{e^{-\bar{N}}}{N!} \prod_{i=1}^{N} I(\tau_i). \tag{6.5}$$

As usual, it is more convenient to deal with a sum than with a product, so the maximization will be performed on the logarithm of the likelihood function,

$$\log \mathcal{L} = -\log N! - \bar{N} + \sum_{i=1}^{N} \log I(\tau_i). \tag{6.6}$$

Additionally, the term $\log N!$ is dependent only on the data set and therefore doesn't change when the production amplitudes are varied, which in turn means that it does not affect the location of the maximum. Hence, we will drop this term from the likelihood function, and we obtain the extended log-likelihood function as

$$\log \mathcal{L} = -\int \mathrm{d}\tau I(\tau)\eta(\tau) + \sum_{i=1}^{N} \log I(\tau_i). \tag{6.7}$$

Experimental acceptance only enters through the first term, experimental data only through the second term. We shall now discuss the evaluation of the first term.

Acceptance is evaluated by Monte Carlo methods. Here, a large number N_{MC} of events τ_i^{MC} corresponding to a flat distribution in the phase-space is generated. These events are then fed through a complete detector simulation, followed by the same event reconstruction and data selection the real data went through. For each event, $\eta(\tau_\ell)$ can then be evaluated. The integral is in turn evaluated by sampling it with the Monte Carlo events. To this end, first insert the intensity function from Eq. (6.2) to obtain

$$\begin{aligned}\int \mathrm{d}\tau I(\tau)\eta(\tau) &= \int \mathrm{d}\tau \sum_i \sum_{jk} \psi_{ij}^*(\tau) A_{ij}^* A_{ik} \psi_{ik}(\tau)\eta(\tau) \\ &= \sum_i \sum_{jk} A_{ij}^* A_{ik} \left[\int \mathrm{d}\tau \psi_{ij}^*(\tau)\psi_{ik}(\tau)\eta(\tau)\right],\end{aligned} \tag{6.8}$$

where on the second line we have interchanged summation and integration. The term in square brackets is independent of the production amplitudes and as such can be evaluated ahead of the maximization. We shall call it the *normalization integral*, given by

$$\mathcal{I}_{ijk} \equiv \int \mathrm{d}\tau \psi_{ij}^*(\tau)\psi_{ik}(\tau)\eta(\tau), \tag{6.9}$$

which we sample with the Monte Carlo events according to[1]

$$\mathcal{I}_{ijk} \approx \frac{\left[\int \mathrm{d}\tau\right]}{N_{\mathrm{MC}}} \sum_{\ell=1}^{N_{\mathrm{MC}}} \psi_{ij}^*(\tau_\ell^{\mathrm{MC}})\psi_{ik}(\tau_\ell^{\mathrm{MC}})\eta(\tau_\ell^{\mathrm{MC}}) \tag{6.10}$$

(here $\left[\int \mathrm{d}\tau\right]$ stands for the total volume of phase-space.) In the usual case where after the simulation the event is either rejected ($\eta = 0$) or accepted ($\eta = 1$), the sum effectively

[1] It is perhaps worth noting that the formulae for the numerical evaluation of the normalization integrals are wrong throughout the literature with the notable exception of [Aston et al., 1985], where the maximization procedure is slightly different, sidestepping the issue. The literature is mostly in the form of internal notes or preprints, such as [Berger, 2011; Chung, 2010; Cummings and Weygand, 2003; Szczepaniak et al., 2004]. In these references, the term $\left[\int \mathrm{d}\tau\right]$ is omitted, leading to a different scale of the production amplitudes obtained. Namely, the maximum is then obtained with the production amplitudes multiplied by $\sqrt{\left[\int \mathrm{d}\tau\right]}$. These references then have to go to lengths to obtain the correct normalization of the predictions made from the partial-wave fit according to the procedure discussed following Eq. (6.13). The significance of the missing factor can be understood by thinking e.g. about the evaluation of $\int_0^1 x^2 \mathrm{d}x$ and $\int_{-1}^1 x^2 \mathrm{d}x$ by this sampling method.

extends only over the N_{acc} accepted events τ_ℓ^{acc},

$$\mathcal{I}_{ijk} \approx \frac{[\int \mathrm{d}\tau]}{N_{\mathrm{MC}}} \sum_{\ell=1}^{N_{\mathrm{acc}}} \psi_{ij}^*(\tau_\ell^{\mathrm{acc}}) \psi_{ik}(\tau_\ell^{\mathrm{acc}}). \tag{6.11}$$

Nevertheless, fractional η can be treated in a straightforward fashion by returning to Eq. (6.10).

After the maximization of the likelihood function, in particular $\bar{N}$ will be very close to the number of observed events N. As a corrollary of this, the quality of the Monte Carlo description can be evaluated by the kinematic validation which we shall pursue in Sec. 8.5. For this, we consider the integral

$$\bar{N} = \int \mathrm{d}\tau I(\tau)\eta(\tau) \tag{6.12}$$

and its numerical evaluation

$$\bar{N} \approx \frac{[\int \mathrm{d}\tau]}{N_{\mathrm{MC}}} \sum_{\ell=1}^{N_{\mathrm{acc}}} I(\tau_\ell^{\mathrm{acc}}). \tag{6.13}$$

It is clear that here the total data sample is reproduced where each accepted MC event contributes with a weight w_ℓ given by

$$w_\ell = \frac{[\int \mathrm{d}\tau]}{N_{\mathrm{MC}}} I(\tau_\ell^{\mathrm{acc}}), \tag{6.14}$$

the sum of these weights being the total number of events. Histogramming any other quantity with this weight allows a comparison between the MC description and the data. If the MC sample closely describes the properties of the data not entering the decay amplitudes – such as location of the primary vertex, azimuthal angle of the plane of the original interaction, the t' distribution etc. –, and if the decay amplitudes are sufficient to describe the properties of the data, then any difference between such a histogram and the data should be of statistical origin. Such comparisons are shown in Sec. 8.5.

To summarize, the fit models the observed distributions of particles by adjusting the production amplitudes such that the angular distributions expected from the combination of the decay amplitudes with the acceptance description match the angular distributions observed in the data. In particular, the data are not acceptance corrected at any point. Quite the contrary, the fit model contains all the information about the detector acceptance.

6.2. Likelihood Function for Combined Fits

One interest of this work was the combined fit of the $\pi^-\eta'$ data selected in different final states where after the decay $\eta' \to \pi^-\pi^+\eta$ the η decays either to two photons or to three pions $\pi^-\pi^+\pi^0$. One thus has to find a likelihood function which allows simultaneously

dealing with both final states.

This can be done as follows: let ρ_1 and $\rho_2 = (1 - \rho_1)$ be the relative branching fractions of the two final states. Then one introduces the intensity functions for the two final states which ought to be given by $I_1(\tau) = \rho_1 I(\tau)$ and $I_2(\tau) = \rho_2 I(\tau)$, and therefore $\log I_\ell(\tau) = \log \rho_\ell + \log I_\ell(\tau)$. We denote the N_ℓ events in each final state τ_i^ℓ. With these definition one has for the predicted numbers of events for each final state

$$\bar{N}_\ell = \int \mathrm{d}\tau I_\ell(\tau)\eta_\ell(\tau) = \rho_\ell \int \mathrm{d}\tau I(\tau)\eta_\ell(\tau), \tag{6.15}$$

where the different acceptance functions for the two final states have been introduced, and for the total number

$$\bar{N} = \bar{N}_1 + \bar{N}_2. \tag{6.16}$$

The acceptances need to be studied in separate Monte Carlo simulations. The real data part of the log-likelihood function decomposes into two parts, one for each final state

$$\begin{aligned}\sum_{i=1}^{N_1} \log I_1(\tau_i^1) + \sum_{i=1}^{N_2} \log I_2(\tau_i^2) =& N_1 \log \rho_1 + \sum_{i=1}^{N_1} \log I(\tau_i^1) \\ &+ N_2 \log \rho_2 + \sum_{i=1}^{N_2} \log I(\tau_i^2),\end{aligned} \tag{6.17}$$

and therefore the combined log-likelihood function can be written

$$\begin{aligned}\log \mathcal{L} =& -\rho_1 \int \mathrm{d}\tau I(\tau)\eta_1(\tau) - (1-\rho_1) \int \mathrm{d}\tau I(\tau)\eta_2(\tau) \\ &+ N_1 \log \rho_1 + \sum_{i=1}^{N_1} \log I(\tau_i^1) + N_2 \log(1-\rho_1) + \sum_{i=1}^{N_2} \log I(\tau_i^2).\end{aligned} \tag{6.18}$$

The normalization integrals introduced in the previous section can be used as before, and the same evaluation of the fit quality as before can be undertaken, considering the different final states separately of course. The generalization to several final-states is obvious. Additionally, besides different final states, the different data sets could also be due to different triggers or even different experiments. The relative branching ρ_1 can be fitted as a free parameter or prescribed.

This combined fit was implemented in the partial-wave program developed during the course of this thesis. This is not the program we used for the final analysis, as it has no means of accounting for the background under the η' or η peaks. Nevertheless, we verify the Monte Carlo description of the spectrometer by checking whether the correct branching fraction obtains when fitting the $\pi^-\eta'$ data from both the final state with the intermediate η decaying to two photons and three photons simultaneously. From the tabulated branching fractions of the η meson [Nakamura et al., 2010] one has

$$\rho_1 \equiv \frac{\mathrm{BR}(\eta \to \gamma\gamma)}{\mathrm{BR}(\eta \to \gamma\gamma) + \mathrm{BR}(\eta \to \pi^-\pi^+\pi^0)} = 63.4\%. \tag{6.19}$$

The data selected for both final states were fitted, and the relative branching fractions obtained in all mass bins are depicted in Fig. 6.1. One sees that the fit indeed finds the correct branching ratio throughout the relevant mass range. Above 2.4 GeV the deviations become significantly larger. We do not draw physical conclusions in that range.

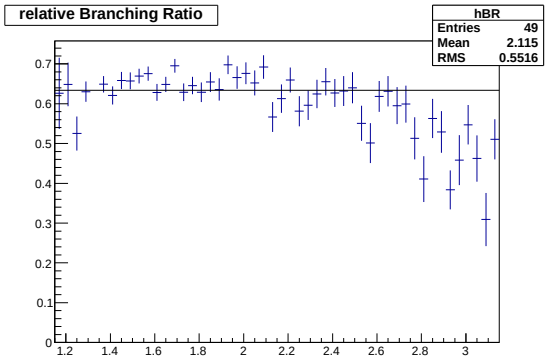

Figure 6.1.: Relative branching obtained for a combined fit of $\pi\eta'$ data in two final states (see text). The expected value is indicated by a horizontal line. It is reproduced fairly well, expcept for the high-mass range where the fit quality deteriorates due to the presence of additional partial waves.

7. Implementation

During the course of this work two programs were used that apply the formalism explained in the previous section to the analysis of the diffractively produced two-pseudoscalar final states $\pi^-\eta$ and $\pi^-\eta'$. One of these programs, developed as part of the dissertation work, implements this analysis as a strict two-body analysis. We shall refer to this program as LMU program. It totals about 5000 lines (145 kB) of `C++` code and uses the `TFitterMinuit` classes distributed with the ROOT libraries [Antcheva et al., 2009] for minimization. This program has also been used for preliminary studies of the centrally produced $\pi^-\pi^+$ system in the reaction $pp \to p_{\text{fast}}\pi^-\pi^+p_{\text{slow}}$ with data from the COMPASS 2009 run [Austregesilo and Schlüter, 2012]. It has also been used for the analysis of $K\pi$ final states shown in the appendix G.

The other program, derived from a program originally developed in the late 1960ies [Ascoli et al., 1970; Hansen et al., 1974], takes the full four-body final state $\pi^-\pi^-\pi^+\pi^0$ or, respectively, $\pi^-\pi^-\pi^+\eta$ into account in order to separate the η (η') from the background. This will be called Protvino program in the remainder of the text, as it's currently developed mainly by D. Ryabchikov at the Protvino Institute of High-Energy Physics. It is also the program used in other COMPASS analyses such as [Adolph et al., 2012; Alekseev et al., 2010]. We shall first discuss the detail of the two-body analysis, then discuss the additional implementation details of the four-body analysis.

7.1. Amplitudes for Two-pseudoscalar States

The angular momentum ℓ of a system of two pseudo-scalars is given by their orbital angular momentum. The amplitude for a two-pseudoscalar system with angular momentum ℓ and angular momentum projection on the z-axis given by m is by elementary quantum mechanics given by the spherical harmonic $Y_m^\ell(\theta, \phi)$ with the usual spherical coordinates. For a fixed mass of the two-pseudoscalar system, its phase space is completely described by the angular variables and the description in term of spherical harmonics is complete. The spherical harmonics are not eigenfunctions of parity, while the strong interaction conserves parity. The implications of parity conservation are implemented as follows: for the type of interactions considered a production plane can be uniquely defined. Therefore, the requirement of parity conservation is most usefully implemented by defining states as eigenfunctions with respect to reflections on the production plane (which equals the parity operation followed by a rotation which takes the particle momenta back to their original values) [Chung, 1997; Chung and Trueman, 1975]. The quantum number corresponding to this operation is called *reflectivity* and takes two values ± 1. The full set of quantum numbers in this basis is then ϵ, ℓ, m where $\epsilon = \pm 1$,

$0 \leq m \leq \ell$ and $m = 0$ only for $\epsilon = -1$. The corresponding basis for the two-pseudoscalar states is formed by the functions

$$Y_m^{\epsilon\ell}(\theta, \phi) \equiv c_m \left(Y_m^\ell(\theta, \phi) - \epsilon(-1)^m Y_{-m}^\ell(\theta, \phi) \right), \tag{7.1}$$

where c_m is a normalization: $1/\sqrt{2}$ for $m \neq 0$ (reflecting the orthogonality of the Y_m^ℓ) and $1/2$ for the case $m = 0$ where the two spherical harmonics are equal. It is worth noting that ϵ is -1 times the eigenvalue of the reflection operator when applied to the state. The value of this choice will become clear below.

The natural frame of reference in which to define the angles going into the spherical harmonics of Eq. (7.1) is the Gottfried-Jackson frame, also called t-channel helicity frame. This frame is defined as the right-handed rest-frame of the produced state ($\pi^-\eta'$) whose axes are chosen such that the x-axis lies in the production plane, the y-axis is orthogonal to it, and the z-axis is along the line of the exchanged momentum, i.e. also fixing the sign, the beam direction as seen in the rest frame.

As shown in Sec. 2.3, the two classes of events $\epsilon = \pm 1$ correspond in the asymptotic limit $s \to \infty$ to different production processes. Additionally, they do not interfere [Chung and Trueman, 1975]. Namely, by the choice of sign mentioned above, $\epsilon = +1$ corresponds to so-called natural transfers where only quantum numbers $J^P = 0^+, 1^-, 2^+, \ldots$ are exchanged, whereas $\epsilon = -1$ corresponds to unnatural exchanges with quantum numbers $J^P = 0^-, 1^+, 2^-, \ldots$. The Pomeron trajectory corresponds to a natural exchange and is expected to be dominant in the regime under study as explained in Sec. 2.1. We will now see that these two classes can be distinguished by eye if looking at the data in the right way.

Making the functional dependence on ϕ explicit, the spherical harmonics can be rewritten as

$$Y_m^\ell(\theta, \phi) = Y_m^\ell(\theta, 0) e^{\mathrm{i}m\phi}, \tag{7.2}$$

and it holds that $Y_{-m}^\ell(\theta, \phi) = (-1)^m (Y_m^\ell(\theta, \phi))^*$ where the asterisk denotes complex conjugation. Inserting this knowledge into Eq. (7.1) one finds

$$Y_m^{+1\,\ell} = 2\mathrm{i}c_m Y_m^\ell(\theta, 0) \sin m\phi, \tag{7.3}$$

and

$$Y_m^{-1\,\ell} = 2c_m Y_m^\ell(\theta, 0) \cos m\phi. \tag{7.4}$$

Therefore the presence of unnatural exchange will manifest itself as non-zero intensity for $\phi = 0$. It is perhaps worth noting that the S-wave $\ell = 0$ can only appear in unnatural exchanges.

Setting $j = (\ell, m)$ we can insert this into the intensity function of Eq. (6.1) by identifying

$$\psi_{ij}(\vartheta, \phi) = Y_m^{i\ell}(\vartheta, \phi), \tag{7.5}$$

and by using as volume element the usual solid-angle integral

$$\mathrm{d}\tau = \mathrm{d}(\cos\vartheta)\mathrm{d}\phi, \quad -1 \leq \cos\vartheta \leq +1, \quad 0 \leq \phi < 2\pi. \tag{7.6}$$

Traditionally, analysis of the $\pi\eta$ or $\pi\eta'$ system includes all amplitudes of spin up to a total of two and $m \leq 1$. Following the convention in the literature, we shall label the waves using a letter from spectroscopic notation $S, P, D \ldots$ together with a subscript $+$, $-$ or 0, which indicates naturality and spin substate at the same time, where $+$ indicates $m = 1$ natural exchange waves, $-$ indicates $m = 1$ unnatural exchange wave, and 0 indicates $m = 0$ waves, which can only correspond to unnatural exchange. We include two additional waves in the analysis: the $m = 2$ natural exchange spin-2 wave, labeled D_{++}, and the $m = 1$ natural exchange spin-4 wave, labeled G_+. Note that one can't add the D_{--} wave at the same time as the D_{++} wave as this would lead to an underdetermination of the angular distributions [Lednev, 1997], but this wave is expected to be strongly suppressed.

We show in Figs. 7.1, 7.2, and 7.3 exemplary angular distributions derived from these amplitudes. For the main waves of interest, which are all natural-parity exchange waves with $m = 1$, the distribution in φ_{GJ} is independent of the particular wave, and therefore not depicted. We can thus show the relevant information in two dimensions, plotting the relative phase shift between the waves on the horizontal axis and $\cos\vartheta_{\mathrm{GJ}}$ along the vertical axis. In the figures we see that changes in relative phase between the waves alter the distributions in $\cos\vartheta_{\mathrm{GJ}}$ significantly. This is what the fit utilizes to extract phase information.

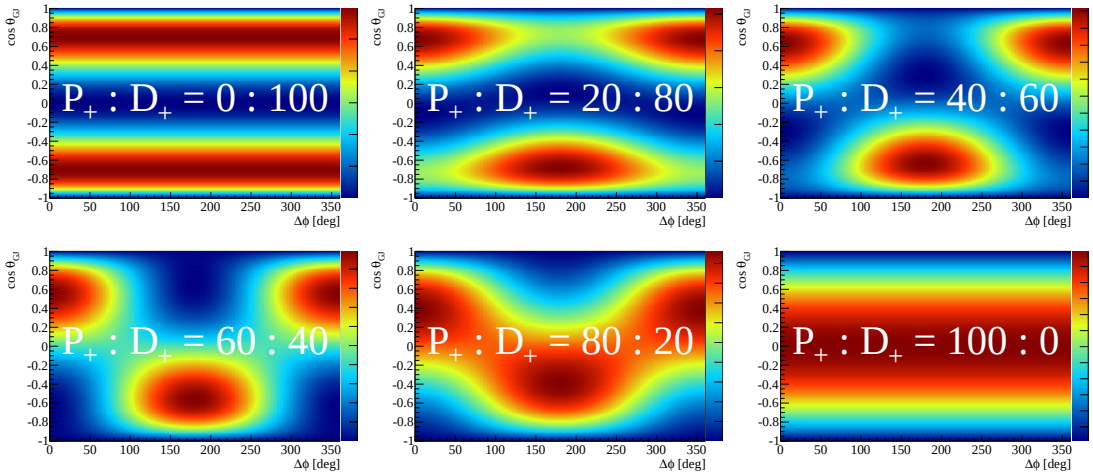

Figure 7.1.: Interference of P_+ and D_+ waves for different relative strength. Each subfigure shows for the relative contribution to the amplitude indicated on the plot the evolution of the angular distribution in terms of $\cos\vartheta_{\mathrm{GJ}}$ as a function of phase-shift. In real data, the phase-shift will be a function of mass and the relative strengths of the different waves will vary as function of mass and thus of phase-shift.

Comparing Fig. 7.1 to the data shown in Figs. 4.8d and 4.10d, we can see certain similar features: near the D_+ wave resonance $a_2(1320)$ we do indeed see a forward and backward peak in intensity, whose relative strength changes rapidly in the case of the

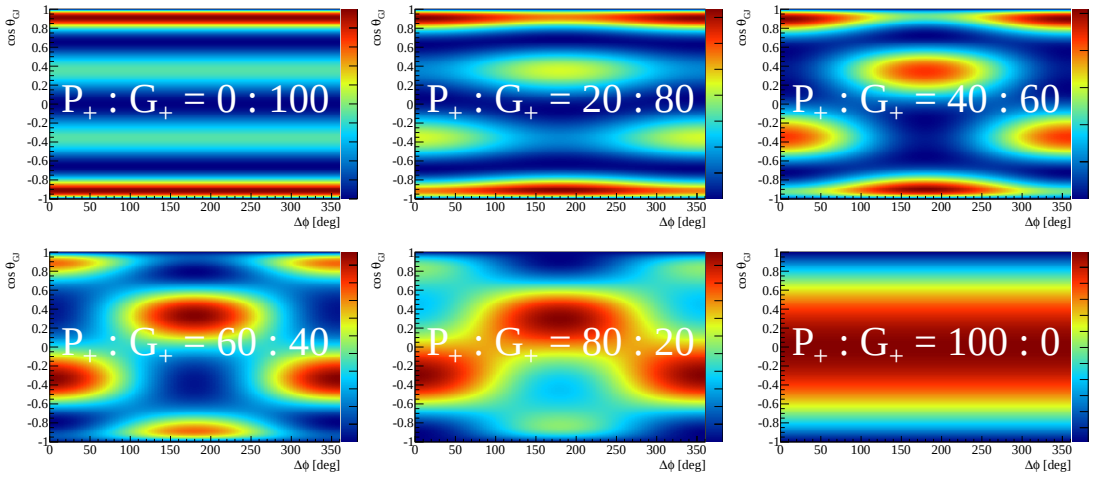

Figure 7.2.: As Fig. 7.1 for P_+ and G_+ wave interference.

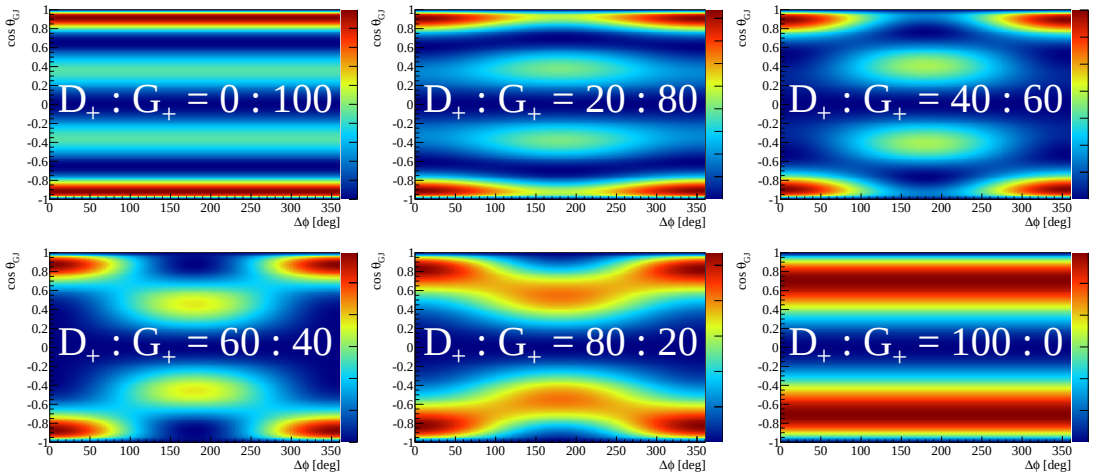

Figure 7.3.: As Fig. 7.1 for D_+ and G_+ wave interference.

$\pi^-\eta'$ data (corresponding to a large P_+ contribution) and slowly in the case of the $\pi^-\eta$ data (small P_+ wave contribution). In the $\pi^-\eta'$ data we can then see a slow shift of intensity between the forward and backward regions taking place for invariant masses between around 1400 and 1800 MeV. Then, near 2 GeV, especially in the $\pi^-\eta$ data, we see a structure resembling the bottom-left plot of Fig. 7.3. Thus, from this alone we can already determine that we should have a strong D_+ wave whose phase changes rapidly near 1300 MeV compared to a P_+ wave which is present in both the $\pi^-\eta$ and $\pi^-\eta'$ data, but which is relatively stronger in $\pi^-\eta'$. We also see that there should be a phase motion between the D_+ and G_+ data in the vicinity of 2 GeV, with little other contribution especially in the case of the $\pi^-\eta$ data. We will see all this confirmed by the actual analysis in the coming sections.

7.2. Ambiguities in the Two-body Analysis

We shall first discuss the technique known as "Barrelet zeros" [Barrelet, 1972] as it is applied to $\pi\pi$ scattering, e.g. [Becker et al., 1979; Estabrooks and Martin, 1975; Hyams et al., 1975], because the situation there is much simpler and the technique becomes clear before applying it to the more complicated situation in decays.

Discrete Ambiguities in $\pi\pi$ Scattering Partial Waves In general, the partial-wave sum for the scattering amplitude of two pions in the case where the highest angular momentum ℓ occuring is L can be written

$$A(s,t) = \sum_{\ell=0}^{L} (2\ell+1) a_\ell(s) P_\ell(z = \cos\theta), \tag{7.7}$$

where the amplitude is expressed as function of the Mandelstam variables s, t and $z = \cos\theta$ can be calculated as function of the two. This is a polynomial of degree L in z and can thus be written as function of its complex-valued *Barrelet zeros* $z_i(s)$, to wit

$$A(s,t) = f(s) \prod_{i=1}^{L} (z - z_i(s)). \tag{7.8}$$

The measured values are the cross-sections at real values of s, z which for fixed s are proportional to the modulus-squared of the amplitude, which for real scattering angles and therefore real values of z is

$$\frac{\mathrm{d}\sigma_{\pi\pi\to\pi\pi}}{\mathrm{d}t} \propto |A(s,t)|^2 = |f(s)|^2 \prod_{i=1}^{L} (z - z_i(s))(z - z_i^*(s)). \tag{7.9}$$

Besides being independent on the overall phase contained in $f(s)$, the value of this expression is invariant under the substitution $z_i \to z_i^*$ for any of the 2^L combinations of the $i \in \{1, \dots L\}$. Therefore, from measurement alone the amplitude Eq. (7.8) can only be determined up to this 2^L-fold ambiguity in the signs of the imaginary parts

of the Barrelet zeros. Since the Legendre polynomials form an orthogonal basis of the space of polynomials, each such ambiguous solution in the form of Eq. (7.8) can be converted back to a set of partial waves in the form of Eq. (7.7) and each such set of partial waves predicts the same angular distributions. The decision which such set of angular distributions catches the physics therefore needs additional input, such as behavior corresponding to known resonances, requirements from analyticity etc.

Discrete Ambiguities in Two-Pseudoscalar Final States in Scattering Experiments Here, the situation is more complicated as one has to deal with two non-interfering contributions coming from natural and unnatural exchange waves, respectively. Additionally, we have to take into account the magnetic quantum number m which is usually ≤ 1. Following the methods of Refs. [Barrelet, 1972; Costa et al., 1980; Gersten, 1969; Martin et al., 1978; Sadovsky, 1991], one can write for the amplitudes after a judicious choice of linear combinations and variables [Chung, 1997]

$$\begin{aligned} g(u) &= c\frac{1}{(1+u^2)^L}\prod_{k=1}^{2L}(u-u_k), \\ h_+(u) &= c'\frac{u}{(1+u^2)^L}\prod_{k=1}^{L-1}(u^2-r_k). \end{aligned} \tag{7.10}$$

where $u = \tan(\vartheta_{\mathrm{GJ}}/2)$ and L is the maximum angular momentum considered. The intensity is related to these in the following way: writing

$$\begin{aligned} h_0(u) &= \frac{1}{\sqrt{2}}(g(u)+g(-u)), \\ h_-(u) &= \frac{1}{2}(g(u)-g(-u)), \end{aligned} \tag{7.11}$$

one has for the intensity function

$$I(\Omega) = \frac{1}{4\pi}\left[|h_0(\vartheta_{\mathrm{GJ}}) + \sqrt{2}h_-(\vartheta_{\mathrm{GJ}})\cos\varphi_{\mathrm{GJ}}|^2 + |\sqrt{2}h_+(\vartheta_{\mathrm{GJ}})\sin\varphi_{\mathrm{GJ}}|^2\right]. \tag{7.12}$$

Relations between the coefficients of the polynomials in Eq. (7.10) and the partial waves are given in Ref. [Chung, 1997]. The ambiguous solutions are now obtained by sequentially trying all combinations of complex conjugates of the zeroes u_k, r_k in Eq. (7.10) and solving for the partial waves.

In the case under consideration, unnatural-exchange waves are absent from the data. In this case, ambiguities only arise when angular momenta of at least three units are present. Additionally, an incomplete set of waves, such as our main set P_+, D_+, G_+, has no ambiguities besides the trivial indeterminacy of the signs of the relative imaginary parts. We return briefly to the question of ambiguities when we include the F_+ wave in Sec. 8.6.2.

Continuous Ambiguities In this section we set out to show how a fit with higher-rank density matrix is not possible in the two-pseudoscalar case when only the information from the angles ϑ_{GJ}, φ_{GJ} is taken into account. The intensity function for a rank-two fit then has the general form

$$I(\vartheta_{\mathrm{GJ}}, \varphi_{\mathrm{GJ}}) = I_1(\vartheta_{\mathrm{GJ}}, \varphi_{\mathrm{GJ}}) + I_2(\vartheta_{\mathrm{GJ}}, \varphi_{\mathrm{GJ}}), \tag{7.13}$$

where I_1, I_2 are the incoherent contributions, which we assume both to be due to natural-parity exchange. The goal of this section is to show that the intensity distribution $I_1 + I_2$ can, by an appropriate choice of partial waves, be expressed with a single set of partial waves, i.e. any distribution where the physics requires rank two can be fitted with a rank-one density matrix. Since the case of rank one is a special case of the case of rank two (set all partial waves in the second component to zero, i.e. $I_2 = 0$), it is then clear that a fit with rank two or higher can't be stable, one has to fit with rank one and then be careful in the physical interpretation to allow for incoherent contributions.

The assertion is easily proven by looking at the relations between the partial waves and the moments of the intensity distribution, which taken together are equivalent to the intensity distribution. The moments are defined in the usual way as

$$H(LM) = \int \mathrm{d}\Omega Y_M^{L*}(\vartheta_{\mathrm{GJ}}, \varphi_{\mathrm{GJ}}) I(\vartheta_{\mathrm{GJ}}, \varphi_{\mathrm{GJ}}). \tag{7.14}$$

Since this is linear one has $H(LM) = H_1(LM) + H_2(LM)$, where $H(LM)$ refers to the moments of I and $H_1(LM)$, $H_2(LM)$ to the moments of I_1, I_2. For the case of only the natural-parity waves P_+, D_+ being present, relevant to the low-mass range, the following linearly independent moments obtain in terms of the production amplitudes,

$$\begin{aligned} H(00) &= |P_+|^2 + |D_+|^2, \\ H(10) &= \frac{1}{\sqrt{5}} \mathrm{Re}(P_+^* D_+), \\ H(40) &= -\frac{4}{21} |D_+|^2. \end{aligned} \tag{7.15}$$

Writing P_1, D_1, P_2, D_2 for the production amplitudes of the partial waves the non-interfering components, one finds from $H(LM) = H_1(LM) + H_2(LM)$ that the same angular distribution is described by the rank-one density matrix with waves P_+, D_+ given by

$$\begin{aligned} |D_+|^2 &= |D_1|^2 + |D_2|^2, \\ |P_+|^2 &= |P_1|^2 + |P_2|^2, \\ \cos\Delta\phi &= \frac{|P_1||D_1| \cos\Delta\phi_1 + |P_2||D_2| \cos\Delta\phi_2}{|P_+||D_+|}, \end{aligned} \tag{7.16}$$

where the $\Delta\phi$ denote the phase differences $\arg(D_+/P_+)$, and similar for $\Delta\phi_1$, $\Delta\phi_2$. This result is unique up to a global phase and the sign of $\Delta\phi$. Note that this solution always exists except in the uninteresting case where either $|D_+|$ or $|P_+|$ is zero and the phase

differences therefore becomes undefined. For the case with an additonal G_+ wave, one derives similar relations. Since the rank-one case can be reached by the limit $D_2 \to 0$, $P_2 \to 0$, there is no unique best description of the data in a rank-two fit.[1] In the special case where $\cos\Delta\phi_1 = \cos\Delta\phi_2 = \cos\Delta\chi$ one can write

$$\cos\Delta\phi = \xi\cos\Delta\chi, \qquad 0 \leq \xi \leq 1, \tag{7.17}$$

where ξ is then a measure of coherence and $\Delta\chi$ is interpreted as the physical phase difference which can be extracted if assumptions about ξ are made [Martin et al., 1978].

This issue seems to have escaped the authors of analyses of the $\pi^-\eta$ and $\pi^-\eta'$ final states with the exception of the authors of Ref. [Chung et al., 1999] who instead go on to show that for the case of a fit which accomodates Breit-Wigner resonances in both the D_+ and P_+ partial waves, one can find a rank-two density matrix which has these same resonances in both non-interfering contributions. From this, they seem to conclude that a successful fit to the rank-one density matrix with both a P-wave resonance and a D-wave resonance implies that even in the presence of non-interfering contributions, this interpretation should hold. How this exercise in algebra should have the stated physical conclusion remains unclear, as only for very specific relative strengths of the various partial waves one will observe the resonances present in the rank-two density matrix with the same functional form in the rank-one fit. Indeed, one can show that under fairly general circumstances, one can find coefficients such that $P_1 = \alpha P$, $D_1 = \beta D$, $P_2 = \gamma P$, $D_2 = \delta D$. For this it is not needed the P and D be Breit-Wigner functions, contrary to what the authors of Ref. [Chung et al., 1999] seem to suggest. What is really shown by Eq. 7.16 is that any interpretation of the results of the mass-independent fit should allow for non-interfering contributions.

7.3. Four-body Analysis of the Two-Pseudoscalar Final States

Selection of the $\eta \to \pi^-\pi^+\pi^0$ or $\eta' \to \pi^-\pi^+\eta$ decays invariably leads to background, both due to the finite resolution of the detector and because of background processes that are unaccounted for. In the two-body analysis of the $\pi^-\eta$ and $\pi^-\eta'$ systems described before, there is no room for the fit to separate these contributions from the data which is of interest, the corresponding intensity will end up being described by the partial waves. It is therefore of interest to devise a strategy which separates out background contributions. In the analysis under description, the full four-body information available is used for this purpose. As shown in Sec. 4.4.1 and Sec. 4.4.2, the isoscalars are observed as peaks with double-Gaussian shape sitting on a rising background. It is also shown there that the decay of the pseudoscalars is not isotropic, but instead decays with large invariant mass of the $\pi^-\pi^+$ pair are favored. This was predicted for the η (see e.g. Ref. [Bijnens and

[1] During the final stages of the preparation of this thesis it was found that the moments for the combination of waves P_+, D_+ and D_{++}, while leading to very similar equations, do not allow the same kind of unique reduction from rank two to rank one. This is due to the additional information contained in the interference of $M = 1$ and $M = 2$ contributions and their different dependence on φ_{GJ}. First attempts of rank-two fits were inconclusive, but the implications could not be studied further.

Ghorbani, 2007] and references therein). On the other hand, theoretical calculations have caught up with experimental data on the η' decays only recently (e.g. Ref. [Escribano et al., 2011] and references therein).

The fit incorporates this additional information in the following way: data are selected in a wide window around the nominal mass of the isoscalar. Then, when calculating the amplitudes for the physical waves, two additional factors appear: one corresponding to the double-Gaussian shape of the η/η' peak (being an amplitude, the square-root of the double-Gaussian function is used), and another one corresponding to the η/η' decay amplitude where the tabulated empirical parametrizations [Nakamura et al., 2010] are used. Additionally, a so-called *flat wave* is introduced whose amplitude is isotropic in the four-body phase-space. This absorbs the background under the isoscalar peak. In App. H we document first steps to a complete four-body partial-wave analysis of the $\pi^-\pi^-\pi^+\eta$ system, which would also account for the bckground under the η' in terms of partial waves.

An analysis in the full four-body space in principle requires a correctly Bose-symmetrized amplitude between the two identical π^- appearing in the final state where both combinations should be added coherently. Nevertheless, given the small width of the isoscalars, the overlap region cannot be disentangled from the experimental smearing, while simultaneously leading to a physical effect only in a very small region of phasespace (estimated by the ratio of the width of the isoscalar divided by the several orders of magnitude larger size of the available phasespace). Therefore, this symmetrization is not performed, both combinations are added incoherently.

Lastly, the four-body phase-space has to be filled by Monte Carlo events. Since in the real data only events are considered where one neutral three-body combination lies in the vicinity of the isoscalar mass, only a small part of the full phase-space contributes in the analysis. The Monte Carlo generation therefore only populates this part of phase-space. In the case of $\eta'\pi^-$ the Monte Carlo generation is isotropic apart from this cut. For the $\eta\pi^-$ generation on the other hand, a weighted Monte Carlo is used to probe the range of the η efficiently with less generated events. Events are generated following a probability distribution which generates more events in the vicinity of the η peak (its functional form as function of the three-body mass is that of a constant plus a Gaussian centered about the η mass). When calculating the normalization integrals, each event is weigthed with the inverse of this probability distribution, leading to an efficient evaluation of the same integral.

8. Results of the Partial-wave Analysis in Mass Bins

In this section we present the results of the mass-independent partial-wave analysis of the $\eta'\pi^-$ and $\eta\pi^-$ data. First, we give the results from fits to the complete data sets and then we show a number of alternative fits and results from the kinematic validation of the fits. Except for Sec. 8.7 where we compare the results obtained with the different partial-wave programs, all figures were obtained with the full four-body analysis program.

Let's quickly recall the knowledge from previous analyses: in the diffractively produced $\eta\pi$ and $\eta'\pi$ systems, D and P wave intensities were observed. In $\eta'\pi$, a previous analysis also found a G-wave intensity [Ryabchikov, 1997]. Charge-exchange reactions also saw S-wave intensities, but since these can only arise from Reggeon exchanges, they are suppressed at 191 GeV where the neutral Pomeron exchange is dominant. In the $\eta\pi^-$ system the D_+-wave was found to be dominant, unlike in the $\eta'\pi^-$ system where the P_+ wave is of comparable strength to the D_+ wave.

8.1. Partial-Wave Analysis of the $\eta'\pi^-$ system

The results of the mass-independent fit to the $\pi^-\eta'$ system are shown in Fig. 8.1. Depicted are the natural-parity waves. On the diagonal, the intensities of the allowed waves are shown, from left to right these are the P_+, the D_+ and the G_+ waves. These three waves together with the flat wave allow to describe the data up to approximately 1.8 GeV. Inclusion of the spin-three F_+ wave is discussed in Sec. 8.6.2. The effect of its addition on the natural-parity waves shown above is a stabilization of the G_+ wave which in the fits shown here has a discontinuity near 2 GeV. The interferences between the waves are shown above and below the diagonal of Fig. 8.1. Above, the relative real parts are plotted, below the relative imaginary parts.

Mass-independent partial-wave analysis confirms the features expected from previous analyses: the unnatural exchange waves are suppressed; in the natural waves, the P_+ wave is the largest wave, showing a broad bump centered around 1.6 GeV. In terms of intensity, is followed by the D_+ wave which shows a peak corresponding to the $a_2(1320)$ near threshold, followed by a broad shoulder which begins to decrease near 2 GeV. The G_+-wave is zero until approximately 1.8 GeV, then shows a structure near 2 GeV, followed by a slowly increasing background. Also, the unnatural waves start to increase in the high-mass range beyond 2 GeV. More on this later.

The phase motions derived from this are depicted in Fig. 8.2. Two features are easily identified with known physical objects: the rapid phase-motion between the P_+ wave and the D_+ wave around 1.3 GeV corresponding to the $a_2(1320)$, and the phase motion

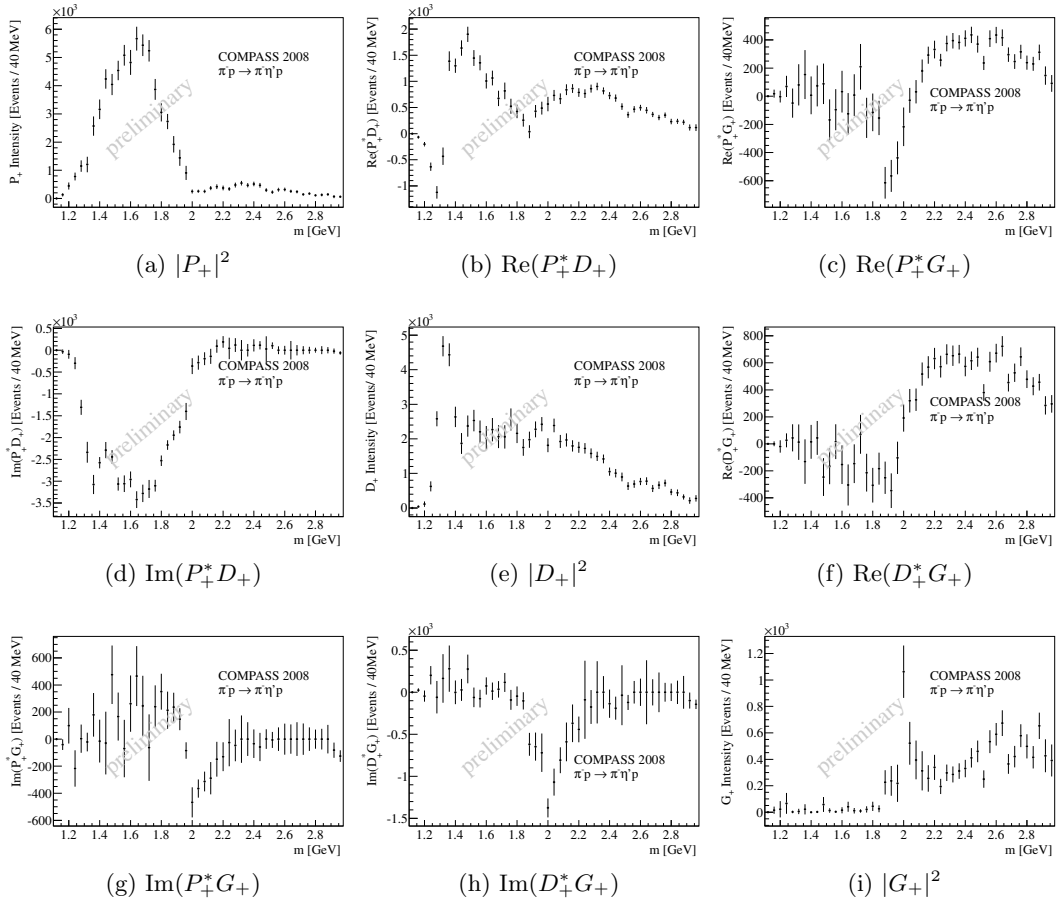

(a) $|P_+|^2$ (b) $\mathrm{Re}(P_+^* D_+)$ (c) $\mathrm{Re}(P_+^* G_+)$

(d) $\mathrm{Im}(P_+^* D_+)$ (e) $|D_+|^2$ (f) $\mathrm{Re}(D_+^* G_+)$

(g) $\mathrm{Im}(P_+^* G_+)$ (h) $\mathrm{Im}(D_+^* G_+)$ (i) $|G_+|^2$

Figure 8.1.: Mass-independent partial-wave analysis of the $\pi^- \eta'$ system. The matrix show on the diagonal the intensities of the P_+, D_+, and G_+ waves. Above the diagonal are shown the respective relative real parts, below the respective relative imaginary parts. The signs of the imaginary parts are not determined by the fit.

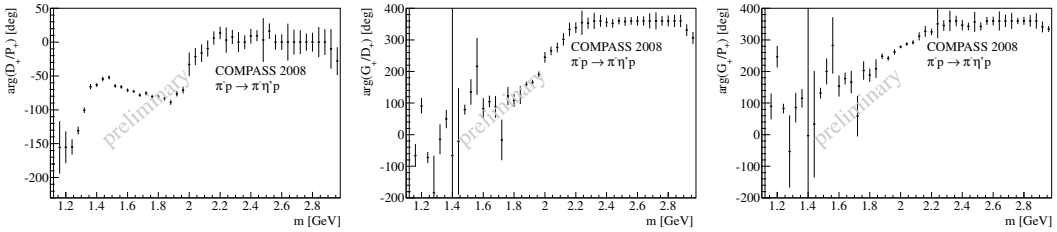

(a) $\arg(D_+/P_+)$ (b) $\arg(G_+/D_+)$ (c) $\arg(G_+/P_+)$

Figure 8.2.: Phase motions in the $\eta'\pi^-$ system. The function arg is the function giving the phase of its complex argument, and thus the phase-difference between numerator and denominator in the fractions.

of the G_+ wave near 2 GeV relative to both the P_+ and the D_+ waves, signifying the presence of the $a_4(2040)$. The remaining phase-motion not associated with established resonances is the one between the P_+ and D_+ waves in the range from approximately 1.5 GeV to 2 GeV where a slow phase-shift is followed by a rapid increase near 2 GeV. These will be studied in the chapter on mass-dependent fits, where different models for these structures will be applied.

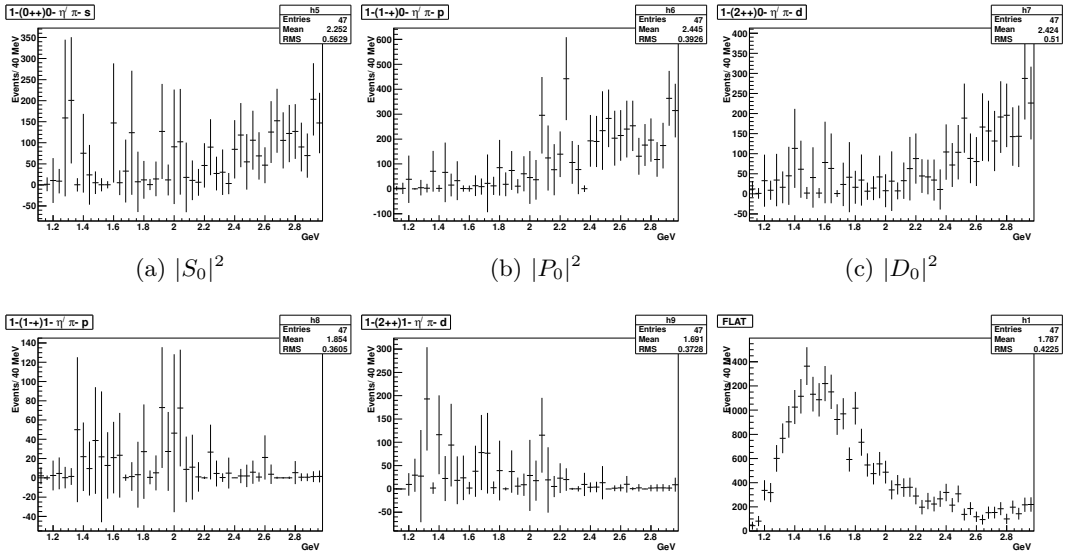

(a) $|S_0|^2$ (b) $|P_0|^2$ (c) $|D_0|^2$

(d) $|P_-|^2$ (e) $|D_-|^2$ (f) flat wave

Figure 8.3.: Intensities obtained in the mass independent fit to the unnatural-parity and flat waves in the $\eta'\pi$ system.

The re-appearance of the unnatural exchange waves visible in Fig. 8.3 in the high-mass range is due to the following reason. As seen in Fig. 4.8d, the data concentrates near $\cos\vartheta_{\mathrm{GJ}} = \pm 1$. This concentration of the data near the edges requires higher and higher

partial waves, rendering the wave set which includes only waves in the range $L = 1, 2, 4$ insufficient which makes the fit attempt other waves. The ϑ distribution of the unnatural waves tends to be sharper, and this is reflected in the fit's propensity for using them. We show in Sec. 8.6.2 how the inclusion of higher-spin waves prevents this rise of the unnatural waves in the high-mass region. This feature will become more clear in Sec. 8.5 where the fit results will be compared to the data.

We also studied inclusion of the D_{++} wave, the $m = 2$ contribution to the spin-two wave. It was found at a relative strength of 3% relative to the D_+ wave, but with large uncertainties, and was not further considered.

8.2. Partial-Wave Analysis of the $\eta\pi^-$ system

The data in the $\eta\pi^-$ channel are dominated by the well-known $a_2(1320)$ resonance. This feature, evident from the invariant mass spectrum, is confirmed by the partial-wave analysis which finds the largest contributions in the D_+ wave. Its $m = 2$ component, the D_{++} wave is found at the 3% level. Besides this well known resonance, it appears again a broad structure in the P_+ wave, this time centered at approximately 1.3 GeV. The intensity in this wave vanishes for masses above approximately 1.8 GeV which implies that the fit sees no forward-backward asymmetry after acceptance corrections in the high-mass range. The P_+ wave intensity is lower in the $\pi^-\eta$ system than in the $\pi^-\eta'$ system, even though the latter has much less available phase-space. We will return to this point in Sec. 8.3. Lastly, the G_+-wave shows a peak compatible with the $a_4(2040)$ near 2 GeV and rises above. In terms of phase motions, the D_+ and D_{++} waves appear phase-locked after they both pick up intensity. While this suggests a similar physical origin of both waves the difference in relative height of the peak to the high-mass shoulder indicates that the shoulder is generated by a different physical process from the main peak.

The phase motions between the P_+ and D_+ waves shows the same behavior as in previous analyses at lower energies [Amelin et al., 2005; Beladidze et al., 1993; Chung et al., 1999; Szczepaniak et al., 2003]. The fit is self-consistent in that the phase motion between and P_+ and D_{++} waves mimics that between the P_+ and D_+ waves, and that the differences are reflected in the phase motion between the D_+ and D_{++} waves. The relative phase-shift between D_+ and G_+ waves is again compatible with the presence of the $a_4(2040)$ resonance. In terms of interpretation it is unfortunate that there's almost no overlap between the P_+-wave and G_+-wave structures, which would allow attributing phase-shifts to individual waves independently of a model.[1]

Around 1.3 GeV we observe a peak in the G_+ wave. This is understood as leakage from the much stronger D_+ wave, where due to an incomplete Monte-Carlo description, the observed intensity distribution is not perfectly described. Namely, the occupancy of the center of the electromagnetic calorimeter does not agree between the fit prediction and the data. Potentially, this is due to a slight mismatch between the momentum transfer distribution used in the Monte Carlo generation and the actual data, we will return to this particular point in Sec. 8.5.

[1] To be precise, if one observed a similar phase-shift between waves A and B as well as between waves A and C, while at the same time no such phase-shift is seen between waves B and C, then one is left with two possibilities: either the phase shift is due to a change of phase of wave A, or waves B and C move in sync. A model that distinguishes between the two possibilities can then be much simpler than if, say, only information on the relative phase-shift between waves A and B is available with no information on wave C.

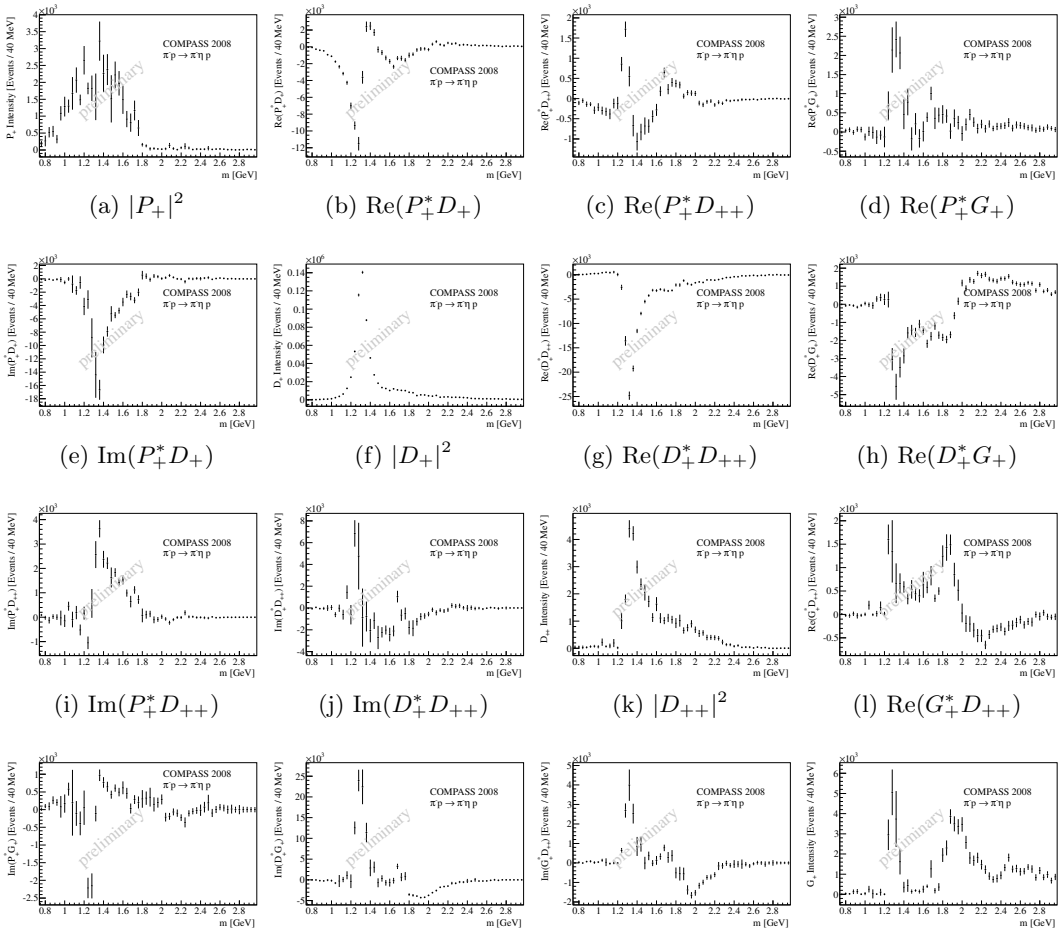

(a) $|P_+|^2$ (b) $\mathrm{Re}(P_+^* D_+)$ (c) $\mathrm{Re}(P_+^* D_{++})$ (d) $\mathrm{Re}(P_+^* G_+)$

(e) $\mathrm{Im}(P_+^* D_+)$ (f) $|D_+|^2$ (g) $\mathrm{Re}(D_+^* D_{++})$ (h) $\mathrm{Re}(D_+^* G_+)$

(i) $\mathrm{Im}(P_+^* D_{++})$ (j) $\mathrm{Im}(D_+^* D_{++})$ (k) $|D_{++}|^2$ (l) $\mathrm{Re}(G_+^* D_{++})$

(m) $\mathrm{Im}(P_+^* G_+)$ (n) $\mathrm{Im}(D_+^* G_+)$ (o) $\mathrm{Im}(G_+^* D_{++})$ (p) $|G_+|^2$

Figure 8.4.: Mass-independent partial-wave analysis of the $\pi^-\eta$ system. The matrix show on the diagonal the intensities of the natural-parity waves. Above the diagonal are shown the respective relative real parts, below the respective relative imaginary parts. The signs of the imaginary parts are not determined by the fit. The dominating D_+ wave leaks into the G_{++} wave in the mass range near 1.3 GeV.

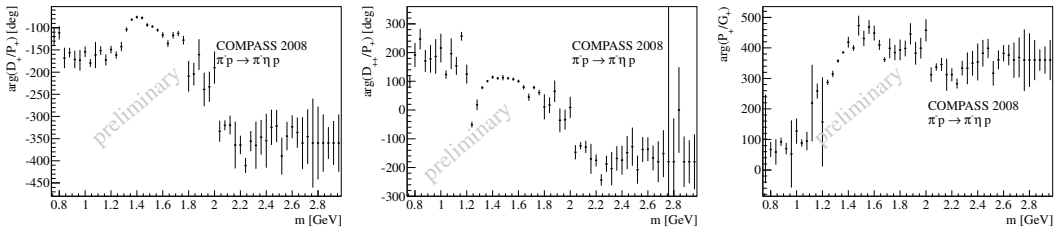

(a) $\arg(D_+/P_+)$ (b) $\arg(D_{++}/P_+)$ (c) $\arg(P_+/G_+)$

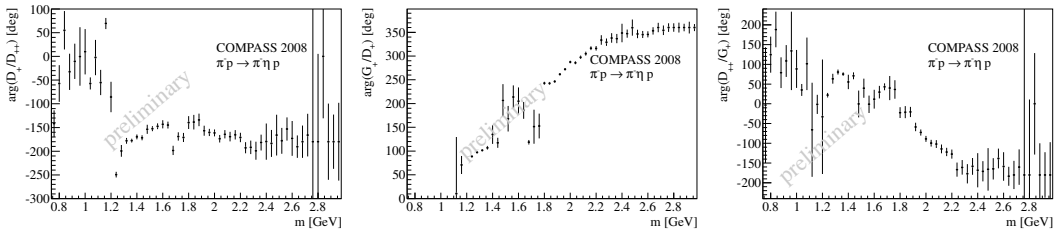

(d) $\arg(D_+/D_{++})$ (e) $\arg(G_+/D_+)$ (f) $\arg(D_{++}/G_+)$

Figure 8.5.: Relative phases of the natural-exchange waves in the $\pi^-\eta$ system.

8.3. Comparison of the Two Systems

As discussed in Sec. 1.1.2, the η and η' mesons mix. Namely, the OZI rule predicts that aside from angular momentum barriers, the amplitudes for initial states with no strangeness content leading to final states with η' or η mesons and no strange quarks in the other final-state particles should behave as [Okubo and Jagannathan, 1977]

$$\frac{A(\eta')}{A(\eta)} \propto \tan\phi, \tag{8.1}$$

with ϕ the pseudoscalar mixing angle in the flavor basis, provided the process can be drawn with a connected quark-line diagram. Intuitively, this is readily understood as the suppression of the production of an $s\bar{s}$ which would need a disconnected quark-line diagram, exactly the case of OZI suppression.

Testing this prediction in the case under study is interesting for two reasons: on the one hand, the production of η mesons via double-Pomeron exchange in the usual picture of the Pomeron as a purely gluonic object need not follow this prediction: when the η is produced from two Pomerons, then only the flavor-neutral couplings of the gluons to the quarks should contribute, and the conditions for application of the OZI rule are not given. On the other hand, the coupling of a $q\bar{q}g$ system – another case where the OZI rule is not applicable – to $\pi\eta'$ is predicted to be enhanced over the coupling to $\pi\eta$ [Close and Lipkin, 1987]. It was already verified by previous experiments that the P_+ possesses this property [Beladidze et al., 1993]. We shall study this property also for the other waves.

In general, cross-sections for the production of the $\pi\eta'$ and $\pi\eta$ system of angular momentum J and mass m that follow the OZI prediction should behave as

$$\frac{\sigma_{\pi\eta'}}{\sigma_{\pi\eta}} = \frac{q'(m)}{q(m)} \frac{F_J^2(q'(m))}{F_J^2(q(m))} \tan^2\phi, \tag{8.2}$$

where $q(m)$ ($q'(m)$) denotes the break-up momentum of the system when decaying to $\pi\eta$ ($\pi\eta'$). General relations of this type are given in [Okubo and Jagannathan, 1977]. The first factor is a phase-space factor, the second, dynamical term corresponds to the angular momentum barrier, the third term describes the mixing between the ηs [Amsler et al., 1992]. The form of the dynamical term is not given a priori and depends on the interaction. For a reaction where an intermediate spin-J resonance decays, the usual Hippel-Quigg factors [von Hippel and Quigg, 1972] are a natural, but not necessary choice [Abele et al., 1997; Amsler et al., 1992]. Since we have seen before that large contributions also take place away from resonances, we take the simple form

$$F_J(q) = q^J, \tag{8.3}$$

which has the required asymptotics near threshold, but makes no further dynamical assumptions. We are thus led to the following way of comparing the amplitudes leading to the two final states under consideration: take the partial-wave amplitude extracted

from the partial-wave amplitude for the $\pi\eta$ final-state; multiply this amplitude with a factor

$$\left(\frac{q'(m)}{q(m)}\right)^{J+1/2} ; \tag{8.4}$$

superimpose the thus obtained amplitudes on the corresponding amplitudes for the $\eta'\pi$ final states. More precisely, the accessible quantities are the interference terms and intensities which always involve products of two amplitudes (not necessarily different), so the corresponding value is scaled with two such factors, one for each partial-wave amplitude. The resulting intensities and interference terms are depicted in Fig. 8.6.

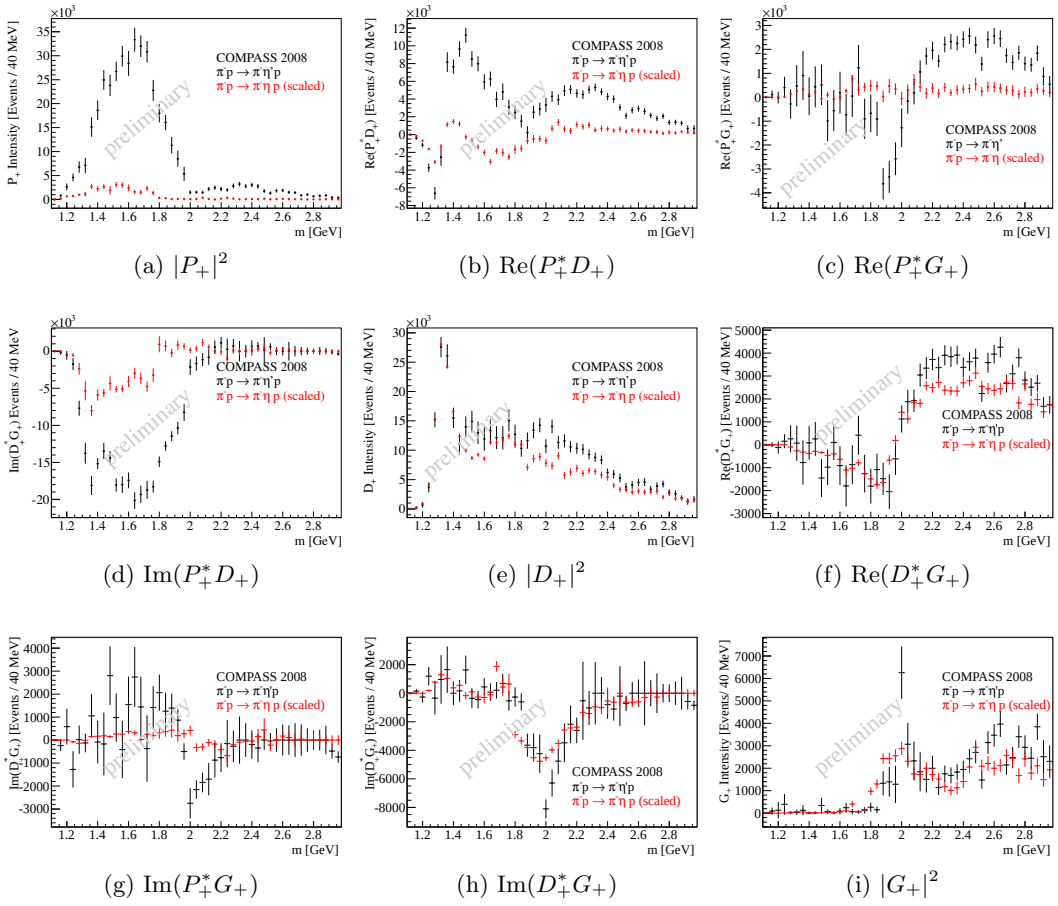

(a) $|P_+|^2$ (b) $\mathrm{Re}(P_+^* D_+)$ (c) $\mathrm{Re}(P_+^* G_+)$

(d) $\mathrm{Im}(P_+^* D_+)$ (e) $|D_+|^2$ (f) $\mathrm{Re}(D_+^* G_+)$

(g) $\mathrm{Im}(P_+^* G_+)$ (h) $\mathrm{Im}(D_+^* G_+)$ (i) $|G_+|^2$

Figure 8.6.: Comparison of the partial-wave amplitudes obtained in the $\pi\eta'$ (black) and $\pi\eta$ systems (red) after re-scaling with the phase-space factors.

The comparison shows two striking features: first, the close similarity of the even partial waves, D_+ and G_+. Subject to further MC studies, the close match in the overall normalization is supposed to be accidental: in Sec. 9.3 we extract relative branching fractions of the $a_2(1320)$ which are at slight tension with theoretical expectations and

tabulated values.

It appears that the physical content of these waves is the same in both final states, even in the high-mass range where non-resonant production is expected to be dominant. On the other hand, the P_+ wave is strongly suppressed in the $\pi\eta$ final state in accordance with the suspected non-$q\bar{q}$ character of this wave. Comparing the phase motions (which are not affected by the scaling procedure) as shown in Fig. 8.7, one finds that the P_+ wave has the same phase relative to the D_+ wave at the $\pi\eta'$ threshold, which suggests a common origin, but it then evolves differently which contradicts them having the same resonant content. The similarity of the scaled D_+ waves suggests that the difference in the relative phase motion of the P_+ and D_+ waves is mainly due to different contents of the P_+ wave. The phase determination of the mass-independent fit is not unique, as the sign of the relative imaginary part cannot be fixed. We thus show two possible branches of the phase determination in the $\pi^-\eta$ system, the red points correspond to the ones shown before, the blue points are mirrored on the -180 deg line. The phase-difference in the $\pi^-\eta'$ system is continuous and remains within the same 180 deg range, so we do not show any alternative branches there. If one takes the mirrored points into account, the phase motion from the P_+-wave in $\pi^-\eta$ overshoots the phase observed in the $\pi^-\eta$ system, but otherwise they turn out fairly similar. Returning to Sec. 7.2, where we discussed the possibility of incoherent contributions, the simplest explanation appears to be an incoherent contribution larger in the $\pi^-\eta'$ data. This contribution – taking the similarity between the D_+ waves into account – would have to be mostly P_+ wave. Then the phase motion near 2 GeV would actually be due to the disappearing of the additional P_+ wave contribution and not to a resonance in the D_+ wave. This in turn would be consistent with the relative phase motion of the D_+ and G_+ waves which shows a phase motion corresponding to a resonance in the G_+ wave but no sign of a 180 degree motion in the opposite direction stemming from a second D_+ wave resonance.

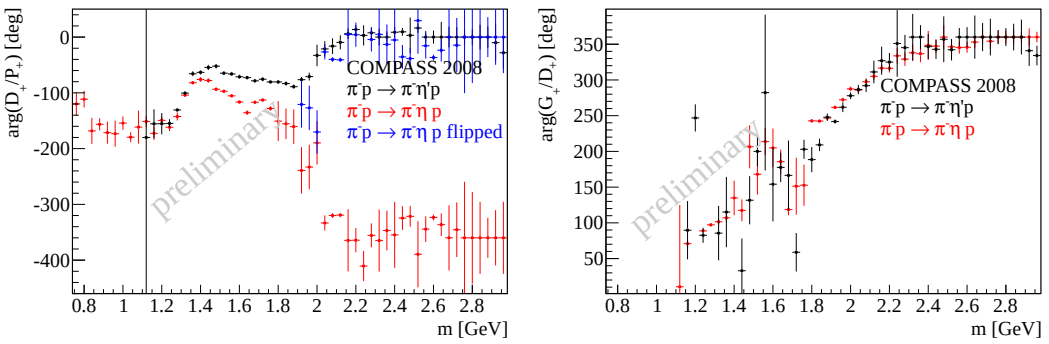

(a) arg(D_+/P_+) (b) arg(G_+/D_+)

Figure 8.7.: Comparison of the relative phases. For the D_+/P_+ comparison we show both ambiguous branches of the phase-motion in the $\pi^-\eta$ system (see text). The relative phase motion of the P_+ and G_+ waves is not shown as they have only very little overlap in the $\pi^-\eta$ data.

Lastly, a comment on the role of angular momentum barrier factors in this comparison: if instead of the simple factors $F_L(q) = q^L$ one uses the angular momentum barrier factors from Eq. (F.9) as in $F_L(q) = B_L((qR)^2)$ with $R \approx 1\,\mathrm{fm}$, the scaling blows up the $\eta\pi$ data relative to the $\eta'\pi$ data, as only for very large values of the breakup momenta the ratio of the angular momentum barrrier factors $B_L((q'R)^2)/B_L((qR)^2)$ becomes comparable to the simpler phase-space factor $(q'/q)^L$. This will be taken up in Sec. 9.3.

8.4. t'-dependent Fits

In order to gain further insight into the production of the $\eta\pi^-$ or $\eta'\pi^-$ pairs, we pursued fits in various ranges of the momentum transfer t'. First, we performed fits where we only included data in the range $0.1\,\mathrm{GeV}^2 < t' < 1\,\mathrm{GeV}^2$, as that is the range covered by the Monte Carlo generation. Fit results were not affected significantly by this. Then we subdivided this range into two ranges of approximately the same content, $0.1\,\mathrm{GeV}^2 < t' < 0.3\,\mathrm{GeV}^2$ ("low-t'") and $0.3\,\mathrm{GeV}^2 < t' < 1\,\mathrm{GeV}^2$ ("high-t'") and performed fits in these two subranges. The only wave where we expect a markedly different dependence on t' is the $M = 2$ D_{++} wave. While for the $M = 1$ waves the expected behavior of the cross-section is $\mathrm{d}\sigma/\mathrm{d}t' \propto t' \exp(-bt')$, one expects the wider $\mathrm{d}\sigma/\mathrm{d}t' \propto t'^2 \exp(-bt')$ for the $M = 2$ wave. In principle, different physical processes contributing could be governed by different exponential functions. As we see from the results of the fits, depicted in Fig. 8.8 for $\eta'\pi^-$ and Fig. 8.9 for $\eta\pi^-$, this appears not to be the case. The intensities as well as the interference terms come out very similarly in the different t' bins. We shall comment briefly on the most important differences below. The unphysical waves are not depicted, they contain no interesting content.

In the $\eta'\pi^-$ there appear two significant differences. First, the P_+ intensity appears to be shifted to a slightly higher mass. This is perhaps important in the physical interpretation. Clearly, the similarity between the different t' bins suggests that if the production mechanism changes at all, it does so very slowly. Therefore we would expect a resonance to appear in the same place in the two fits. This suggests that P_+ wave is not saturated by a resonance. This will be studied during the course of mass-dependent fits, discussed in Sec. 9. Secondly, the G_+ wave intensity looks very different in the two momentum transfer ranges. Actually, the interference terms are very stable, so one is left to assume that this difference in the intensity is due to an instability of the fit in this range due to the too-simple model, as was previously hinted at in the fits over the whole t' range.

As for what concerns the $\eta\pi^-$ data, there are again two striking differences. First, the $M = 2$ D_{++} wave is much more pronounced at higher values of t'. This will be quantified in the section on mass-dependent fits. Secondly, the interference between P_+ and D_+ wave changes between the two momentum transfer ranges. To be precise, in the interference plot, the minimum of the high-t' curve is much shallower than that of the low-t' curve. The P_+ wave intensity itself seems to be slightly lower in the high-t' range, but this difference appears to lie within error bars. Lastly, the unphysical G_+ wave intensity in the range of 1.3 GeV is not affected by the choice of t' bin, which is

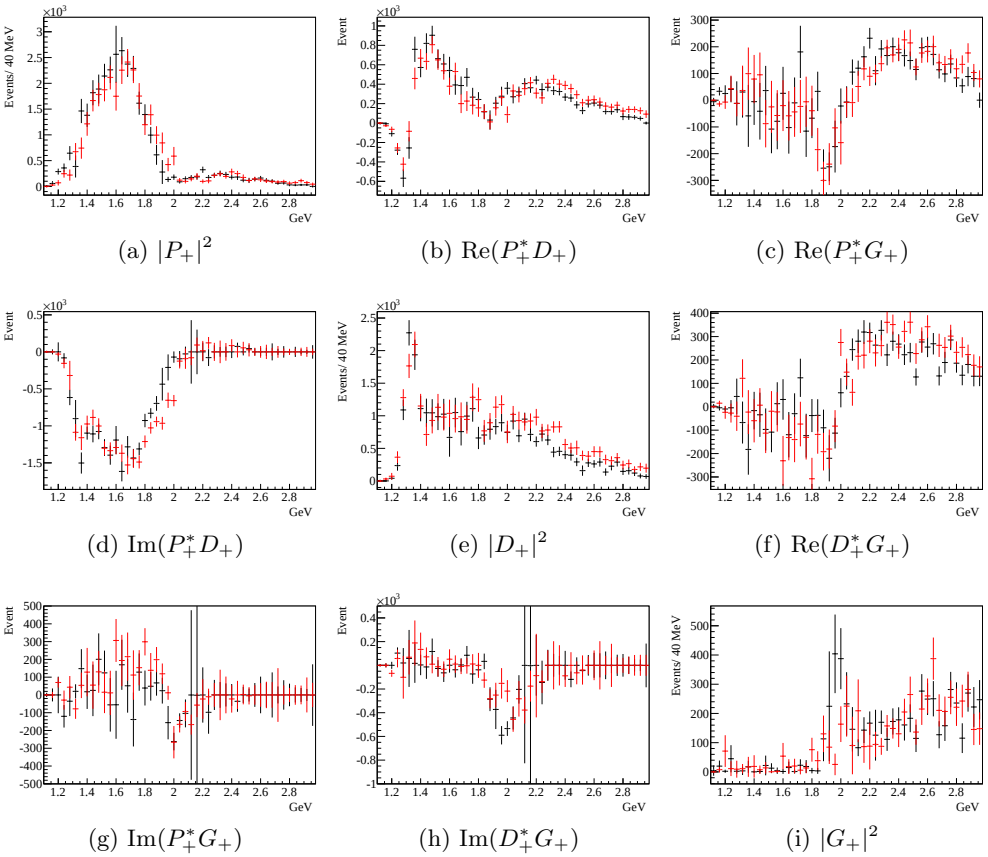

(a) $|P_+|^2$ (b) $\mathrm{Re}(P_+^* D_+)$ (c) $\mathrm{Re}(P_+^* G_+)$

(d) $\mathrm{Im}(P_+^* D_+)$ (e) $|D_+|^2$ (f) $\mathrm{Re}(D_+^* G_+)$

(g) $\mathrm{Im}(P_+^* G_+)$ (h) $\mathrm{Im}(D_+^* G_+)$ (i) $|G_+|^2$

Figure 8.8.: Natural parity waves in $\eta'\pi^-$ for low (black) and high (red) t' bins. Display as in Fig. 8.1.

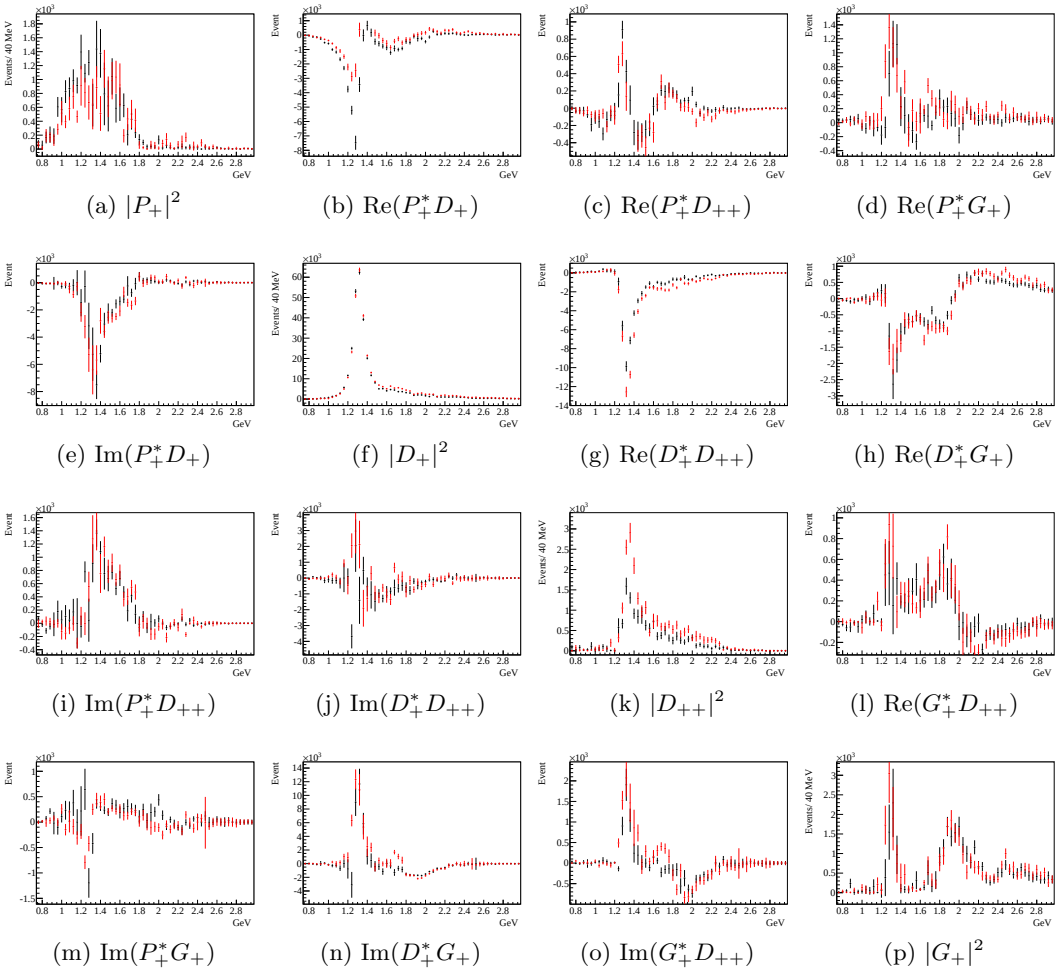

(a) $|P_+|^2$ (b) $\mathrm{Re}(P_+^* D_+)$ (c) $\mathrm{Re}(P_+^* D_{++})$ (d) $\mathrm{Re}(P_+^* G_+)$

(e) $\mathrm{Im}(P_+^* D_+)$ (f) $|D_+|^2$ (g) $\mathrm{Re}(D_+^* D_{++})$ (h) $\mathrm{Re}(D_+^* G_+)$

(i) $\mathrm{Im}(P_+^* D_{++})$ (j) $\mathrm{Im}(D_+^* D_{++})$ (k) $|D_{++}|^2$ (l) $\mathrm{Re}(G_+^* D_{++})$

(m) $\mathrm{Im}(P_+^* G_+)$ (n) $\mathrm{Im}(D_+^* G_+)$ (o) $\mathrm{Im}(G_+^* D_{++})$ (p) $|G_+|^2$

Figure 8.9.: Natural parity waves in $\eta\pi^-$ for low (black) and high (red) t' bins. Display as in Fig. 8.4.

a manifestation of the low dependence of the lab momenta on the initial momentum transfer.

8.5. Kinematic Validation

As discussed in Sec. 6.1, the quality of the fit can be assessed by comparing the predictions made by the fit with the real data. In Figs. 8.10 to 8.18, we show comparisons of a number of representative quantities in various mass ranges. The boundaries of the mass ranges are in sequence $(m_\pi + m_\eta)$ — $(m_\pi + m_{\eta'})$ — m_{a_2} — $(m_{a_2} + \Gamma_{a_2})$ — 1.6 GeV — 2 GeV. The range below the $\pi\eta'$ threshold is only shown for the $\pi\eta$ data. In each of the ranges, the same set of variables and is shown. The measured data are represented by black dots. The fit prediction is decomposed into the contributions of the three incoherent parts: the flat wave (green), the unnatural-parity waves (blue) and the natural-parity waves (red). The flat wave contributions is determined by the size of the window about the $\eta^{(\prime)}$ peak. Varying the size of this window showed no important effect on the physical waves. Statistical fluctuations are expected to be smaller in the Monte Carlo predictions than in the data, given that the Monte Carlo data sample is at least ten times larger than the real data sample in each mass bin. We briefly comment on the variables that are shown and explain their meaning:

(a): this is the distribution of the z coordinate of the primary vertices which are initially generated following a flat distribution over the target.

(b): distribution of the momentum transfer t' to the target.

(c): these show the invariant mass of the neutral three-body system $\pi^-\pi^+\pi^0$ or $\pi^-\pi^+\eta$ which contains the η or η', respectively. The flat wave does not have the three-body peak, whereas the natural and unnatural exchange waves do contain it. The quality of the description can therefore be assessed comparing the peak and its neighborhood.

(d), (e), (f): distributions of the momenta of the final state particles, $p(\eta)$, $p(\pi^+)$ and $p(\pi^-)$. Since there are two π^- in the final state, there are two entries per event in the $p(\pi^-)$ plots. Except for acceptance effects, this latter plot should consist of two components, one identical to the $p(\pi^+)$ distribution (which comes from the η, η' decay), the other coming from the accompanying π^- in $\pi^-\eta$, $\pi^-\eta'$.

(g), (h): distributions of the emission angles φ_{GJ}, $\cos\vartheta_{\mathrm{GJ}}$ of the η (η') in the $\pi^-\eta$ ($\pi^-\eta'$) rest systems. In order to uniquely identify the η (η') from the two possible combinations, a tighter window (± 20 MeV) has been applied before filling these plots. This explains the relatively smaller contribution of the flat wave compared to the other plots.

Note that the partial-wave amplitudes and therefore the fit are only sensitive to the angular distributions in the rest-frame of the mesonic system. This already explains the large deviation seen in the t' distribution: two things are at play. On the one hand, the

data was processed with no cut on the values of t' whereas the Monte Carlo generation only included $t' > 0.1\,\mathrm{GeV}^2$. Since the fit predicts the number of observed events the integrals of the data and fit distribution will match, blowing up the fit prediction histogram which only extends over a smaller range. No significant changes in the fit results were observed when only including data with $t' > 0.1\,\mathrm{GeV}^2$. On the other hand, the t' distribution appears steeper in the data than in the fit results. The t' distribution used in the generator was obtained by a fit to the complete data set, not taking any dependency on mass into account. As the t' distributions of the fit results approach the data closer for higher masses, it appears that the original extraction of the t' distribution was dominated by the high mass range (including data beyond the upper limit of these plots, 2 GeV). Monte Carlo studies showed no strong dependency of the acceptance on t' away from the trigger threshold [Diefenbach, 2011]. These two observations, together with the lack of direct dependence of the fit variables on t' then explain how these deviations can persist even in a good fit. For comparison, we show in App. E the same plots where in the fit the data were restricted to the range $0.1\,\mathrm{GeV}^2 < t' < 1\,\mathrm{GeV}^2$

For the $\pi\eta$ data the fit matches the data exceedingly well in the three central mass ranges. In the lowest bin shown in Fig. 8.10, one notes the large contribution of the flat wave. Looking at the $m(\pi^-\pi^+\pi^0)$ distribution, one notes a bump corresponding to the $\omega(782)$. The fit does not know about the ω and therefore doesn't model it. We verified by means of side-bin studies that its presence does not distort the η peak. Studies of mass spectra revealed the most likely origin of this contribution being the low-mass tail of the $b_1(1235)$ produced in the same final state by the reaction $\pi^- p \to b_1^- p$ with subsequent decays $b_1^- \to \pi^-\omega$ and $\omega \to \pi^-\pi^+\pi^0$. No comparable effect can be observed in the $\pi^-\eta'$ data where one could expect the $f_1(1285)$ to reflect in a similar way in the mass ranges of Figs. 8.17 and 8.18.

In the highest-mass $\pi\eta$ bin depicted in Fig. 8.14, one sees in the $p(\pi^-)$ distribution a contribution that is not accounted for where very fast π^- are emitted. It was shown in additional studies which are briefly discussed in Sec. 8.6.2, that these could be accommodated with additional high spin waves, namely the F_+ wave with $J^P = 3^-$ and by going up to spin six for the highest masses. The range where these contributions appear matches roughly what one sees in a double-Regge model for the case of $K\bar{K}$ production in $\pi^- p$ collisions, albeit at lower beam energy [Shimada et al., 1978]. Comparing to the corresponding mass range for $\pi\eta'$ in Fig. 8.18, one notes that this contribution does not stand out there. Again, studies that go beyond the scope of this thesis showed that the data could be better accommodated introducing an F_+ wave for $\pi^-\eta'$ masses above approximately 1.8 GeV. At even higher masses a similar high-momentum peak also appears in the $\pi^-\eta'$ data (not shown). These additional waves also remove the need for the unnatural exchange waves that become important at high masses, as seen for instance in Fig. 8.14h, where the unnatural wave intensity depicted in blue tries to make up for the incomplete description at the phase-space edges while the corresponding φ_{GJ} distribution shows no signs of deviating from a purely natural-parity distribution with a flat background.

One sees throughout that the η and η' peaks are nicely saturated by the fit, which illustrates that the background subtraction procedure works, and the description of the

η and η' resolution is accurate enough.

Comparisons of a few additional quantities, integrated over the whole mass range below 2 GeV are shown for $\pi^-\eta$ in Fig. 8.19 and for $\pi^-\eta'$ in Fig. 8.20. Again, data and fit are in very good agreement. Three remarks are in place concerning the plots showing the azimuthal emission angle of the recoil proton. First, this angle is not the discrete angle measured by the recoil proton detector but instead reconstructed from momentum conservation (formulae in App. C). Second, one part of the detector was excluded, as its response in terms of momentum transfer squared t was found to be different from the remainder of the detector, and no complete parameterization of the detector's performance was available in time for this thesis. Third, for the same reason a simple performance parameterization was extracted from the $\pi^-\eta$ data and also applied to the $\pi^-\eta'$ data, verifying its quality. The pictures show two features: a fast oscillation corresponding to the varying performance of the slabs of the recoil proton detector (which the aforementioned performance parameterization models), and a slow oscillation reflecting the shape of the spectrometer (which is taken into account by the usual Monte Carlo simulation). The recoil proton detector being an essential part of the trigger, the observed good agreement is very satisfying. Yet, given its importance even finer details should be taken into account. Work towards these ends was still ongoing by the time of completion of this thesis.

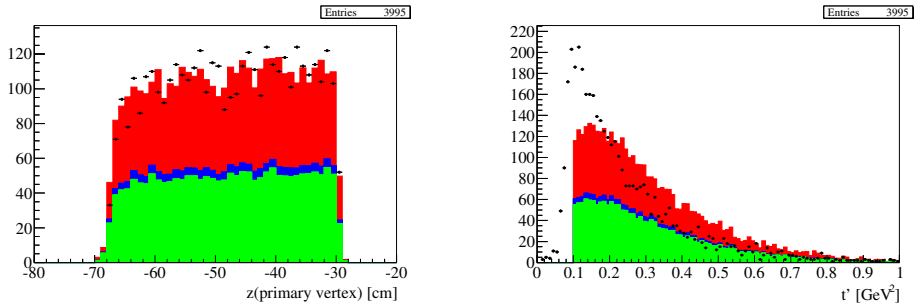

(a) z of primary vertex

(b) t'

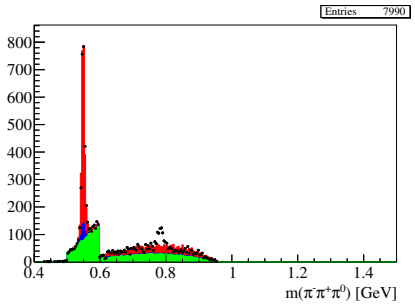

(c) $m(\pi^-\pi^+\pi^0)$ (two combinations)

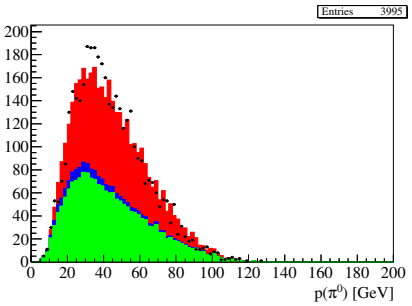

(d) $p(\pi^0)$

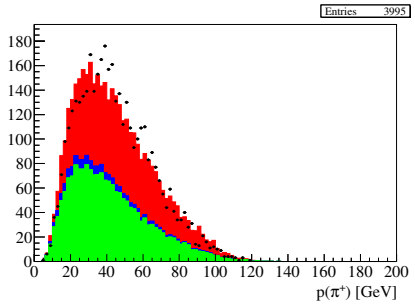

(e) $p(\pi^+)$

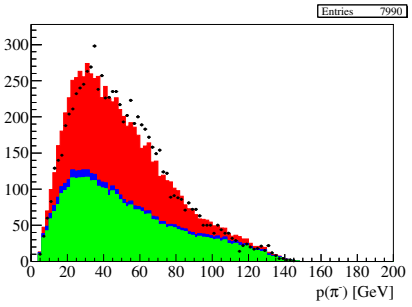

(f) $p(\pi^-)$ (two entries per event)

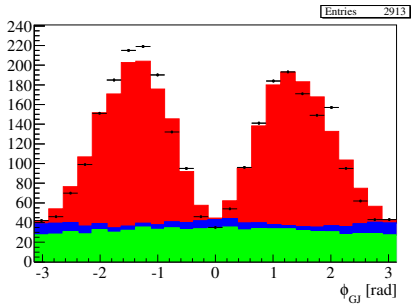

(g) φ_{GJ}

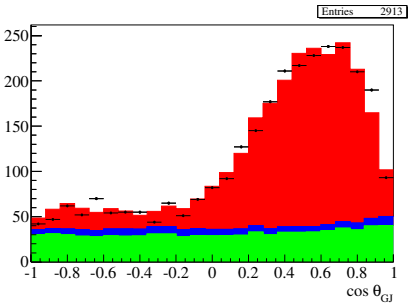

(h) $\cos\vartheta_{\mathrm{GJ}}$

Figure 8.10.: Comparison between $\pi^-\eta$ data and fit prediction for $m \in [m_\pi + m_\eta, m_\pi + m_{\eta'}] = [687\,\mathrm{MeV}, 1097\,\mathrm{MeV}]$. The data are represented by the black points. The (stacked) histograms illustrate the incoherent components of the fit result. In green the FLAT wave, in blue the unnatural exchange waves and in red the physical natural-parity waves. The sum of the three histograms should match the data.

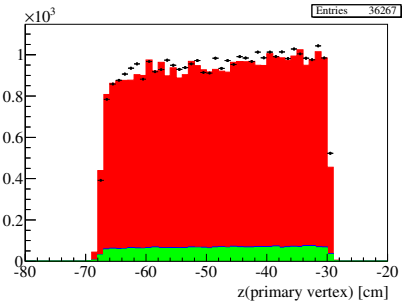

(a) z of primary vertex

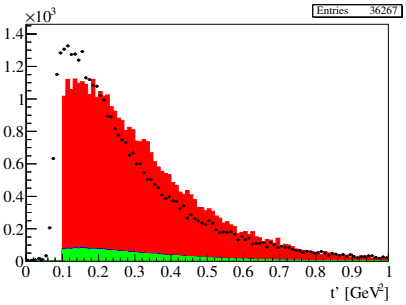

(b) t'

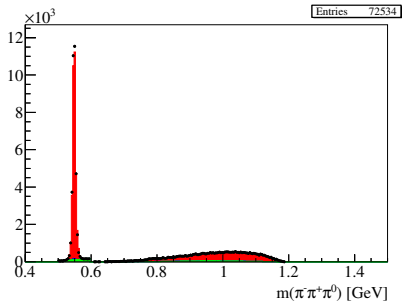

(c) $m(\pi^-\pi^+\pi^0)$ (two combinations)

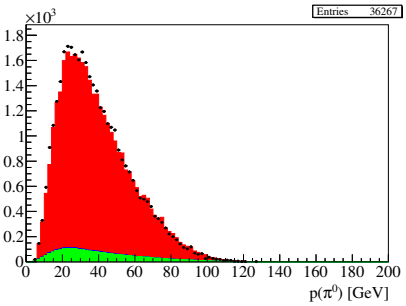

(d) $p(\pi^0)$

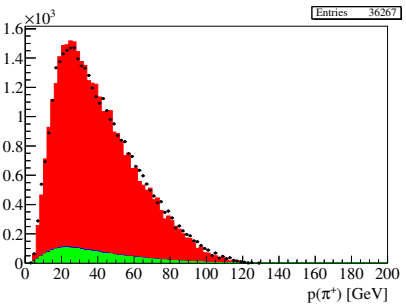

(e) $p(\pi^+)$

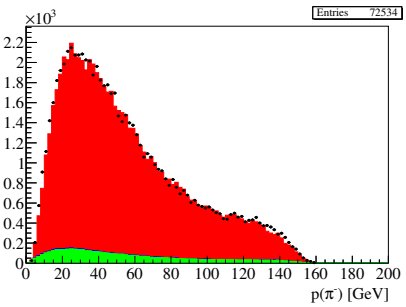

(f) $p(\pi^-)$ (two entries per event)

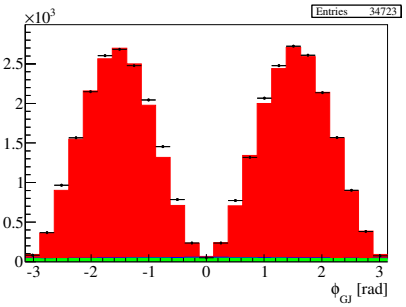

(g) φ_{GJ}

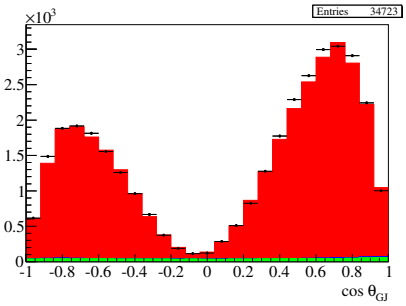

(h) $\cos\vartheta_{\mathrm{GJ}}$

Figure 8.11.: Comparison between $\pi^-\eta$ data and fit prediction for $m \in [m_\pi + m_{\eta'}, m_{a_2}] = [1097\,\mathrm{MeV}, 1318\,\mathrm{MeV}]$. Other details as in Fig. 8.10.

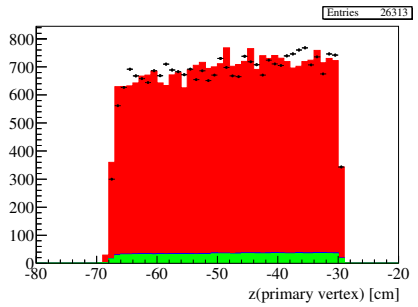

(a) z of primary vertex

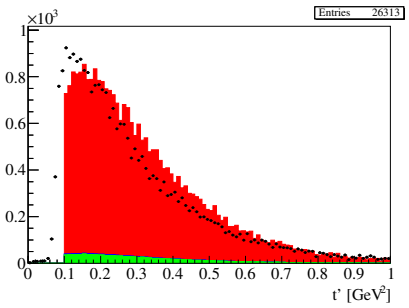

(b) t'

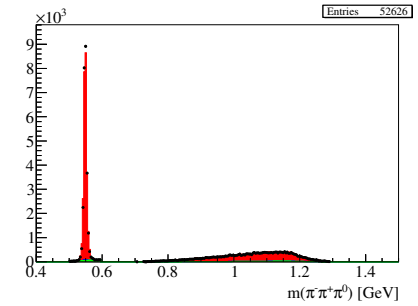

(c) $m(\pi^-\pi^+\pi^0)$ (two combinations)

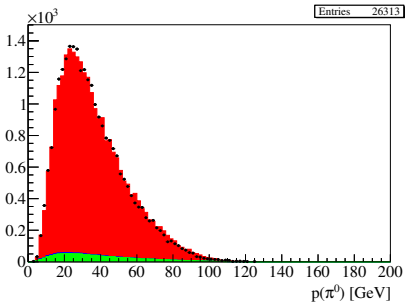

(d) $p(\pi^0)$

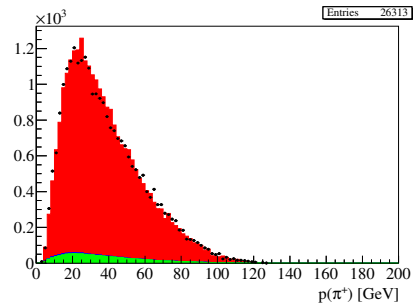

(e) $p(\pi^+)$

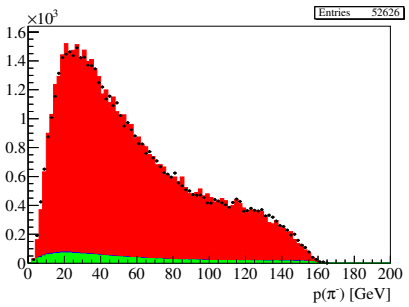

(f) $p(\pi^-)$ (two entries per event)

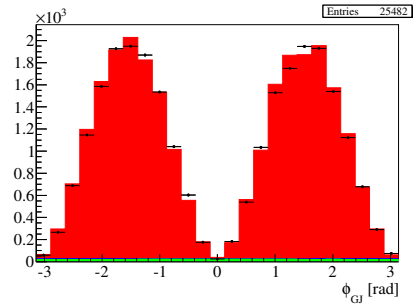

(g) φ_{GJ}

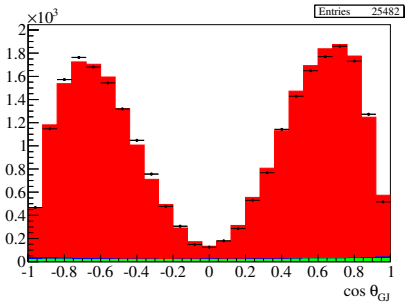

(h) $\cos\vartheta_{\mathrm{GJ}}$

Figure 8.12.: Comparison between $\pi^-\eta$ data and fit prediction for $m \in [m_{a_2}, m_{a_2}+\Gamma_{a_2}] = [1318\,\mathrm{MeV}, 1425\,\mathrm{MeV}]$. Other details as in Fig. 8.10.

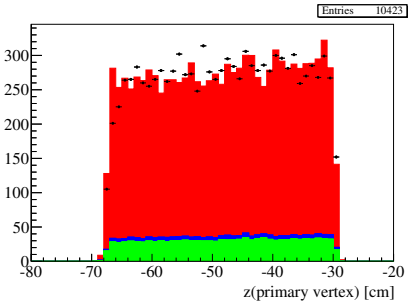

(a) z of primary vertex

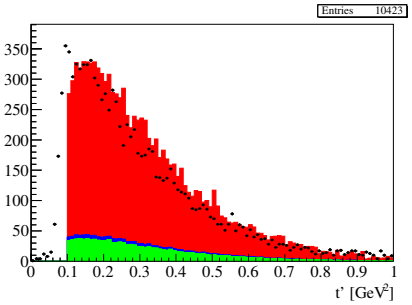

(b) t'

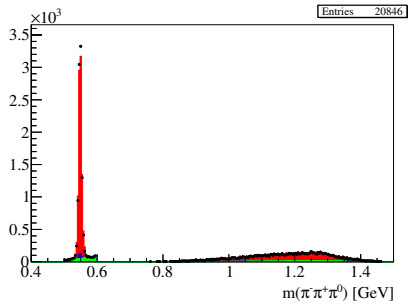

(c) $m(\pi^-\pi^+\pi^0)$ (two combinations)

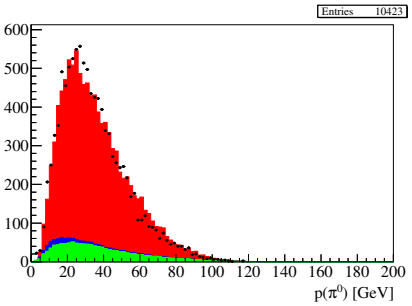

(d) $p(\pi^0)$

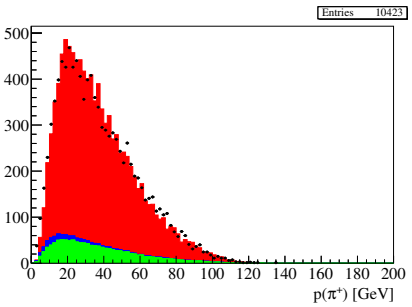

(e) $p(\pi^+)$

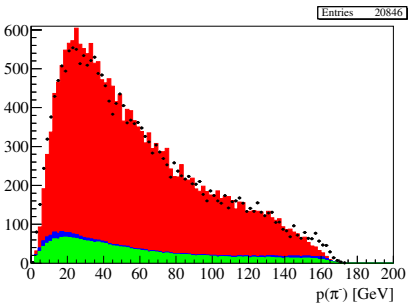

(f) $p(\pi^-)$ (two entries per event)

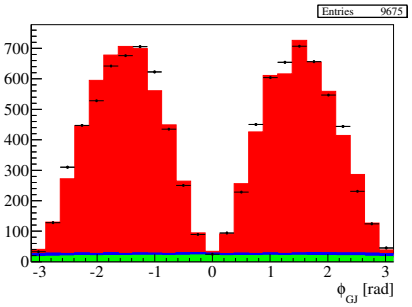

(g) φ_{GJ}

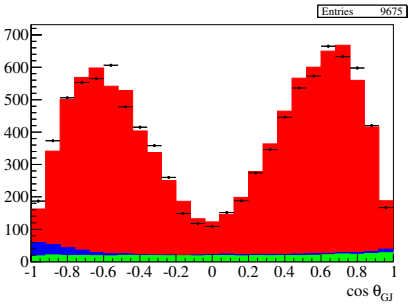

(h) $\cos\vartheta_{\mathrm{GJ}}$

Figure 8.13.: Comparison between $\pi^-\eta$ data and fit prediction for $m \in [m_{a_2} + \Gamma_{a_2}, 1.6\,\mathrm{GeV}] = [1425\,\mathrm{MeV}, 1600\,\mathrm{MeV}]$. Other details as in Fig. 8.10.

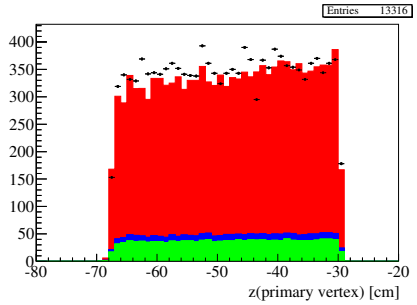

(a) z of primary vertex

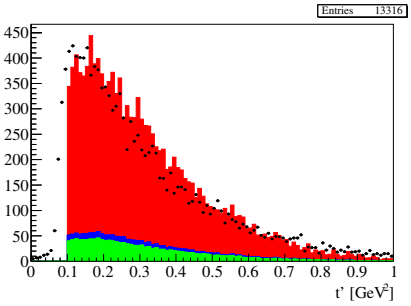

(b) t'

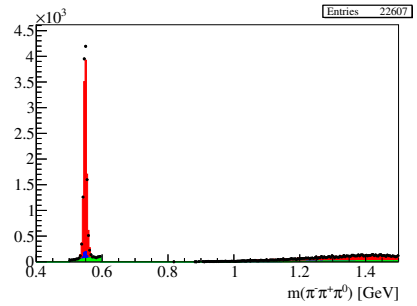

(c) $m(\pi^-\pi^+\pi^0)$ (two combinations)

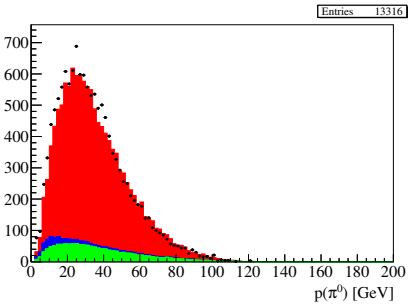

(d) $p(\pi^0)$

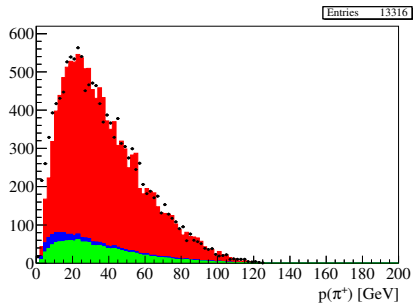

(e) $p(\pi^+)$

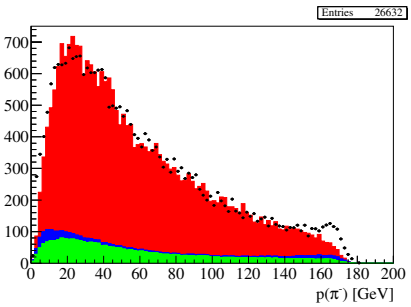

(f) $p(\pi^-)$ (two entries per event)

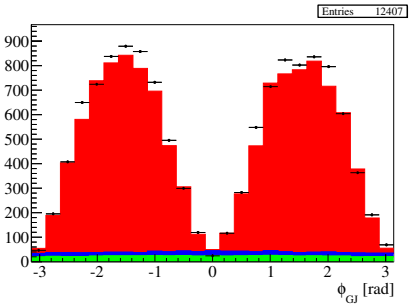

(g) φ_{GJ}

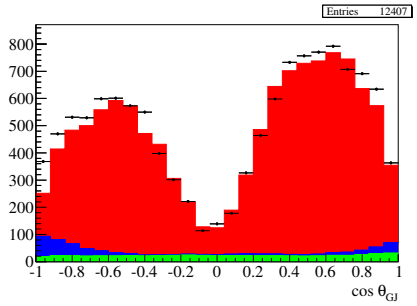

(h) $\cos\vartheta_{\mathrm{GJ}}$

Figure 8.14.: Comparison between $\pi^-\eta$ data and fit prediction for $m \in [1.6\,\mathrm{GeV}, 2\,\mathrm{GeV}]$. Other details as in Fig. 8.10.

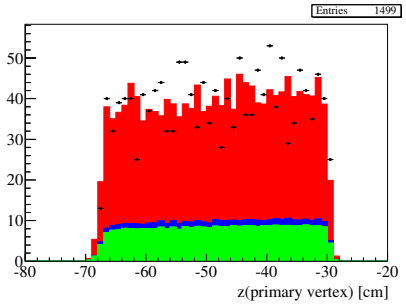

(a) z of primary vertex

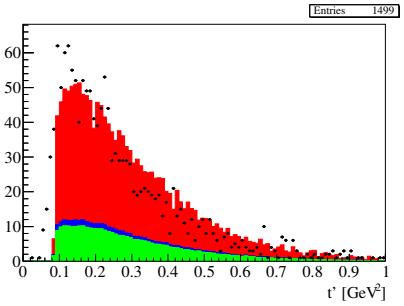

(b) t'

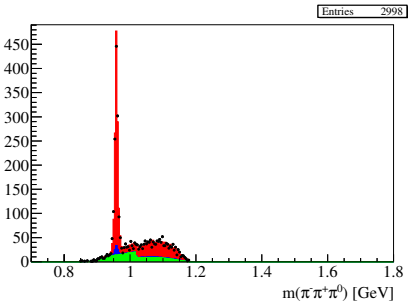

(c) $m(\pi^-\pi^+\eta)$ (two combinations)

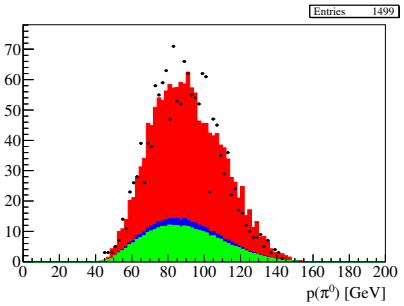

(d) $p(\eta)$

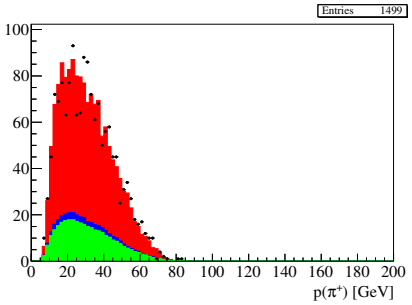

(e) $p(\pi^+)$

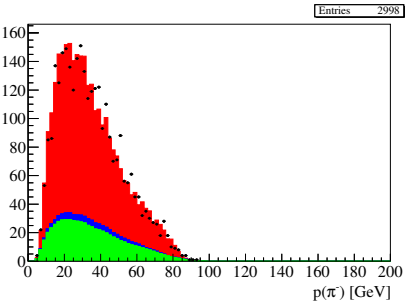

(f) $p(\pi^-)$ (two entries per event)

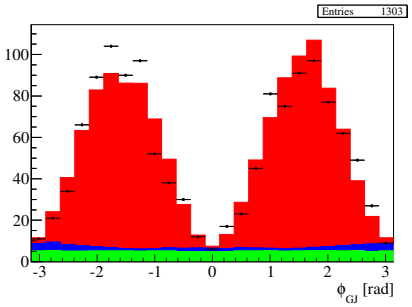

(g) φ_{GJ}

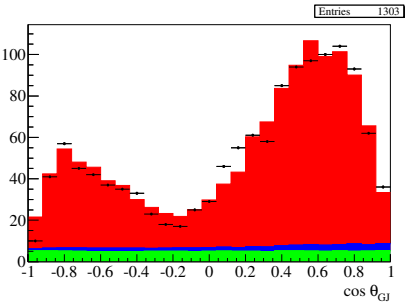

(h) $\cos\vartheta_{\mathrm{GJ}}$

Figure 8.15.: Comparison between $\pi^-\eta'$ data and fit prediction for $m \in [m_\pi + m_{\eta'}, m_{a_2}] = [1097\,\mathrm{MeV}, 1318\,\mathrm{MeV}]$. Other details as in Fig. 8.10.

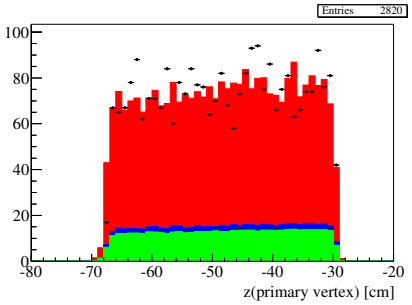

(a) z of primary vertex

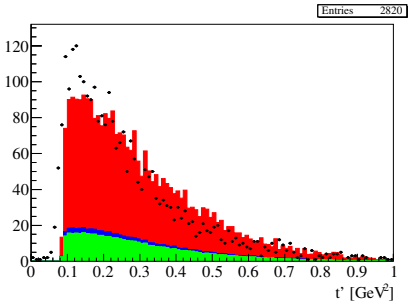

(b) t'

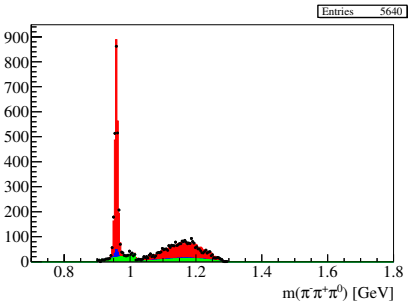

(c) $m(\pi^-\pi^+\eta)$ (two combinations)

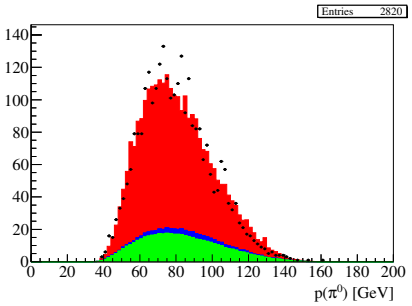

(d) $p(\eta)$

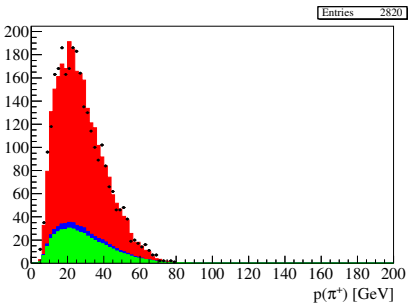

(e) $p(\pi^+)$

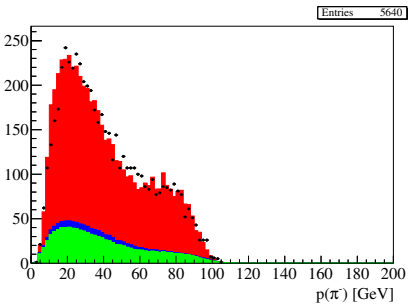

(f) $p(\pi^-)$ (two entries per event)

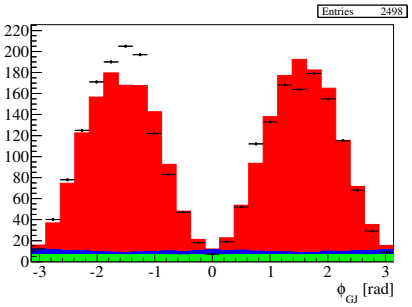

(g) φ_{GJ}

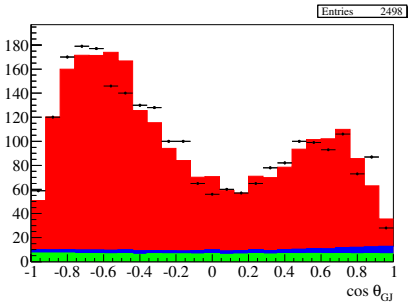

(h) $\cos\vartheta_{\mathrm{GJ}}$

Figure 8.16.: Comparison between $\pi^-\eta'$ data and fit prediction for $m \in [m_{a_2}, m_{a_2} + \Gamma_{a_2}] = [1318\,\mathrm{MeV}, 1425\,\mathrm{MeV}]$. Other details as in Fig. 8.10.

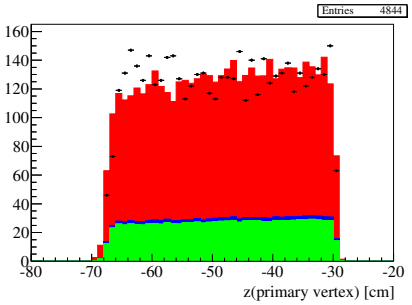

(a) z of primary vertex

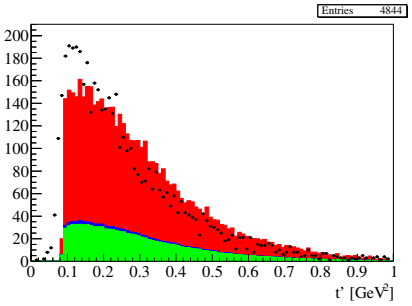

(b) t'

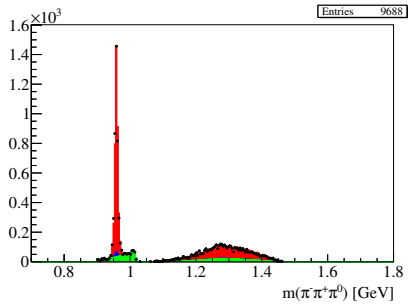

(c) $m(\pi^-\pi^+\eta)$ (two combinations)

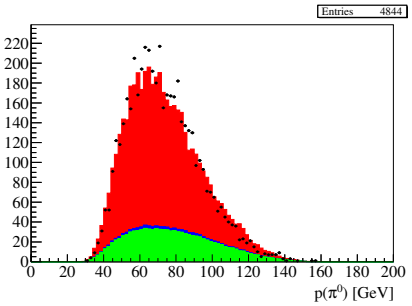

(d) $p(\eta)$

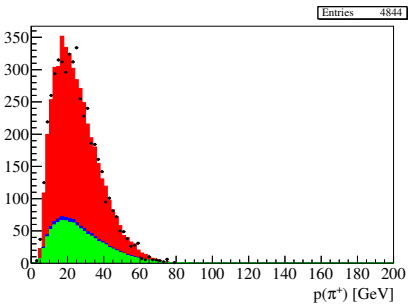

(e) $p(\pi^+)$

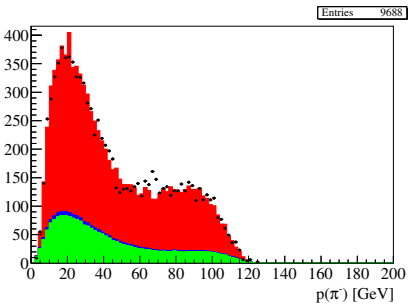

(f) $p(\pi^-)$ (two entries per event)

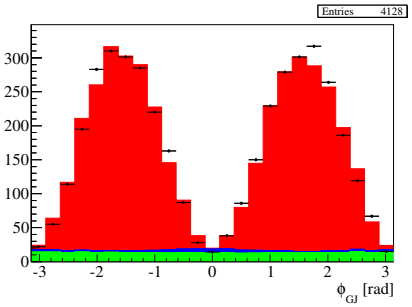

(g) φ_{GJ}

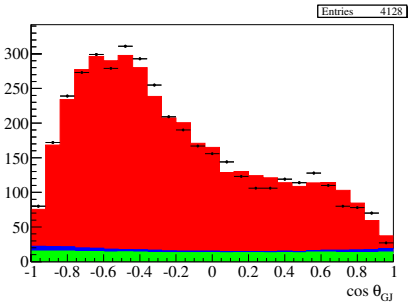

(h) $\cos\vartheta_{\mathrm{GJ}}$

Figure 8.17.: Comparison between $\pi^-\eta'$ data and fit prediction for $m \in [m_{a_2} + \Gamma_{a_2}, 1.6\,\mathrm{GeV}] = [1425\,\mathrm{MeV}, 1600\,\mathrm{MeV}]$. Other details as in Fig. 8.10.

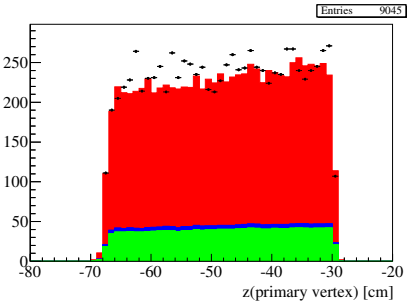

(a) z of primary vertex

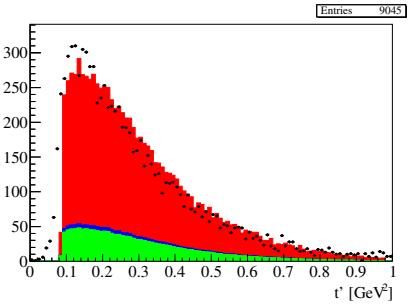

(b) t'

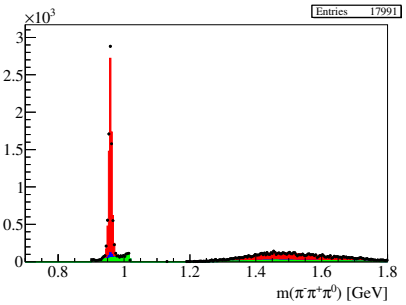

(c) $m(\pi^-\pi^+\eta)$ (two combinations)

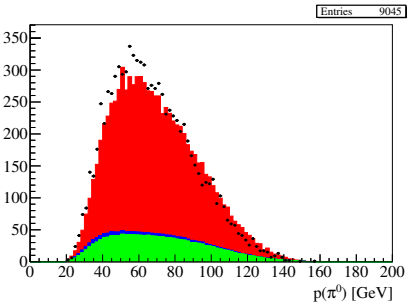

(d) $p(\eta)$

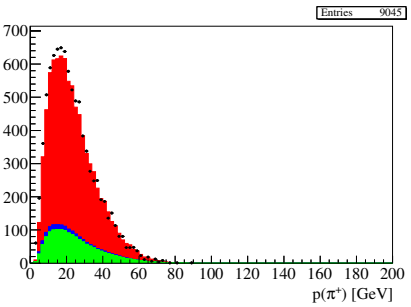

(e) $p(\pi^+)$

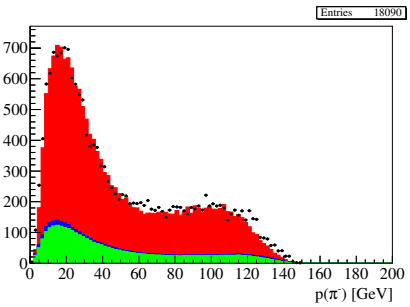

(f) $p(\pi^-)$ (two entries per event)

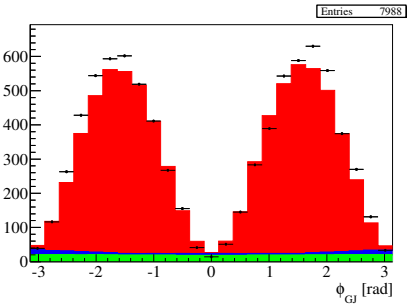

(g) φ_{GJ}

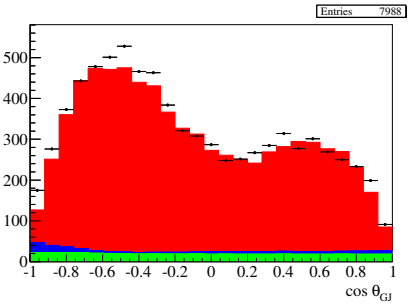

(h) $\cos\vartheta_{\mathrm{GJ}}$

Figure 8.18.: Comparison between $\pi^-\eta'$ data and fit prediction for $m \in [1.6\,\mathrm{GeV}, 2\,\mathrm{GeV}]$. Other details as in Fig. 8.10.

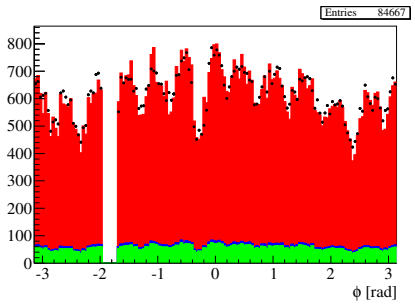

(a) Azimuthal emission angle of the recoil proton

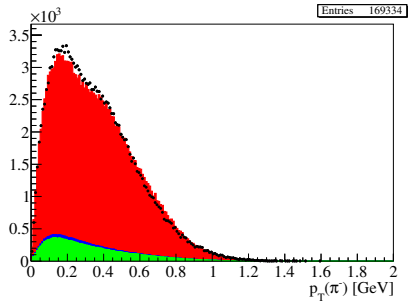

(b) Transverse momentum of the π^- (two entries per event)

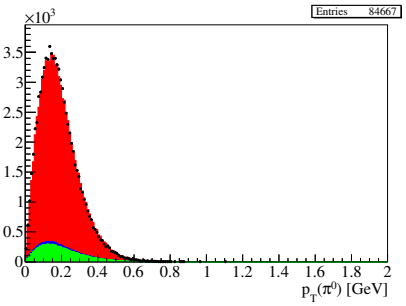

(c) Transverse momentum of the π^0

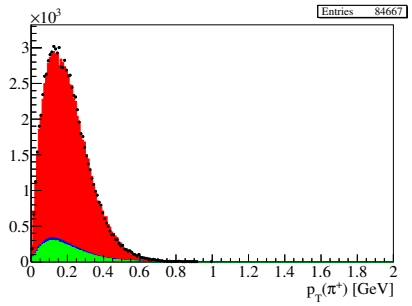

(d) Transverse momentum of the π^+

Figure 8.19.: Comparison between $\pi^-\eta$ data and fit prediction for additional quantities for $m(\pi^-\eta) < 2\,\text{GeV}$. Color code as in Fig. 8.10.

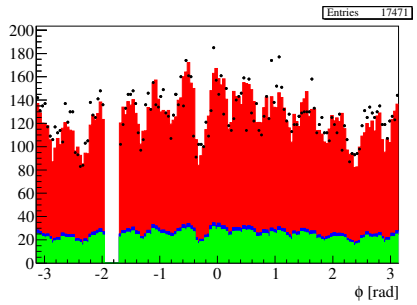

(a) Azimuthal emission angle of the recoil proton.

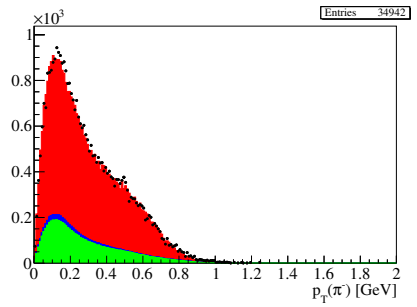

(b) Transverse momentum of the π^- (two entries per event)

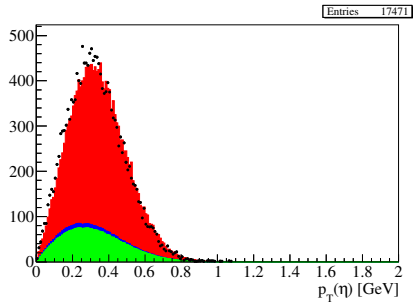

(c) Transverse momentum of the η

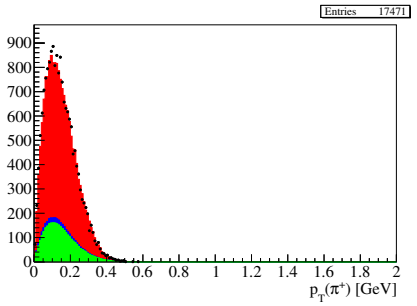

(d) Transverse momentum of the π^+

Figure 8.20.: Comparison between $\pi^-\eta'$ data and fit prediction for additional quantities for $m(\pi^-\eta') < 2\,\text{GeV}$. Color code as in Fig. 8.10.

8.6. Alternative Combinations of Waves

8.6.1. The Low-Mass G_+ Wave in $\eta\pi^-$

The fits we showed previously in Fig. 8.1 show an unphysical enhancement in the 4^{++} G_+ wave near 1.3 GeV, where the dominant D_+ wave peaks. In order to study the origin of this contribution, we performed fits where this wave was not made available to the fits in the mass bins below 1.5 GeV. The effect of this can be seen in Fig. 8.21. The sharp unphysical structure previously visible in the G_+ wave now settles on the 1^{-+} wave, while not affecting its phase relative to the D_+ wave significantly. Studies of photon impact points in the electromagnetic calorimeters lead to the conclusion that this leakage is caused by an incomplete description of the acceptance of the very populated central region of the forward electromagnetic calorimeter ECAL2. Since a new production of the data was underway by the time of the finishing of this thesis, further studies were delayed until this new production with rewritten calorimeter code becomes available.

8.6.2. Fits With Higher Spins

Already in the discussion of the kinematic validation, we mentioned the necessity for higher-spin contributions. These are expected to appear due to the presence of non-resonant contributions which clearly dominate the high-mass range and which, when decomposed into partial waves will populate several partial waves. Additionally, previous analyses of related reactions, such as $\pi^- p \to K^- K^0_S p$ in Ref. [Cleland et al., 1982a; Martin et al., 1978], showed such contributions.[2] In general, they pose several problems. First, the ambiguities discussed in Sec. 7.2 need to be resolved. In principle, these ambiguities affect data with only natural-parity contributions when spins of at least three units of angular momentum are included [Chung, 1997]. Yet, they didn't arise so far because even though we introduced the G_+ wave with $J = 4$, we didn't also introduce the spin-three F_+ wave. The resulting set, not forming a complete basis, is unambiguous. Still, there are several indications that further contributions are needed for the fit presented in this work. First, it shows slight instabilities: for instance the jump in the G_+-wave intensity near 2 GeV in Fig. 8.1, where a slight change in the acceptance description could make the intensity in that bin appear in the P_+ wave

[2] Due to the background subtraction needed in our analysis, their technique of moment analysis using a linear-algebra technique for acceptance correction cannot be applied to our analysis. This moments technique is based on the observation that the observed intensity is the product of the spectrometer acceptance function and the intensity expected without any detector acceptance effects, i.e. the acceptance corrected intensity distribution which contain the actual physics information. Moments here refers to the standard technique of decomposing a function on the sphere in terms of spherical harmonics. Inserting the moments decomposition of the unknown acceptance-corrected intensity and of the known acceptance function into the equation for the moments decomposition of the observed intensity, $H_{\text{observed}}(LM) = \int \mathrm{d}\Omega\, Y_M^{L*}(\vartheta_{\text{GJ}}, \varphi_{\text{GJ}}) I_{\text{observed}}(\vartheta_{\text{GJ}}, \varphi_{\text{GJ}})$, the integral can be evaluated with standard formulae, and one obtains a matrix relation between the observed moments and the acceptance corrected, expected moments. Inverting this matrix then allows extraction of the acceptance corrected moments. The moments are related to the partial waves by quadratic equations. The ambiguities discussed in Sec. 7.2 appear during the solution of these equations.

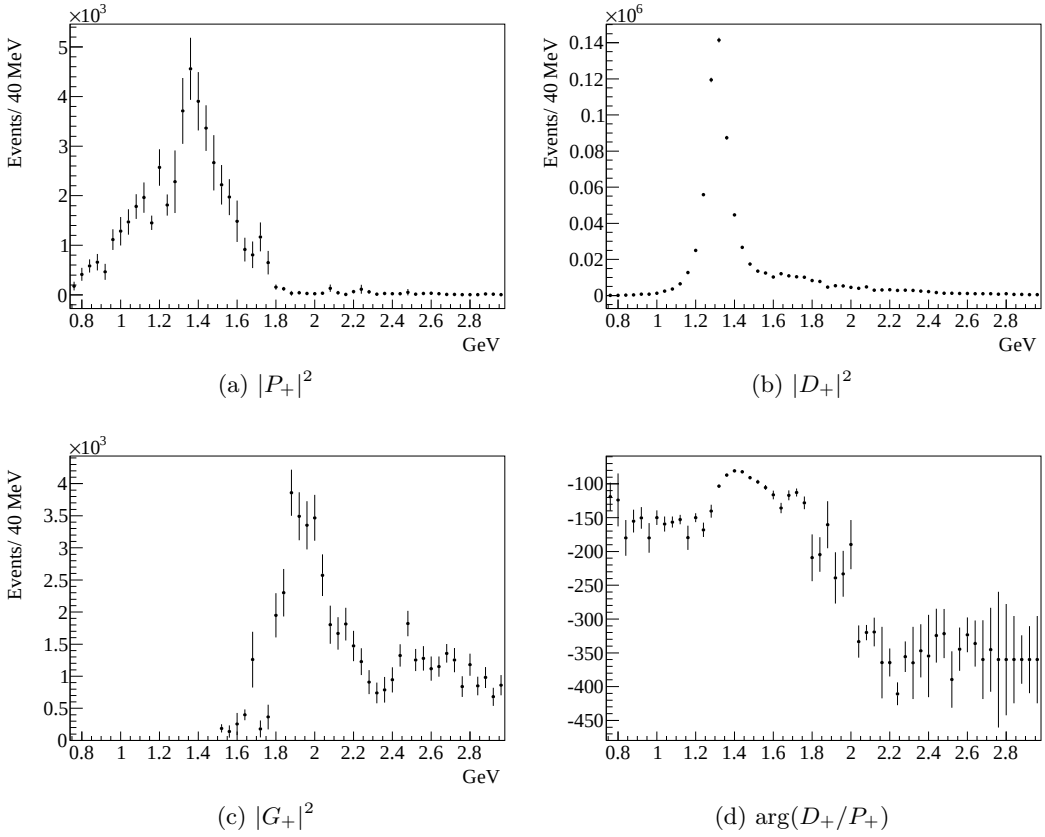

(a) $|P_+|^2$ (b) $|D_+|^2$

(c) $|G_+|^2$ (d) $\arg(D_+/P_+)$

Figure 8.21.: Results of fits to the $\eta\pi^-$ system with the 4^{++} wave introduced only above 1.5 GeV. One sees that the leakage around 1.3 GeV previously observed in the 4^{++} wave now has moved to the 1^{-+} wave. The phase motion between P_+ and D_+, on the other hand, is fairly resilient to this problem. The G_+ wave has changed only insofar, as it is now zero below 1.5 GeV.

instead. Secondly, we have also seen in Sec. 8.5 that the description of the data cannot reproduce all kinematic features.

We thus extended the fit to include the F_+ wave for invariant masses above 1.5 GeV (for $\eta\pi^-$) and above 1.8 GeV (for $\eta'\pi^-$), and the spin-five H_+ wave together with the spin-six I_+ wave above 2.3 GeV. These ranges were suggested by the induced change in the log-likelihood function: inclusion below these limits lead to no significant change in the log-likelihood function. I.e. the price of introducing the ambiguities was not justified by an increased quality of the fit. On the other hand, above these limit significant changes in the value of the log-likelihood function were observed.

We will only show the intensities of the various waves. The ambiguity was resolved by choosing the solution found with the smallest intensity for the F_+ wave. This way the results most closely resemble the fit results given previously.[3] We show the results for the $\pi^-\eta$ channel in Fig. 8.22 and for the $\pi^-\eta'$ channel in Fig. 8.23. We see large error bars in the bins containing the thresholds for the additional waves, probably due to a misalignment between the mass bins and the threshold values. In the $\eta'\pi$ we see that the 4^{++} wave has stabilized, the jump at 2 GeV has disappeared. Also, this wave rises much slower at high masses compared to the previous fits. In the $\eta\pi$ data no significant changes can be observed. In both cases the unnatural parity exchange waves become compatible with zero (not pictured), illustrating their unphysical character and justifying their omission in future analysis.

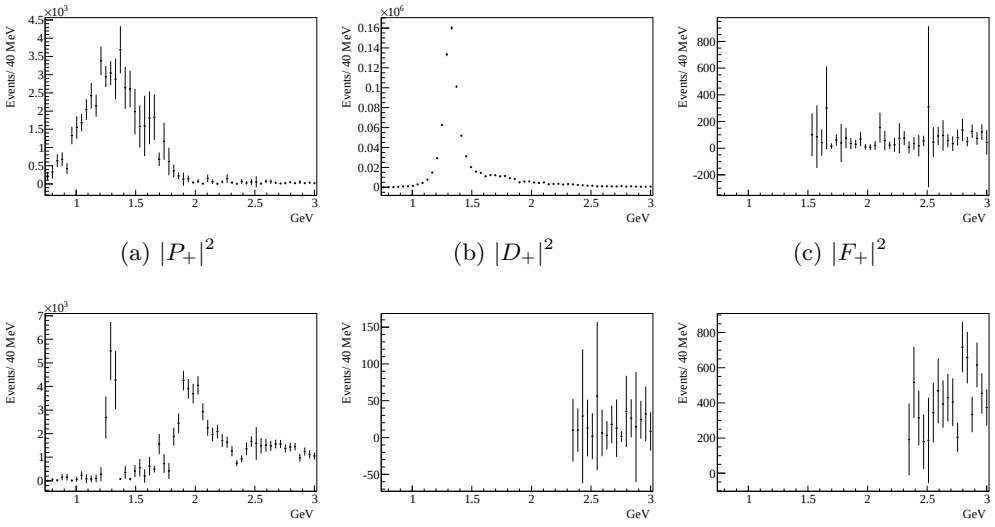

(a) $|P_+|^2$ (b) $|D_+|^2$ (c) $|F_+|^2$

(d) $|G_+|^2$ (e) $|H_+|^2$ (f) $|I_+|^2$

Figure 8.22.: Intensitis of natural-parity waves for the $\eta\pi^-$ data when including additional waves (see text).

[3]This approach was developed by D. Ryabchikov.

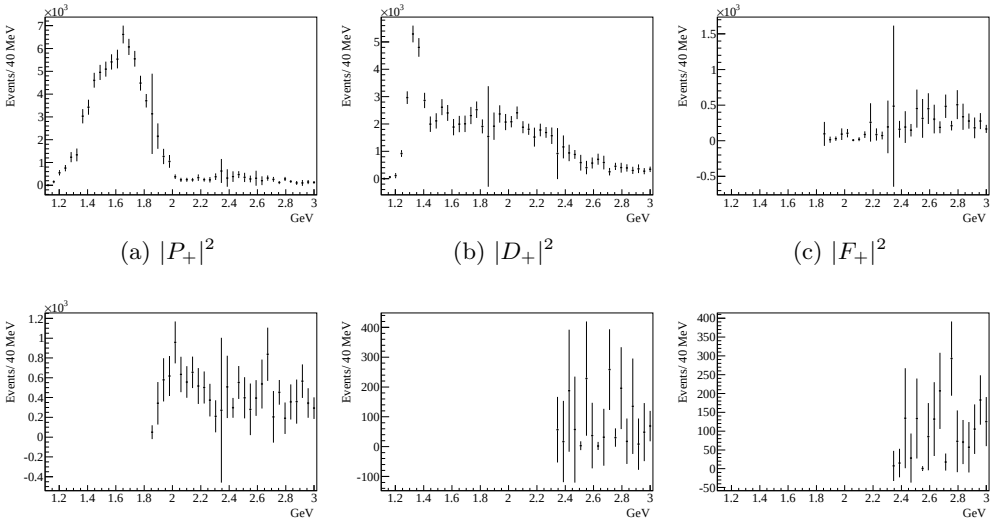

(a) $|P_+|^2$ (b) $|D_+|^2$ (c) $|F_+|^2$

(d) $|G_+|^2$ (e) $|H_+|^2$ (f) $|I_+|^2$

Figure 8.23.: Intensitis of natural-parity waves for the $\eta'\pi^-$ data when including additional waves (see text).

8.7. Comparison Between Different Approaches to the Partial-Wave Analysis

As discussed in Sec. 7, our main analysis was done with a program taking the complete four-body dynamics of the $\pi^-\pi^+\pi^-\eta$ or, respectively, $\pi^-\pi^+\pi^-\pi^0$ final-state into account in order to extract background contributions that cannot be attributed to the $\pi^-\eta'$ or $\pi^-\eta$ final states. Nevertheless, we pursued the analysis in parallel with a homegrown program that only takes the two-body final-state into account. This was done both to ensure our understanding of the procedure and to verify the results obtained in the more complicated approach.

In this section we shall briefly present a comparison of the results obtained with both programs. Since the Monte Carlo simulation is not exchangeable between both programs, and since we didn't want to waste CPU time, not all refinements have gone into the Monte Carlo simulations pursued for the two-body analysis. So besides differences due to the subtracted background in the four-body analysis, we also expect differences stemming from this. Additionally, bins were offset by 5 MeV, which facilitates simultaneous plotting.

We show in Fig. 8.24 the results for the intensities of the natural-parity waves from the LMU program overlaid in red on the results from the Protvino program. The programs agree on all the main features, even the error bars come out comparable in size. Besides a small difference in the total number of events extracted from the fit, the most significant difference is the different choice of value in the aforementioned unstable bin at 2 GeV: here, the LMU program chose to shift intensity from the G_+ wave into the P_+ wave, which

intuitively coincides with the observation discussed in Sec. 8.6.2 that the introduction of the F_+ wave stabilizes this region. Likewise, in Fig. 8.25 we compare the phases. Again, the different programs coincide very well. Deviations in the phases relative to the G_+ wave at low-masses are expected, as intensities are very low in that range. Again, we observe the jump near 2 GeV, and again the solution from the LMU program is discontinuous.

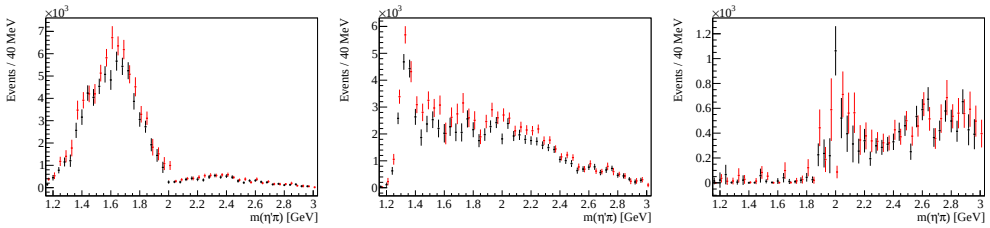

(a) $|P_+|^2$ (b) $|D_+|^2$ (c) $|G_+|^2$

Figure 8.24.: Intensities of the natural-parity waves extracted with the Protvino program (black) and the LMU program (red) for the $\pi^-\eta'$ data.

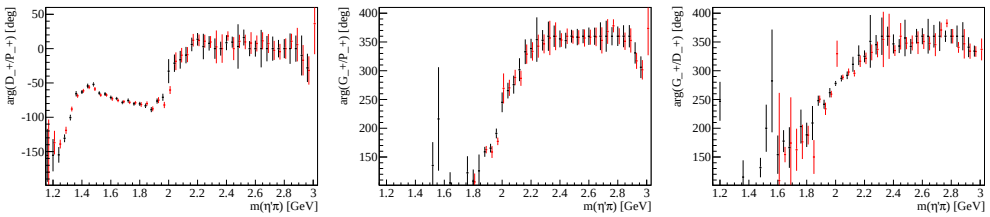

(a) $\arg(D_+/P_+)$ (b) $\arg(G_+/P_+)$ (c) $\arg(G_+/D_+)$

Figure 8.25.: Relative phases of the natural-parity waves extracted with the Protvino program (black) and the LMU program (red) for the $\pi^-\eta'$ data.

We show the same kind of comparison for the $\pi^-\eta$ data. Since we didn't have the same data set available for the LMU program as was used with the Protvino program, the intensities returned from the LMU program are rescaled with a factor two to roughly match the results obtained with the Protvino program. This explains the larger (statistical) error bars on the fit results from the LMU program. The intensities are shown in Fig. 8.24. Except for different behavior with respect to the leakage from the $a_2(1320)$, the agreement is very good. The same can be said for the relative phases, except for a slight disagreement on the rising edge of the $a_2(1320)$.

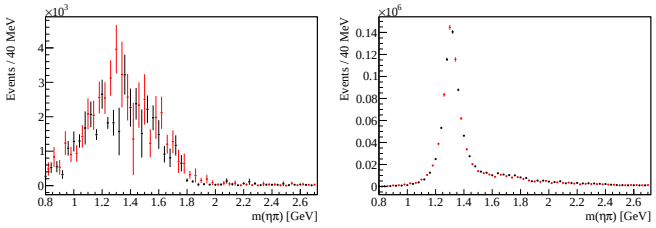

(a) $|P_+|^2$ (b) $|D_+|^2$

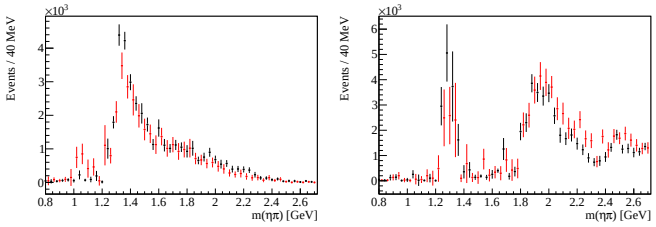

(c) $|D_{++}|^2$ (d) $|G_+|^2$

Figure 8.26.: Intensities of the natural-parity waves extracted with the Protvino program (black) and the LMU program (red) for the $\pi^-\eta$ data.

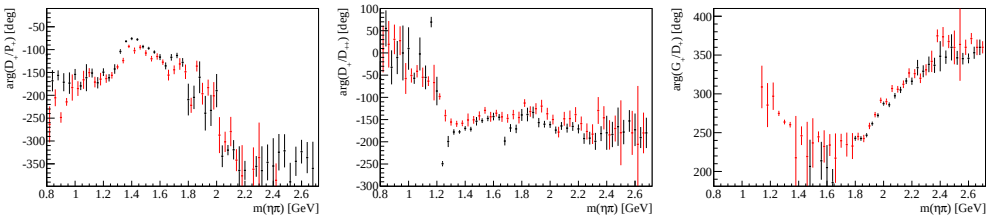

(a) $\arg(D_+/P_+)$ (b) $\arg(D_+/D_{++})$ (c) $\arg(G_+/D_+)$

Figure 8.27.: Relative phases of the natural-parity waves extracted with the Protvino program (black) and the LMU program (red) for the $\pi^-\eta$ data.

9. Mass-dependent Fits

The mass-dependent fit offers an interpretation of the data by fitting a physical model to the results obtained in the mass-independent fit. From the remarks in Sec. 7.2, it is clear that the relative phases have to be taken with a grain of salt. This is further supported by the observations made during the comparison of the relative phases obtained in the $\pi^-\eta$ and $\pi^-\eta'$ data in Sec. 8.3. Nevertheless, in order to reproduce the steps taken by previous analyses, we assume the data to be fully coherent, and therefore the phase motions to give an accurate picture of the physics. In order to avoid the sign ambiguity in the relative imaginary parts and therefore the phases, we fit the intensities and relative real parts of the waves with Breit-Wigner functions of the form described in App. F.

9.1. Mass-dependent Fit of the $\eta\pi^-$ System

Here we set out to fit the results from the mass-independent partial-wave fit to the $\pi^-\eta$ system shown in Sec. 8.2, thus finding an economical, simultaneous description of the D_+, D_{++}, P_+ and G_+ waves, where we additionally demand that the resonances appearing in the D_+ and D_{++} waves be the same.

In Fig. 9.1 we show results from the fit to the D_+ and D_{++} waves. The ingredients used for the fit of these waves are:

- A dynamical Breit-Wigner which takes the spin and known branchings of the $a_2(1320)$ into account. The same BW is used for both the $M = 1$ and $M = 2$ wave. (Shown in black.)
- A Breit-Wigner function for a second 2^{++} resonance. The same Breit-Wigner function is used for both the $M = 1$ and $M = 2$ wave. (Shown in green.)
- An exponential background of the shape $\exp(-\alpha q^2)$ where α is a fit parameter and q is the break-up momentum. These are separately fitted for the two waves. (Shown in cyan. The sum of the cyan and green curves taking into account interference, is shown in magenta.)
- The Breit-Wigners and backgrounds are multiplied by phase-space factors which include the angular-momentum barriers (these are already included in the formulae of App. F.) Since the same Breit-Wigner functions are used in the description of the D_+ and D_{++} waves, they are also multiplied with the same phase-space factors.

In Fig. 9.2, we show the corresponding results for the D_+ and P_+ waves from the same fit. The P_+ wave is fitted with one Breit-Wigner (magenta) and a background as before

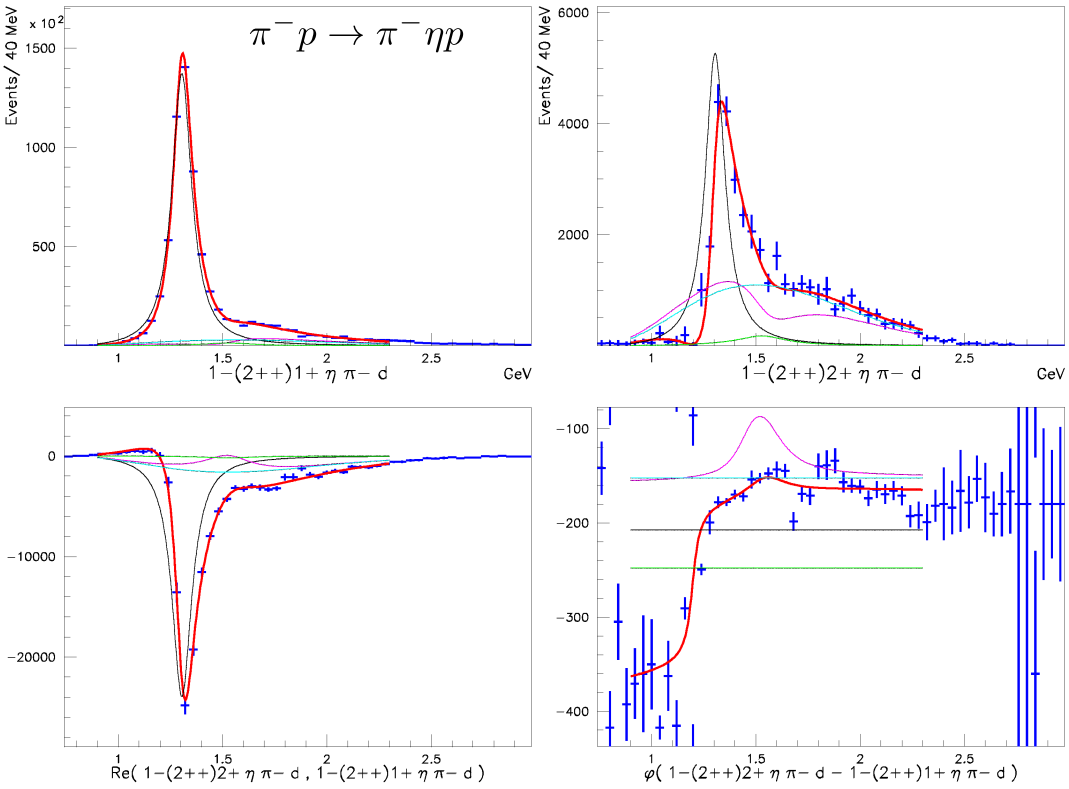

Figure 9.1.: Mass-dependent fit to $\eta\pi$ showing the fit of the $M = 1$ and $M = 2$ components D_+ and D_{++}. The plots show from left to right, from top to bottom: the D_+ intensity, the D_{++} intensity, $\mathrm{Re}(D^*_{++}D_+)$, the relative phase $\arg(D_{++}/D_+)$. The full fit is depicted by the thick red line, for the other colors, see text.

(green). One notes that the Breit-Wigner function is shifted to higher masses compared to the data points. Constructive and destructive interference with the background accounts for this, in a way similar to a model where the observation of a $\pi(1400)$ in the $\eta\pi$ final state was explained as the interference of the $\pi(1600)$ observed in other final states with a non-resonant background [Donnachie and Page, 1998]. Leaving aside the interpretation, this is due to the small error bars of the almost vanishing P_+ intensity near 2 GeV (Fig. 9.2). Any deviations there blow up the χ^2 function calculated during the fit. Therefore destructive interference between the resonance and the background increases the χ^2 value significantly. Future analysis would have to revisit this aspect. Including the F_+ and other higher waves may also lead to small modifications.

Finally, in Fig. 9.3 we show the remaining wave, the G_+ wave where the $a_4(2040)$ shows up. It is accompanied by a background which rises very rapidly at very high

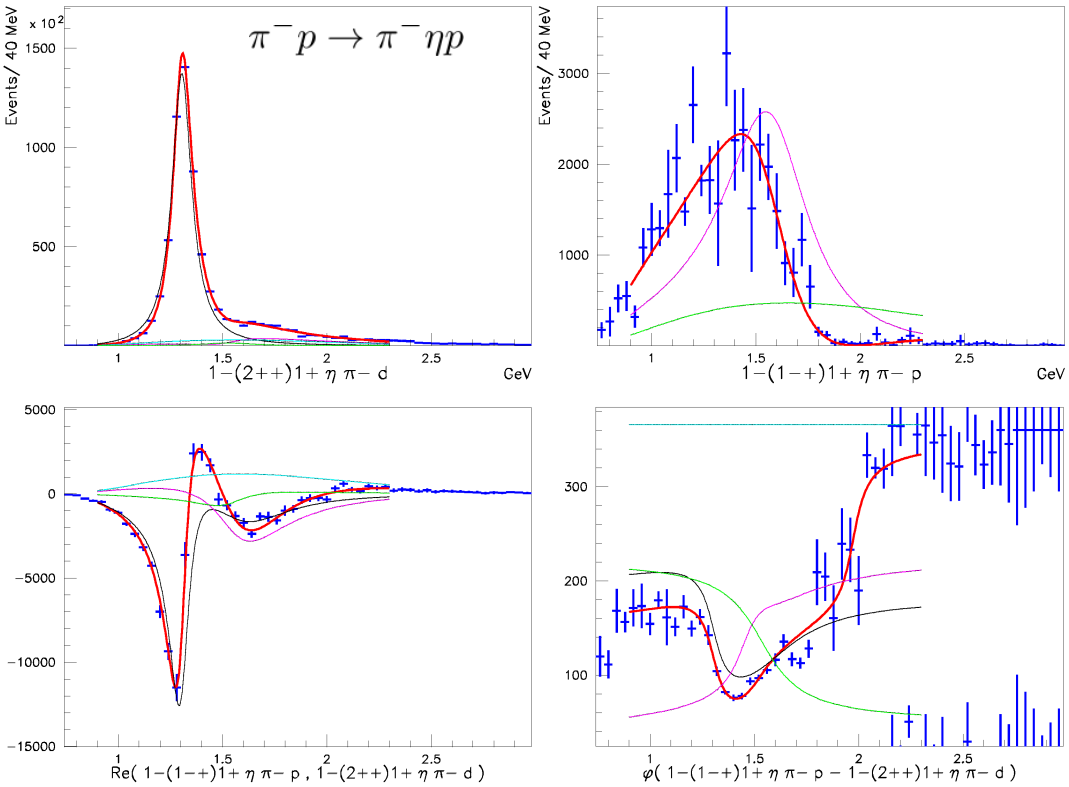

Figure 9.2.: Mass-dependent fit to $\eta\pi$ showing the fit of the D_+ and P_+ waves. The plots show from left to right, from top to bottom: the D_+ intensity (same as in Fig. 9.1), the P_+ intensity, $\mathrm{Re}(P_+^* D_+)$, $\mathrm{Im}(P_+^* D_+)$, and the relative phase $\arg(P_+/D_+)$. The full fit is depicted by the thick red line, for the other colors, see text.

masses but which remains well-contained within the fit range.

We omit showing the intereference terms between the subdominant waves P_+, D_{++}, G_+. Suffice to say that the fit manages to describe all of them with quality comparable to what was shown before. A mass-dependent fit that didn't include the D_{++} yields very similar results.

The numerical results of the fit are summarized in Tab. 9.1. The different waves were included in the following ranges:

$$\begin{aligned} D_+ &: \quad 0.9 < m < 2.3\,\mathrm{GeV} \\ D_{++} &: \quad 1.2 < m < 2.3\,\mathrm{GeV} \\ P_+ &: \quad 0.9 < m < 2.3\,\mathrm{GeV} \\ G_+ &: \quad 1.6 < m < 2.3\,\mathrm{GeV} \end{aligned}$$

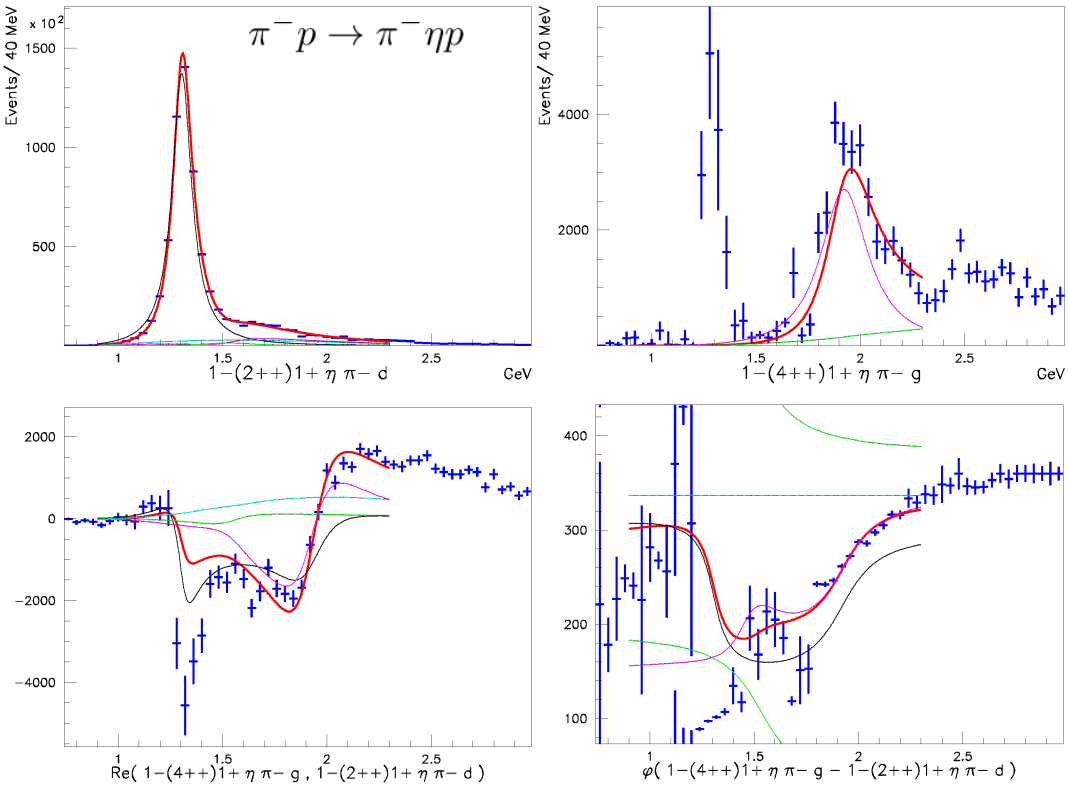

Figure 9.3.: Mass-dependent fit to $\eta\pi$ showing the fit of the D_+ and G_+ waves. The plots show from left to right, from top to bottom: the D_+ intensity (same as in Fig. 9.1), the G_+ intensity, $\mathrm{Re}(G_+^* D_+)$, the relative phase $\arg(G_+/D_+)$. The full fit is depicted by the thick red line, for the other colors, see text.

Additionally, the data was binned in two bins in the momentum transfer t' with approximately identical content, $0.1\,\mathrm{GeV}^{-2} < t' < 0.25\,\mathrm{GeV}^{-2}$ and $0.25\,\mathrm{GeV}^{-2} < t' < 1.0\,\mathrm{GeV}^{-2}$, and the data then was fitted in a combined fit, requiring the same shapes of all components, but allowing different strengths. Here the following integrated intensities of the D_{++} wave relative to the D_+ wave were found:

$$0.1 < t' < 0.25 : 2.71\%$$
$$0.25 < t' < 1.0 : 6.03\%.$$

This yields a slope $b = 8.3\,\mathrm{GeV}^{-2}$ if integrating the expected $t'^2 \exp(-bt')$ dependence for the D_{++} wave, which coincides with the values obtained in the $\pi^-\pi^-\pi^+$ analysis [Haas, 2012]. This also coincides with the naïve picture that higher spin projections can only be obtained for larger scattering angles.

J^{PC}	state	$m \pm$ stat.	$\Gamma \pm$ stat
2^{++}	$a_2(1320)$	$1.314\,\text{GeV} \pm 0.9\,\text{MeV}$	$116\,\text{MeV} \pm 2.2\,\text{MeV}$
2^{++}	$a_2'(1700)$	$1.527\,\text{GeV} \pm 0.3\,\text{MeV}$	$297\,\text{MeV} \pm 42\,\text{MeV}$
1^{-+}	$\pi_1(1600)$	$1.556\,\text{GeV} \pm 25\,\text{MeV}$	$500\,\text{MeV} \pm 25\,\text{MeV}$
4^{++}	$a_4(2040)$	$1.915\,\text{GeV} \pm 8.6\,\text{MeV}$	$279\,\text{MeV} \pm 23.7\,\text{MeV}$

Table 9.1.: Fit results for the individual resonant contributions to the $\eta\pi$ system. The errors given are only statistical errors.

9.2. Mass-dependent Fit of the $\eta'\pi^-$ System

Similarly, we performed a fit of the $\eta'\pi$ system. In order to obtain a stable fit which describes the broad D_+ wave, the a_2' had to be fixed to "reasonable" values. Another difference compared to the $\pi^-\eta$ system is that no D_{++} wave was included, as it could not be cleanly extracted in the mass-independent fit due to its low strength. For the results see Tab. 9.2.

J^{PC}	state	$m \pm$ stat.	$\Gamma \pm$ stat	
2^{++}	$a_2(1320)$	$1.307\,\text{GeV} \pm 3.6\,\text{MeV}$	$116.5\,\text{MeV} \pm 7\,\text{MeV}$	
2^{++}	$a_2'(1700)$	$1.6\,\text{GeV}$	$275\,\text{MeV}$	(fixed)
1^{-+}	$\pi_1(1600)$	$1.783\,\text{GeV} \pm 19\,\text{MeV}$	$388\,\text{MeV} \pm 18\,\text{MeV}$	
4^{++}	$a_4(2040)$	$1.956\,\text{GeV} \pm 17\,\text{MeV}$	$234\,\text{MeV} \pm 31\,\text{MeV}$	

Table 9.2.: Fit results for the individual waves contributing to the $\eta'\pi$ system. The errors given are only statistical errors.

We show in Figs. 9.4 and 9.5 the results from mass-dependent fits to the $\eta'\pi^-$ system. The fit model contains the following ingredients:

- The D_+ wave is composed of a dynamical width Breit-Wigner, which incorporates the known branchings of the $a_2(1320)$ (depicted in magenta), a second Breit-Wigner which is fixed at the mass given in the table below (depicted in cyan), and an exponential background of the form given before (depicted in green, its interference with the $a_2(1320)$ BW is shown in black. The importance of using the dynamical width Breit-Wigner is illustrated in Fig. F.1 in the appendix.
- The P_+ wave is parameterized by a fixed-width Breit-Wigner (depicted in magenta) and an exponential background (green).
- The G_+ wave is parameterized by a Breit-Wigner (green) and an exponential background (cyan).

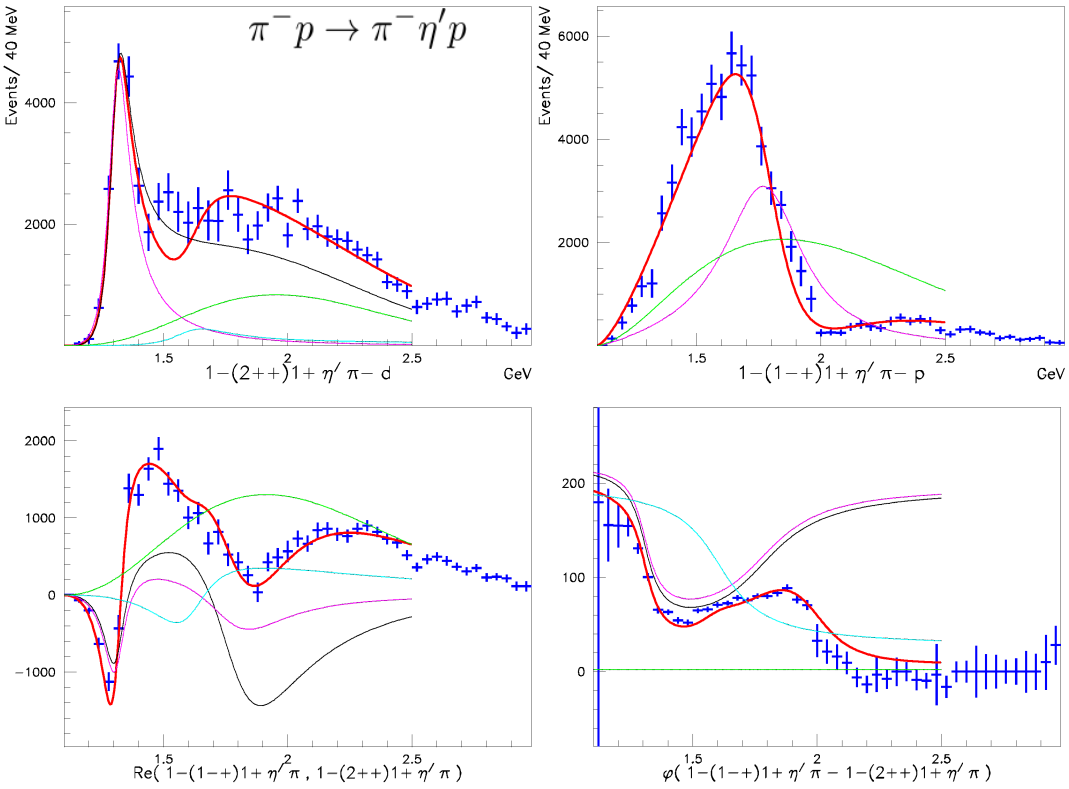

Figure 9.4.: Mass-dependent fit to $\eta'\pi$ showing the fit of the D_+ and P_+ waves. The plots show from left to right, from top to bottom: the D_+ intensity, the P_+ intensity, $\mathrm{Re}(P_+^* D_+)$, the relative phase $\arg(P_+/D_+)$. The full fit is depicted by the thick red line, for the other colors, see text.

- The Breit-Wigners and backgrounds are multiplied by phase-space factors which include the angular-momentum barriers (these are already included in the formulae of App. F.)

It is perhaps noteworthy that the simple model for the P_+ wave manages to account for its shape into the range well above 2 GeV. On the other hand, a resonant interpretation is difficult, as the fit requires a huge non-resonant background, while at the same time the phase-motion, determined only relative to the D_+ depends on the details of the parametrization of the D_+ wave. This parametrization could not be brought into accordance with the results from the $\pi^-\eta$ data, even though we saw in Sec. 8.3 that the main features are shared between the two final states. We assume that this is due to the way this kind of analysis ignores incoherent contributions which we previously considered a likely explanation of the seeming incompatible in the observed phase-motions of the two final states.

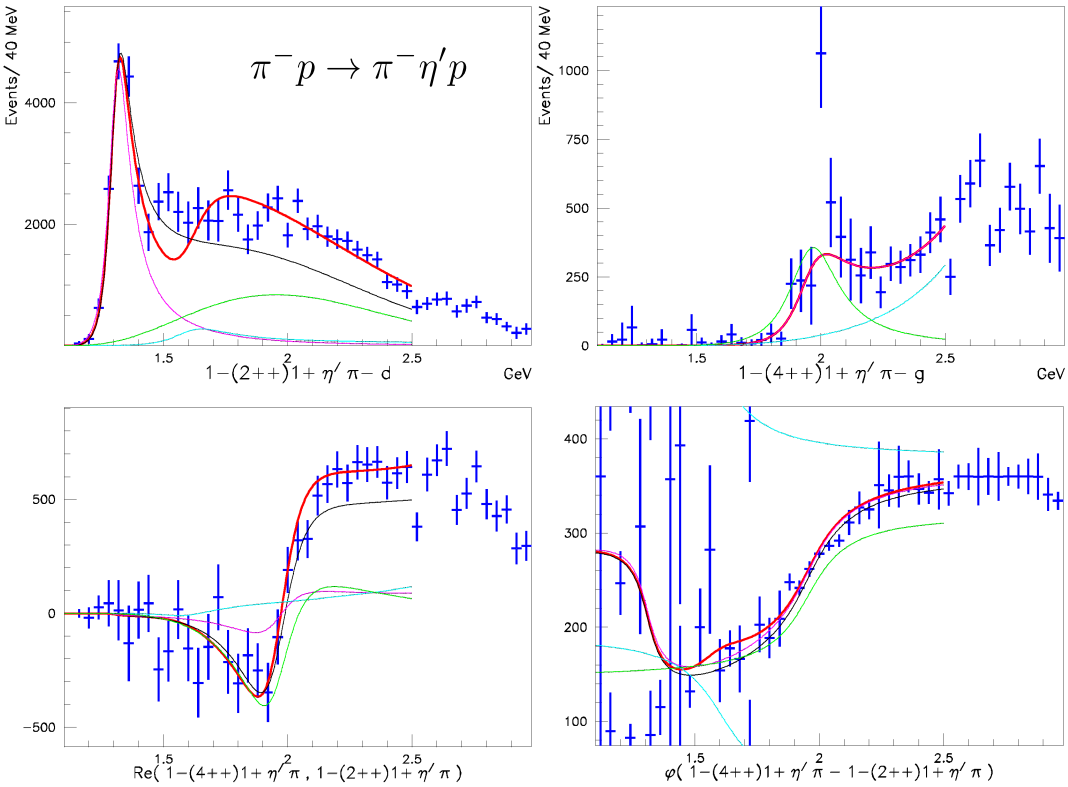

Figure 9.5.: Mass-dependent fit to $\eta'\pi$ showing the fit of the D_+ and G_+ waves. The plots show from left to right, from top to bottom: the D_+ (same as in Fig. 9.4) intensity, the G_+ intensity, $\mathrm{Re}(G_+^* D_+)$, the relative phase $\arg(D_+/G_+)$. The full fit is depicted by the thick red line, for the other colors, see text.

9.3. Extraction of Branching Fractions

We will now use the results from this section to determine branching ratios of the established resonances $a_2(1320)$ and $a_4(2040)$ and will compare these to the world average values and to predictions made from the $\eta - \eta'$ mixing.

Below, we give the total numbers of $a_2(1320)$ and $a_4(2040)$ resonance decays observed in the two final states as calculated by integrating the result from the mass-dependent fit. Taking into account the branching fractions of the η', η and π^0 decays[1], we also calculate the ratio ρ of the branching fractions (errors are only statistical, due to the huge background beneath the $a_2(1320)$ in $\pi^-\eta'$ it has a large systematic error):

Resonance	$N(\pi^-\eta)$	$N(\pi^-\eta')$	$\rho = \frac{BR(\pi^-\eta')}{BR(\pi^-\eta)}$
$a_2(1320)$	$(5.31 \pm 0.13) \cdot 10^5$	$(2.15 \pm 0.19) \cdot 10^4$	$(5.3 \pm 0.5)\%$
$a_4(2040)$	$(2.29 \pm 0.30) \cdot 10^4$	$(2.71 \pm 0.41) \cdot 10^3$	$(16 \pm 2.6)\%$

The tabulated value for the relative branching of the $a_2(1320)$ is [Nakamura et al., 2010]

$$\rho_{\mathrm{PDG}} = \frac{BR(a_2(1320) \to \eta'\pi)}{BR(a_2(1320) \to \eta\pi)} = \frac{0.53 \pm 0.09}{14.5 \pm 1.2} = (3.7 \pm 0.7)\%,$$

which is at slight tension with our value. The value ρ_{PDG} was obtained from the following measurements: by the VES collaboration in two publications, $\rho = 0.034 \pm 0.08 \pm 0.05$ [Beladidze et al., 1992] and $\rho = 0.047 \pm 0.01 \pm 0.04$ [Beladidze et al., 1993], and by the Crystal Barrel collaboration who give a value $\rho = 0.032 \pm 0.009$ [Abele et al., 1997]. We see that the later VES value agrees with ours within errors. To our knowledge, no such comparison was previously undertaken for the $a_4(2040)$.

In order to compare with theoretical predictions, where assumptions about the resonance shape may be different from ours, we also give the ratios r of the peak heights h corrected for the branching ratios of the subsequent decays:

Resonance	$h(\pi^-\eta)$	$h(\pi^-\eta')$	ratio $r = \frac{h(\pi^-\eta')}{h(\pi^-\eta)} \times BR$
$a_2(1320)$	$1.35 \cdot 10^5$	$4.5 \cdot 10^3$	4.4%
$a_4(2040)$	$2.6 \cdot 10^3$	$3.5 \cdot 10^2$	17%

Lineshape effects should affect the a_2 which is close to the $\pi\eta'$ threshold much more than the a_4. Comparing to the previous table, we find this expectation confirmed.

Ignoring effects of the widths of the resonances, we can approximate the expected ratios by

$$\rho \equiv \frac{\sigma(\pi\eta')}{\sigma(\pi\eta)} = \frac{q'}{q} \left(\frac{F_J(q')}{F_J(q)} \right)^2 \tan^2 \phi, \tag{9.1}$$

[1]The correction factor is $(BR(\eta \to \pi^-\pi^+\pi^0) \times BR(\pi^0 \to \gamma\gamma))/(BR(\eta' \to \pi^-\pi^+\eta) \times BR(\eta \to \gamma\gamma)) = 1.32$.

where q, q' are evaluated at the nominal mass of the resonance[Amsler et al., 1992]. Since our mass for the $a_4(2040)$, $m_{\text{fit}}(a_4) = 1.92\,\text{GeV}$, (consistent with other COMPASS analyses [Alekseev et al., 2010; Haas, 2012]) is significantly lower than the value given in the particle data tables [Nakamura et al., 2010], $m_{\text{PDG}}(a_4) = 2.001 \pm 0.001\,\text{GeV}$, we use both values in the calculation. For the $a_2(1320)$ we use the tabulated mass value $m(a_2) = 1.318\,\text{GeV}$. In order to compare to Ref. [Bramon et al., 1999], we calculate values using $F_L(q) = q^L$, and also the forms more suited to our fit, where the angular momentum barriers from Eq. (F.9) were used. We assume the world-average value of the pseudoscalar mixing angle [Feldmann et al., 1998] $\tan^2\phi = 0.67$. The results are given in Tab. 9.3.

Resonance	$F_L(q)$	expected ratio $\frac{\pi^-\eta'}{\pi^-\eta}$	observed ratio ρ	observed ratio r
$a_2(1320)$	q^2	0.029	0.053 ± 0.005	0.044
$a_2(1320)$	$B_2((qR)^2)$	0.12		
$a_4(2040)_{\text{PDG}}$	q^4	0.13	0.16 ± 0.026	0.17
$a_4(2040)_{\text{PDG}}$	$B_4((qR)^2)$	0.37		
$a_4(2040)_{\text{fit}}$	q^4	0.10		
$a_4(2040)_{\text{fit}}$	$B_4((qR)^2)$	0.32		

Table 9.3.: Expected ratios from Eq. (9.1) compared to observed ratios of the cross-section and ratio of peak height.

We see that the observed numbers systematically lie above the expected numbers in Tab. 9.3. The best match is found by comparing peak heights and taking the simple phase-space factors q^L. If we assume that an overall scale is wrong, we can correct for this scale by comparing the ratios of deviation from the expected value, i.e.

$$\frac{r_{\text{observed}}(a_2)}{r_{\text{expected}}(a_2, q^2)} = \frac{0.044}{0.029} = 1.51, \qquad \frac{r_{\text{observed}}(a_4)}{r_{\text{expected}}(a_4^{\text{PDG}}, q^4)} = \frac{0.17}{0.13} = 1.31. \tag{9.2}$$

And thus, adjusting to the ratios found for the $a_2(1320)$ resonance, we do indeed find that the ratios for η' production to η production decays of the $a_4(2040)$ resonance is close to the value expected from η'–η mixing. The good agreement with the value for the relative branching $a_2 \to \eta'\pi$ and $a_2 \to \eta\pi$ suggests a systematic error either in the theoretical calculation or the extraction that is not yet accounted for.

10. Conclusions

We have studied the reactions $\pi^- p \to \pi^- \eta p$ and $\pi^- p \to \pi^- \eta' p$ at momentum transfers to the target in the range $0.1\,\mathrm{GeV}^2 < -t < 1\,\mathrm{GeV}^2$. Initially, this was motivated by previous claims of a spin-exotic resonance in the P-wave of these reactions. We have selected and analyzed data taken by COMPASS in 2008. Our analysis employed the technique of partial-wave analysis, which we described in detail. We compared the results between two different implementations. As a new component of the apparatus, we developed a $2\,\mathrm{m} \times 2\,\mathrm{m}$ veto detector.

We found significant P-wave intensities in both final states. We also found known resonances and further structure in the D_+ and G_+ waves. Due to the higher bombarding energy compared to previous studies of these channels, and due to the large acceptance of the COMPASS experiment, we could follow the partial-wave decomposition to masses beyond 2 GeV. We found that at high masses rapidity-gap kinematics arise, where a Regge description of the data is more economic, and correspondingly extracted additional partial-waves in the fit. We found that the waves D_+ and G_+ show very similar behavior between the $\pi^-\eta$ and $\pi^-\eta'$ systems, once phase-space factors are taken into account. This similarity is not given for the P_+ wave which is enhanced in the $\pi^-\eta'$ system compared to the $\pi^-\eta$ system, even before taking into account the larger $\pi^-\eta$ phase-space. The phase motion of the P_+-wave relative to the D_+-wave also shows different behavior in the two systems, though the phase-difference agrees on the $\pi^-\eta'$ threshold.

Resonance parameters, including relative branching fractions, of the $a_2(1320)$ (in the D_+ wave) and the $a_4(2040)$ (in the G_+ wave) are found to be in agreement between both channels and with other measurements (where available). A resonant interpretation of the P_+-wave contributions in the vein of previous analyses was possible by including large background terms and by adding additional resonance terms into the D_+ wave. Nevertheless, the fit needs to accomodate strong interferences between backgrounds and resonances. We also find from mathematical considerations that this type of analysis does not account correctly for incoherent contributions to the data set, which we find likely given distinct differences between the phase-motions observed in the two channels.

In a preliminary common analysis of the complete $\pi^-\pi^+\pi^-\eta$ system, which we discuss in App. H, we find comparable integrated intensities for the intensities of the $\eta'\pi^-\ 1^{-+}$ P-wave and the $\pi^- f_1\ 1^{-+}$ S-wave and D-wave.

A. Averaged Material Properties

In this appendix we collect some of the standard formulas used to calculate quantities relevant to the Monte Carlo description of calorimeters. Given a molecule or mixture composed of materials with nuclear charge numberss Z_i and nuclear masses A_i where n_i atoms of each species i are present, one then defines the molecular weight A_{mol} and molecular nuclear charge number Z_{mol} as (following CONS110-1 in [GEANT])

$$A_{\mathrm{mol}} = \sum_i n_i A_i, \qquad Z_{\mathrm{mol}} = \sum_i n_i Z_i. \tag{A.1}$$

The fraction by weight p_i of each species is then

$$p_i = \frac{n_i A_i}{A_{\mathrm{mol}}}. \tag{A.2}$$

In order to calculate averaged quantities one can then employ the effective nuclear charge and mass

$$A_{\mathrm{eff}} = \sum_i p_i A_i, \qquad Z_{\mathrm{eff}} = \sum_i p_i Z_i. \tag{A.3}$$

Electromagnetic shower development is parametrized in terms of the radiation length X_0 and the critical energy E_{crit}. The radiation length for an element can be approximated by

$$\frac{1}{\rho X_0} = 4\alpha r_0^2 N_A \frac{1}{A} Z(Z + \xi(Z)) \left(\ln \frac{183}{Z^{1/3}} - F_C(Z) \right), \tag{A.4}$$

where α is the fine-structure constant, r_0 the classical electron radius, N_A Avogadro's number (in $\left[\mathrm{g\,mol^{-1}}\right]$), and the functions $\xi(Z)$ and $F_C(Z)$ are given by

$$\begin{aligned} F_C(Z) = (\alpha Z)^2 \Big(& \frac{1}{1+(\alpha Z)^2} + 0.2026 - 0.0369(\alpha Z)^2 \\ & + 0.0083(\alpha Z)^4 - 0.0020(\alpha Z)^6 \Big), \end{aligned} \tag{A.5}$$

$$\xi(Z) = \frac{\ln 1440 - \frac{2}{3}\ln Z}{\ln 183 - \frac{1}{3}\ln Z - F_C(Z)}. \tag{A.6}$$

For a compound the radiation length is averaged as

$$\frac{1}{\rho X_0} = \sum_i \frac{p_i}{\rho_i X_{0i}}. \tag{A.7}$$

The critical energy in the sense of Rossi's approximation B (p. 224 in [Rossi, 1952], also p. 27 in [Wigmans, 2000]) can be approximated by [Grindhammer and Peters, 1993]

$$E_{\text{crit}}\,[\text{MeV}] = 2.66 \times \left(\frac{Z\rho X_0}{A}\right)^{1.1}, \tag{A.8}$$

where ρX_0 is given in units of $[\text{g}\,\text{cm}^{-2}]$. For a sampling calorimeter one additionally needs the sampling frequency F_S and the relative response of the calorimeter to electrons and minimum-ionizing particles, denoted e/mip. The sampling frequency is defined as

$$F_S = \frac{\rho X_0}{d_a + d_p}, \tag{A.9}$$

where ρX_0 is the effective radiation length and d_a (d_p) denotes the thickness of the active (passive) layers of the sampling calorimeter. In words, the sampling frequency is the number of calorimeter layers within an effective radiation length. The relative response can be approximated via

$$\frac{e}{\text{mip}} \approx \frac{1}{1 + 0.007(Z_p - Z_a)}, \tag{A.10}$$

where the indices again correspond to the passive and active materials.

B. Tracks in a Magnetic Field

From the Lorentz force

$$\boldsymbol{F} = Cq\boldsymbol{\beta} \times \boldsymbol{B}, \tag{B.1}$$

where C is a constant depending on the choice of units, q is the charge of the particle passing through the magnetic field $\boldsymbol{B}$ with velocity $\boldsymbol{\beta} = \mathrm{d}\boldsymbol{x}/\mathrm{d}t$ and $\boldsymbol{F}$ is the force exerted on the particle, one obtains the equation of motion

$$m\gamma \frac{\mathrm{d}^2\boldsymbol{x}}{\mathrm{d}t^2} = \kappa q \boldsymbol{\beta}(t) \times \boldsymbol{B}(\boldsymbol{x}(t)), \tag{B.2}$$

where again κ is a constant that depends on the choice of units, m is the particle mass and γ is the usual Lorentz factor

$$\gamma \equiv (1 - \boldsymbol{\beta}^2)^{-(1/2)}. \tag{B.3}$$

In the usual system of units ($\boldsymbol{B}$ in Tesla (T), masses, energy and momentum in GeV, $\boldsymbol{x}$ in meters, t in seconds), one has

$$\kappa = 0.299792458 \, \frac{\mathrm{GeV}}{\mathrm{T} \cdot \mathrm{m}}, \tag{B.4}$$

where the numerical value is the same as for the speed of light c.

The trajectory can be parametrized in terms of the trajectory length s as measured from some arbitrary starting point, $\frac{\mathrm{d}s}{\mathrm{d}t} = v$ as

$$\frac{\mathrm{d}^2\boldsymbol{x}}{\mathrm{d}s^2} = \frac{\kappa q}{P} \frac{\mathrm{d}\boldsymbol{x}}{\mathrm{d}s} \times \boldsymbol{B}(\boldsymbol{x}(s)), \tag{B.5}$$

where the momentum (unchanged in the propagation) $P = \beta\gamma m$ was introduced. In fixed-target experiments it is common to parametrize tracks as function of z instead of s. This requires obviously that tracks never turn backwards. Denoting derivatives with respect to z by primes, one has

$$s' = \sqrt{1 + x'^2 + y'^2} \tag{B.6}$$

and obtains after the variable transformation

$$\begin{aligned} x'' &= \tfrac{\kappa q}{P} s' \left(x'y'B_x - (1 + x'^2)B_y + y'B_z \right), \\ y'' &= \tfrac{\kappa q}{P} s' \left((1 + y'^2)B_x - x'y'B_y - x'B_z \right). \end{aligned} \tag{B.7}$$

After fixing some value of z, the track is completely specified by five variables: $(x, y, x', y', q/P)$. One colloquially calls this tuple of numbers *the helix of the track at z* (see e.g. [Bock et al., 1990]).[1]

As a special case that allows simple estimation think of a magnetic field that is homogeneous, of strength B and parallel to the y axis for $0 < z < Z$, and a particle initially flying along the z axis with momentum P. The remaining non-trivial equation of motion inside magnetic field has the form

$$x'' = \frac{\kappa q B}{P} \left(1 + x'^2\right)^{3/2} \tag{B.8}$$

which describes a circle with radius

$$R = \frac{P}{\kappa q B}. \tag{B.9}$$

Provided $Z < R$, the particle will escape on the other side, shifted to

$$x(z = Z) = R - \sqrt{R^2 - Z^2}, \tag{B.10}$$

and the inclination of the track will be

$$x'(z \geq Z) = \frac{Z}{\sqrt{R^2 - Z^2}} = \frac{BZ}{\sqrt{\frac{P^2}{\kappa^2 q^2} - (BZ)^2}}, \tag{B.11}$$

where the latter form is useful, as usually the integrated field $\int B \, \mathrm{d}z$ is given. For fast particles this can be approximated

$$x'(x \geq Z) \approx \kappa B Z \frac{q}{P}. \tag{B.12}$$

For instance, the integrated field of SM1 in the COMPASS experiment is 1 Tm, approximating the field as homogeneous over the length of the magnet, $Z = 110\,\mathrm{cm}$, for a particle of momentum 1 GeV the bending radius will be $R = 3.7\,\mathrm{m}$ which corresponds to a deflection angle at the exit of the magnet of $\operatorname{atan} x' = 300\,\mathrm{mrad}$.

[1] In a homogeneous magnetic field, and without radiation, the most general trajectory a charged particle can describe is a helix. Of course, the given parametrization in terms of z doesn't allow for the general case, and in a real experiment the particle will leave the magnetic field at some point. Therefore, this usage of *helix* is jargon.

C. Determination of the Beam Momentum

In this appendix we shall show how to calculate the beam momentum given the information available in the COMPASS hadron setup, namely the direction of the beam, the mass of the target, the mass of the recoil and the four-vector p_3 of the forward going system. Here, we consider the measurement of the recoil momentum by the RPD imprecise and thus avoid using it. In the laboratory frame, we write

- p_1: the beam four-momentum with known mass $p_1^2 = E_1^2 - \boldsymbol{p}_1^2 = m_\pi^2$ and known direction such that the scattering angle $\vartheta \equiv \angle \boldsymbol{p}_1 \boldsymbol{p}_3$ is known,
- $p_2 = (m_p, 0, 0, 0)$: the four-vector of the target with m_p the proton mass,
- p_3: the known four-momentum of the forward system, $p_3 = (E_3, \boldsymbol{p}_3)$ with invariant mass m_3, and
- p_4: the unknown four-momentum of the recoil with $p_4^2 = m_p^2$.

One then has for the Mandelstam variables from Eq. (2.1), judiciously avoiding p_4,

$$\begin{aligned} s &= (p_1 + p_2)^2 = m_\pi^2 + m_p^2 + 2m_p E_1, \\ t &= (p_1 - p_3)^2 = m_\pi^2 + m_3^2 - 2E_1 E_3 + 2|\boldsymbol{p}_1||\boldsymbol{p}_3| \cos\vartheta, \\ u &= (p_2 - p_3)^2 = m_p^2 + m_3^2 - 2m_p E_3. \end{aligned} \tag{C.1}$$

The goal is to find $|\boldsymbol{p}_1| = \sqrt{E_1^2 - m_\pi^2}$. Inserting Eq. (C.1) into the relation between the Mandelstam variables Eq. (2.2),

$$s + t + u = \sum_i m_i^2 = m_\pi^2 + 2m_p^2 + m_3^2,$$

one obtains immediately the quadratic equation

$$\begin{aligned} 0 = {} & |\boldsymbol{p}_1|^2 \left(|\boldsymbol{p}_3|^2 \cos^2\vartheta - (E_3 - m_p)^2 \right) \\ & + |\boldsymbol{p}_1||\boldsymbol{p}_3| \cos\vartheta \left(m_\pi^2 + m_3^2 - 2m_p E_3 \right) \\ & + \frac{1}{4} \left(m_\pi^2 + m_3^2 - 2m_p E_3 \right)^2 - m_\pi^2 (E_3 - m_p)^2. \end{aligned} \tag{C.2}$$

This can be solved with the standard quadratic formula. The signs have been chosen such that the positive root is appropriate. For other beams or targets replace m_π and m_p accordingly. An approximate solution can be found e.g. in [Weitzel, 2008].

D. Solving Least Squares Problems

A commonly used estimator in physics analyses is the least-squares estimator which has certain welcome properties, besides being fairly easy to understand (details e.g. in [James, 2006]).

D.1. Unconstrained Case

The mission is to find $\boldsymbol{x} \in \mathbb{R}^n$ that minimizes

$$(\boldsymbol{A}\boldsymbol{x} - \boldsymbol{b})^2 \equiv \min, \tag{D.1}$$

where $\boldsymbol{A} \in \mathbb{R}^{m \times n}$ is of rank $k \leq m \leq n$ and $\boldsymbol{b} \in \mathbb{R}^m$. The general solution is obtained by singular value decomposition (SVD) (details e.g. in [Brandt, 1999; Lawson and Hanson, 1987]), where $\boldsymbol{A}$ is decomposed into three matrices, according to

$$\boldsymbol{A} = \boldsymbol{U}\boldsymbol{S}\boldsymbol{V}^T \tag{D.2}$$

with the following properties:

- $\boldsymbol{U} \in \mathbb{R}^{m \times m}$, $\boldsymbol{U}$ orthogonal, i.e. $\boldsymbol{U}^T = \boldsymbol{U}^{-1}$,
- $\boldsymbol{V} \in \mathbb{R}^{n \times n}$, $\boldsymbol{V}$ orthogonal, i.e. $\boldsymbol{V}^T = \boldsymbol{V}^{-1}$, and
- $\boldsymbol{S} \in \mathbb{R}^{m \times n}$, where $\boldsymbol{S}$ has the form

$$\boldsymbol{S} = \begin{pmatrix} s_1 & 0 & 0 & \cdots & & & \\ 0 & s_2 & 0 & \cdots & & & \\ 0 & 0 & \ddots & & & & \\ \vdots & \vdots & \vdots & s_k & 0 & \cdots & \\ 0 & 0 & 0 & 0 & 0 & \cdots & \\ & & & & & \ddots & \\ \vdots & \vdots & \vdots & \vdots & \vdots & & 0 \end{pmatrix} \tag{D.3}$$

where the $s_i \neq 0$ are the *singular values* of $\boldsymbol{A}$. For sake of notational simplicity, we shall call $\boldsymbol{s} \equiv \mathrm{diag}(s_i)$, i.e. the non-singular upper left part of $\boldsymbol{S}$.

With this notation, the least-squares problem Eq. (D.1) can be rewritten in the equivalent form

$$(\boldsymbol{S}\boldsymbol{V}^T\boldsymbol{x} - \boldsymbol{U}^T\boldsymbol{b})^2 \equiv \min\,. \tag{D.4}$$

Introducing $\boldsymbol{p} \equiv \boldsymbol{V}^T\boldsymbol{x}$ and $\boldsymbol{g} \equiv \boldsymbol{U}^T\boldsymbol{b}$ and writing them as k-vector and $(n-k)$-vector, $\boldsymbol{p} = \begin{pmatrix} \boldsymbol{p}_1 \\ \boldsymbol{p}_2 \end{pmatrix}$ and, respectively, as k-vector and $(m-k)$-vector $\boldsymbol{g} \equiv \begin{pmatrix} \boldsymbol{g}_1 \\ \boldsymbol{g}_2 \end{pmatrix}$, one obtains as equivalent form of Eq. D.1

$$(\boldsymbol{s}\cdot\boldsymbol{p}_1 - \boldsymbol{g}_1)^2 + (\boldsymbol{0}\cdot\boldsymbol{p}_2 - \boldsymbol{g}_2)^2 \equiv \min\,. \tag{D.5}$$

The first parenthesis can always be put to zero by choosing $\boldsymbol{p}_1 = \boldsymbol{s}^{-1}\boldsymbol{g}_1$, and the second has the value $(\boldsymbol{g}_2)^2$ independent of the value of $\boldsymbol{p}_2$, i.e. for any $\boldsymbol{p}_2$, $\boldsymbol{x}_{\min} \equiv \boldsymbol{V}\begin{pmatrix} \boldsymbol{s}^{-1}\boldsymbol{g}_1 \\ \boldsymbol{p}_2 \end{pmatrix}$ is a solution of the least-squares problem. For $k = n$, the solution is unique. Otherwise, the solution of minimal length is obtained by setting $\boldsymbol{p}_2 \equiv 0$, where this follows from the orthogonality of $\boldsymbol{V}$.

Putting everything together, writing $\boldsymbol{V}_1$ for the first m columns of $\boldsymbol{V}$ and $\boldsymbol{U}_1$ for the first k columns of $\boldsymbol{U}$, the solution of the least squares problem can be written

$$\boldsymbol{x} \equiv \boldsymbol{A}^\dagger\boldsymbol{b} \equiv \boldsymbol{V}_1\boldsymbol{s}^{-1}\boldsymbol{U}_1^T\boldsymbol{b}, \tag{D.6}$$

where we have introduced the *pseudo-inverse* $\boldsymbol{A}^\dagger$ of $\boldsymbol{A}$. By linear error propagation, the covariance matrix $\boldsymbol{C}$ of $\boldsymbol{x}$ given the covariance matrix $\boldsymbol{C}_{\boldsymbol{b}}$ of $\boldsymbol{b}$ is then

$$\boldsymbol{C} = \boldsymbol{A}^\dagger\boldsymbol{C}_{\boldsymbol{b}}(\boldsymbol{A}^\dagger)^T. \tag{D.7}$$

D.2. Constrained Case

A set of linear constraints can be written

$$\boldsymbol{E}\boldsymbol{x} - \boldsymbol{c} = 0. \tag{D.8}$$

Here $\boldsymbol{x}$ is as before, $\boldsymbol{c} \in \mathbb{R}^l$, $\boldsymbol{E} \in \mathbb{R}^{l\times n}$ and $\boldsymbol{E}$ is of maximal rank $l < n$. Our task now is to find in the set of the solutions $\boldsymbol{x}$ of Eq. (D.8) the solution where the least-squares form Eq. (D.1) takes the smallest value.

The approach taken is straightforward: first one determines the subspace of solutions of Eq. (D.8), then one rewrites Eq. (D.1) as a problem on that subspace. Then the solution can be obtained as before. The first step is achieved again by singular value decomposition. The rest is algebra.

We write the singular value decomposition of $\boldsymbol{E}$ as

$$\boldsymbol{E} = \boldsymbol{H}\boldsymbol{R}\boldsymbol{K}^T, \tag{D.9}$$

where in the same way as before $\boldsymbol{H}$ is an orthogonal $(l \times l)$ matrix, $\boldsymbol{K}$ is an orthogonal $(n \times n)$ matrix and $\boldsymbol{R}$ is an $(l \times n)$ matrix which is zero except for the diagonal elements. From $l < n$ and $\mathrm{rg}\boldsymbol{E} = l$ it follows that the first l columns of $\boldsymbol{R}$ form a diagonal matrix where all diagonal elements are non-zero. We call this submatrix $\boldsymbol{r}$. For ease of notation we also write $\boldsymbol{K} = (\boldsymbol{K}_1|\boldsymbol{K}_2)$, where $\boldsymbol{K}_1$ consists of the first l columns of $\boldsymbol{K}$, $\boldsymbol{K}_2$ of the remaining $(n - l)$. The aimed-for division into subspaces is now obtained by writing $\boldsymbol{K}^T\boldsymbol{x} \equiv \begin{pmatrix} \xi_1 \\ \xi_2 \end{pmatrix}$ (ξ_1 has l rows, ξ_2 has $(n - l)$), which immediately implies

$$x = \boldsymbol{K}_1\xi_1 + \boldsymbol{K}_2\xi_2, \tag{D.10}$$

from which, by the structure of $\boldsymbol{R}$ (used in the last equality) one has for any solution of Eq. (D.8)

$$\boldsymbol{c} = \boldsymbol{E}\boldsymbol{x} = \boldsymbol{E}\boldsymbol{K}_1\xi_1 + \boldsymbol{E}\boldsymbol{K}_2\xi_2 = \boldsymbol{E}\boldsymbol{K}_1\xi_1. \tag{D.11}$$

Solving for ξ_1, one then has the general solution

$$\boldsymbol{x} = \boldsymbol{K}_1\boldsymbol{r}^{-1}\boldsymbol{H}^T\boldsymbol{c} + \boldsymbol{K}_2\xi_2, \tag{D.12}$$

where only ξ_2 is arbitrary. Inserting this equation into Eq. (D.1) and solving the resulting equation in ξ_2, one then obtains the solution of the constrained problem.

Explicitly, it remains to minimize

$$(\boldsymbol{A}\boldsymbol{x} - \boldsymbol{b})^2 = \Big(\boldsymbol{A}(\boldsymbol{K}_1\boldsymbol{r}^{-1}\boldsymbol{H}^T\boldsymbol{c} + \boldsymbol{K}_2\xi_2) - \boldsymbol{b}\Big)^2 \tag{D.13}$$

as a function of ξ_2. Putting this in the form of Eq. (D.1),

$$\Big(\boldsymbol{A}\boldsymbol{K}_2\xi_2 - (\boldsymbol{b} - \boldsymbol{A}\boldsymbol{K}_1\boldsymbol{r}^{-1}\boldsymbol{H}^T\boldsymbol{c})\Big)^2, \tag{D.14}$$

hopefully makes transparent what remains to be done. Explicitly, using the pseudo-inverse, one has

$$\boldsymbol{x} = \Big(\boldsymbol{K}_1(\boldsymbol{E}\boldsymbol{K}_1)^\dagger - \boldsymbol{K}_2(\boldsymbol{A}\boldsymbol{K}_2)^\dagger\boldsymbol{A}\boldsymbol{K}_1\boldsymbol{r}^{-1}\boldsymbol{H}^T\Big)\,\boldsymbol{c} + \boldsymbol{K}_2(\boldsymbol{A}\boldsymbol{K}_2)^\dagger\boldsymbol{b}. \tag{D.15}$$

Given the covariance matrices $\boldsymbol{C}_b$ and $\boldsymbol{C}_c$ of $\boldsymbol{b}$ and $\boldsymbol{c}$, respectively, the covariance matrix for $\boldsymbol{x}$ can now be read off (replace $\boldsymbol{M}\boldsymbol{b}$ by $\boldsymbol{M}\boldsymbol{C}_b\boldsymbol{M}^T$ and likewise for $\boldsymbol{c}$, where $\boldsymbol{M}$ represents the matrix in front).

D.3. Application to Measured Data

For measured data $\boldsymbol{x}$ with covariance matrix $\boldsymbol{C}$, the least-squares form for changes $\boldsymbol{\epsilon}$ in $\boldsymbol{x}$ (such as result from a fit) is usually written

$$\chi^2 \equiv \boldsymbol{\epsilon}^T\boldsymbol{C}^{-1}\boldsymbol{\epsilon}. \tag{D.16}$$

This can be brought into the form of Eq. (D.1) by using the Cholesky decomposition of the positive-definite, symmetric matrix $\boldsymbol{C}^{-1}$ (see e.g. [Brandt, 1999])

$$\boldsymbol{C}^{-1} \equiv \boldsymbol{H}^T \boldsymbol{H}, \tag{D.17}$$

where by definition of the decomposition, $\boldsymbol{H}$ is an upper-diagonal square matrix, i.e. its elements below the diagonal are zero. With it, one can immediately write

$$\chi^2 = (\boldsymbol{H}\boldsymbol{\epsilon})^2 \tag{D.18}$$

which is a special case of the form Eq. (D.1).

For non-linear constraints, the solution can be obtained by linearization and iteration. I.e., given the non-linear constraint $\boldsymbol{f}(\boldsymbol{x}) = 0$, linearize around some starting point $\boldsymbol{x}_0$, for instance the measured values, writing

$$\boldsymbol{f}(\boldsymbol{x}) = \boldsymbol{f}(\boldsymbol{x}_0) + \left.\frac{\partial \boldsymbol{f}}{\partial \boldsymbol{x}}\right|_{\boldsymbol{x}=\boldsymbol{x}_0} \cdot (\boldsymbol{x} - \boldsymbol{x}_0). \tag{D.19}$$

Then one solves for the constraint

$$\boldsymbol{E}\boldsymbol{x} - \boldsymbol{c} = 0 \tag{D.20}$$

where the previous notation was restored by writing

$$\boldsymbol{E} \equiv \left.\frac{\partial \boldsymbol{f}}{\partial \boldsymbol{x}}\right|_{\boldsymbol{x}=\boldsymbol{x}_0}, \text{and } \boldsymbol{c} \equiv \boldsymbol{E}\boldsymbol{x}_0 - \boldsymbol{f}(\boldsymbol{x}_0). \tag{D.21}$$

The procedure is then iterated, using the results from the previous iteration as starting point, until a satisfying fit is obtained.

E. Kinematic Validation in Restricted t' Range

In this appendix we collect plots comparing the fit prediction with the data in the same way as in the plots shown in Figs. 8.10 to 8.20 in Sec. 8.5, but with the data restricted to the range $0.1\,\mathrm{GeV}^2 < t' < 1\,\mathrm{GeV}^2$. We see that the t' distribution of the Monte Carlo still does not match the data, but we also see that the fit quality of the fits shown in the main text is not inferior to that shown here. This is because the distribution of transverse momenta is determined by the breakup momenta much more than by the initial production process, to wit compare Fig. 8.19 to Fig. E.10 as well as Fig. 8.20 to Fig. E.11. This observation holds true especially for small values of t' where the deviations between the distributions in MC and the real data are largest.

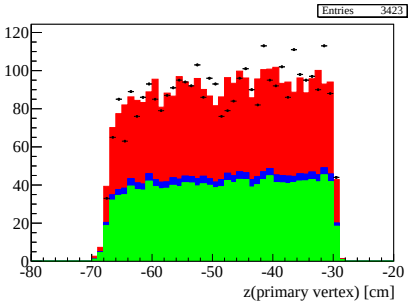

(a) z of primary vertex

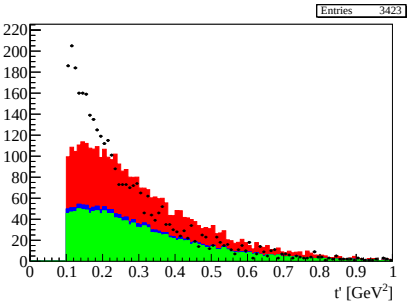

(b) t'

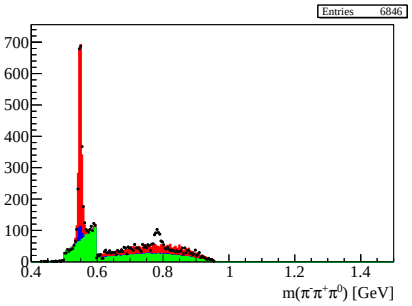

(c) $m(\pi^-\pi^+\pi^0)$ (two combinations)

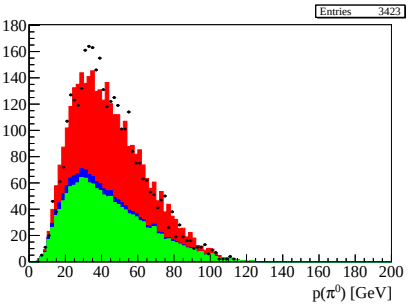

(d) $p(\pi^0)$

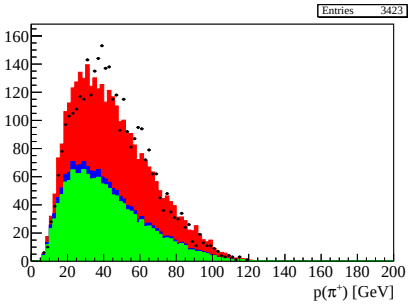

(e) $p(\pi^+)$

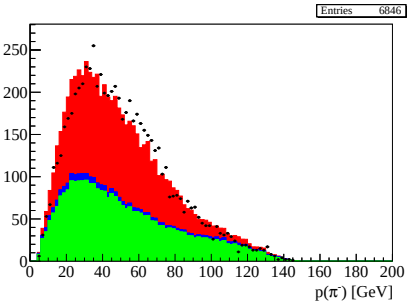

(f) $p(\pi^-)$ (two entries per event)

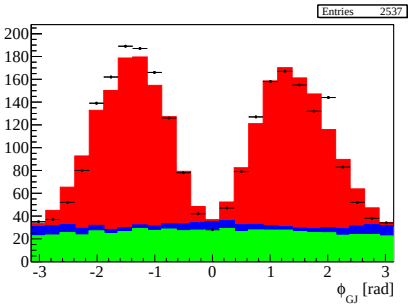

(g) φ_{GJ}

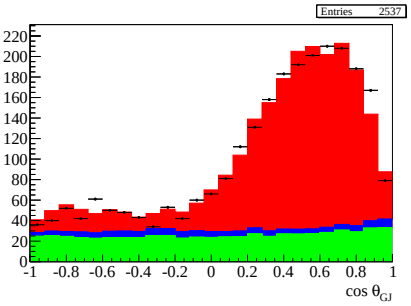

(h) $\cos\vartheta_{\mathrm{GJ}}$

Figure E.1.: Comparison between $\pi^-\eta$ data and fit prediction for $m \in [m_\pi + m_\eta, m_\pi + m_{\eta'}] = [687\,\mathrm{MeV}, 1097\,\mathrm{MeV}]$. Other details as in Fig. 8.10.

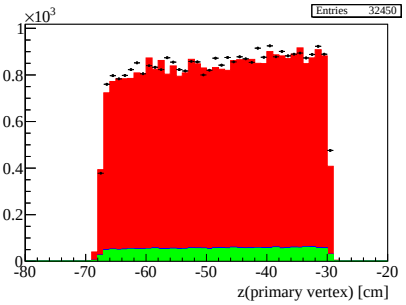

(a) z of primary vertex

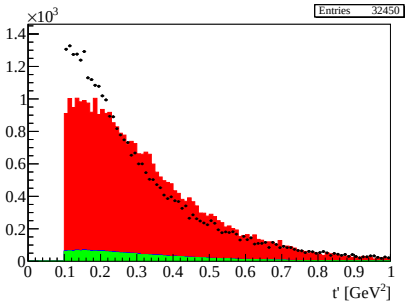

(b) t'

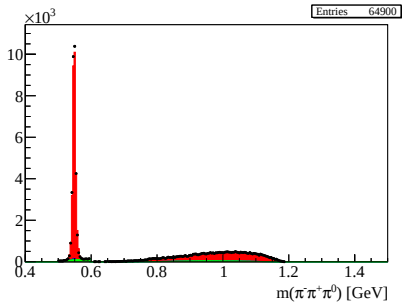

(c) $m(\pi^-\pi^+\pi^0)$ (two combinations)

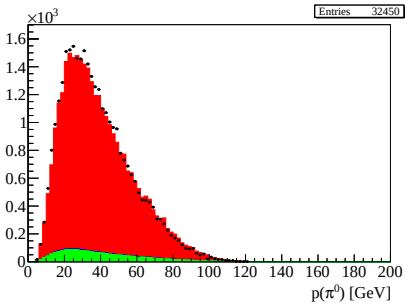

(d) $p(\pi^0)$

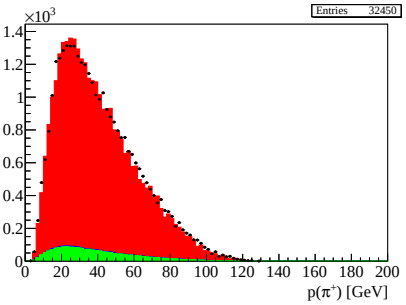

(e) $p(\pi^+)$

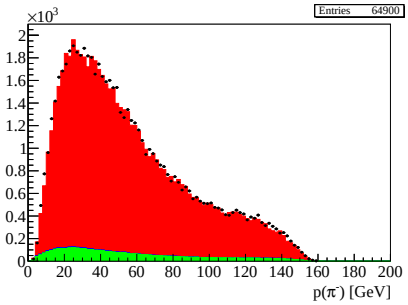

(f) $p(\pi^-)$ (two entries per event)

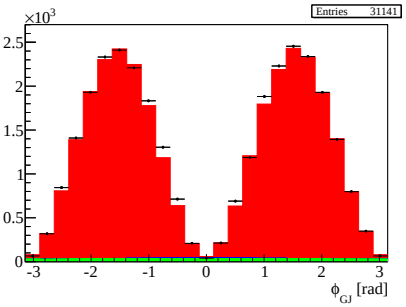

(g) φ_{GJ}

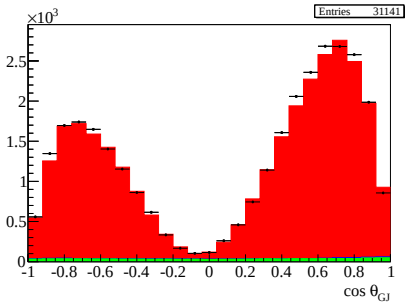

(h) $\cos\vartheta_{\mathrm{GJ}}$

Figure E.2.: Comparison between $\pi^-\eta$ data and fit prediction for $m \in [m_\pi + m_{\eta'}, m_{a_2}] = [1097\,\mathrm{MeV}, 1318\,\mathrm{MeV}]$. Other details as in Fig. 8.10.

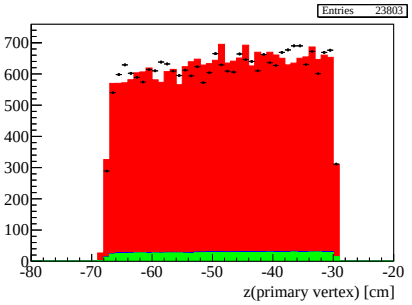

(a) z of primary vertex

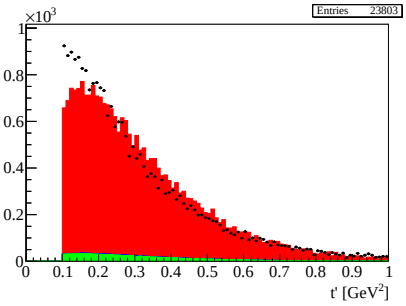

(b) t'

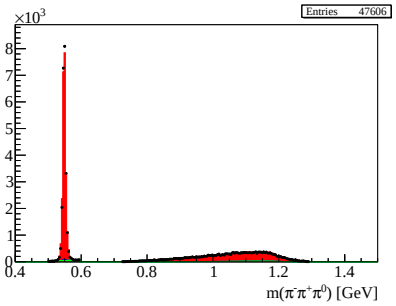

(c) $m(\pi^-\pi^+\pi^0)$ (two combinations)

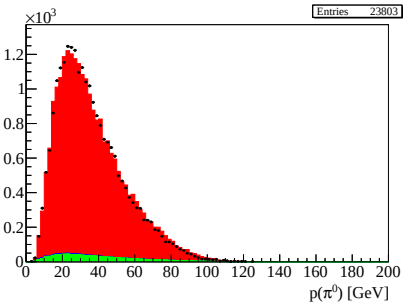

(d) $p(\pi^0)$

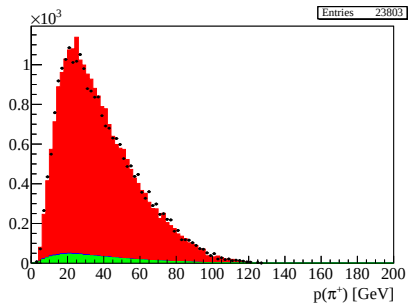

(e) $p(\pi^+)$

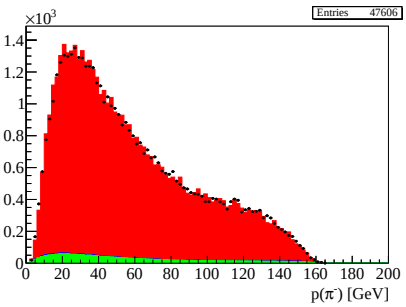

(f) $p(\pi^-)$ (two entries per event)

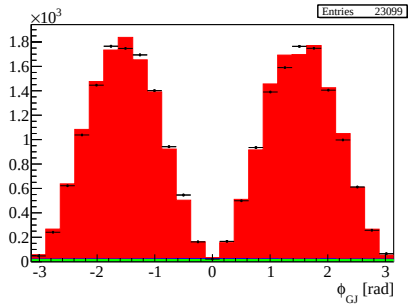

(g) φ_{GJ}

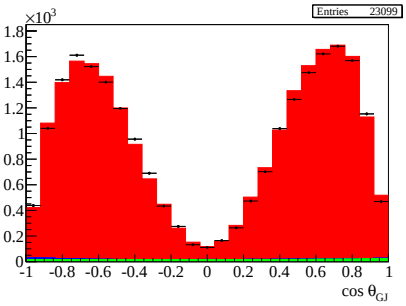

(h) $\cos\vartheta_{\mathrm{GJ}}$

Figure E.3.: Comparison between $\pi^-\eta$ data and fit prediction for $m \in [m_{a_2}, m_{a_2}+\Gamma_{a_2}] = [1318\,\mathrm{MeV}, 1425\,\mathrm{MeV}]$. Other details as in Fig. 8.10.

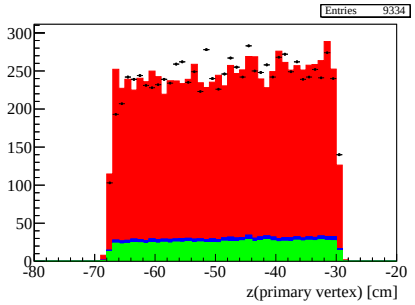

(a) z of primary vertex

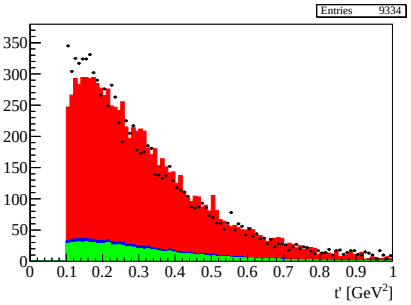

(b) t'

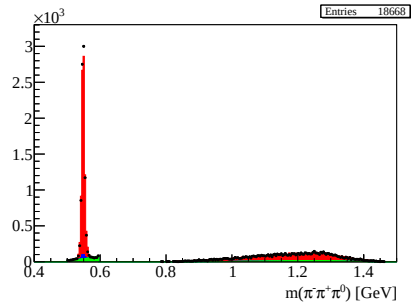

(c) $m(\pi^-\pi^+\pi^0)$ (two combinations)

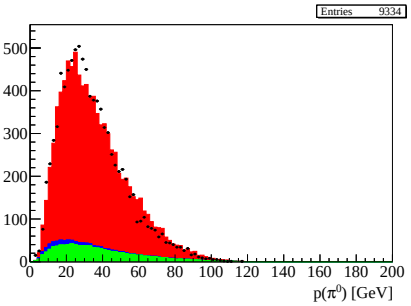

(d) $p(\pi^0)$

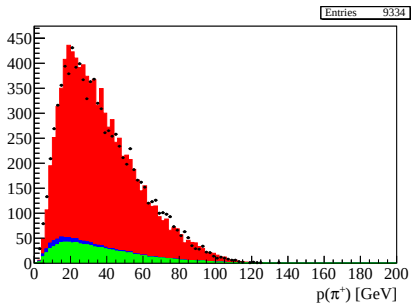

(e) $p(\pi^+)$

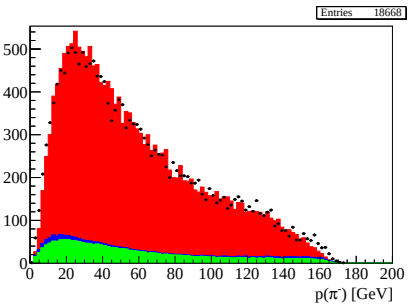

(f) $p(\pi^-)$ (two entries per event)

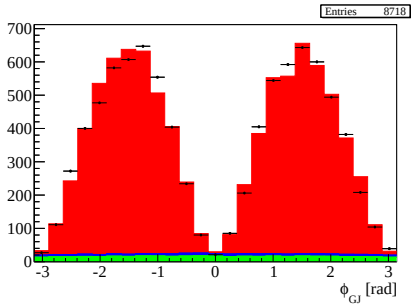

(g) φ_{GJ}

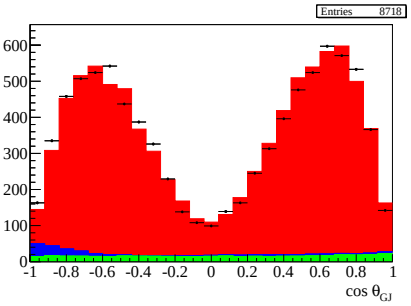

(h) $\cos\vartheta_{\mathrm{GJ}}$

Figure E.4.: Comparison between $\pi^-\eta$ data and fit prediction for $m \in [m_{a_2} + \Gamma_{a_2}, 1.6\,\mathrm{GeV}] = [1425\,\mathrm{MeV}, 1600\,\mathrm{MeV}]$. Other details as in Fig. 8.10.

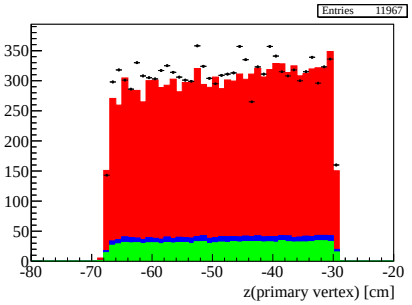

(a) z of primary vertex

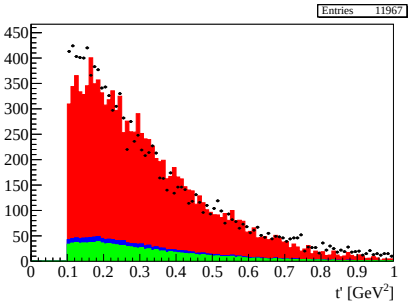

(b) t'

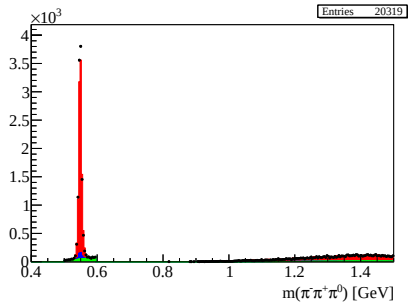

(c) $m(\pi^-\pi^+\pi^0)$ (two combinations)

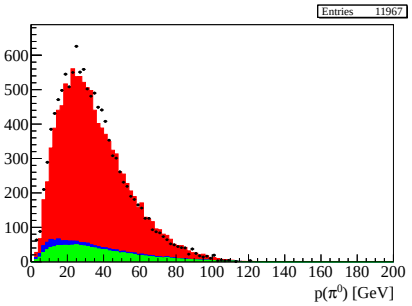

(d) $p(\pi^0)$

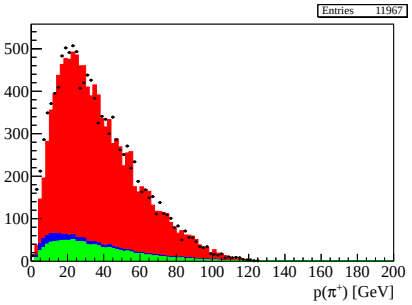

(e) $p(\pi^+)$

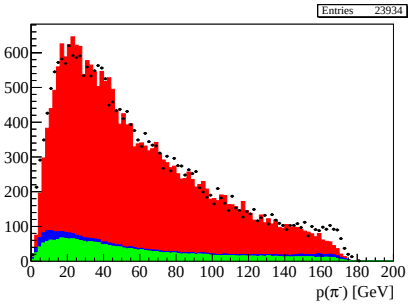

(f) $p(\pi^-)$ (two entries per event)

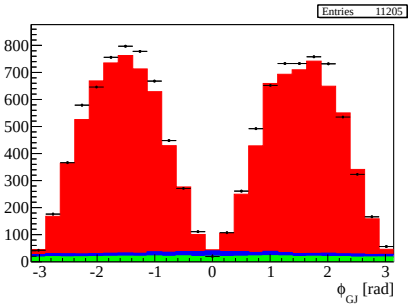

(g) φ_{GJ}

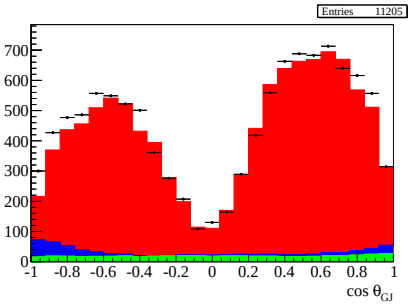

(h) $\cos\vartheta_{\mathrm{GJ}}$

Figure E.5.: Comparison between $\pi^-\eta$ data and fit prediction for $m \in [1.6\,\mathrm{GeV}, 2\,\mathrm{GeV}]$. Other details as in Fig. 8.10.

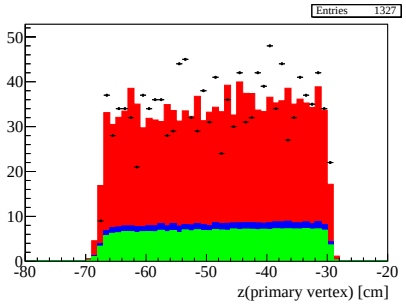

(a) z of primary vertex

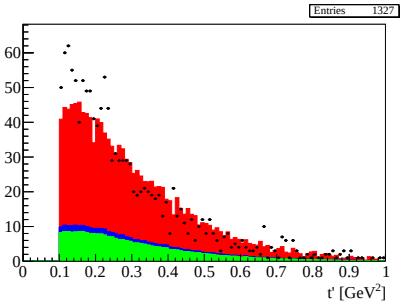

(b) t'

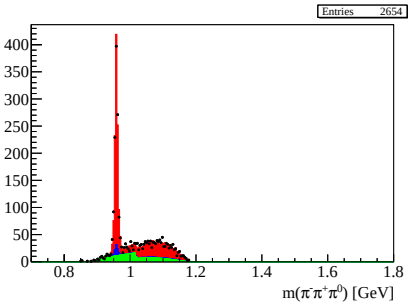

(c) $m(\pi^-\pi^+\eta)$ (two combinations)

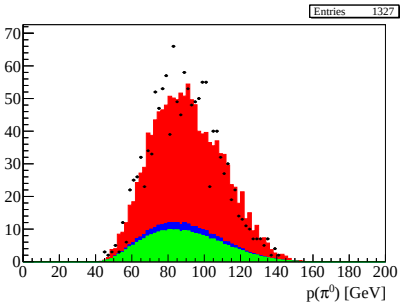

(d) $p(\eta)$

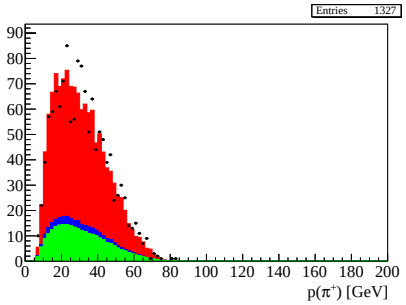

(e) $p(\pi^+)$

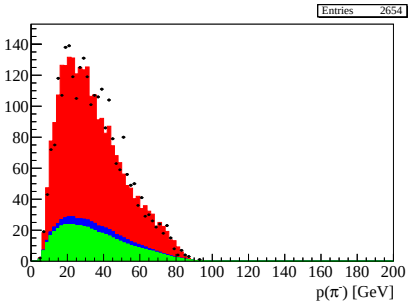

(f) $p(\pi^-)$ (two entries per event)

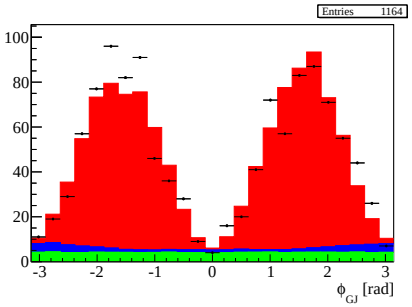

(g) φ_{GJ}

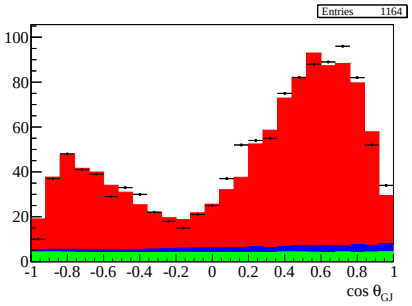

(h) $\cos\vartheta_{\mathrm{GJ}}$

Figure E.6.: Comparison between $\pi^-\eta'$ data and fit prediction for $m \in [m_\pi + m_{\eta'}, m_{a_2}] = [1097\,\mathrm{MeV}, 1318\,\mathrm{MeV}]$. Other details as in Fig. 8.10.

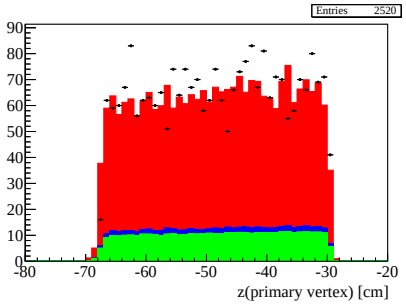

(a) z of primary vertex

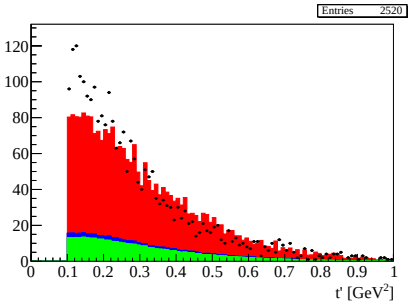

(b) t'

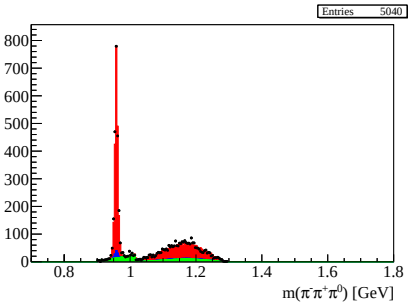

(c) $m(\pi^-\pi^+\eta)$ (two combinations)

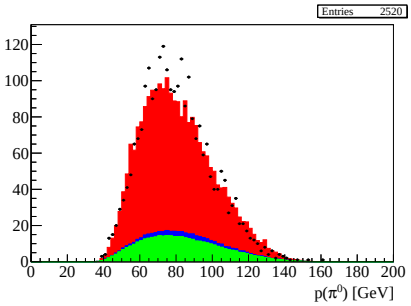

(d) $p(\eta)$

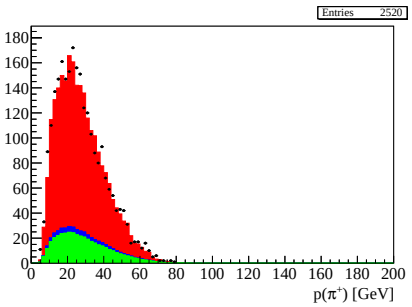

(e) $p(\pi^+)$

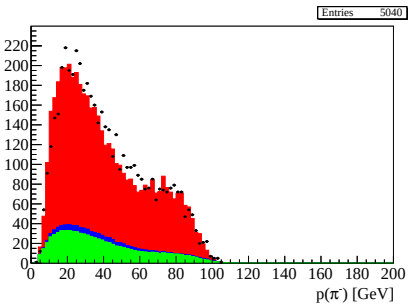

(f) $p(\pi^-)$ (two entries per event)

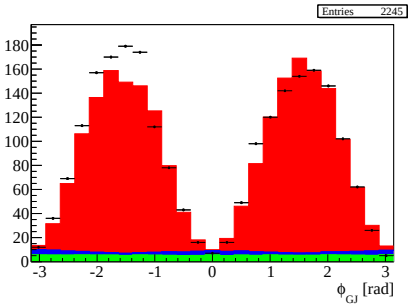

(g) φ_{GJ}

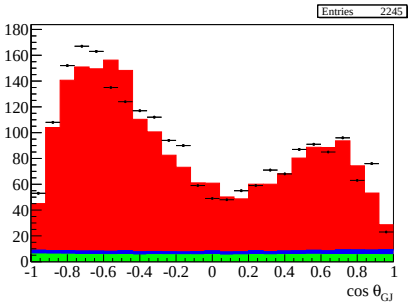

(h) $\cos\vartheta_{\mathrm{GJ}}$

Figure E.7.: Comparison between $\pi^-\eta'$ data and fit prediction for $m \in [m_{a_2}, m_{a_2}+\Gamma_{a_2}] = [1318\,\mathrm{MeV}, 1425\,\mathrm{MeV}]$. Other details as in Fig. 8.10.

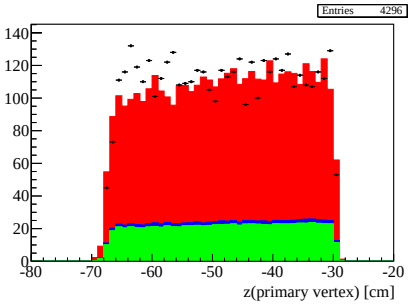

(a) z of primary vertex

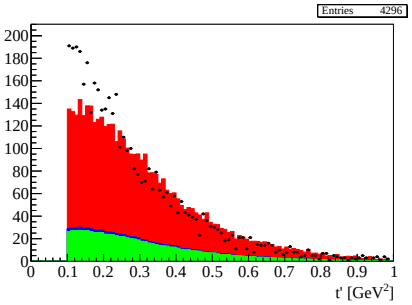

(b) t'

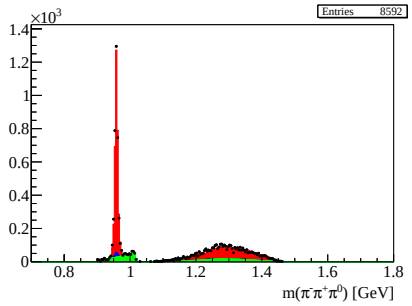

(c) $m(\pi^-\pi^+\eta)$ (two combinations)

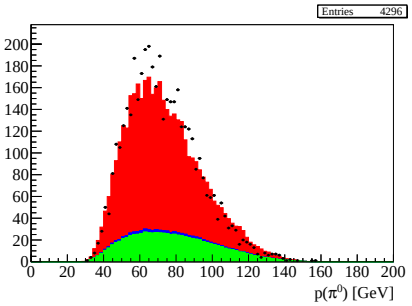

(d) $p(\eta)$

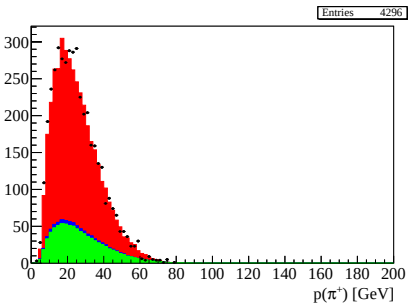

(e) $p(\pi^+)$

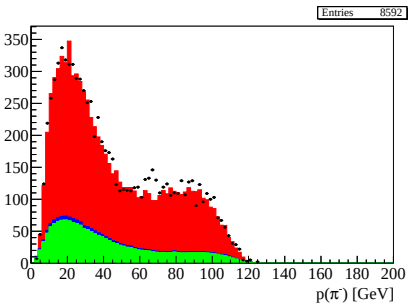

(f) $p(\pi^-)$ (two entries per event)

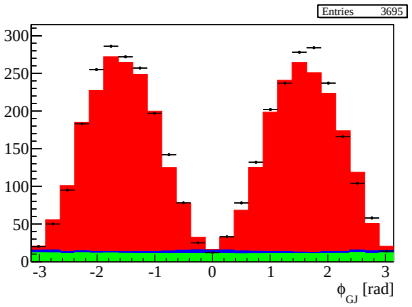

(g) φ_{GJ}

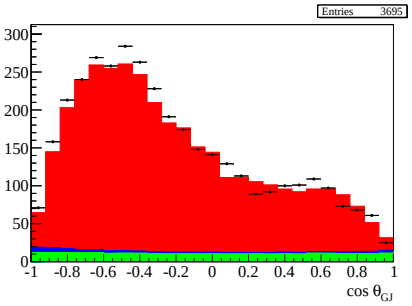

(h) $\cos\vartheta_{\mathrm{GJ}}$

Figure E.8.: Comparison between $\pi^-\eta'$ data and fit prediction for $m \in [m_{a_2} + \Gamma_{a_2}, 1.6\,\mathrm{GeV}] = [1425\,\mathrm{MeV}, 1600\,\mathrm{MeV}]$. Other details as in Fig. 8.10.

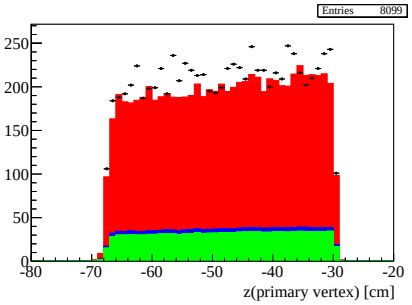

(a) z of primary vertex

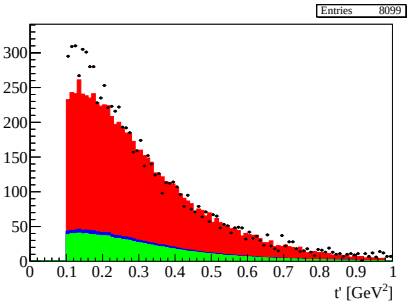

(b) t'

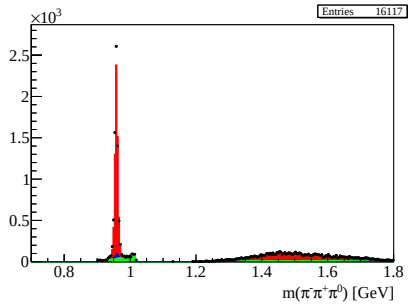

(c) $m(\pi^-\pi^+\eta)$ (two combinations)

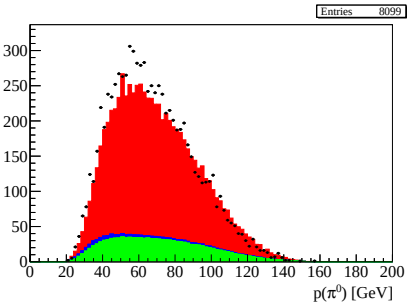

(d) $p(\eta)$

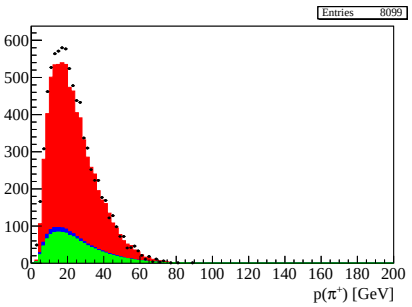

(e) $p(\pi^+)$

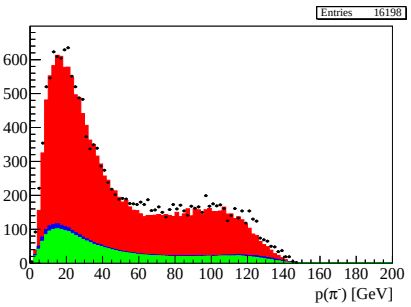

(f) $p(\pi^-)$ (two entries per event)

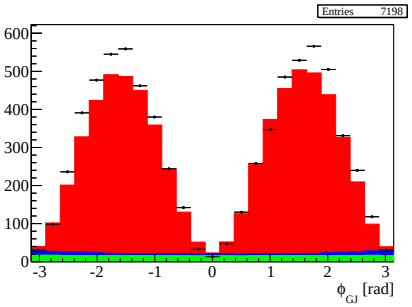

(g) φ_{GJ}

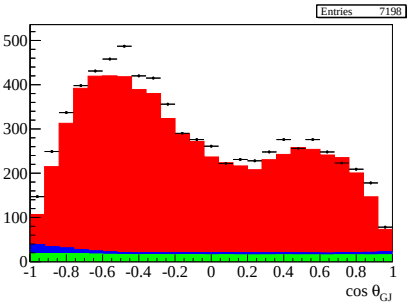

(h) $\cos\vartheta_{\mathrm{GJ}}$

Figure E.9.: Comparison between $\pi^-\eta'$ data and fit prediction for $m \in [1.6\,\mathrm{GeV}, 2\,\mathrm{GeV}]$. Other details as in Fig. 8.10.

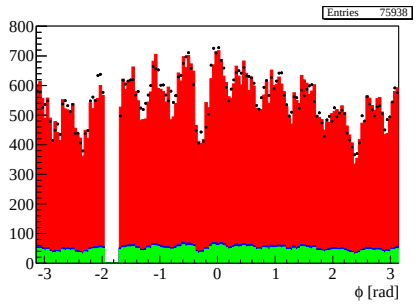

(a) Azimuthal emission angle of the recoil proton

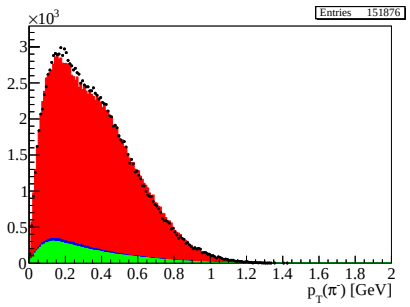

(b) Transverse momentum of the π^- (two entries per event)

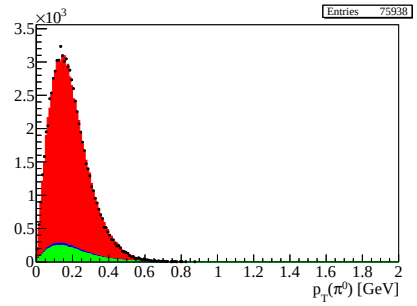

(c) Transverse momentum of the π^0

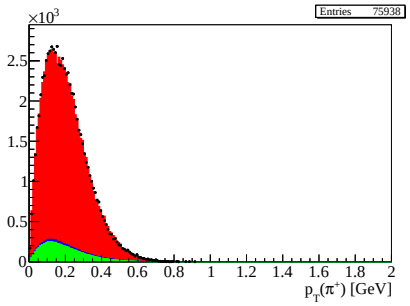

(d) Transverse momentum of the π^+

Figure E.10.: Comparison between $\pi^-\eta$ data and fit prediction for additional quantities for $m(\pi^-\eta) < 2\,\text{GeV}$. Color code as in Fig. 8.10.

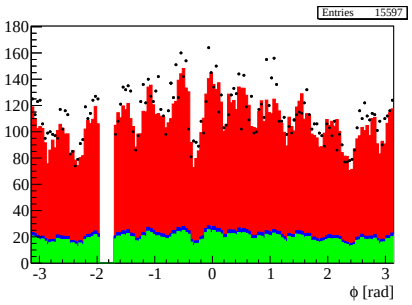

(a) Azimuthal emission angle of the recoil proton.

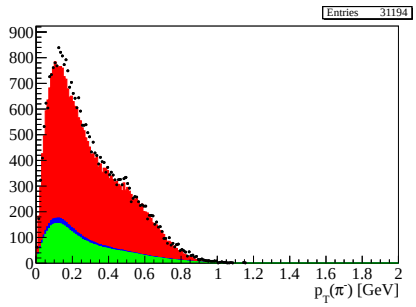

(b) Transverse momentum of the π^- (two entries per event)

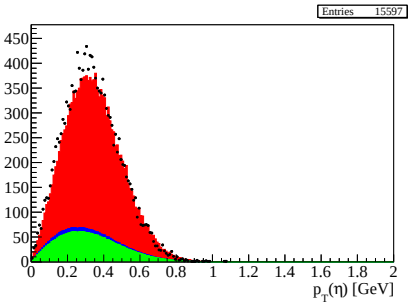

(c) Transverse momentum of the η

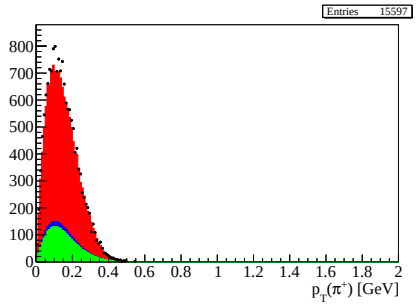

(d) Transverse momentum of the π^+

Figure E.11.: Comparison between $\pi^-\eta'$ data and fit prediction for additional quantities for $m(\pi^-\eta') < 2\,\text{GeV}$. Color code as in Fig. 8.10.

F. Cross-section Formula

This appendix collects a few useful formula, mostly concerning the mass-dependent fit. Following Ref. [Jackson, 1964], the differential cross-section for the production and subsequent decay of a resonance can be written in factored form

$$\mathrm{d}\sigma = F\mathrm{d}\Phi_n|\mathcal{M}|^2 = F\mathrm{d}\Phi_n|f(m)|^2|A(m,\Omega)|^2. \tag{F.1}$$

Here F is a flux factor, $\mathrm{d}\Phi_n \equiv \mathrm{d}\Phi_n(P;p_1,\dots p_n)$ the Lorentz-invariant n-body phase-space for a system of total momentum P, and $\mathcal{M}$ is the amplitude which is assumed to factor into a part $f(m)$ which describes the production of the resonance for a given invariant mass m and into a part $A(m,\Omega)$ which describes its decay (Ω are the invariant masses and angles describing the decay). In our case there are three particles in the final state, the $\pi\eta$ ($\pi\eta'$) pair and the recoil proton. The phase-space can be factored as follows

$$\mathrm{d}\Phi_3(P;p_1,\dots p_n) = (2\pi)^3\mathrm{d}m^2\mathrm{d}\Phi_2(Q;p_1,p_2)\mathrm{d}\Phi_2(P;Q,p_3), \tag{F.2}$$

where Q is a four-vector with $Q^2 = m^2$. We can now write the cross-section in factorized form, to wit

$$\mathrm{d}\sigma = \underbrace{(2\pi)^3F|f(m)|^2\mathrm{d}\Phi_2(P;Q,p_3)}_{\mathrm{d}\sigma_{\mathrm{prod}}(m)} \times \underbrace{|A(m,\Omega)|^2\mathrm{d}m^2\mathrm{d}\Phi_2(Q;p_1,p_2)}_{\text{dynamics of the resonance}}. \tag{F.3}$$

Propagation and decay of the resonance are now separated from its production.[1] The two-body phase-space in the rest-frame where $Q = (m,\mathbf{0})$ is

$$\mathrm{d}\Phi_2(m;\mathbf{p},-\mathbf{p}) = \frac{|\boldsymbol{p}|\mathrm{d}\Omega}{4(2\pi)^6 m}. \tag{F.4}$$

We shall now discuss the the dynamical term

$$|A(m,\Omega)|^2\mathrm{d}m^2\mathrm{d}\Phi_2(Q;p_1,p_2) = 2m|A(m,\Omega)|^2\mathrm{d}m\,\mathrm{d}\Phi_2(Q;p_1,p_2).$$

We assume that the resonance amplitude can be written as

$$A(m,\Omega) = BW(m)\times\psi(m,\Omega), \tag{F.5}$$

where $\psi(m,\Omega)$ is the known decay amplitude which encodes the kinematic requirements and, in an isobar model, dynamical assumptions about the decay. The mass-indepedent fit gives us the amplitudes with its dependencies on the production and the decay in-

[1] Ref. [Pišút and Roos, 1968] identifies a number of assumptions made in this type of formulas.

tegrated out. We are thus left with a sampling in m of what was suggestively denoted $BW(m)$ which we want to model in order to extract the physical content of the partial waves.

For a single resonance, the usual form is that of a Breit-Wigner resonance,

$$BW(m) = \frac{\sqrt{m\Gamma(m)}}{m^2 - m_0^2 - im_0\Gamma_{\text{tot}}(m)}. \tag{F.6}$$

Here m_0 is the nominal mass of the resonance, $\Gamma(m)$ is its partial width for the decay under consideration, which is usually parametrized as

$$\Gamma(m) = \Gamma_0 \frac{q}{m}\frac{m_0}{q_0}\left(\frac{B_L((qR)^2)}{B_L((q_0R)^2)}\right)^2, \tag{F.7}$$

with q the breakup momentum for mass m, q_0 its value at resonance, B_L the Blatt-Weisskopff factors [Chung, 2010; von Hippel and Quigg, 1972] which ensure the correct asymptotic behavior, required by analyticity, for the orbital angular moemntum L of the decay, and R an empirical interaction radius which is commonly taken to be 1 fm, but which can be fitted as a free parameter. Γ_0 is then the nominal partial width of the resonance decaying into the particular channel under consideration. The total width is given as the sum over the partial widths Eq. (F.7) weigthed with their branching ratios, i.e.

$$\Gamma_{\text{tot}}(m) = \sum_i BR_i\Gamma_i(m) \quad \text{where} \quad \sum_i BR_i = 1. \tag{F.8}$$

Since (above threshold) the phase of the Breit-Wigner function is determined by its denominator which is independent of the decay channels, the Breit-Wigner phase is determined by the leading channels. For reference, we give the first few angular momentum barrier factors in the normalization $B_L(1) = 1$ of Ref. [Chung, 2010] (the other common normalization $B_L(z) \to 1$ for $z \to \infty$ is obtained by dropping the factor in the numerator)

$$\begin{aligned}
B_0(z) &= 1, \\
B_1(z) &= \sqrt{\frac{2z}{z+1}}, \\
B_2(z) &= \sqrt{\frac{13z^2}{(z-3)^2+9z}}, \\
B_3(z) &= \sqrt{\frac{277z^3}{z(z-15)^2+9(2z-5)^2}}, \\
B_4(z) &= \sqrt{\frac{12746z^4}{(z^2-45z+105)^2+25z(2z-21)^2}}.
\end{aligned} \tag{F.9}$$

For the $a_2(1320)$, the following parameters were used for the final states, their (orbital)

angular momenta and branching fractions:

$$a_2(1320) \to \pi\rho: \quad L = 2 \quad BR = 0.8$$
$$a_2(1320) \to \pi\eta: \quad L = 2 \quad BR = 0.2.$$

The branching to $\pi\eta'$ was neglected, as were the other tabulated decays modes from Ref. [Nakamura et al., 2010]. The importance of using the dynamical width, coupled-channel Breit-Wigner function is illustrated in Fig. F.1, where one can see that the single-channel Breit-Wigner function introduces a spurious mass shift as well as a spurious phase-motion compared to a description taking the leading channels into account.

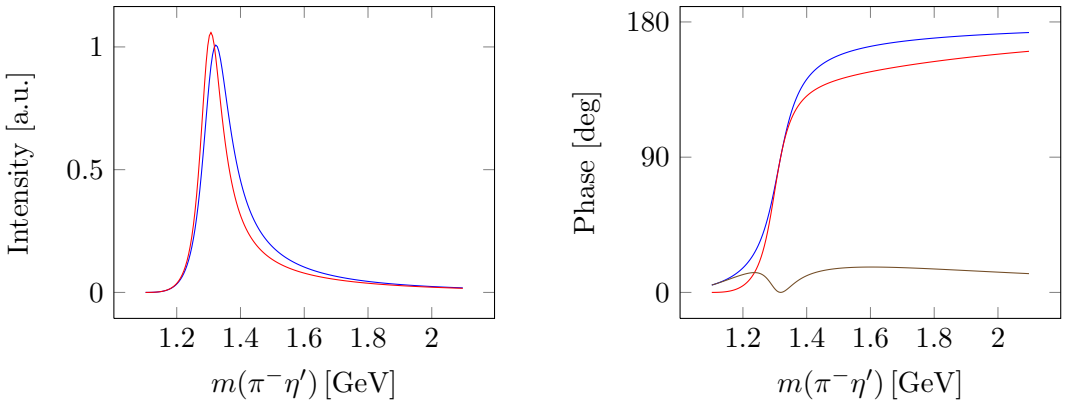

Figure F.1.: Importance of the dynamical width Breit-Wigner for the description of the $a_2(1320) \to \pi^-\eta'$ decay. —— shows the single-channel Breit-Wigner, —— shows the coupled-channel Breit-Wigner. Additionally, in the right plot the relative difference in phase of the two Breit-Wigner amplitudes is plotted as ——.

G. Further Two-Body Final States

In this appendix we quickly summarize some results obtained for the reactions $K^- p \to K^0_S \pi^- p$ and $\pi^- p \to K^0_S K^- p$ on a subset of the 2008 data. The same reactions at lower beam momenta were previously analyzed by Refs. [Cleland et al., 1982a,b; Martin et al., 1978]. Since kinematic considerations show that the charged particles lie largely outside the acceptance of the RICH detector, the data samples were selected by identifying the beam particle as either a kaon or a pion and then tagging strangeness by the displaced $K^0_S \to \pi^-\pi^+$ decay. The CEDAR purity turned out insufficient to select a clean pion beam, therefore we didn't perform partial-wave analysis on the $K^- K^0_S$ data, which is large polluted by $\pi^- K^0_S$ data. Instead we show that some of the same features as in the $\pi^-\eta$ data arise in this channel in Fig. G.1. A possible source for these data is the COMPASS 2009 positive hadron beam data: during the data taking, one CEDAR was set up for π^+ identification. This should allow for a clean selection of the $\pi^+ p \to K^+ K^0_S p$ reaction.

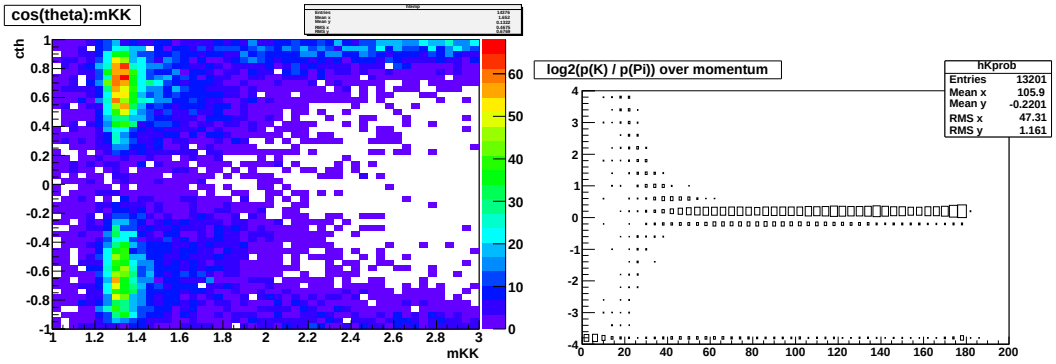

Figure G.1.: The left plot shows $\cos\vartheta_{\mathrm{GJ}}$ vs. $m(KK)$ where we clearly see the $a_2(1320)$ resonance. At high masses we see the same kind of forward-backward peaking also observed in the $\pi^-\eta^{(\prime)}$ states. The right plot illustrates the contamination from the kaon beam. As a function of the momentum of the charged track emanating from the primary vertex, we depict the logarithm of ratio of the RICH likelihoods for kaon and pion for this track. Where the RICH cannot distinguish the particles, we see the same likelihoods, i.e. the logarithm of the ratio is zero, and at low momenta where the RICH is efficient, we see two branches: one for pions and one for kaons. Since strangeness is tagged by the K^0_S, and assuming the target stays intact, this in turn means that the beam contains a large admixture of kaons.

In 2008 the CEDARs were set to positive Kaon identification. Therefore a clean kaon

beam sample could be obtained and we could perform partial-wave analysis on the $K\pi$ data, where we find the known kaon resonance $K^*(892)$ in the P_+ wave and $K^*(1430)$ in the D_+ wave. This is illustrated in Fig. G.2. Acceptance correction were not taken into account for this analysis. The data are a subset of the 2008 data.

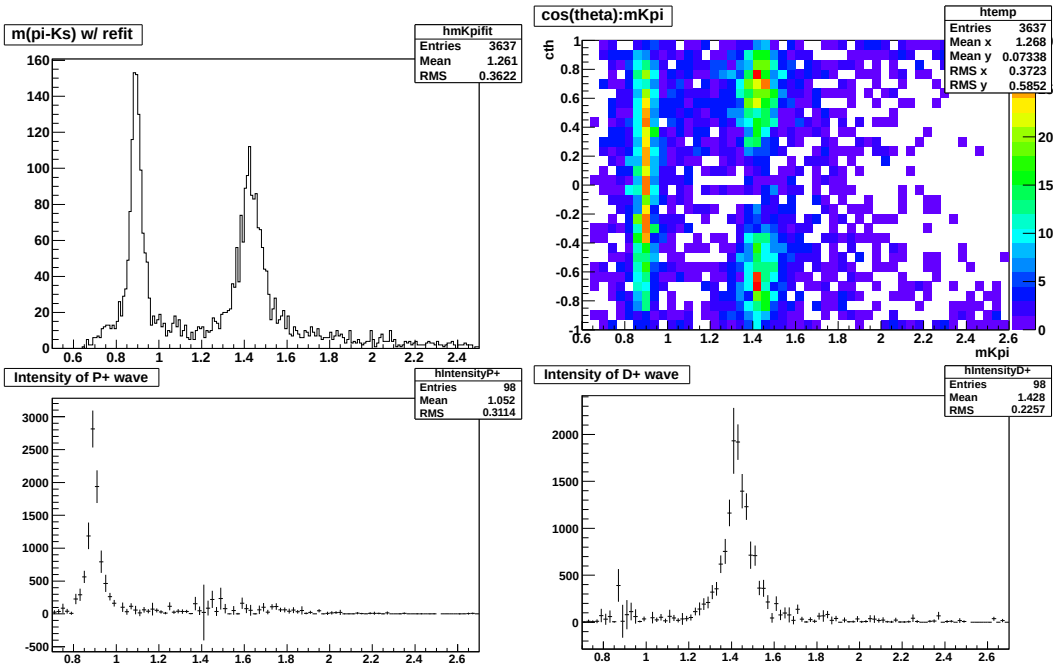

Figure G.2.: These plots show the $K^0_S\pi^-$ data. On the top left we see the invariant mass spectrum, where we already see that it's dominated by the $K^*_1(892)$ and $K^*_2(1430)$ resonances. In the top right we see again mass vs. $\cos\vartheta_{\mathrm{GJ}}$, where the spin-1 and spin-2 nature of the resonances is already evident. This is confirmed by the partial wave results depicted in the lower row, where on the left we see the P_+ wave, on the right the D_+ wave. The observed masses and widths are compatible with the tabulated values [Nakamura et al., 2010]. Keep in mind the difference in axis ranges between the upper and lower plot.

H. Partial-Wave Analysis of the $\pi^-\pi^-\pi^+\eta$ System

As mentioned in Sec. 1.2, one of the main channels where one expects to see decays of a hybrid meson is the $\pi^- f_1$ channel. The main decay channel of the f_1 resonance is $\pi\pi\eta$, and indeed we find the f_1 as a strong peak in the invariant mass spectrum for the $\pi^-\pi^+\eta$ system in Fig. 4.9a.

Since the f_1 peak sits on a huge background, an analysis will have to take into account the full four-body system, also taking into account other intermediate states such as $\eta a_2(\to \pi\rho)$, $\rho a_2(\to \eta\pi)$ and $\rho a_0(\to \eta\pi)$, where the subsequent decay of the second particle is given in brackets, or reflections from the $\pi^-\eta'$ data, leading to a difficult task. Additionally, experimental resolution smears the sharp f_1 peak and this has to be taken into account when calculating isobar amplitudes for the πf_1 partial waves. We follow a procedure developed at the VES experiment: from a fit to the f_1 peak with a smeared Breit-Wigner function taking the tabulated mass and width of the f_1, the width of the Gaussian smearing is determined. In calculating the amplitudes, the real and imaginary parts are then smeared separately by folding the Breit-Wigner amplitudes with a Gaussian of half the width determined for the smearing of the intensity. Additionally, charge-conjugation invariance imposes symmetry requirements on the $f_1 \to \pi^-\pi^+\eta$ decay amplitude. Therefore, the f_1 amplitude should not be decomposed further, but instead be written in a way that engulfs this knowledge.

This is not the only technical difficulty in the analysis. Another concerns the highly anisotropic phase-space population. Together with the large four-body phase-space, an isotropic population of the phase-space as in Eq. (6.9) would lead to very inefficient use of computing time. Therefore a combination of weighted generators has to be used in the analysis.

The required work for all these tasks was found to exceed the time-constraints of this PhD thesis, especially as also work on the Monte Carlo infrastructure, ECAL calibration, kinematic fitting software and analysis software was necessary. Nevertheless, a preliminary analysis was performed with the purely geometrical Monte Carlo software discussed in Sec. 3.4.3, and we collect some of the preliminary results in this appendix. Also, the dissertation of H. Yang concerns itself with this analysis.

We mention that the production characteristics of the f_1 meson at COMPASS are discussed in Ref. [Wöhrmann, 2010]. One of the observations made there is that at high invariant masses of the $\pi^- f_1$ system a forward-backward peaking is observed similar to the one in the $\pi^-\eta$ and $\pi^-\eta'$ systems.

In the Dalitz plot of Fig. H.1, taking into account that the background beneath the f_1 peak also appears in the Dalitz plot, we see that the f_1 decays mainly via $f_1 \to a_0(980)\pi$.

Interference with the decay via $\eta(\pi\pi)_S$ leads to a peculiar structure.

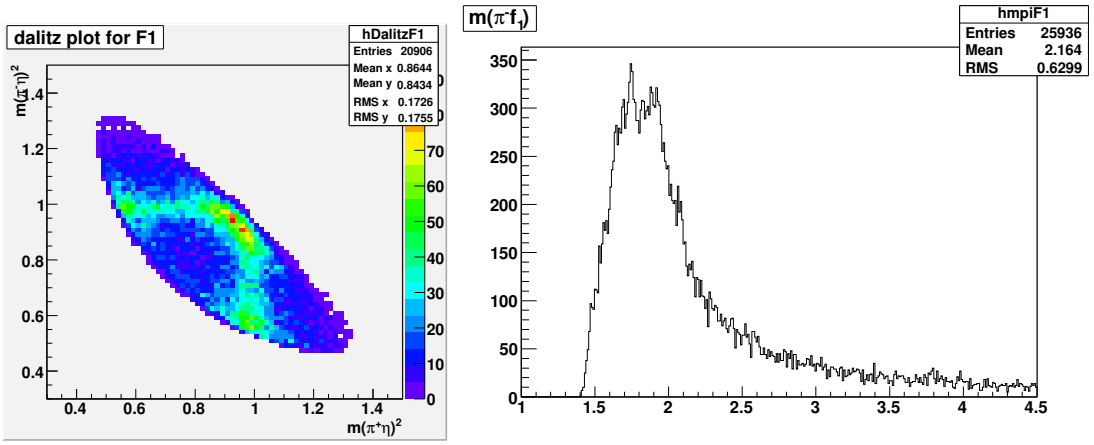

Figure H.1.: Overall features of the $\pi^- f_1$ final state. On the left the Dalitz plot for the $\pi^-\pi^+\eta$ data in a mass-window around the f_1 peak. On the right the mass spectrum obtained combining the data from the mass window with the remaining pion.

In the following we show some waves in the $\pi^- f_1$ subsystem. The $\pi^-\eta'$ subsystem is also included in this analysis, its amplitudes treated incoherently with the remainder of the data, in accordance with the considerations of Sec. 7.3. This work was done in collaboration with D. Ryabchikov, who presented results obtained with the same program using data from the VES collaboration at the Hadron2011 conference.[1]

Fig. H.2 shows the intensities of the main waves in the $\pi^- f_1$ system. The labeling is $J^{PC} M^\epsilon \pi^- f_1 W$, where W refers to the orbital angular momentum of the $\pi^- f_1$ system in spectroscopic notation and the other symbols have their common meanings. Unlike the two pseudo-scalar case treated in the rest of this thesis, the spin of the f_1 can couple with the orbital angular momentum, and thus total orbital momentum J is no longer redundant with the orbital momentum.

We see broad bumps in the 1^{++} and 1^{-+} waves centered at about 1.8 GeV. In the 1^{-+} D-wave this bump is shifted towards higher masses compared with the S-wave. This is consistent with the influence of angular momentum barriers. In the 4^{++} wave, we see a bump which probably corresponds to the $a_4(2040)$. The apparent higher mass compared to our main analysis (see Sec. 9.3) is again probably due to angular momentum barriers.

Corresponding phase-motions are shown in Fig. H.3. We see that both 1^{-+} waves are phase-locked with respect to each other, in accordance with a resonant interpretation. Their phase is also constant with respect to the 1^{++} wave. An interpretation in terms of resonances thus requires the simultaneous introduction of a non-established resonance in both 1^{-+} and 1^{++} waves. See D. Ryabchikov's aforementioned presentation for the problems this poses on an interpretation. Besides these, we also see that the 4^{++} wave

[1] The results do not appear in the conference proceedings but the presentation is available online at `http://www.slac.stanford.edu/econf/C110613/slides/154-slides.pdf`.

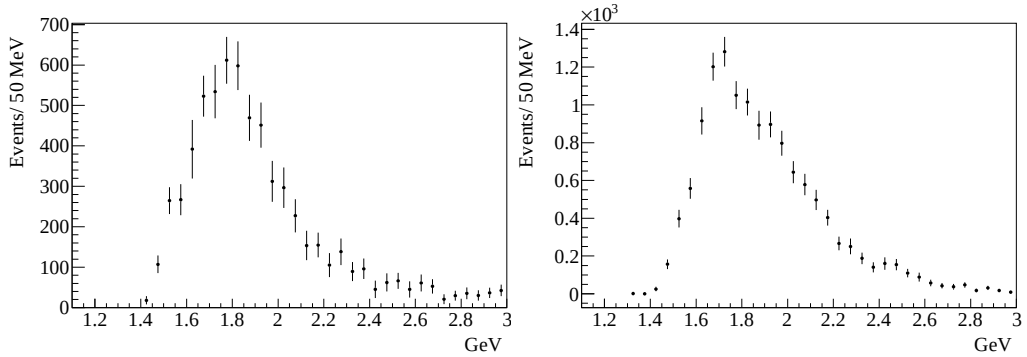

(a) $1^{-+}1^{+}\pi^{-}f_1S$ (b) $1^{++}0^{+}\pi^{-}f_1P$

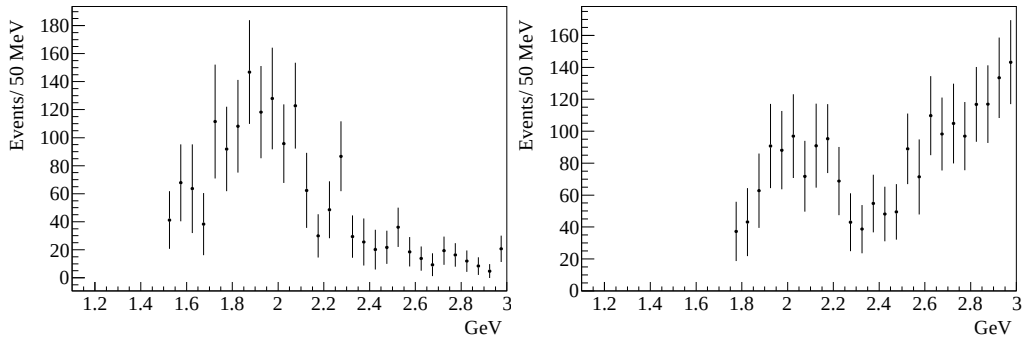

(c) $1^{-+}1^{+}\pi^{-}f_1D$ (d) $4^{++}1^{+}\pi^{-}f_1F$

Figure H.2.: Main $\pi^{-}f_1$ waves.

shows a very clean phase-motion with respect to the other waves, consistent with an interpretation of the bump around 2 GeV as due to the $a_4(2040)$ resonance. This decay mode has not been previously observed. Finally, we point out that waves containing the contested $\eta(1295)$ which decays to $\pi^{-}\pi^{+}\eta$ do not appear to be necessary for a convincing fit of the data.

For reference, we give the integrated intensities for the exotic 1^{-+} waves for its different decays. These numbers include acceptance corrections only for the geometrical acceptance of the spectrometer. We show the numbers for different integration ranges, owing to different thresholds and the near-absence of the $\pi\eta'$ P-wave above 2 GeV:

Decay	$1.2-2$ GeV	$1.5-2$ GeV	$1-3$ GeV
$\pi\eta'$ P-wave	4427	4279	5108
πf_1 S-wave	4846		6338
πf_1 D-wave	1011		1617

Our data show no strong preference for the decay to πf_1.

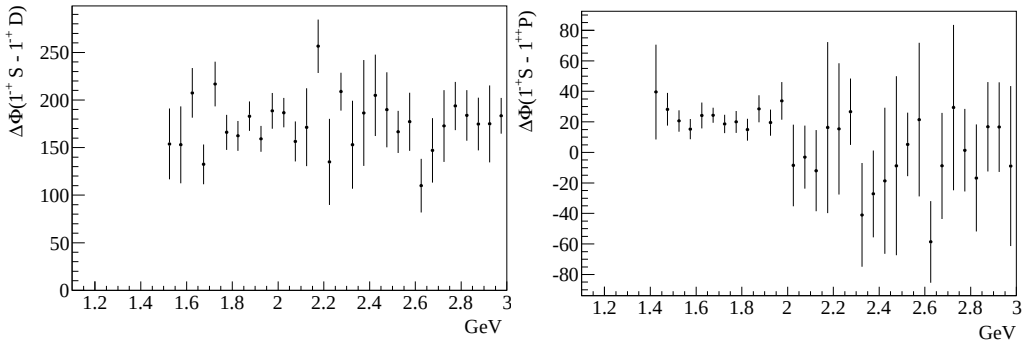

(a) $\arg(1^{-+}S/1^{-+}D)$ (b) $\arg(1^{-+}S/1^{++}P)1^{++}0^{+}\pi^{-}f_1P$

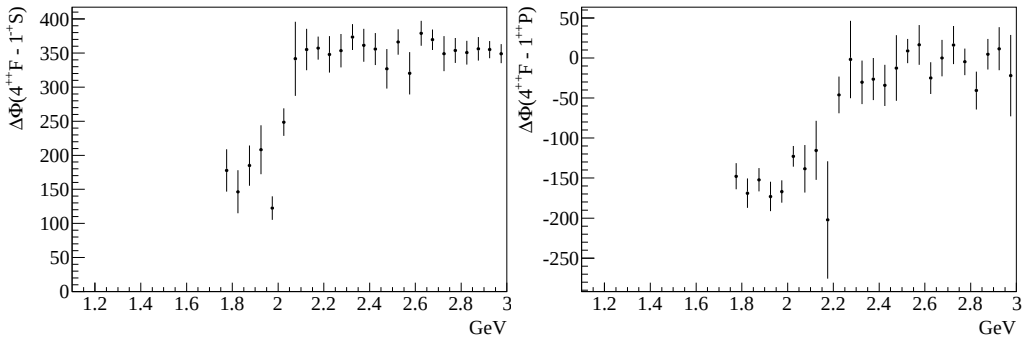

(c) $\arg(4^{++}F/1^{-+}S)1^{-+}1^{+}\pi^{-}f_1D$ (d) $\arg(4^{++}F/1^{++}P)4^{++}1^{+}\pi^{-}f_1F$

Figure H.3.: Phases between the main $\pi^{-}f_1$ waves. The 1^{-+} and 1^{++} waves show no significant relative phase motion. The 4^{++} shows a phase motion compatible with the $a_4(2040)$ compared to both other waves.

I. The final state $\pi^-\pi^+\pi^-\pi^0\pi^0$

Here we briefly show some features of the channel which is selected by adding a π^0 to our $\pi^-\eta$ selection: $\pi^-\pi^+\pi^-\pi^0\pi^0$, which contains the channel $\pi b_1(1235)$, or, since the b_1 almost exclusively decays to $\pi\omega$, the channel $\pi^-\pi^0\omega$. Note that both isospin substates b_1^- and b_1^0 appear. In Fig. I.1 we see how this state is selected. We notice in passing that the $\eta \to \pi^-\pi^+\pi^0$ is very much suppressed compared to our $\pi^-\eta$ selection. A mass spectrum for the $\pi\eta$ systems (not shown) contains an $a_0(980)$ peak. A possible interpretation for this appearance of the a_0 is as a result of the isospin violating $f_0 \leftrightarrow a_0$ mixing. Since the f_0 contribution is well understood from COMPASS's $\pi^-\pi^+\pi^-$ analysis, this would open a way to a measurement of the isospin violation in a similar vein as a recent analysis by the VES collaboration [Dorofeev et al., 2011].

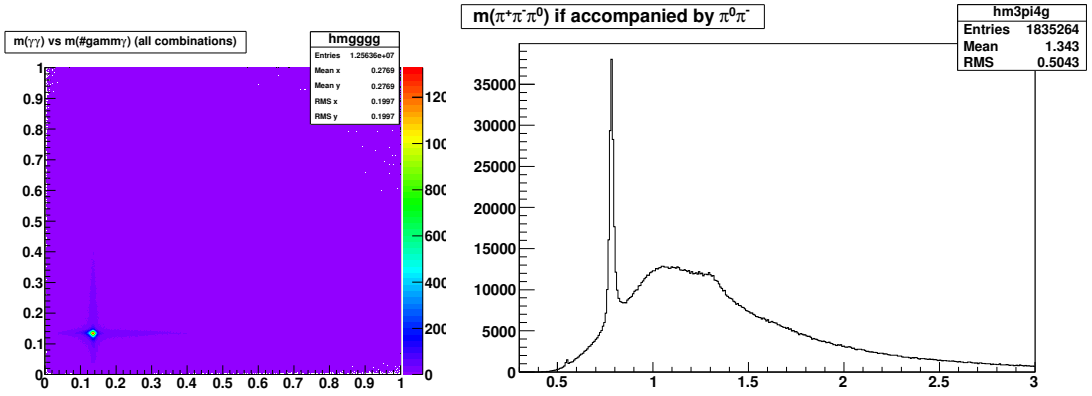

Figure I.1.: Selection of the $\pi^-\pi^+\pi^-\pi^0\pi^0$ final state. We show on the left the invariant masses of photon pairs against the corresponding other combination, the $\pi^0\pi^0$ peak can be amde out clearly (fully symmetrized, 6 entries per event). On the right we show the mass spectrum for the $\pi^-\pi^+\pi^0$ subsystem where for each event all four combinations are shown.

Selecting the ω with a mass cut, we can investigate the structure of the $\omega\pi^-\pi^+$ system as shown in Fig. I.2. Near the three-body threshold we see the $a_2(1320)$ meson. This was cut out in a previous analysis of the $\pi^- b_1$ channel [Lu et al., 2005]. At higher three-body masses, we find a large fraction of events decaying via the $\rho(770)$ meson, especially in the mass range around 1800 MeV where the a_2' is predicted which dominantly decays to $\rho\omega$ [Barnes et al., 1997]. Besides this, the $b_1(1235)$ can be made out in both combinations of $m(\omega\pi)$. We note that the $a_2(1320)$ lies below the $\rho\omega$ threshold, yet the decay fraction to $\pi\pi\omega$ is roughly 10% [Nakamura et al., 2010]. Unfortunately, we do not have a Dalitz

plot available. The particle data group actually lists no study of the $a_2 \to \omega\pi\pi$ decay after 1974, and a spin-parity analysis of the enhancement has never taken place, with a total of only a few hundred events observed in the listed measurements. Therefore, it's certainly a worthy endeavour to study this in COMPASS data.

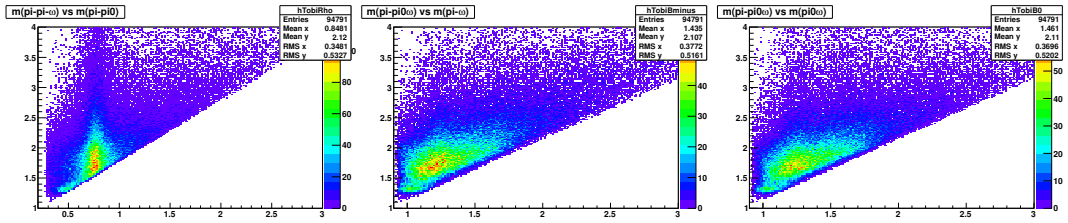

(a) $m(\pi^-\pi^0)$ vs. $m(\pi^-\pi^0\omega)$ (b) $m(\pi^-\omega)$ vs. $m(\pi^-\pi^0\omega)$ (c) $m(\pi^0\omega)$ vs. $m(\pi^-\pi^0\omega)$

Figure I.2.: Goldhaber plots illustrating the composition of the $\pi^-\pi^0\omega$ system. In each plot, the vertical axis represents the invariant mass of the $\pi^-\pi^0\omega$ system, the horizontal axis the invariant mass of a two-body subsystem.

Danksagung

Diese Arbeit wäre nicht entstanden ohne die Unterstützung meines Doktorvaters Wolfgang Dünnweber und meiner Münchner Gruppe, Črtomir Zupančič, Martin Faessler, Jean-François Rajotte, Massimo Bettinelli und Meike Dlaboha, sowie Yang Hao. Wesentliche Beiträge wurden durch die von mir getrietzten Bacheloranden, Masteranden und Diplomanden Kumud Dhibar, Zoha Roushan, Hauke Wöhrmann und Max Diefenbach, sowie von Christoph Raab (bei E18) geleistet. Ich hoffe, ich habe im Text auf ihre Beiträge im vollen Umfange verwiesen, doch ich bezweifle es. In Genf konnte ich immer mit Sasha Zvyagin und Reiner Geyers Unterstützung und Interesse rechnen. Otmar Biebel versprach mir ein zügiges Zweitgutachten und sorgte immer für funktionierende Kaffeemaschinen. Beides wesentliche Teile einer erfolgreichen Promotion.

Working with Dima Ryabchikov has been one of the great pleasures of this thesis. His curiosity has been a major drive in my trying to figure out these data. I used his software, several of his ideas, and profited immensely from the additional work he did during his crosscheck. His contributions cannot be overestimated.

Auch gilt mein Dank Stephan Paul, der meine Arbeit unterstützte, wo es möglich war. Mit seiner ganzen E18-Gruppe habe ich zusammengearbeitet, doch hervorheben möchte ich Alex Austregesilo, dessen Interesse an meinem PWA-Programm es zu einem tatsächlich funktionierenden gemacht hat.

I cannot remember how often I cursed at the COMPASS collaboration. Nevertheless, I can say that I enjoyed being a part of this community, and that I learned lots from all of you. In particular, I would like to thank Frank Nerling, Claude Marchand and Andrea Bressan, who have supported me very much, and my go-to-person for any question concerning the experiment, Johannes Bernhard.

This research was supported by the state of Bavaria, the Bundesministerium für Bildung und Forschung, the Maier-Leibnitz-Laboratorium der Universität München und der Technischen Universität München, dem Excellenzcluster Origin and Structure of the Universe. They all collaborated in making my contractual situation an always exciting game of alternating alternatives.

Ich widme diese Arbeit meinem Vater, der ihre Fertigstellung nicht mehr erlebt hat.

Bibliography

Abbon, P. et al. (COMPASS collaboration). *The COMPASS Experiment at CERN*. Nucl. Inst. Meth., A577:455–518, 2007. arXiv:hep-ex/0703049, URL http://dx.doi.org/10.1016/j.nima.2007.03.026. Cited on pages 21 and 40.

Abbon, P., et al. *The experience of building and operating COMPASS RICH-1*. Nucl. Inst. Meth., A639:15–19, 2011. URL http://dx.doi.org/10.1016/j.nima.2010.10.102. Cited on page 34.

Abele, A. et al. (Crystal Barrel collaboration). *Study of the $\pi^0\pi^0\eta'$final state in $\bar{p}p$ annihilation at rest*. Phys. Lett., B404:179–186, 1997. URL http://dx.doi.org/10.1016/S0370-2693(97)00526-1. Cited on pages 12, 103, and 136.

Abele, A. et al. (Crystal Barrel collaboration). *Exotic $\eta\pi$ state in $\bar{p}d$ annihilation at rest into $\pi^-\pi^0\eta p_{spectator}$*. Phys. Lett., B423:175–184, 1998. URL http://dx.doi.org/10.1016/S0370-2693(98)00123-3. Cited on page 11.

Abele, A. et al. (Crystal Barrel collaboration). *Evidence for a $\pi\eta$-P-wave in $\bar{p}p$-annihilations at rest into $\pi^0\pi^0\eta$*. Phys.Lett., B446:349–355, 1999. URL http://dx.doi.org/10.1016/S0370-2693(98)01544-5. Cited on page 11.

Adamovich, M. et al. (BEATRICE collaboration). *WA92: A fixed target experiment to trigger on and identify beauty particle decays*. Nucl. Inst. Meth., A379:252–270, 1996. URL http://dx.doi.org/10.1016/0168-9002(96)00480-9. Cited on page 39.

Adams, G. et al. (E852 collaboration). *Observation of a new $J^{PC} = 1^{-+}$ exotic state in the reaction $\pi^-p \to \pi^+\pi^-\pi^-p$ at 18 GeV/c*. Phys. Rev. Lett., 81:5760–5763, 1998. URL http://dx.doi.org/10.1103/PhysRevLett.81.5760. Cited on page 13.

Adams, G. et al. (CLEO collaboration). *Amplitude analyses of the decays $\chi_{c1} \to \eta\pi^+\pi^-$ and $\chi_{c1} \to \eta'\pi^+\pi^-$*. Phys. Rev. D, 84:112009, 2011. arXiv:1109.5843, URL http://dx.doi.org/10.1103/PhysRevD.84.112009. Cited on page 12.

Ader, J., et al. *Splitting of the cross-section into natural and unnatural parity exchange contributions for quasi-two-body reactions*. Nuovo Cim. A, 56:952–966, 1968. ISSN 0369-3546. 10.1007/BF02751610, URL http://dx.doi.org/10.1007/BF02751610. Cited on page 19.

Adolph, C. et al. (COMPASS collaboration). *First Measurement of Chiral Dynamics in $\pi^-\gamma \to \pi^-\pi^-\pi^+$*. Phys. Rev. Lett., 108:192001, 2012. arXiv:1111.5954, URL http://dx.doi.org/10.1103/PhysRevLett.108.192001. Cited on page 87.

Agostinelli, S. et al. (GEANT4 collaboration). *Geant 4 – a simulation toolkit*. Nucl. Inst. Meth., A506:250–303, 2003. URL http://dx.doi.org/10.1016/S0168-9002(03)01368-8. Cited on page 49.

Alde, D. et al. (IHEP-IISN-LANL-LAPP collaboration). *Evidence for a 1^{-+} Exotic Meson*. Phys. Lett., B205:397, 1988. URL http://dx.doi.org/10.1016/0370-2693(88)91686-3. Cited on page 11.

Alekseev, M. et al. (COMPASS collaboration). *Observation of a $J^{PC} = 1^{-+}$ exotic resonance in diffractive dissociation of 190 GeV/c π^- into $\pi^-\pi^-\pi^+$*. Phys. Rev. Lett., 104:241803, 2010. arXiv:0910.5842, URL http://dx.doi.org/10.1103/PhysRevLett.104.241803. Cited on pages 13, 87, and 137.

Alekseev, M. et al. (COMPASS collaboration). *The COMPASS 2008 Spectrometer*, 2012. To be submitted to Nucl. Instr. and Meth. A. Cited on pages 21, 46, and 59.

Alexandrov, Y. et al. *CHEOPS: CHarm Experiment with Omni-Purpose Setup*. 1995. URL http://wwwcompass.cern.ch/compass/publications/loi/loi_cheops.ps.gz. Cited on page 21.

Allison, J. et al. *Geant4 developments and applications*. IEEE Trans. Nucl. Sci., 53:270, 2006. URL http://dx.doi.org/10.1109/TNS.2006.869826. Cited on page 49.

Amelin, D. (VES collaboration). *Status of 0^{-+} in $\omega\pi^-\pi^0$ and $\pi^+\pi^-\pi^-$ channels*. In Chung and Wilutzki, editors, *Hadron Spectroscopy: Seventh international conference*, volume 432 of *AIP Conf. Proc.*, pages 770–773. 1998. URL http://dx.doi.org/10.1063/1.56088. Cited on page 13.

Amelin, D., et al. *Investigation of the reaction $\pi^-p \to \eta'\pi^0 n$ at the VES spectrometer*. Phys. Atom. Nucl., 67:1408–1415, 2004. URL http://dx.doi.org/10.1134/1.1777297. Cited on page 12.

Amelin, D. et al. *Investigation of Hybrid States in the VES Experiment at the Institute for High Energy Physics (Protvino)*. Phys. Atom. Nucl., 68:359–371, 2005. URL http://dx.doi.org/10.1134/1.1891185. Cited on pages 12, 13, and 100.

Amsler, C. and Törnqvist, N.A. *Mesons beyond the naive quark model*. Phys. Rept., 389:61–117, 2004. URL http://dx.doi.org/10.1016/j.physrep.2003.09.003. Cited on page 3.

Amsler, C. et al. (Crystal Barrel collaboration). *The pseudoscalar mixing angle Θ_{PS} from η and η' production in $\bar{p}p$ annihilation at rest*. Phys. Lett., B294:451–456, 1992. URL http://dx.doi.org/10.1016/0370-2693(92)91547-M. Cited on pages 103 and 137.

Antcheva, I. et al. *ROOT – A C++ framework for petabyte data storage, statistical analysis and visualization*. Comput. Phys. Commun., 180:2499–2512, 2009. URL http://dx.doi.org/10.1016/j.cpc.2009.08.005. Cited on pages 30 and 87.

Aoyagi, H., et al. *Study of the $\eta\pi^-$ system in the $\pi^- p$ reaction at 6.3 GeV/c*. Phys. Lett., B314:246–254, 1993. URL http://dx.doi.org/10.1016/0370-2693(93)90456-R. Cited on page 11.

Ascoli, G., et al. *Partial Wave Analysis of the 3π Decay of the A_2*. Phys. Rev. Lett., 25:962, 1970. URL http://dx.doi.org/10.1103/PhysRevLett.25.962. Cited on page 87.

Astbury, P. et al. (NA14 collaboration). *MEASUREMENT OF DEEP INELASTIC COMPTON SCATTERING OF HIGH ENERGY PHOTONS*. Phys. Lett., B152:419, 1985. URL http://dx.doi.org/10.1016/0370-2693(85)90521-0. Cited on page 39.

Aston, D., Lasinski, T.A., and Sinervo, P.K. *The SLAC Three-Body Partial Wave Analysis System*. Technical Report SLAC-0287, SLAC, 1985. Cited on page 83.

Austregesilo, A. and Schlüter, T. (COMPASS collaboration). *Partial-Wave Analysis of the Centrally Produced $\pi^+\pi^-$ System in pp Reactions at COMPASS*. In *Proceedings of QNP2012*. 2012. To be published, PoS(QNP2012)098. Cited on page 87.

Balitsky, I., Diakonov, D., and Yung, A. *EXOTIC MESONS WITH $J^{PC} = 1^{-+}$ FROM QCD SUM RULES*. Phys. Lett., B112:71–75, 1982. URL http://dx.doi.org/10.1016/0370-2693(82)90908-X. Cited on page 3.

Barberis, D. et al. (WA102 collaboration). *A Study of pseudoscalar states produced centrally in pp interactions at 450 GeV/c*. Phys. Lett., B427:398–402, 1998. arXiv:hep-ex/9803029, URL http://dx.doi.org/10.1016/S0370-2693(98)00403-1. Cited on page 76.

Barberis, D. et al. (WA102 collaboration). *Experimental evidence for a vector-like behavior of Pomeron exchange*. Phys. Lett., B467:165–170, 1999. arXiv:hep-ex/9909013, URL http://dx.doi.org/10.1016/S0370-2693(99)01186-7. Cited on page 76.

Barlow, R. *Extended maximum likelihood*. Nucl. Inst. Meth., A297(3):496 – 506, 1990. URL http://dx.doi.org/10.1016/0168-9002(90)91334-8. Cited on page 82.

Barnes, T., Close, F.E., and Swanson, E.S. *Hybrid and conventional mesons in the flux tube model: Numerical studies and their phenomenological implications*. Phys. Rev., D52:5242–5256, 1995. arXiv:hep-ph/9501405, URL http://dx.doi.org/10.1103/PhysRevD.52.5242. Cited on page 3.

Barnes, T., et al. *$Q\bar{Q}G$ Hybrid Mesons in the MIT Bag Model*. Nucl.Phys., B224:241, 1983. Cited on page 3.

Barnes, T., et al. *Higher Quarkonia*. Phys. Rev., D55:4157–4188, 1997. arXiv:hep-ph/9609339, URL http://dx.doi.org/10.1103/PhysRevD.55.4157. Cited on pages 3, 11, and 169.

Barrelet, E. *A new point of view in the analysis of two-body reactions.* Nuovo Cim. A, 8:331–371, 1972. URL http://dx.doi.org/10.1007/BF02732655. Cited on pages 91 and 92.

Baum, G. et al. (COMPASS Collaboration collaboration). *COMPASS: A Proposal for a Common Muon and Proton Apparatus for Structure and Spectroscopy.* 1996. URL http://wwwcompass.cern.ch/compass/proposal/ps/proposal.ps.gz. Cited on page 21.

Becker, H. et al. (CERN-Cracow-Munich collaboration). *A model-independent partial-wave analysis of the $\pi^+\pi^-$ system produced at low four-momentum transfer in the reaction $\pi^- p \uparrow\rightarrow \pi^+\pi^- n$ at 17.2 GeV/c.* Nucl. Phys., B151:46, 1979. URL http://dx.doi.org/10.1016/0550-3213(79)90426-7. Cited on page 91.

Beladidze, G. et al. (VES collaboration). *Observation of the decay $a_2(1320)^- \rightarrow \pi^-\eta'$.* Z. Phys., C54:235–238, 1992. URL http://dx.doi.org/10.1007/BF01566651. Cited on pages 12, 67, 69, and 136.

Beladidze, G. et al. (VES collaboration). *Study of $\pi^- N \rightarrow \eta\pi^- N$ and $\pi^- N \rightarrow \eta'\pi^- N$ reactions at 37 GeV/c.* Phys. Lett., B313:276–282, 1993. URL http://dx.doi.org/10.1016/0370-2693(93)91224-B. Cited on pages 11, 12, 69, 100, 103, and 136.

Berger, N. *Partial wave analysis at BES III harnessing the power of GPUs.* AIP Conf. Proc., 1374:553–556, 2011. arXiv:1108.5673, URL http://dx.doi.org/10.1063/1.3647201. Cited on page 83.

Bernard, C., et al. *Lattice calculation of 1^{-+} hybrid mesons with improved Kogut-Susskind fermions.* Phys. Rev., D68:074505, 2003. arXiv:0301024, URL http://dx.doi.org/10.1103/PhysRevD.68.074505. Cited on page 3.

Bernhard, J. *Aufbau des inneren Rings eines Recoildetektors am COMPASS-Experiment.* Master's thesis, Johannes Gutenberg Universität Mainz, 2007. URL http://wwwcompass.cern.ch/compass/publications/theses/2007_dpl_bernhard.pdf. Cited on page 25.

Bernhard, J., et al. (COMPASS collaboration). *Comment on 'Material Evidence of a 38 MeV Boson'.* 2012. arXiv:1204.2349. Cited on page 57.

Bijnens, J. and Ghorbani, K. *$\eta \rightarrow 3\pi$ at Two Loops In Chiral Perturbation Theory.* JHEP, 0711:030, 2007. arXiv:0709.0230, URL http://dx.doi.org/10.1088/1126-6708/2007/11/030. Cited on page 94.

Binon, F. et al. (IHEP – IISN – LAPP collaboration). *HODOSCOPE MULTIPHOTON SPECTROMETER GAMS-2000.* Nucl. Inst. Meth., A248:86, 1986. URL http://dx.doi.org/10.1016/0168-9002(86)90501-2. Cited on pages 39 and 40.

Binon, F. et al. (IHEP-IISN-LAPP collaboration). *A Combined Photon-Hadron Hodoscope Calorimeter.* Nucl. Inst. Meth., A269:101, 1988. URL http://dx.doi.org/10.1016/0168-9002(88)90866-2. Cited on page 36.

Bock, R., et al. *Data analysis techniques for high-energy physics experiments*. Cambridge University Press, 1990. Cited on page 142.

Bookwalter, C. (CLAS collaboration). *The Search for Exotic Mesons in $\gamma p \to \pi^+\pi^+\pi^- n$ with CLAS at Jefferson Lab*. In B. Grube, S. Paul, and N. Brambilla, editors, *Proceedings of the XIV International Conference on Hadron Spectroscopy*, eConf C110613. 2011. arXiv:1108.6191, URL http://www.slac.stanford.edu/econf/C110613. Cited on page 13.

Bovet, C., Milner, S., and Placci, A. *The Cedar Project. Cherenkov Differential Counters with Achromatic Ring Focus*. IEEE Trans. Nucl. Sci., 25:572–576, 1978. Cited on page 25.

Bramon, A., Escribano, R., and Scadron, M. *The $\eta - \eta'$ mixing angle revisited*. Eur. Phys. J., C7:271–278, 1999. arXiv:hep-ph/9711229, URL http://dx.doi.org/10.1007/s100529801009. Cited on pages 10 and 137.

Brandt, S. *Datenanalyse*. Spektrum Akademischer Verlag, 4th edition, 1999. English translation of the 3rd ed. available. Cited on pages 144 and 147.

Bychkov, V.N. et al. *The large size straw drift chambers of the COMPASS experiment*. Nucl. Inst. Meth., A556:66–79, 2006. Cited on page 29.

Chanowitz, M.S. and Sharpe, S.R. *Hybrids: Mixed States of Quarks and Gluons*. Nucl. Phys., B222:211, 1983. URL http://dx.doi.org/10.1016/0550-3213(83)90635-1. Cited on page 3.

Chew, G. and Frautschi, S.C. *REGGE TRAJECTORIES AND THE PRINCIPLE OF MAXIMUM STRENGTH FOR STRONG INTERACTIONS*. Phys. Rev. Lett., 8:41–44, 1962. URL http://dx.doi.org/10.1103/PhysRevLett.8.41. Cited on page 14.

Chung, S. *Formulas for Partial-Wave analysis*. Technical report, BNL, 2010. URL http://wwwcompass.cern.ch/twiki/pub/HadronAnalysis/PWAWorkshop/pwaform1.pdf. Cited on pages 83 and 161.

Chung, S. et al. (E852 collaboration). *Evidence for exotic $J^{PC} = 1^{-+}$ meson production in the reaction $\pi^- p \to \eta\pi^- p$ at 18 GeV/c*. Phys. Rev., D60:092001, 1999. arXiv:hep-ex/9902003, URL http://dx.doi.org/10.1103/PhysRevD.60.092001. Cited on pages 11, 94, and 100.

Chung, S., et al. *Exotic and $q\bar{q}$ resonances in the $\pi^+\pi^-\pi^-$ system produced in $\pi^- p$ collisions at 18 GeV/c*. Phys. Rev., D65:072001, 2002. Cited on page 13.

Chung, S.U. *Techniques of amplitude analysis for two pseudoscalar systems*. Phys. Rev., D56:7299–7316, 1997. URL http://dx.doi.org/10.1103/PhysRevD.56.7299. Cited on pages 87, 92, and 123.

Chung, S.U. and Trueman, T.L. *Positivity conditions on the spin density matrix: A simple parametrization*. Phys. Rev., D11:633–646, 1975. URL http://dx.doi.org/10.1103/PhysRevD.11.633. Cited on pages 19, 82, 87, and 88.

Cleland, W., et al. *RESONANCE PRODUCTION IN THE REACTION* $\pi^{\pm}p \to K^0_S K^{\pm}p$ *AT* 30 *AND* 50 GeV/c. Nucl. Phys., B208:228–261, 1982a. URL http://dx.doi.org/10.1016/0550-3213(82)90115-8. Cited on pages 123 and 163.

Cleland, W., et al. *Study of the Reactions* $K^{\pm}p \to K^0_S\pi^{\pm}p$ *at* 30 *and* 50 GeV/s*: Description of the apparatus and amplitude analysis of the* $K^0_S\pi$ *system*. Nucl. Phys., B208:189–227, 1982b. URL http://dx.doi.org/10.1016/0550-3213(82)90114-6. Cited on page 163.

Close, F. and Lipkin, H. *New Experimental Evidence for Four Quark Exotics: the Serpukhov* $\phi\pi$ *Resonance and the GAMS* $\eta\pi$ *Enhancement*. Phys. Lett., B196:245–250, 1987. URL http://dx.doi.org/10.1016/0370-2693(87)90613-7. Cited on pages 12 and 103.

Close, F.E. and Page, P.R. *The Production and Decay of Hybrid Mesons by Flux-Tube Breaking*. Nucl. Phys., B443:233–254, 1995. arXiv:hep-ph/9411301, URL http://dx.doi.org/10.1016/0550-3213(95)00085-7. Cited on pages 3 and 11.

Close, F.E. and Schuler, G.A. *Central production of mesons: Exotic states versus Pomeron structure*. Phys. Lett. B, 458:127–136, 1999a. arXiv:hep-ph/9902243, URL http://dx.doi.org/10.1016/S0370-2693(99)00450-5. Cited on page 17.

Close, F.E. and Schuler, G.A. *Evidence that the pomeron transforms as a nonconserved vector current*. Phys. Lett., B464:279–285, 1999b. arXiv:hep-ph/9905305, URL http://dx.doi.org/10.1016/S0370-2693(99)00875-8. Cited on pages 17, 76, and 78.

Cohen-Tannoudji, G., Salin, P., and Morel, A. *A Simple Formulation of High-Energy Exchange Models in Terms of Direct-Channel Amplitudes*. Nuovo Cim. A, 55:412–422, 1968. ISSN 0369-3546. URL http://dx.doi.org/10.1007/BF02857563. Cited on page 19.

Collins, P. and Martin, A. *Hadron reaction mechanisms*. Rept. Prog. Phys., 45:335, 1982. URL http://dx.doi.org/10.1088/0034-4885/45/4/001. Cited on pages 15 and 17.

Collins, P. and Martin, A. *Hadron Interactions*. Graduate Student Series in Physics. Adam Hilger Ltd., 1984. Cited on pages 15 and 17.

Costa, G. et al. (Bari-Bonn-CERN-Glasgow-Liverpool-Milano-Vienna collaboration). *An Amplitude Analysis of the* K^+K^- *System Produced in the Reaction* $\pi^-p \to K^+K^-n$ *AT* 10 GeV/c. Nucl. Phys., B175:402–434, 1980. URL http://dx.doi.org/10.1016/0550-3213(80)90020-6. Cited on page 92.

Crede, V. and Meyer, C. *The Experimental Status of Glueballs*. Prog. Part. Nucl. Phys., 63:74–116, 2009. arXiv:0812.0600. Cited on page 3.

Cummings, J. and Weygand, D. *An Object-Oriented Approach to Partial Wave Analysis*. Technical report, 2003. arXiv:physics/0309052v1. Cited on page 83.

Davydov, V.A. et al. *Particle Identification in a Hodoscope Cherenkov Spectrometer.* Nucl. Inst. Meth., 145:267, 1977. URL http://dx.doi.org/10.1016/0029-554X(77)90420-7. Cited on page 36.

Dhibar, K. *The Sandwich Veto Detector for COMPASS, CERN.* Master's thesis, Guru Gobind Singh Indraprastha University, 2008. Cited on page 46.

Diefenbach, M. *Monte Carlo Analysis of The Acceptances in the $\pi^-\eta'$ and $\pi^-\eta$ Final States at COMPASS (CERN).* Master's thesis, LMU, 2011. URL http://wwwcompass.cern.ch/compass/publications/theses/2011_bac_diefenbach.pdf. Cited on pages 36, 41, and 110.

Donnachie, A. and Page, P.R. *Interpretation of experimental J^{PC} exotic signals.* Phys. Rev., D58:114012, 1998. arXiv:hep-ph/9808225, URL http://dx.doi.org/10.1103/PhysRevD.58.114012. Cited on pages 12 and 130.

Donnachie, S., et al. *Pomeron Physics and QCD.* Camb. Monogr. Part. Phys. Nucl. Phys. Cosmol. Cambridge University Press, 2002. Cited on pages 17 and 79.

Dorofeev, V. et al. (VES collaboration). *The $J^{PC} = 1^{-+}$ hunting season at VES.* AIP Conf. Proc., 619:143–154, 2002. arXiv:hep-ex/0110075, URL http://dx.doi.org/10.1063/1.1482444. Cited on page 13.

Dorofeev, V., et al. *Measurement of the $f_1(1285) \to \pi^+\pi^-\pi^0$ decay.* Eur. Phys. J., A47:68, 2011. Cited on page 169.

Dudek, J.J. *The lightest hybrid meson supermultiplet in QCD.* Phys. Rev., D84:074023, 2011. arXiv:1106.5515, URL http://dx.doi.org/10.1103/PhysRevD.84.074023. Cited on page 2.

Dzierba, A. et al. *Study of the $\eta\pi^0$ spectrum and search for a $J^{PC} = 1^{-+}$ exotic meson.* Phys. Rev., D67:094015, 2003. arXiv:hep-ex/0304002, URL http://dx.doi.org/10.1103/PhysRevD.67.094015. Cited on page 12.

Dzierba, A.R. et al. *A partial wave analysis of the $\pi^-\pi^-\pi^+$ and $\pi^-\pi^0\pi^0$ systems and the search for a $J^{PC} = 1^{-+}$ meson.* Phys. Rev., D73:072001, 2006. arXiv:hep-ex/0510068, URL http://dx.doi.org/10.1103/PhysRevD.73.072001. Cited on page 13.

Escribano, R., Masjuan, P., and Sanz-Cillero, J.J. *Chiral dynamics predictions for $\eta' \to \eta\pi\pi$.* JHEP, 1105:094, 2011. arXiv:1011.5884, URL http://dx.doi.org/10.1007/JHEP05(2011)094. Cited on page 95.

Estabrooks, P. and Martin, A.D. *$\pi\pi$ Partial Waves from 0.6 to 1.8 GeV.* Nucl. Phys., B95:322, 1975. URL http://dx.doi.org/10.1016/0550-3213(75)90048-6. Cited on page 91.

Feinberg, E. and Pomerančuk, I. *High energy inelastic diffraction phenomena.* Nuov. Cim., 3:652–671, 1956. URL http://dx.doi.org/10.1007/BF02746068. Cited on page 14.

Feldmann, T. *Quark structure of pseudoscalar mesons.* Int. J. Mod. Phys., A15:159–207, 2000. arXiv:hep-ph/9907491. Cited on page 10.

Feldmann, T., Kroll, P., and Stech, B. *Mixing and decay constants of pseudoscalar mesons.* Phys. Rev., D58:114006, 1998. arXiv:hep-ph/9802409, URL http://dx.doi.org/10.1103/PhysRevD.58.114006. Cited on pages 10 and 137.

Forden, G.E. and Saxon, D.H. *IMPROVING VERTEX POSITION DETERMINATION USING A KINEMATIC FIT.* Nucl. Instrum. Meth., A248:439–450, 1986. URL http://dx.doi.org/10.1016/0168-9002(86)91031-4. Cited on page 33.

Frautschi, S.C., Gell-Mann, M., and Zachariasen, F. *Experimental Consequences of the Hypothesis of Regge Poles.* Phys. Rev., 126:2204–2218, 1962. Cited on page 15.

Frühwirth, R., et al. *Data Analysis Techniques for High-Energy Physics.* Cambridge University Press, second edition, 2000. Cited on pages 31 and 32.

Gasser, J. and Leutwyler, H. *Chiral Perturbation Theory to One Loop.* Annals Phys., 158:142, 1984. URL http://dx.doi.org/10.1016/0003-4916(84)90242-2. Cited on page 1.

Gasser, J. and Leutwyler, H. *Chiral Perturbation Theory: Expansions in the Mass of the Strange Quark.* Nucl. Phys. B, 250:465, 1985. URL http://dx.doi.org/10.1016/0550-3213(85)90492-4. Cited on page 1.

Gautheron, F. et al. (COMPASS collaboration). *COMPASS-II Proposal.* 2010. URL http://wwwcompass.cern.ch/compass/proposal/compass-II_proposal/compass-II_proposal.pdf. Cited on page 21.

GEANT. *GEANT – Detector Description and Simulation Tool.* CERN, 1994. Cited on pages 40 and 139.

Gell-Mann, M. *Factorization of Coupling to Regge Poles.* Phys. Rev. Lett., 8:263–264, 1962. URL http://dx.doi.org/10.1103/PhysRevLett.8.263. Cited on page 15.

Gell-Mann, M. *A Schematic Model of Baryons and Mesons.* Phys. Lett., 8:214–215, 1964. URL http://dx.doi.org/10.1016/S0031-9163(64)92001-3. Cited on pages 1 and 7.

Gersten, A. *Ambiguities of complex phase-shift analysis.* Nucl. Phys., B12:537–548, 1969. URL http://dx.doi.org/10.1016/0550-3213(69)90072-8. Cited on page 92.

Glashow, S., Iliopoulos, J., and Maiani, L. *Weak Interactions with Lepton-Hadron Symmetry.* Phys. Rev. D, 2:1285–1292, 1970. URL http://dx.doi.org/10.1103/PhysRevD.2.1285. Cited on page 33.

Godfrey, S. and Isgur, N. *Mesons in a Relativized Quark Model with Chromodynamics.* Phys. Rev., D32:189–231, 1985. URL http://dx.doi.org/10.1103/PhysRevD.32.189. Cited on page 2.

Good, M. and Walker, W. *Diffraction Dissociation of Beam Particles.* Phys. Rev., 120:1857–1860, 1960. URL http://dx.doi.org/10.1103/PhysRev.120.1857. Cited on page 14.

Gottfried, K. and Jackson, J.D. *On the Connection between Production Mechanism and Decay of Resonances at High Energies.* Nuovo Cim., 33:309–330, 1964. URL http://dx.doi.org/10.1007/BF02750195. Cited on page 19.

Govaerts, J., et al. *COUPLED QCD SUM RULES FOR HYBRID MESONS.* Nucl. Phys., B284:674, 1987. Cited on page 3.

Gribov, V., Dokshitzer, Y., and Nyiri, J. *Strong Interactions of Hadrons at High Energies.* Cambridge University Press, 2009. Cited on page 75.

Grindhammer, G. and Peters, S. *The parameterized simulation of electromagnetic showers in homogeneous and sampling calorimeters.* 1993. arXiv:hep-ex/0001020. Cited on pages 38, 41, 42, and 140.

Grindhammer, G., Rudowicz, M., and Peters, S. *THE FAST SIMULATION OF ELECTROMAGNETIC AND HADRONIC SHOWERS.* Nucl. Inst. Meth., A290:469, 1990. URL http://dx.doi.org/10.1016/0168-9002(90)90566-0. Cited on pages 38, 41, and 42.

Haas, F. *Private communication, March 2012*, 2012. Cited on pages 132 and 137.

Hansen, J.D., et al. *Formalism and Assumptions Involved in Partial Wave Analysis of Three-Meson Systems.* Nucl. Phys., B81:403, 1974. URL http://dx.doi.org/10.1016/0550-3213(74)90241-7. Cited on pages 18, 82, and 87.

Heisenberg, W. *Über den Bau der Atomkerne. I.* Z. Phys., 77:1–11, 1932. URL http://dx.doi.org/10.1007/BF01342433. Cited on page 7.

Hong-Mo, C., Kajantie, K., and Ranft, G. *A Regge Model for High-Energy Collisions Producing Three Final Particles.* Nuovo Cim. A, 49:157–182, 1967a. ISSN 0369-3546. URL http://dx.doi.org/10.1007/BF02739081. Cited on page 17.

Hong-Mo, C., et al. *Double Regge analysis of high-energy experiments producing three final particles.* Nuovo Cim. A, 51:696–716, 1967b. ISSN 0369-3546. URL http://dx.doi.org/10.1007/BF02721738. Cited on page 17.

Hyams, B., et al. *A study of the $\pi\pi$ phase-shift solutions in the mass region* 1.0 *to* 1.8 *GeV from* $\pi^- p \to \pi^-\pi^+ n$ *at* 17.2 *GeV.* Nucl. Phys. B, 100:205, 1975. URL http://dx.doi.org/10.1016/0550-3213(75)90616-1. Cited on page 91.

Isgur, N., Kokoski, R., and Paton, J. *Gluonic Excitations of Mesons: Why They Are Missing and Where to Find Them.* Phys. Rev. Lett., 54:869, 1985. URL http://dx.doi.org/10.1103/PhysRevLett.54.869. Cited on pages 3 and 11.

Isgur, N. and Paton, J.E. *Flux-tube model for hadrons in QCD.* Phys. Rev., D31:2910, 1985. URL http://dx.doi.org/10.1103/PhysRevD.31.2910. Cited on page 2.

Ivanov, E.I. et al. (E852 collaboration). *Observation of exotic meson production in the reaction $\pi^- p \to \eta' \pi^- p$ at 18 GeV/c.* Phys. Rev. Lett., 86:3977–3980, 2001. arXiv:hep-ex/0101058, URL http://dx.doi.org/10.1103/PhysRevLett.86.3977. Cited on pages 12, 69, and 79.

Ivashkin, A.P. et al. *Scintillation ring hodoscope with WLS fiber readout.* Nucl. Inst. Meth., A394(3):321 – 331, 1997. ISSN 0168-9002. URL http://dx.doi.org/DOI:10.1016/S0168-9002(97)00657-8. Cited on page 44.

Jackson, J. *Remarks on the Phenomenological Analysis of Resonances.* Nuovo Cim., 34:1644–1666, 1964. URL http://dx.doi.org/10.1007/BF02750563. Cited on page 160.

James, F. *Statistical Methods in Experimental Physics.* World Scientific, 2nd edition, 2006. Second edition of the homonymous book by W.T. Eadie et al. Cited on page 144.

Jasinski, P. *Analysis of Diffractive Dissociation of K^- into $K^-\pi^+\pi^-$ on a Liquid Hydrogen Target at the COMPASS Spectrometer.* Ph.D. thesis, Johannes Gutenberg Universität Mainz, 2012. URL http://wwwcompass.cern.ch/compass/publications/theses/2012_phd_jasinski.pdf. Cited on pages 24, 25, 35, and 43.

Johnson, K. *The M.I.T. Bag Model.* Acta Phys. Polon., B6:865, 1975. Cited on page 2.

Jones, H. *Groups, representations and physics.* Adam Hilger, 1990. Cited on page 6.

Kaidalov, A. et al. *Central exclusive diffractive production as a spin-parity analyser: from hadrons to Higgs.* Eur. Phys. J., C31:387–396, 2003. arXiv:hep-ph/0307064, URL http://dx.doi.org/10.1140/epjc/s2003-01371-5. Cited on page 17.

Kalman, R. *A New Approach to Linear Filtering and Prediction Problems.* Trans. ASME J. Basic Eng., 82:35–45, 1960. Cited on page 31.

Karyukhin, A. et al. *Radiation hardness study on molded scintillation tiles and wavelength shifting fibers.* Nucl. Inst. Meth., B117(4):415 – 420, 1996. ISSN 0168-583X. URL http://dx.doi.org/DOI:10.1016/0168-583X(96)00301-1. Cited on page 44.

Ke, H.W., Li, X.Q., and Wei, Z.T. *Determining the $\eta - \eta'$ mixing by the newly measured $BR(D(D_s) \to \eta(\eta') + \bar{l} + \nu_l$ [sic!].* Eur. Phys. J., C69:133–138, 2010. arXiv:0912.4094, URL http://dx.doi.org/10.1140/epjc/s10052-010-1383-6. Cited on page 11.

Ketzer, B., et al. *Performance of triple GEM tracking detectors in the COMPASS experiment.* Nucl. Inst. Meth., A535:314–318, 2004. Cited on page 29.

Kibble, T. *Feynman Rules for Regge Particles.* Phys. Rev., 131:2282–2291, 1963. URL http://dx.doi.org/10.1103/PhysRev.131.2282. Cited on pages 17 and 20.

Kleinknecht, K. *Detektoren für Teilchenstrahlung.* Teubner, 4th edition, 2005. Cited on page 38.

Klempt, E. and Zaitsev, A. *Glueballs, Hybrids, Multiquarks. Experimental facts versus QCD inspired concepts.* Phys. Rept., 454:1–202, 2007. arXiv:hep-ph/0708.4016, URL http://dx.doi.org/10.1016/j.physrep.2007.07.006. Cited on page 3.

Kobayashi, M., et al. *Radiation hardness of lead glasses TF1 and TF101.* Nucl. Inst. Meth., A345:210–212, 1994. URL http://dx.doi.org/10.1016/0168-9002(94)90990-3. Cited on page 40.

Kronfeld, A. and Quigg, C. *Resource Letter: Quantum Chromodynamics.* Am. J. Phys., 78:1081–1116, 2010. arXiv:1002.5032, URL http://dx.doi.org/10.1119/1.3454865. Cited on page 1.

Kuhn, J. et al. (E852 collaboration). *Exotic meson production in the $f_1(1285)\pi^-$ system observed in the reaction $\pi^- p \to \eta\pi^+\pi^-\pi^- p$ at 18 GeV/c.* Phys. Lett., B595:109–117, 2004. arXiv:hep-ex/0401004, URL http://dx.doi.org/10.1016/j.physletb.2004.05.032. Cited on page 13.

Landau, L. and Lifchitz, E. *Électrodynamique quantique*, volume 4 of *Physique théorique.* Éditions Mir Moscou, 2ème edition, 1989. Cited on page 6.

Latorre, J., Pascual, P., and Narison, S. *SPECTRA AND HADRONIC COUPLINGS OF LIGHT HERMAPHRODITE MESONS.* Z. Phys., C34:347, 1987. URL http://dx.doi.org/10.1007/BF01548817. Cited on page 3.

Lawson, C. and Hanson, R. *Solving Least Squares Problems.* Classics in Applied Mathematics. Society for Industrial Mathematics, 1987. Cited on page 144.

Lednev, A. (GAMS collaboration). *Study of the reaction $\pi^- p \to \eta\pi^0 n$ at 32, 38 and 100 GeV/c.* In S.U. Chung and H. Willutzki, editors, *Hadron Spectroscopy – Seventh International Conference*, number 432 in AIP Conference Proceedings, pages 253–263. 1997. Cited on page 89.

Lednev, A. *Shower reconstruction in nonideal electromagnetic calorimeters.* Instrum. Exp. Tech., 54:756–759, 2011. Cited on page 38.

Leo, W. *Techniques for Nuclear and Particle Physics Experiments.* Springer, second revised edition edition, 1994. Cited on page 27.

Leutwyler, H. *On the 1/N expansion in chiral perturbation theory.* Nucl. Phys. Proc. Suppl., 64:223–231, 1998. arXiv:hep-ph/9709408, URL http://dx.doi.org/10.1016/S0920-5632(97)01065-7. Cited on page 2.

Lipkin, H.J. *Quarks for pedestrians*. Phys. Rept., 8:173–268, 1973. URL http://dx.doi.org/10.1016/0370-1573(73)90002-1. Cited on page 6.

Lu, M. et al. (E852 collaboration). *Exotic meson decay to* $\omega\pi^0\pi^-$. Phys. Rev. Lett., 94:032002, 2005. arXiv:hep-ex/0405044, URL http://dx.doi.org/10.1103/PhysRevLett.94.032002. Cited on pages 13, 62, and 169.

Mandelstam, S. *An Extension of the Regge Formula*. Ann. Phys., 19(2):154–261, 1959. Cited on page 14.

Martin, A. et al. *A Study of Isospin 1 Meson States Using* $10\,GeV/c$ K^-K^0 *Production Data*. Phys. Lett., B74:417, 1978. URL http://dx.doi.org/10.1016/0370-2693(78)90693-7. Cited on pages 92, 94, 123, and 163.

Mathieu, V. and Vento, V. $\eta - \eta'$ *mixing in the flavor basis and large N*. Phys. Lett., B688:314–318, 2010a. arXiv:1003.2119, URL http://dx.doi.org/10.1016/j.physletb.2010.04.021. Cited on page 11.

Mathieu, V. and Vento, V. *Pseudoscalar glueball and* $\eta - \eta'$ *mixing*. Phys. Rev., D81:034004, 2010b. arXiv:0910.0212, URL http://dx.doi.org/10.1103/PhysRevD.81.034004. Cited on page 11.

Meyer, C. and Van Haarlem, Y. *Status of exotic-quantum-number mesons*. Phys. Rev., C82:025208, 2010. arXiv:1004.5516, URL http://dx.doi.org/10.1103/PhysRevC.82.025208. Cited on page 3.

Mineev, O. et al. *Photon sandwich detectors with WLS fiber readout*. Nucl. Inst. Meth., A494(1-3):362 – 368, 2002. ISSN 0168-9002. URL http://dx.doi.org/DOI:10.1016/S0168-9002(02)01493-6. Cited on page 44.

Nakamura, K. et al. (Particle Data Group collaboration). *Review of particle physics*. J. Phys., G37:075021, 2010. URL http://dx.doi.org/10.1088/0954-3899/37/7A/075021. Cited on pages 16, 33, 56, 71, 79, 85, 95, 136, 137, 162, 164, and 169.

Nappi, E. et al. (Hadron-Muon collaboration). *Semi-inclusive Muon Scattering from a Polarised Target*. 1995. URL http://wwwcompass.cern.ch/compass/publications/loi/loi_hmc.ps.gz. Cited on page 21.

Okubo, S. and Jagannathan, K. *Tests of the quark-line rule for the* $\eta\eta'$ *complex*. Phys. Rev., D15:177–183, 1977. URL http://dx.doi.org/10.1103/PhysRevD.15.177. Cited on page 103.

Omnès, R. and Froissart, M. *Mandelstam Theory and Regge Poles*. Frontiers in Physics. W. A. Benjamin, Inc., 1963. Cited on page 14.

Orear, J. *Notes on Statistics for Physicists*, 1958. University of California rep. UCRL-8417, URL http://nedwww.ipac.caltech.edu/level5/Setp01/Orear/Orear.html. Cited on page 82.

Page, P.R. *Why Hybrid Meson Coupling to Two S-wave Mesons is Suppressed.* Phys. Lett., B402:183–188, 1997. arXiv:hep-ph/9611375, URL http://dx.doi.org/10.1016/S0370-2693(97)00438-3. Cited on pages 3 and 11.

Page, P.R., Swanson, E.S., and Szczepaniak, A.P. *Hybrid meson decay phenomenology.* Phys. Rev., D59:034016, 1999. arXiv:hep-ph/9808346, URL http://dx.doi.org/10.1103/PhysRevD.59.034016. Cited on page 3.

Perl, M.L. *High Energy Hadron Physics.* John Wiley & Sons, Inc., 1974. Cited on page 79.

Photonis. *Photomultiplier Tubes Catalogue.* Photonis, 2007. Cited on page 46.

Pišút, J. and Roos, M. *Rho-Meson Shape.* Nucl. Phys., B6:325–352, 1968. URL http://dx.doi.org/10.1016/0550-3213(68)90001-1. Cited on page 160.

Raab, C. *Analysis of the $\eta'\pi$ and $\eta\pi$ Final States in COMPASS Data.* Master's thesis, TU, 2011. Cited on page 56.

Regge, T. *Introduction to complex orbital momenta.* Nuovo Cim., 14:951, 1959. URL http://dx.doi.org/10.1007/BF02728177. Cited on page 14.

Reinnarth, J. (Crystal Barrel collaboration). *Evidence for an exotic partial wave in $\pi\eta'$.* Nucl. Phys., A692:268c–274c, 2001. URL http://dx.doi.org/10.1016/S0375-9474(01)01186-1. Cited on page 12.

Rossi, A., et al. *Experimental Study of the Energy Dependence in Proton Proton Inclusive Reactions.* Nucl. Phys., B84:269, 1975. URL http://dx.doi.org/10.1016/0550-3213(75)90307-7. Cited on page 14.

Rossi, B. *High-Energy Particles.* Prentice-Hall, Inc., 1952. Cited on page 140.

Roushan, Z. *Inbetriebnahme eines Sandwich-Veto-Detektors am COMPASS-Experiment.* Master's thesis, LMU, 2009. Cited on page 55.

Ruiz de Elvira, J., et al. *Chiral Perturbation Theory, the $1/N_c$ expansion and Regge behaviour determine the structure of the lightest scalar meson.* Phys. Rev., D84:096006, 2011. arXiv:1009.6204, URL http://dx.doi.org/10.1103/PhysRevD.84.096006. Cited on page 2.

Ruschke, A. Private communication, May 2012. Cited on page 52.

Ryabchikov, D. (E852 collaboration). *Study of the reaction: $\pi^- p \to \eta\pi^+\pi^-\pi^- p$ in E852 experiment.* In S.U. Chung and H. Willutzki, editors, *Hadron Spectroscopy – Seventh International Conference*, number 432 in AIP Conf. Proc., pages 527–530. 1997. URL http://dx.doi.org/10.1063/1.56008. Cited on page 96.

Sadovsky, S. *On the Ambiguities in the Partial Wave Analysis of $\pi^- p \to \eta\pi^0 n$ reaction.* Technical report, IHEP 91-75, IHEP Protvino, 1991. Cited on page 92.

Sadovsky, S. *Comments to the partial wave analysis of the $\eta\pi$ system produced in peripheral pip-interactions.* Nucl. Phys., A655:131–136, 1999. URL http://dx.doi.org/10.1016/S0375-9474(99)00191-8. Cited on page 11.

Schlüter, T. (COMPASS collaboration). *The COMPASS sandwich veto detector and a first look at kaonic final states from a $\pi^-(190\,GeV)$ beam on a proton target.* Eur. Phys. J., C, 2009. To be published, arXiv:1108.4295. Cited on page 75.

Schlüter, T. (COMPASS collaboration). *Study of kaonic final states in $\pi^- p$ at 190 GeV.* AIP Conf. Proc., 1257:462–466, 2010. arXiv:1108.4303, URL http://dx.doi.org/10.1063/1.3483372. Cited on page 75.

Schlüter, T., et al. *Large-Area Sandwich Veto Detector with WLS Fibre Readout for Hadron Spectroscopy at COMPASS.* Nucl. Inst. and Meth., A654:219, 2011a. ISSN 0168-9002. arXiv:1108.4587, URL http://dx.doi.org/10.1016/j.nima.2011.05.069. Cited on page 44.

Schlüter, T. et al. *Release note for the $\pi^-\eta'$ reconstructed from 2008 data*, 2011b. Cited on page 64.

Schmid, C. *Direct-Channel Resonances from Regge-Pole Exchange.* Phys. Rev. Lett., 20:689–691, 1968. URL http://dx.doi.org/10.1103/PhysRevLett.20.689. Cited on page 17.

Shimada, T., Martin, A., and Irving, A. *DOUBLE REGGE EXCHANGE PHENOMENOLOGY.* Nucl. Phys., B142:344, 1978. URL http://dx.doi.org/10.1016/0550-3213(78)90209-2. Cited on pages 17 and 110.

St. Gobain 2002. *Data Sheet 06-02.* Saint-Gobain Inc., 2002. Cited on page 45.

St. Gobain 2005. *Data Sheet 03-05.* Saint-Gobain Inc., 2005. Cited on page 45.

Szczepaniak, A., Swat, M., and Teige, S. *Partial Wave Formalism and S-wave parametrization.* Technical report, Indiana University, 2004. URL http://dustbunny.physics.indiana.edu/3pi_paper/note_016/note_016.pdf. Cited on page 83.

Szczepaniak, A., et al. *$\eta\pi$ and $\eta'\pi$ Spectra and Interpretation of Possible Exotic $J^{PC} = 1^{-+}$ Mesons.* Phys. Rev. Lett., 91:092002, 2003. arXiv:hep-ph/0304095, URL http://dx.doi.org/10.1103/PhysRevLett.91.092002. Cited on pages 12 and 100.

't Hooft, G. *How Instantons Solve the $U(1)$ Problem.* Phys. Rept., 142:357–387, 1986. URL http://dx.doi.org/10.1016/0370-1573(86)90117-1. Cited on page 11.

Thompson, D. et al. (E852 collaboration). *Evidence for Exotic Meson Production in the Reaction $\pi^- p \to \eta\pi^- p$ at 18 GeV/c.* Phys. Rev. Lett., 79:1630–1633, 1997. arXiv:hep-ex/9705011, URL http://dx.doi.org/10.1103/PhysRevLett.79.1630. Cited on pages 11 and 67.

Thompson, G., et al. (Bologna-Florence-Genoa-Milan-Oxford-Pavia collaboration). *Partial-wave analyses of the $(3\pi)^-$ system in the reaction $\pi^- p \to \pi^-\pi^-\pi^+ p$ at 11.2 GeV/c.* Nucl. Phys., B101(2):285 – 303, 1975. ISSN 0550-3213. URL http://dx.doi.org/DOI:10.1016/0550-3213(75)90599-4. Cited on pages 18 and 19.

Tuan, S., Ferbel, T., and Dalitz, R. *COMMENTS ON THE EVIDENCE FOR A 1^{-+} EXOTIC MESON.* Phys. Lett., B213:537, 1988. Cited on pages 11 and 12.

Ullaland, O. *Fluid systems for RICH detectors.* Nucl. Inst. Meth., A553:107–113, 2005. URL http://dx.doi.org/10.1016/j.nima.2005.08.033. Cited on page 34.

Veneziano, G. *Construction of a Crossing-Simmetric, Regge-Behaved Amplitude for Linearly Rising Trajectories.* Nuovo Cim., A57:190–197, 1968. URL http://dx.doi.org/10.1007/BF02824451. Cited on page 17.

von Hippel, F. and Quigg, C. *Centrifugal-barrier effects in resonance partial decay widths, shapes, and production amplitudes.* Phys. Rev., D5:624–638, 1972. URL http://dx.doi.org/10.1103/PhysRevD.5.624. Cited on pages 103 and 161.

Weinberg, S. *Phenomenological Lagrangians.* Physica, A96:327, 1979. URL http://dx.doi.org/10.1016/0378-4371(79)90223-1. Cited on page 1.

Weitzel, Q. *Precision Meson Spectroscopy: Diffractive Production at COMPASS and Development of a GEM-based TPC for PANDA.* Ph.D. thesis, Technische Universität München, 2008. URL http://wwwcompass.cern.ch/compass/publications/theses/2008_phd_weitzel.pdf. Cited on page 143.

Wigmans, R. *Calorimetry.* Oxford University Press, 2000. Cited on pages 36 and 140.

Wöhrmann, H. *Diffraktive Produktion von Drei-Körper-Endzuständen in $\pi^- p$-Wechselwirkung am COMPASS-Experiment (CERN).* Master's thesis, LMU, 2010. URL http://wwwcompass.cern.ch/compass/publications/theses/2010_dpl_woehrmann.pdf. Cited on pages 52, 55, 56, 79, and 165.

Yershov, N. et al. *Long sandwich modules for photon veto detectors.* Nucl. Inst. Meth., A543(2-3):454 – 462, 2005. ISSN 0168-9002. URL http://dx.doi.org/DOI:10.1016/j.nima.2004.11.051. Cited on page 44.

Zweig, G. *An SU_3 model for strong interaction symmetry and its breaking*, 1964a. CERN-TH-401, URL http://cdsweb.cern.ch/record/352337?ln=en. Cited on pages 1 and 7.

Zweig, G. *An SU_3 model for strong interaction symmetry and its breaking II*, 1964b. CERN-TH-412, URL http://cdsweb.cern.ch/record/570209/files/cern-th-412.pdf. Cited on pages 1 and 7.